School of Electrical Engineering, Computing and Mathematical Sciences
Curtin Institute of Radio Astronomy
International Centre of Radio Astronomy Research

Mapping the Galaxy in 3D Using Observations of HII Region Absorption with the MWA

Hongquan Su

This thesis is presented for the Degree of
Doctor of Philosophy
of
Curtin University

July 2022

To the best of my knowledge and belief this thesis contains no material previously published by any other person except where due acknowledgement has been made. This thesis contains no material which has been accepted for the award of any other degree or diploma in any university.

"Always do your best in whatever you do."

- Charles F. Bolden

Acknowledgements

This thesis would not have been possible without the support and guidance of my supervisors Jean-Pierre Macquart, Natasha Hurley-Walker, Naomi McClure-Griffiths, and Carole Jackson. The contributions from any of them are unique and essential, no matter the order listed above. I really appreciate their time spent with me and their contributions to this thesis. In particular, the GLEAM survey led by Natasha is the basis of this thesis and many other successful projects. The clear and critical scientific thinking of J-P kept me focused on the right questions to think about. The strong Galactic science background of Naomi made my topic well connected with other Galactic science. The writing skills learned from Carole benefited the writing of this thesis and many reports.

I thank Steven Tingay for suggestions regarding synchrotron emission, James Miller-Jones for comments on my candidacy and presentations, Paul Hancock for explaining the Aegean package[1] (Hancock et al., 2012, 2018), Randall Wayth for explaining the operation of the MWA, Cathryn Trott for suggestions about error estimation, Christopher Jordan for discussing HII region detections, and Wenwu Tian for explaining kinematic distances.

I thank Sammy McSweeney for teaching me English during weekly English classes, which are not only practical but also entertaining. Sammy's kindness inspires me to contribute more to the community.

Thank you to Thomas Russell for teaching me data correlation and giving me advice both on my academic career and life. Thank you to Cormac Reynolds for giving

[1] https://github.com/PaulHancock/Aegean

me a casual job. Thank you to Ryan Urquhart, Hayley Bignall and Teresa Slaven-Blair for their kind lifts.

I am grateful to the people in the Curtin Institute of Radio Astronomy (CIRA) for their success in creating a friendly and supportive community. I enjoyed the Journal Club, Python Club, International Lunch, and Lantern Festival. Many people get involved in these events, including Clancy James, Steven Murray, Richard Plotkin, Sarah White, Marcin Solkolowski, Andrew Williams, John Morgan, Christofer Jordan, Ramesh Bhat, Gemma Anderson, Rajan Chhetri, Budi Juswardy, Benjamin McKinley, Mengyao Xue, Ronniy Joseph, Pikky Atri, Bella Nasirudin, Dilpreet Kaur, Bradley Meyers, Bach Nguyen, Stefan Duchesne, and many others. I thank Angela Dunleavy for making me feel that CIRA is my home. I thank CIRA for providing a table tennis table and Brendan McGann, Alec Duncan, Zhonghua Sun, Qingzeng Yan for enjoying table tennis with me.

This scientific work makes use of the Murchison Radio-astronomy Observatory, operated by CSIRO. We acknowledge the Wajarri Yamatji people as the traditional owners of the Observatory site. Support for the operation of the Murchison Widefield Array (MWA) is provided by the Australian Government (NCRIS), under a contract to Curtin University administered by Astronomy Australia Limited. We acknowledge the Pawsey Supercomputing Centre which is supported by the Western Australian and Australian Governments. I thank the financial supports from the Chinese Scholarship Council and the Curtin University.

I give special thanks to my wife Jun-Huan and my parents for their mental support.

Abstract

The Galactic plane is full of diffuse synchrotron emission at radio frequencies less than $\sim$1 GHz, generated from the interaction between cosmic ray electrons and the Galactic magnetic field. Radio surveys map the projection of this emission onto the plane of the sky. However, the 3D distribution of this diffuse emission from the Milky Way is not well characterized. Absorption from HII regions embedded in the synchrotron-emitting plasma at frequencies less than about 150 MHz provides a means to probe the 3D synchrotron distribution, by enabling us to separate the total synchrotron emission along the line of sight into two columns: one from the HII region to the Galactic edge, and the other from the HII region to the Sun.

This project maps the distribution of the synchrotron emission along the line of sight in the Galactic plane using data from the GaLactic and Extragalactic All-sky MWA survey (GLEAM) in the frequency range from 72 to 231 MHz, with better angular resolution by a factor of $>$5 than previous surveys at these frequencies. The GLEAM survey significantly enhanced the sensitivity to HII regions, increasing the number of detectable HII region absorption features from tens to hundreds. For the HII regions with known distances, we derive the synchrotron distribution in the Milky Way disk from 152 HII region absorption observations over $-40^\circ < l < 40^\circ$ at the six frequencies 76.2, 83.8, 91.5, 99.2, 106.9, and 114.6 MHz from GLEAM.

Previous methods of synchrotron emissivity do not work for measurements with missing flux on short baselines. Another problem is that the methods rely on the HII region being highly opaque. We solved these two problems by developing a new method using multi-frequency observations and by utilizing the Haslam et al. (1981) map in

our analysis. The new method we developed help derived the synchrotron emissivity and the HII region optical depth at six frequencies from 152 absorption features. This improved method also derived the emissivity from HII regions to the Sun.

We build four simple models to re-construct the emissivity distribution as a function of the Galactocentric radius using our initial 47 emissivities. A simple model which divides the Galactic disk into two circles with different radius is found to best account for our observed emissivity distribution. The emissivity near the Galactic centre is the highest ($\sim$2.0 K pc^{-1}), while the emissivity in the Galactic edge region is lowest ($\sim$0.3 K pc^{-1}). Our improved method contains much more information about emissivity distribution which will benefit future attempts to model the Galactic synchrotron distribution.

We further identify all the HII regions detected in the Galactic longitude range of $-40^{\circ} < l < 40^{\circ}$ from both their emission features and absorption features across the whole observing band. We find 588 HII regions in total, and present their integrated flux density at 20 frequencies in the range from 76 to 227 MHz. About 50 of them have turnover frequencies within the GLEAM band, enabling the derivation of constraints on the emission measure, electron density, mass of ionized gas, and the Lyman continuum photoionization rate of these HII regions.

List of Abbreviations

ATCA Australia Telescope Compact Array

BANE the Background and Noise Estimation tool

CMB Cosmic Microwave Background

CMZ Central Molecular Zone

EM emission measure

EoR Epoch of Reionization

FWHM Full Width at Half Maximum

GBT Green Bank Telescope

GLEAM GaLactic and Extragalactic All-sky MWA survey

HRDS HII Region Discovery Survey

LMC Large Magellanic Cloud

LOFAR Low Frequency Array

MWA Murchison Widefield Array

PWN Pulsar Wind Nebulae

RRL Radio Recombination Lines

rms root mean square

SGPS Southern Galactic Plane Survey

SHRDS Southern HII Region Discovery Survey

SKA Square Kilometre Array

THOR the HI/OH/Recombination line survey

UV Ultraviolet

VGPS VLA Galactic Plane Survey

VLA Very Large Array

WMAP Wilkinson Microwave Anisotropy Probe

Contents

List of Tables

List of Figures

List of Publications

Publications directly used in the thesis include:

1. **H. Su**, N. Hurley-Walker, C. A. Jackson, N. M. McClure-Griffiths, S. J. Tingay, L. Hindson, P. Hancock, R. B. Wayth, B. M. Gaensler, L. Staveley-Smith, J. Morgan, M. Johnston-Hollitt, E. Lenc, M. E. Bell, J. R. Callingham, K. S. Dwarkanath, B.-Q. For, A. D. Kapińska, B. McKinley, A. R. Offringa, P. Procopio, C. Wu, and Q. Zheng (2017a, March). Galactic synchrotron emissivity measurements between $250^\circ < l < 355^\circ$ from the GLEAM with the MWA. MNRAS, 465, 3163–3174. DOI: 10.1093/mnras/stw2959

2. **H. Su**, N. Hurley-Walker, C. A. Jackson, N. M. McClure-Griffiths, S. J. Tingay, L. Hindson, P. Hancock, R. B. Wayth, B. M. Gaensler, L. Staveley-Smith, J. Morgan, M. Johnston-Hollitt, E. Lenc, M. E. Bell, J. R. Callingham, K. S. Dwarkanath, B.-Q. For, A. D. Kapińska, B. McKinley, A. R. Offringa, P. Procopio, C. Wu, and Q. Zheng (2017b, November). ***Erratum***: Galactic synchrotron emissivity measurements between $250^\circ < l < 355^\circ$ from the GLEAM with the MWA. MNRAS, 472, 828–834. DOI: 10.1093/mnras/stx2129

3. **H. Su**, J. P. Macquart, N. Hurley-Walker, N. M. McClure-Griffiths, C. A. Jackson, S. J. Tingay, W. W. Tian, B. M. Gaensler, B. McKinley, A. D. Kapińska, L. Hindson, P. Hancock, R. B. Wayth, L. Staveley-Smith, J. Morgan, M. Johnston-Hollitt, E. Lenc, M. E. Bell, J. R. Callingham, K. S. Dwarkanath, B.-Q. For,

A. R. Offringa, P. Procopio, C. Wu, and Q. Zheng (2018, September). Galactic synchrotron distribution derived from 152 HII region absorption features in the full GLEAMsurvey. MNRAS, 479, 4041–4055. DOI: 10.1093/mnras/sty1732

Publications not directly used in the thesis include:

- L. Hindson, M. Johnston-Hollitt, N. Hurley-Walker, J. R. Callingham, **H. Su**, J. Morgan, M. Bell, G. Bernardi, J. D. Bowman, F. Briggs, R. J. Cappallo, A. A. Deshpande, K. S. Dwarakanath, B.-Q. For, B. M. Gaensler, L. J. Greenhill, P. Hancock, B. J. Hazelton, A. D. Kapinska, D. L. Kaplan, E. Lenc, C. J. Lonsdale, B. Mckinley, S. R. McWhirter, D. A. Mitchell, M. F. Morales, E. Morgan, D. Oberoi, A. Offringa, S. M. Ord, P. Procopio, T. Prabu, N. U. Shankar, K. S. Srivani, L. Staveley-Smith, R. Subrahmanyan, S. J. Tingay, R. B. Wayth, R. L. Webster, A. Williams, C. L. Williams, C. Wu, and Q. Zheng (2016, May). A Large-Scale, Low-Frequency Murchison Widefield Array Survey of Galactic HII regions between $260 < l < 340$. PASA, 33:e020. DOI: 10.1017/pasa.2016.19

Table of contributions

Table 1: Declaration of contributions to this thesis. The first column is the Chapter number and the second one is the publication number from the List of Publications.

Chap.	Pub.Num.	Status	Contributions
2	1 & 2	Published	**H. Su** (78%): data analysis; modelling; paper writing
			N. Hurley-Walker (10%): data calibration; supervision; comments
			C. A. Jackson (5%): supervision; comments
			N. M. McClure-Griffiths (5%): supervision; comments
			Other co-authors (2%): comments
3	3	Published	**H. Su** (71%): data analysis; paper writing
			J.-P. Macquart (10%): methodology; supervision; comments
			N. Hurley-Walker (10%): data calibration; supervision; comments
			N. M. McClure-Griffiths (5%): supervision; comments
			C. A. Jackson (2%): comments
			Other co-authors (2%): comments
4	None	In preparation	**H. Su** (∼74%): data analysis; paper writing
			N. Hurley-Walker (∼10%): data calibration; supervision; comments
			J.-P. Macquart (∼10%): methodology; supervision; comments
			N. M. McClure-Griffiths (∼2%): comments
			C. A. Jackson (∼2%): comments
			Other co-authors (∼2%): comments

The only thing in the thesis was not produced by me is the data calibration and imaging of the GLEAM survey. This was performed by Natasha Hurley-Walker.

Chapter 1

Introduction

1.1 Review of the Milky Way

Our Galaxy, the Milky Way, is a spiral galaxy consisting of a disk with several spiral arms and a bar near its centre (see Fig. 1.2). The disk rotates with nearly a constant speed at radii $4 \lesssim R \lesssim 20$ kpc (Mróz et al., 2019), with the Sun located in the disk at a Galactocentric distance of 8.34 ± 0.16 kpc (Reid et al., 2014). The Sun is located in the Local Arm, as recently investigated in detail in Xu et al. (2016), who accurately measured distances to star-forming regions, and found that the Local Arm is comparable to the Galactic major spiral arms, such as Sagittarius, in its pitch angle and star formation rate.

The rotation curve of the Milky Way, its circular velocity as a function of the Galactocentric distance, can help constrain the mass distribution of the Milky Way, including its dark matter (e.g. Weber and de Boer 2010). Many efforts have been made to derive the Galactic rotation curve. The tangent point method of neutral hydrogen (see Fig. 1.1) is a powerful means to trace the rotation velocity inside the solar circle (Clemens, 1985; Fich et al., 1989; Levine et al., 2008; McClure-Griffiths and Dickey, 2007; Sofue et al., 2009; McClure-Griffiths and Dickey, 2016). For regions beyond the

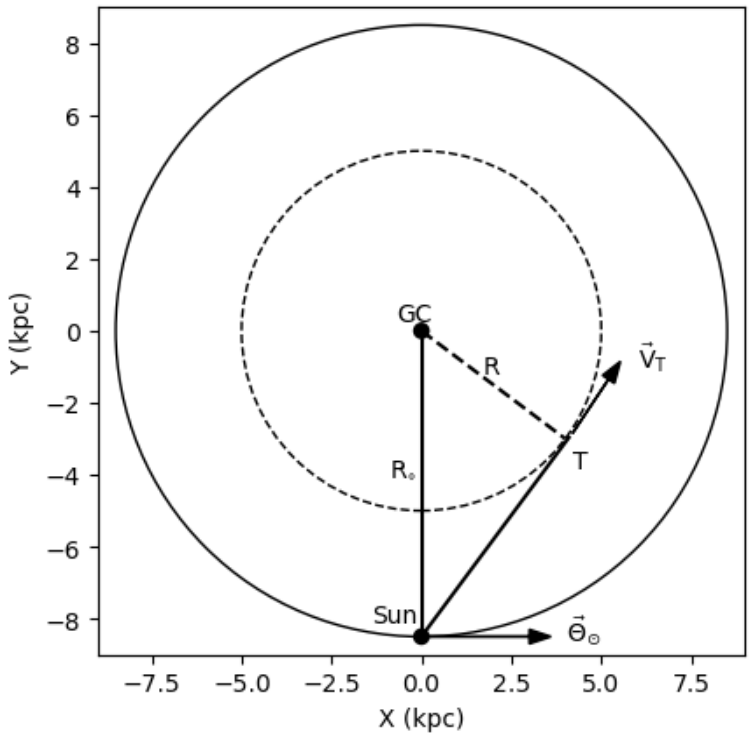

Figure 1.1: The geometry of the Sun, Galactic centre (GC), and tangent point (T) drawn from the vantage point of the south Galactic pole. The Sun is at radius $R_\circ$ with a circular velocity of $\vec{\Theta}_\odot$. The tangent point is at radius R with a velocity of $\vec{V}_T$.

solar circle, no tangent velocity is available for deriving the rotation curve. Different tracers with measured distances and radial velocities can help to constrain the rotation curve, such as HI (e.g. Merrifield 1992), HII regions (e.g. Brand and Blitz 1993), and red clump giants (Huang et al., 2016).

One challenge of observing the full three-dimensional structure of the Galaxy is that we are embedded in the Galactic plane, so we observe radiation integrated along the line of sight. Many efforts have been made to reveal the three-dimensional distribution of clouds, stars, dust, magnetic fields, and cosmic rays.

Stars in the Milky Way are becoming an important tracer of the Galactic structure thanks to extensive surveys such as *Gaia*, and the Sloan Digital Sky Survey. The *Gaia* spacecraft aims to astronomically measure the positions and distances of stars, with the

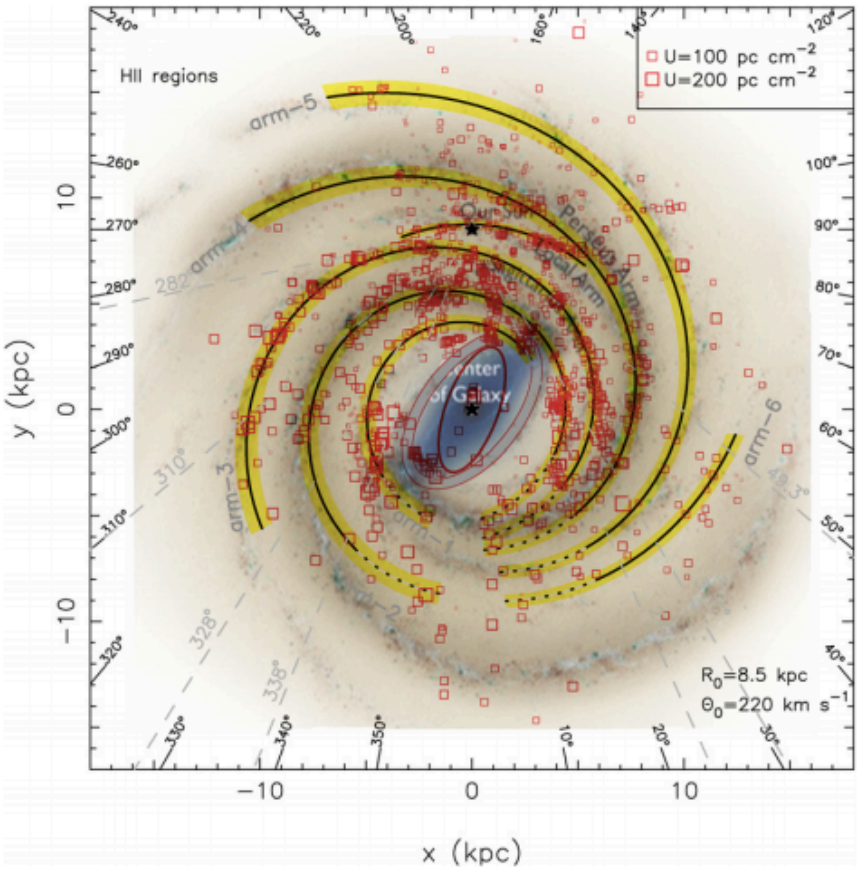

Figure 1.2: The Milky Way spiral structure (blue and gray, NASA/JPL-Caltech/R. Hurt) overlaid with observed HII regions (red squares) adapted from Hou and Han (2014). The yellow arms are fitted from the distribution of HII regions with their symbol area proportional to the excitation parameters.

Gaia collaboration et al. (2018) recently reporting the detection of 1.3 billion sources with positions, distances and proper motions in our Galaxy. The median uncertainty of the measured position and proper motion for the bright sources ($G < 14$ mag) is 0.03 mas and 0.07 mas yr^{-1}, respectively. These measurements probe the velocity field of stars in the Galactic plane. The initial results show the Galactic plane has negative and positive Galactocentric radial velocity gradients, indicating a non-axisymmetric kinematic oscillation (Gaia collaboration et al., 2018); therefore, our Galaxy is not an axisymmetric system at equilibrium. Such patterns are difficult to discover without the full-sky 3D view of the Galaxy velocity. Furthermore, observations from the Sloan Digital Sky Survey have revealed the structure of rings and radial waves in star counts in the anti-centre direction of the Milky Way, which may be the result of disk oscillations and might relate to the spiral arms (Xu et al., 2015).

The structure of the Milky Way is riddled with features due to tidal stripping and mergers. The stellar density in the halo of the Milky Way does not vary smoothly as a power law with galactocentric radius. In nearly all directions, its stellar distribution shows large structures with scale lengths of $\sim$10 kpc. These structures are likely associated with the streamers of tidally stripped stars, dwarf galaxies, and globular clusters (Newberg et al., 2002).

Hydrogen in the Milky Way, mainly in the form of neutral hydrogen (HI), constitutes the majority ($\sim$90%) of the total visible Galactic mass (Nakanishi and Sofue, 2016). HI clouds radiate at the frequency of 1.4 GHz from the transition between the two hyperfine levels of the hydrogen in the ground state. This emission line can be used to trace the spiral structure of the Milky Way because its intensity reflects the column density of neutral hydrogen, and its radial velocity can be used to deduce its location. Oort et al. (1958) first used this method to show the distribution of neutral hydrogen in the Galaxy. Levine et al. (2006) revealed the structure outside of the so-

lar circle, i.e. the circular orbit of the Sun surrounding the centre of the Milky Way. They measured the surface density of neutral hydrogen outside of the solar circle in the Galactic disk using data from the Leiden-Argentine-Bonn survey (LAB, Kalberla et al. 2005). This revealed a clear multi-armed spiral structure after a number of small features (e.g. background galaxies) and large features (e.g. clouds and spurs coming off the disk) were subtracted from the data. They also found the HI surface density of arm regions to be triple that of the inter-arm regions. The Galactic disk is not strictly flat, with its outer disk warping upwards (northwards) in the first and second quadrants, and downwards on the opposite side (Burke, 1957; Kerr, 1957). Although most abundant in the disk region, HI clouds also exist in the halo of the Milky Way in the form of both dense (bright, narrow line-widths and relatively cold) and diffuse (faint, broad line-widths and relatively warm) high-velocity HI gas (e.g. Moss et al. 2017). We refer the reader to the review by Kalberla and Kerp (2009) for further details on the distribution of HI in our Galaxy.

The Galactic plane has been surveyed at multiple radio frequencies from 10 MHz to 5 THz (see e.g. Zheng et al. 2017; Heyer and Dame 2015; Kalberla and Kerp 2009). A large number of surveys have been conducted at 1.4 GHz where it is feasible to undertake surveys of the entire sky. For instance, the northern sky has been mapped by the Very Large Array (VLA) Galactic Plane Survey (VGPS), which produced HI and spectral line maps (Stil et al., 2006), while the Southern Galactic Plane Survey (SGPS) charted the southern sky, both in total intensity (McClure-Griffiths et al., 2005), and polarisation (Haverkorn et al., 2006). The SGPS revealed entirely new structure in the Galaxy: a previously unidentified spiral arm at a galactocentric radius of 18-24 kpc (McClure-Griffiths et al., 2004) demonstrated the ability of these surveys to chart the large-scale structure of the Milky Way. Recently, a deep survey of the northern sky, the HI/OH/Recombination line survey (THOR), was undertaken in full polarisation using

the Very Large Array (VLA) (Beuther et al., 2016). Its angular resolution is improved by a factor of >5 from 60″ (VLA Galactic Plane Survey (VGPS)) and 120″ (SGPS) to 20″, which is an angular resolution comparable to most infrared and millimetre surveys. the HI/OH/Recombination line survey (THOR) observed the HI line, four ground state OH lines, and 19 Hα recombination lines as well as the L-band continuum between 1 and 2 GHz. It is useful for studying a variety of astrophysical objects, such as finding hypercompact HII regions (Yang et al., 2019). THOR enabled detailed studies of supernova remnants, HII regions, molecular clouds, magnetic fields in the Milky Way, as well as extragalactic background sources. With the THOR survey, Wang et al. (2018) identified 840 HII regions, 52 SNRs, 164 PNe, 38 pulsars, 699 ultra-steep spectrum sources ($\alpha < -1.3$), and ∼9000 unclassified sources.

The ionized hydrogen, denoted by HII, also traces the spiral arms. Usually, HII regions are born in the arm regions and are the host of masers whose distances might be accurately measured by the parallax method (Reid et al., 2014). Much effort has been dedicated to determine the distances of HII regions to trace the spiral structure (e.g., Downes et al. 1980; Caswell and Haynes 1987; Araya et al. 2002). (Paladini et al., 2004) used 550 HII regions to analyse the spatial distribution of HII regions. Hou and Han (2014) use 2500 HII regions and 2100 other sources to trace the spiral arms (as shown in their Fig. 10).

The molecular gas distribution is also used to probe the structure of our Galaxy. Dame et al. (2001) produced a new composite CO cloud survey of the entire Milky Way by combining the observations of the CfA 1.2 m telescope and 31 previous CO surveys obtained over the last two decades of the 20th century. This survey covers the entire Milky Way and consists of 488,000 spectra over a strip $\mid b \mid < 5^{\circ}$ in latitude. This survey shows information on individual CO clouds, and clearly displays the main structural features of the Galactic molecular clouds. Specifically, it shows that these

clouds are mainly confined to the inner spiral arms of the Milky Way. The molecular spiral arms with intense CO emission shown in this survey is located beyond and just inside the solar circle, i.e. near the Perseus arm and the Carina arm. Pettitt et al. (2014) simulated nearly all features in the CO cloud survey of Dame et al. (2001) by using smoothed particle hydrodynamics and inferred the arm/bar geometry of our Galaxy. Their models favour a bar pattern (see Fig. 1.2) speed of 50−60 km s^{-1} kpc^{-1} and an arm pattern speed of ∼20 km s^{-1} kpc^{-1}.

The velocity-integrated line intensity of molecular gas ^{12}CO (J=1-0) (W_{CO}) can be applied to derive the column density of molecular hydrogen (N_{H_2}) by using a conversion factor (X_{CO}) defined as

$$X_{CO} = \frac{N_{H_2}}{W_{CO}}. \tag{1.1}$$

This conversion factor is widely used because CO is much easier to detect compared to H_2 (see e.g. Narayanan et al. 2012). CO has relatively high abundance (about 10^{-4}/H_2 in the Milky Way), high atmospheric transmission, and low temperatures and densities for excitation. However, H_2 is difficult to observe because it has no permanent dipole moment, so its lowest detectable spectral line is an electric quadrupole transition. This line requires a gas temperature of about 500 K, which is much higher than typical temperature $\sim$ 10 K of the cold molecular clouds.

Dust in the Milky Way represents only 1% of the mass of the interstellar medium, but it absorbs ∼30% of all starlight (Draine, 2003). Dust mainly pervades the Galactic plane. Recently, Green et al. (2015) revealed the 3D distribution of the dust in the Milky Way using the reddening of 800 million stars observed by Pan-STARRS 1 (an optical and near-infrared telescope located on Mount Haleakala, Hawaii) and 2MASS (the Two Micron All-Sky Survey, Skrutskie et al. 2006). This dust map can be used to deduce the reddening in any given direction and distance covering three-quarters of the sky out to a distance of several kpc. The angular resolution of the map is in the range

from 3.4′ to 13.7′, enabling the map to reveal structures from filaments to large cloud complexes. The 3D dust map is useful for correcting the extinction on the Galactic Plane and measuring distances to objects with known reddening.

1.2 Diffuse Galactic synchrotron radiation

Radio continuum observations can directly map the two-dimensional (2D) distribution of the whole sky. Such maps exist at multiple frequencies from MHz to GHz (e.g. Haslam et al. 1981; Dwarakanath and Udaya Shankar 1990; Alvarez et al. 1997; Roger et al. 1999). de Oliveira-Costa et al. (2008) and Zheng et al. (2017) contain a summary of such surveys. These maps are from single-dish observations with flux density absolutely calibrated.

The emission from these global sky maps comprises six main components: synchrotron emission, the Cosmic Microwave Background (CMB), neutral hydrogen emission, warm dust, cold dust, and free-free emission (see Fig. 5 in Zheng et al. 2017). The diffuse synchrotron emission is the dominant component in the frequency range from several MHz to GHz. The relativistic electrons accelerated in the Galactic magnetic field generate the synchrotron emission. The total radiative power of a synchrotron-emitting electron (P) is

$$P \propto B^2 E^2 \tag{1.2}$$

where B is the strength of the magnetic field, and E is the electron energy (Westfold, 1959; Epstein and Feldman, 1967). The total radiative power of all synchrotron-emitting electrons in a radio source is the summary of each electron's power, therefore the relation in Equation 1.2 also works for a radio source with many electrons. each still hold this relation. Given the degeneracy between B and E, models seeking to reproduce the synchrotron emission power need to include both the Galactic distribu-

tion of the magnetic field and cosmic-ray electrons. Therefore, observing the diffuse emission in the Galaxy and comparison with models is fundamental for studying the Galactic magnetic field and cosmic-ray electrons, and their distribution and propagation in the Galaxy (see e.g. Orlando and Strong 2013).

The contribution of extragalactic backgrounds to the Galactic synchrotron signal is usually neglected over a wide range of frequencies. One extragalactic component is the CMB, with a blackbody temperature of 2.7 K. The other large component, particularly at metre wavelengths, is the non-thermal background originating from unresolved extragalactic sources. Its brightness temperature drops from $\sim$1100 K to $\sim$2.4 K in the frequency range from 45 to 408 MHz (Guzmán et al., 2011).

The main signal present in the Galactic maps at radio frequencies of tens or hundreds of MHz is the Galactic diffuse synchrotron emission. The most widely-used map for investigating the Galactic diffuse synchrotron radiation is that of Haslam et al. 1981 (hereafter referred to as the "Haslam map") at the frequency of 408 MHz with an angular resolution of $51'$. The Haslam map combines data from surveys using the Parkes 64-metre, Bonn 100-metre, Jodrell Bank MkI, and Jodrell Bank MkIA telescopes. It is dominated by synchrotron emission, with minor contributions from free-free emission and absorption. Remazeilles et al. (2015)[1] has recently re-processed the raw Haslam 408 MHz data and produced an improved map with extra-galactic sources removed.

The main feature of the diffuse Galactic synchrotron radiation is its non-thermal power-law spectrum (Bordovitsyn, 1999). Because the relativistic electrons have a power-law distribution, the resultant synchrotron radiation is also expected to be a power-law spectrum under the condition that collisions of the electrons are negligible. The typical spectral index (α) of the Galactic synchrotron emission is about -2.7 ($S_\nu \propto \nu^\alpha$). However, it varies with frequency. Below 408 MHz, the sky-averaged spectral

[1]https://lambda.gsfc.nasa.gov/product/foreground/fg_2014_haslam_408_info.cfm

index is -2.519 $\pm$ 0.018; above 408 MHz, it becomes -2.715 $\pm$ 0.082 (Zheng et al., 2017). The spectral index also changes according to the direction we observe. Guzmán et al. (2011) investigated the Galactic spectral index of the whole sky between 45 and 408 MHz, showing it changes between -2.1 and -2.7 mainly because of thermal free-free absorption.

1.3 The Galactic magnetic field and cosmic ray electrons

The Galactic magnetic field affects many physical processes, and can therefore be measured by observing several phenomena caused by the magnetic field, e.g. diffuse synchrotron emission from cosmic-ray electrons (e.g. Sun et al. 2008), thermal emission and starlight polarisation caused by dust grains (e.g. Draine 2003; Planck Collaboration et al. 2018), Faraday rotation of linearly polarised emission (e.g. Han et al. 2006), and Zeeman splitting of emission and absorption lines from clouds (e.g. Crutcher et al. 1993). Han (2017) summarises the observational processes for investigating the interstellar and intergalactic magnetic fields.

Models of the Galactic magnetic field tend to utilise observational results from multiple methods. For example, Sun et al. (2008) and Sun & Reich (2010) constrained the 3D distribution of the Galactic magnetic field using both the total intensity and linear polarisation of Galactic synchrotron emission, and the rotation measures of extragalactic sources. Jansson and Farrar (2012a,b) further improved the fit by including an out-of-the-plane field and the striated random component using data from the Wilkinson Microwave Anisotropy Probe (WMAP) synchrotron emission map and $\sim$40, 000 extragalactic rotation measures. The orientation of this component has zero mean and rms strength $\sim$20% larger than the regular field. Haverkorn et al. (2019) introduced

the IMAGINE software pack aiming to modelling of the Galactic magnetic filed by using Bayesian inference.

The Galactic magnetic field is usefully decomposed into two main components: a large-scale regular field and a small-scale random field. These two components are each in the range of 2$\sim$5 μG. The regular fields are mainly composed of the disk component and the toroidal halo component. The disk component has a shape similar to that of the spiral arms, but varies in different models (see e.g. Sun et al. 2008; Jansson and Farrar 2012a). The halo component is toroidal and has different signs above and below the Galactic plane. The random fields have a coherence length of the order of 100 pc and possibly originate from hydrodynamic turbulence (Haverkorn et al., 2008) and supernovae or outflows (Gaensler and Johnston, 1995).

The spatial distribution of the comic-ray electrons is far from well-known and various models have been investigated in several works, such as an exponential spatial distribution as used in Sun et al. (2008) or a derived spatial distribution, such as one derived using GALPROP[2] as used in Jansson and Farrar (2012a,b). Specifically, the spatial distribution of the cosmic-ray electrons in the Galactic disk in Sun et al. (2008) is written as

$$N(R,z) = N_0 \exp\left(-\frac{\mathrm{R}-\mathrm{R}_\odot}{8\,\mathrm{kpc}} - \frac{|z|}{1\,\mathrm{kpc}}\right), \tag{1.3}$$

where N is the number density of the cosmic-ray electrons, R is the Galactocentric radius, and z is the distance to the Galactic plane. However, this distribution of cosmic-ray electrons is an approximation and far from well-constrained. Obvious spiral arm structures have been added in the thermal electron model in NE2001 (which charts the distribution of electrons with much lower energies than those of cosmic-ray electrons, see Cordes and Lazio 2002, 2003) and a warp of the outer Galactic disk has been included in the new model of Galactic free electrons (Yao et al., 2017). Similar or more

[2]https://galprop.stanford.edu

complex structures are expected to be evident in the cosmic-ray electron distribution.

Improved measurements of the synchrotron emission are needed to further constrain the distributions of the cosmic-ray electrons and the magnetic field. One limitation of the synchrotron emission observations is that their information is integrated along the line-of-sight. However, this shortcoming can sometimes be circumvented: intervening objects with a high density of free electrons can absorb the synchrotron emission behind them, and therefore split the total emission into two columns; one from the object to the Sun and the other from the object to the Galactic edge. In this manner, HII regions are ideal probes of Galactic structure because of their large number and large angular sizes compared with other objects (e.g. Nord et al. 2005, 2006). Other objects with smaller angular sizes, such as Pulsar Wind Nebulae (PWN) and planetary nebulae, will be observed greater in numbers in absorption in future low frequency radio observations. Tracing the magnetic field and cosmic-ray electron using the 3D tomography of the synchrotron emission have not been widely used, mainly because of the limited number of measurements that can break the total line-of-sight emission into multiple segments. This thesis aims to detect and characterise a substantially increased quantity of absorbing HII regions in order to enhance our understanding of the full 3D distribution of synchrotron emission in our Galaxy.

1.4 Galactic HII regions

An HII region is a zone of hydrogen that is ionized, usually due to incident ultraviolet photons from nearby young and massive stars (see Fig. 1.3). A balance between the photoionization and the random recombination of ion and electron is reached at the edge of the Strömgren sphere, whose radius is typically a few pc. A young star of the spectral classes O or B, emits energetic ultraviolet radiation, ionizing hydrogen

of the surrounding interstellar medium. The photons can travel further distances to ionize more of the medium. The radius of the ionized sphere grows with time until an equilibrium between the ionization rate and the recombination rate, depending on the temperature and luminosity of the ionizing star. In the equilibrium, for every newly ionized hydrogen atom there is a newly created hydrogen atom from recombination. This phenomenon was derived in theory by Bengt Strömgren in 1937 and later named Strömgren sphere after him. The Stömgren radius is the maximum distance at which ultraviolet from the star will keep hydrogen ionized. The Radio Recombination Lines (RRL) from the recombination of free electrons and protons yield the velocity of HII regions, which can help to derive the kinematic distance of the HII regions (see e.g. Anderson et al. 2015). Beside line emission, HII regions also radiate continuum emission produced by free electrons passing by ions without being captured, i.e. thermal bremsstrahlung. The ratio between the intensities of this continuum and RRL emission are used to measure the electron temperature of the HII region (Mansfield, 1969).

We give a brief overview of HII region catalogues here. The HII Region Discovery Survey (HRDS) is a RRL and continuum emission survey aiming to detect all HII regions in the Galactic disk between 4 and 11 GHz (Anderson et al., 2011; Bania et al., 2012; Anderson et al., 2015) mainly using Green Bank Telescope (GBT) observations (Bania et al., 2010). The HRDS has discovered $\sim$800 HII regions by detecting RRLs. The Southern HII Region Discovery Survey (SHRDS) is its southern hemisphere counterpart, observing the third and fourth quadrants of the Galactic disk (Brown et al., 2017) with the Australia Telescope Compact Array (ATCA). It has detected RRLs from 36 HII region candidates so far. Wenger et al. (2019) measured the $\sim$7 GHz radio continuum peak flux densities and positions of 80 previously known and 298 candidate HII regions, and detected 77 and 267 RRL velocity components toward HII regions and HII region candidates respectively with the ATCA.

An HII region catalogue with over 8000 Galactic HII regions and HII region candidates was built by Anderson et al. (2014) based on the mid-infrared (12 and 22 μm) observations using *WISE* and other existing surveys. The on-line version[3] of this catalogue is the most up to date version, with new observations from Anderson et al. (2015, 2018). A number of HII region catalogues were built from observations at different frequencies. For example, at low radio frequencies of about 100 MHz, Hindson et al. (2016) built an HII region catalogue of 306 HII regions using an early set of GLEAM images, all of which matched with those in the *WISE* HII region catalogue. At the comparatively high frequency of 5 GHz, 239 ultra-compact HII regions (UCHIIs) are detected in the Co-Ordinated Radio 'N' Infrared Survey for High-mass star formation (CORNISH)[4] by Kalcheva et al. (2018).

The electron temperature is an important parameter when measuring the synchrotron emissivity blocked by an HII region. Balser et al. (2015) listed the electron temperature of 230 HII regions. Recently, Brown et al. (2017) measured the electron temperature of 36 HII regions with RRL detections in HII regions in their SHRDS survey. The electron temperature ($T_{\rm e}$) can be calculated from

$$T_{\rm e} = \left[7103.3 \left(\frac{\nu_{\rm L}}{\rm GHz} \right)^{1.1} \left(\frac{T_{\rm C}}{T_{\rm L(H^+)}} \right) \left(\frac{\Delta V({\rm H^+})}{\rm km\ s^{-1}} \right)^{-1} (1+y)^{-1} \right]^{0.87} {\rm K} \qquad (1.4)$$

$$y \equiv \frac{n(^4{\rm He^+})}{n({\rm H^+})} = \frac{T_{\rm L(^4He^+)} \Delta V(^4{\rm He^+})}{T_{\rm L(H^+)} \Delta V({\rm H^+})} \qquad (1.5)$$

where $\nu_{\rm L}$ is the RRL rest frequency, $T_{\rm C}$ is the continuum peak intensity, $T_{\rm L}$ is the H or He RRL intensity, and ΔV is the H or He RRL Full Width at Half Maximum (FWHM) linewidth (Balser et al., 2015; Quireza et al., 2006).

Although the electron temperature is essential for measuring the emissivity, not all HII regions have known electron temperatures. Fortunately, a statistical relation exists

[3] http://astro.phys.wvu.edu/wise

[4] http://cornish.leeds.ac.uk/public/index.php

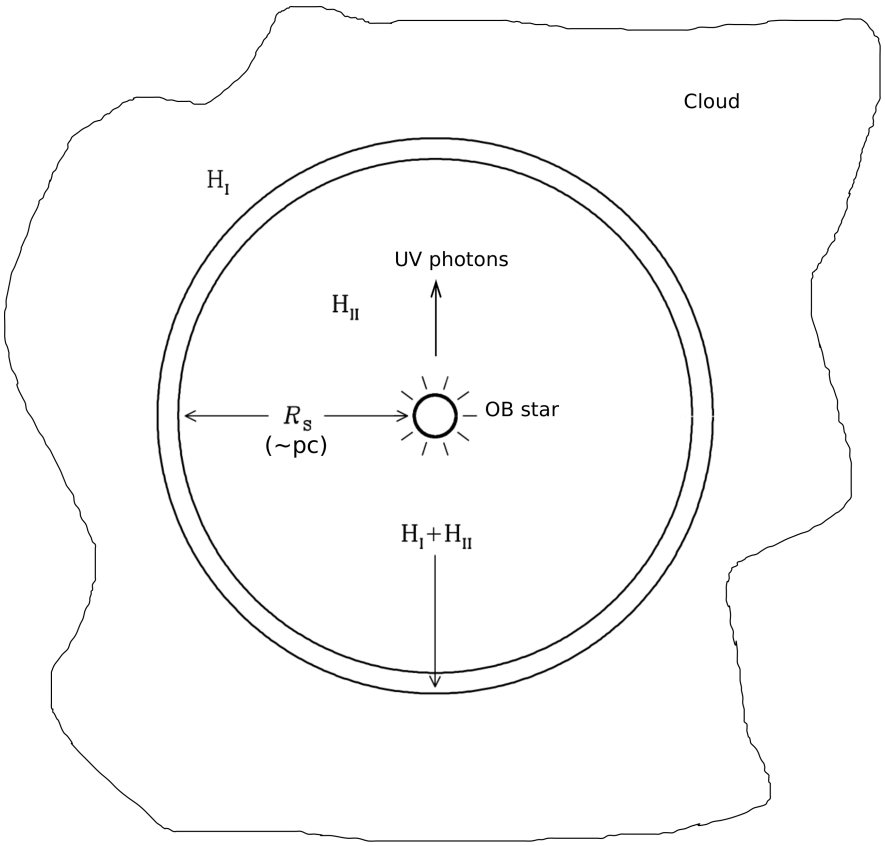

Figure 1.3: A cartoon of an HII region formed in an HI cloud. The centre of the HII region contains one or several young and massive stars, which radiate Ultraviolet (UV) photons that ionize the surrounding neutral hydrogen. The ionization and recombination reach balance at the edge of the Strömgren sphere, at a radius of several parsecs.

between the electron temperature and the distance from HII regions to the centre of the Galaxy. The electron temperature ($T_{\rm e}$) decreases with Galactocentric radius, $R_{\rm gal}$, because the density of coolants (heavy elements) decreases with the $R_{\rm gal}$. The recent statistics in Balser et al. (2011) show that $T_{\rm e} \propto R_{\rm gal}$.

The distance of the HII region is also essential for calculating the average emissivity along the path. Three ways are widely used for measuring distances of HII regions: geometrically (parallax), kinematically (rotation curve), and spectrophotometrically.

The parallax distance method is the most accurate to obtain distances to HII regions. It measures the proper motion of water and methanol masers associated with HII regions, taking advantage of VLBI techniques in the radio band (e.g. Reid et al. 2014).

The kinematic distance is more widely used. It is based on the assumed Galactic rotation model, which gives the relation between the radial velocity of objects and their distance to the Sun. One commonly used Galactic model takes the Galactocentric distance of the Sun to be $R_{\odot}$ = 8.5 kpc, and the Galactic uniform rotation velocity $\Theta_{\odot}$ = 220 km s^{-1} from the IAU 1985 standard (Kerr and Lynden-Bell, 1986). Many efforts have been made to improve the measured rotation curve (e.g. Fich et al. 1989; Merrifield 1992; Bhattacharjee et al. 2014). Even with more accurate rotation curve, the kinematic distance ambiguities still exit due to one radial velocity corresponding to two distinct locations in the inner Galaxy. This ambiguities may be solved by HII region absorption observations for (Nord et al., 2006).

For the work in this thesis, the distances and electron temperatures of the HII regions are the two most important parameters. The kinematic distances of HII regions have been widely measured (Balser et al., 2011; Quireza et al., 2006; Kolpak et al., 2003) and have been redone with distance ambiguity resolved using three methods: HI emission absorption, H_2CO absorption, and HI self-absorption (Balser et al., 2015).

Table 1.1: Summary of the spectral indices for different types of Galactic sources.

Type of sources	Spectral index range	Reference
HII region	-0.1∼2.0	2, 4
Supernova remnant	-0.5	1
Galactic synchrotron	-0.8 $\pm$ 0.2	5
Background radio galaxies	-0.85	3
PWN	-0.3∼0.0	6, 7

Reference: 1. Green 2014, 2. Kurtz 2005, 3. Lisenfeld and Völk 2000, 4. Mezger and Henderson 1967, 5. Platania et al. 1998, 6. Weiler and Sramek 1988, 7. Gaensler and Slane 2006.

The more accurate parallax method has also been used to measure the distance of 100 HII regions (Reid et al., 2014). Quireza et al. (2006) found distances and electron temperatures for 114 HII regions over all the Galactic plane. Balser et al. (2011) found distances and electron temperatures for 81 HII regions over the Galactic longitude range $l = 0^\circ - 250^\circ$.

The Wide-field Infrared Survey Explorer (*WISE*, Wright et al., 2010) observed the whole sky centred at wavelengths of 3.4, 4.6, 12 and 22 μm. The 22 μm emission mainly traces the small dust grains in the ionized gas of HII regions. The 12 μm emission is more extended than the sphere traced by the 22 μm emission because it traces the surrounding fluorescence of polycyclic aromatic hydrocarbon (PAH) molecules in ultra-violet radiation fields (e.g. Deharveng et al. 2010; Anderson et al. 2014).

HII regions have a wide distribution in the Galactic disk. Most HII regions with known distances have Galactocentric distances of 3∼15 kpc (Anderson et al., 2015). Detections of HII regions at greater distance (even near the edge of the star formation disk) have nonetheless been observed. Sanna et al. (2017) measured a Heliocentric dis-

tance of about 20 kpc to a water maser source located in a star formation region with the trigonometric parallax method. This source is toward the direction of the Galactic centre, and its Galactocentric radius is about 12 kpc. HII regions with larger Galactocentric radii of $>$19 kpc are measured by Anderson et al. (2015), and are probably located at the outer limit of the star formation disk.

HII regions can be classified into six types: Supergiant, Giant, Classical, Compact, Ultracompact, and Hypercompact, according to the physical size. These types vary greatly in their physical properties, such as the electron density, emission measure (EM), and ionized mass, as shown in Table 1.2. HII regions are consists of a mixture of environments of different densities and the filling factor is defined as the volume fraction of an HII region occupied by matter. Assuming that different types of HII regions share the same filling factor, the emission measure of the six types of HII regions follows $N_e^2 \times d$ where N_e is the electron density and d is the diameter of the HII region.

Giant and Supergiant HII regions are formed by the ionizing photos of massive star clusters, while other HII regions are formed by a few OB stars. The most massive and largest supergiant HII region known is 30 Doradus in the Large Magellanic Cloud (LMC) (Jones, 1969), also known as the Tarantula Nebula, with a size of $\sim$400 pc at a distance of $\sim$50 kpc. The star cluster NGC 2070 at its centre contributes the energy to illuminate this nebula. The closest observed supernova explosion at modern times, Supernova 1987A, occurred in this nebula. Other giant HII regions include the Orion Nebula, NGC 604 in the Triangulum Galaxy.

Compact, ultra-compact and hyper-compact HII regions represent the early stage of the HII region evolution, in which massive stars begin to ionise their surrounding interstellar medium (e.g. Urquhart et al. 2013). Such HII regions are detectable through their free-free emission and far-infrared emission, tracing the dense conditions

Table 1.2: Typical parameters of different types of HII regions. This table is adapted from Kurtz (2005).

Type	Size (pc)	Density (cm^{-3})	EM (pc cm^{-6})	Ionized Mass ($M_\odot$)
Supergiant	> 100	~ 10	$\sim 10^5$	$10^6 - 10^8$
Giant	~ 100	~ 30	$\sim 5 \times 10^5$	$10^3 - 10^6$
Classical	~ 10	~ 100	$\sim 10^6$	$\sim 10^5$
Compact	< 0.5	$> 5 \times 10^3$	$> 10^7$	~ 1
Ultra-compact	< 0.1	$> 10^4$	$> 10^7$	$\sim 10^{-2}$
Hyper-compact	< 0.03	$> 10^6$	$> 10^{10}$	$\sim 10^{-3}$

in molecular clouds. These HII regions can be distinguished from background (compact) radio galaxies by their thermal free-free continuum spectra, thermal infra-red emission from hot dust, and association with molecular cloud clumps.

The Lyman continuum hydrogen photoionization rate ($N_{\rm Ly}$) can be related back to the integrated flux density (S_ν) of an HII region. If an HII region is in photoionization equilibrium and optically thin at frequencies higher than 5 GHz (Carpenter et al., 1990),

$$N_{\rm Ly} = 9.0 \times 10^{43} \left(\frac{S_\nu}{\rm mJy}\right) \left(\frac{d}{\rm kpc}\right)^2 \left(\frac{\nu}{5\ {\rm GHz}}\right)^{0.1} {\rm photon\ s^{-1}} \tag{1.6}$$

where d is the distance from the HII region to the Sun and ν is the observing frequency. This equation is suitable for optically thin HII regions but (obviously) will underestimate the Lyman continuum flux for optically thick HII regions.

1.5 Galactic HII region absorption

The radio continuum optical depth of an HII region (τ_ν) is often expressed as (Altenhoff, 1960; Lang, 1980)

$$\tau_\nu \approx 8.235 \times 10^{-2}\, \mathrm{T_e^{-1.35}}\, \nu^{-2.1}\, \mathrm{EM}, \qquad (\nu \ll 10^{10}\, \mathrm{T_e}, \mathrm{T_e} < 9 \times 10^5\, \mathrm{K}) \qquad (1.7)$$

where T_e is the electron temperature of the HII region in K, ν is the observing frequency in GHz, and EM is the emission measure in parsec cm^{-6}. The conditions for the above approximation are satisfied for most HII regions at radio frequencies less than several hundreds of MHz.

At frequencies of about 100 MHz and below, many HII regions are opaque against the bright synchrotron emission (Fig. 1.4). Nearly all the emission behind these HII regions towards the Earth along the line of sight is absorbed by the free electrons through free-free absorption (Mezger and Henderson, 1967; Kurtz, 2005).

Analyses of the absorption properties of HII regions dates back at least to the 1950s (Scheuer and Ryle, 1953) followed by Jones and Finlay (1974); Caswell (1976); Krymkin (1978); Deshpande and Sastry (1986); Odegard (1986); Abramenkov and Krymkin (1990). These works measured absorption in a limited numbers of HII regions (usually less than 10) at frequencies from 10 to 70 MHz. For instance, Jones and Finlay (1974) measured two emissivities along the direction of two large HII regions, RCW 108 and the Carina nebula, near the frequency of 29.9 MHz with an angular resolution of 48′. They calculated the average emissivity on the Galactic Plane of $\sim$30,000 K kpc^{-1} at the same frequency. Caswell (1976) calculated the average emissivity of synchrotron emission near the local spiral arm of $\sim$240 K kpc^{-1} based on 7 emissivities in the direction of HII regions at 10 MHz with an angular resolution of 120′. The emissivity at 10 MHz is lower than that at 30 MHz because the ionosphere absorbs most of the synchrotron emission at frequencies below $\sim$10 MHz (Caswell,

1976). The ionosphere introduces reflection, refraction, and propagation delay for observing radio emission. The total propagation delay, integrated along the line of sight at frequencies around 10 MHz, results in a phase rotation, producing large phase errors (de Gasperin et al., 2018).

A significant further advance was made by Nord et al. (2006) with the calculation of 42 emissivities behind HII regions based on 74 MHz VLA observations with an angular resolution of about $10'$. These measurements provided valuable information of the synchrotron distribution behind HII regions along the line of sight. However, the synchrotron emissivities in front of these HII regions could not be deduced for the lack of a reasonable estimate of the total brightness along the line of sight. Besides, the low angular resolutions of these observations limited the number of detected HII regions with absorption features. Therefore, the number of measurements was still insufficient to answer outstanding fundamental questions relating to Galactic structure, namely whether the synchrotron emission distribution is correlated with the spiral arm structure, and whether the warp (Burke, 1957; Kerr, 1957) of the Galactic disk affects the synchrotron distribution.

Polderman et al. (2019) used the low-frequency absorption measurements of HII regions collected from the literature to model the synchrotron distribution and found current Galactic magnetic field models plus a constant cosmic ray density model does not fit well with the absorption measurements. Polderman et al. (2020) further confirmed that the current Galactic magnetic field models with a GALPROP generated cosmic ray density cannot fit well with these measurements, possibly because of distances to HII regions catalogued at the kinematic far distance are not well confined.

Other sources embedded in the Galactic disk, containing a high density of free electrons, such as Pulsar Wind Nebulae (PWN; Gaensler and Slane 2006) and planetary nebulae, can also absorb the synchrotron emission. However, most of these are difficult

to detect by existing wide-field radio telescopes because of their small angular sizes of less than several arcseconds.

Building models is an effective way to find possible structures of the distribution of the synchrotron emission from observations. Simplified models have been built to probe the distribution of the synchrotron emission along our line of sight. Taking advantage of their 42 HII region absorption measurements, Nord et al. (2006) found a low emissivity region within 3 kpc of the Galactocentric centre. Using the 2D Haslam map only, Beuermann et al. (1985) presented a 3D model of the synchrotron emission in the Galactic disk. Their basic underlying assumptions were the existence of spiral structure, and the existence of thin and disk components. The spiral structure is assumed because the profile of the brightness temperature with the Galactic longitude exhibits peaks or steps. With these two assumptions and several other model assumptions, they found both thin and thick disk components show spiral structure, with the spiral pattern consistent with the four arm model proposed by Georgelin and Georgelin (1976). Future models will be more powerful to derive the synchrotron distribution with both the 2D maps and larger number of line-of-sight separation measurements.

1.6 MWA and GLEAM

The observations presented in this thesis are performed by the MWA[5] (Tingay et al., 2013; Bowman et al., 2013) located at the Murchison Radio-astronomy Observatory in the mid-west of Western Australia.

The so-called 'Phase I MWA' consists of 128 aperture arrays (tiles) with baseline lengths ranging from 7.7 to 2864 metres, corresponding to angular scales from about 30° to $2'$. This phase was in full operation from 2012 to 2017. Fig. 1.5 shows one of the

[5]http://www.mwatelescope.org

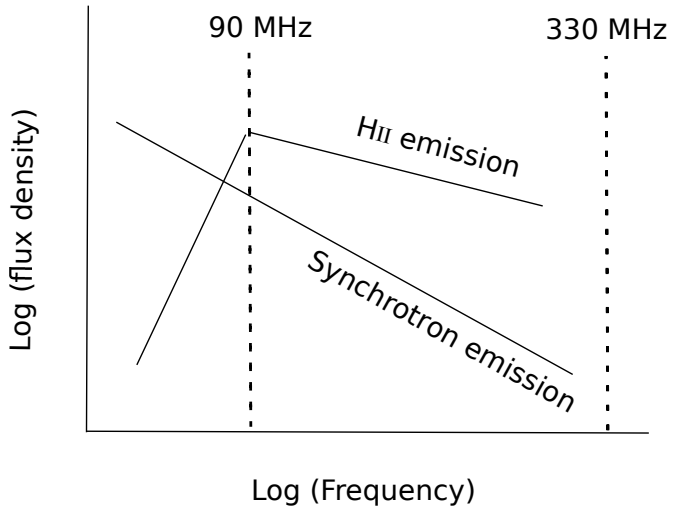

Figure 1.4: Schematic spectrum of an optically thick HII region, and the Galactic synchrotron emission from cosmic-ray electrons at radio frequencies. The spectral index ($S_\nu \propto \nu^\alpha$) of an HII region ranges from 2 to -0.1 (Mezger and Henderson, 1967; Kurtz, 2005). The brightness temperature spectral index of synchrotron emission is about -2.7 (de Oliveira-Costa et al., 2008). The flux density of an HII region increases with frequency when it is optically thick, while the Galactic synchrotron emission shows the opposite trend. HII regions are observed as opaque holes at lower frequencies and become much brighter than their surrounding backgrounds at higher frequencies.

128 tiles of the MWA. Each tile consists of 4 $\times$ 4 dual-polarisation dipole antennas. The MWA operates over the frequency range from 72 to 230 MHz. A summary of the parameters about the MWA is in Table 1.3. Tingay et al. (2013) describes in detail the MWA system and its performance characteristics. Bowman et al. (2013) summarised its four main scientific objectives, which are Epoch of Reionization (EoR), Galactic and extra-Galactic science, the Magellanic Clouds, and cosmic-ray mapping. In this thesis, we focus on the last one, specifically, mapping the emissivity of cosmic-ray leptons.

The MWA was updated to 'Phase II' during 2017. In this phase the array consists of two different observing configurations: a compact array of redundant baselines for Epoch of Reionisation studies, and an extended array with a maximum baseline length of 5 kilometres, for imaging science (Wayth et al., 2018).

The MWA is one of the three precursors of the Square Kilometre Array (SKA)[6]. The other two are the Australian SKA Pathfinder (ASKAP, Johnston et al. 2007), and the MeerKAT[7] which work at the frequency range approximately of 580 to 3500 MHz with X-band in design. An SKA Pathfinder observing at similar frequencies with those of the MWA is the Low Frequency Array (LOFAR, van Haarlem et al. 2013). Its High Band Antennas (HBA) work at 110-240 MHz and Low Band Antennas (LBA) work at 10-90 MHz. LOFAR is located in the Northern Hemisphere and can observe the HII regions located in a Galactic longitude range of $30^\circ < l < 180^\circ$. However, most Galactic HII regions are in the range of -$40^\circ < l < 40^\circ$, where the MWA can observe well.

The MWA has incredibly high survey speed due to its wide field-of-view and instantaneous u, v-coverage (see Fig. 1.6). Typical snapshot observations with the MWA

[6]https://www.skatelescope.org

[7]http://public.ska.ac.za/meerkat

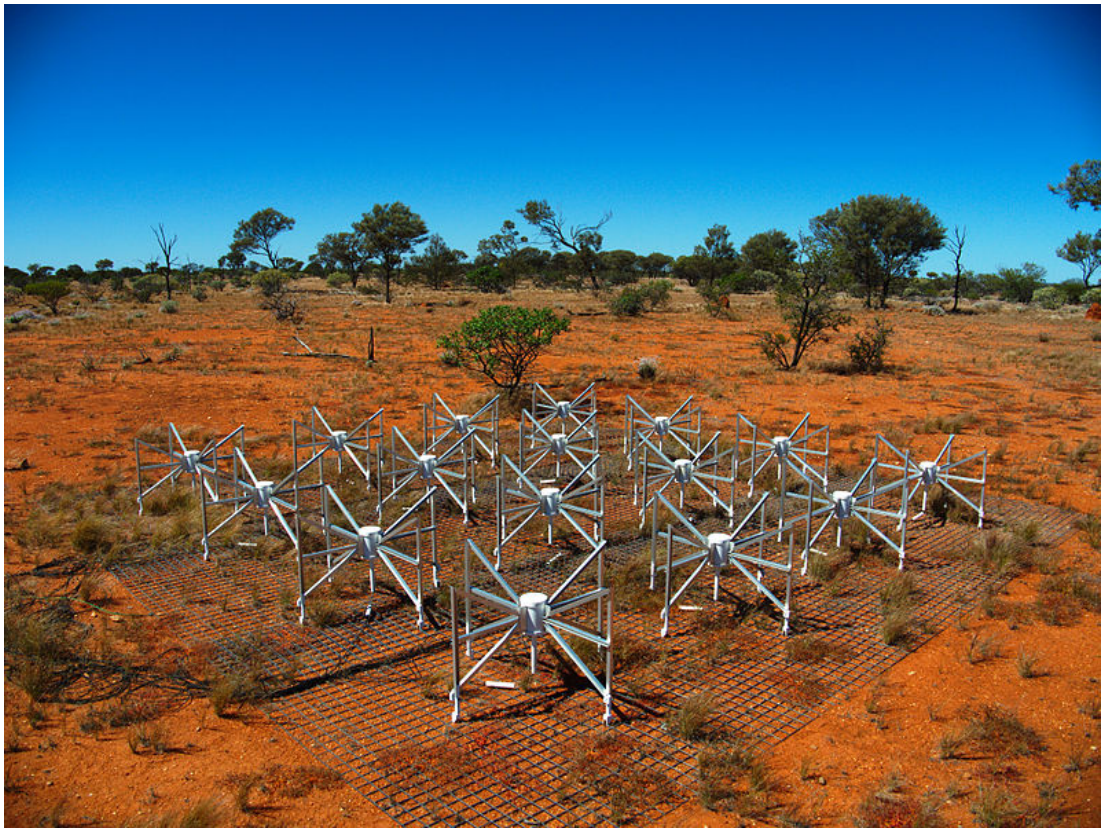

Figure 1.5: Image of one tile of the MWA. Image credit: Natasha Hurley-Walker.

are between two and five minutes long, so that a single time-invariant primary beam model can be used. Its field of view is about 30° by 30°, indicating that it only needs about 50 pointings to cover the whole southern sky. For each pointing, it only takes 2 minutes for one snapshot, being used for observing HII regions and the diffuse synchrotron emission. Integrated beam is typically performed in the image plane, in order to reduce thermal noise.

A notable recent output of the MWA is the GLEAM survey, covering the entire sky south of declination $+25^{\circ}$ over the frequency range 72 to 231 MHz divided into five bands with each band to be 30.72 MHz wide (Wayth et al., 2015). The band around 137 MHz is removed to avoid the satellite interference contamination. GLEAM surveys the sky using meridian drift scans that takes advantage of the large field of view of the MWA. The frequency resolution of GLEAM was 40 kHz in its first year and was 10 kHz during its second year.

The calibration and imaging of the GLEAM data is described in Hurley-Walker et al. (2017). Hurley-Walker et al. (accepted) publish GLEAM images of the Galactic plane over $345^{\circ} < l < 67^{\circ}$, $180^{\circ} < l < 240^{\circ}$, $|b| < 10^{\circ}$. The GLEAM survey has surface brightness sensitivity ranges from 50 to 100 mJy beam^{-1} for the range of angular sizes from 5° to 15° (Hindson et al., 2016). A summary of the parameters about the MWA and GLEAM is given in Table 1.3.

1.7 Aims and significance

The overall aim of this thesis is to map the synchrotron emissivity distribution on the Galactic plane by measuring discrete emissivities along different lines of sight (Chapter 2 and Chapter 3) using intervening HII regions to separate out the Galactic synchrotron emission into components anterior to and posterior to the HII region location.

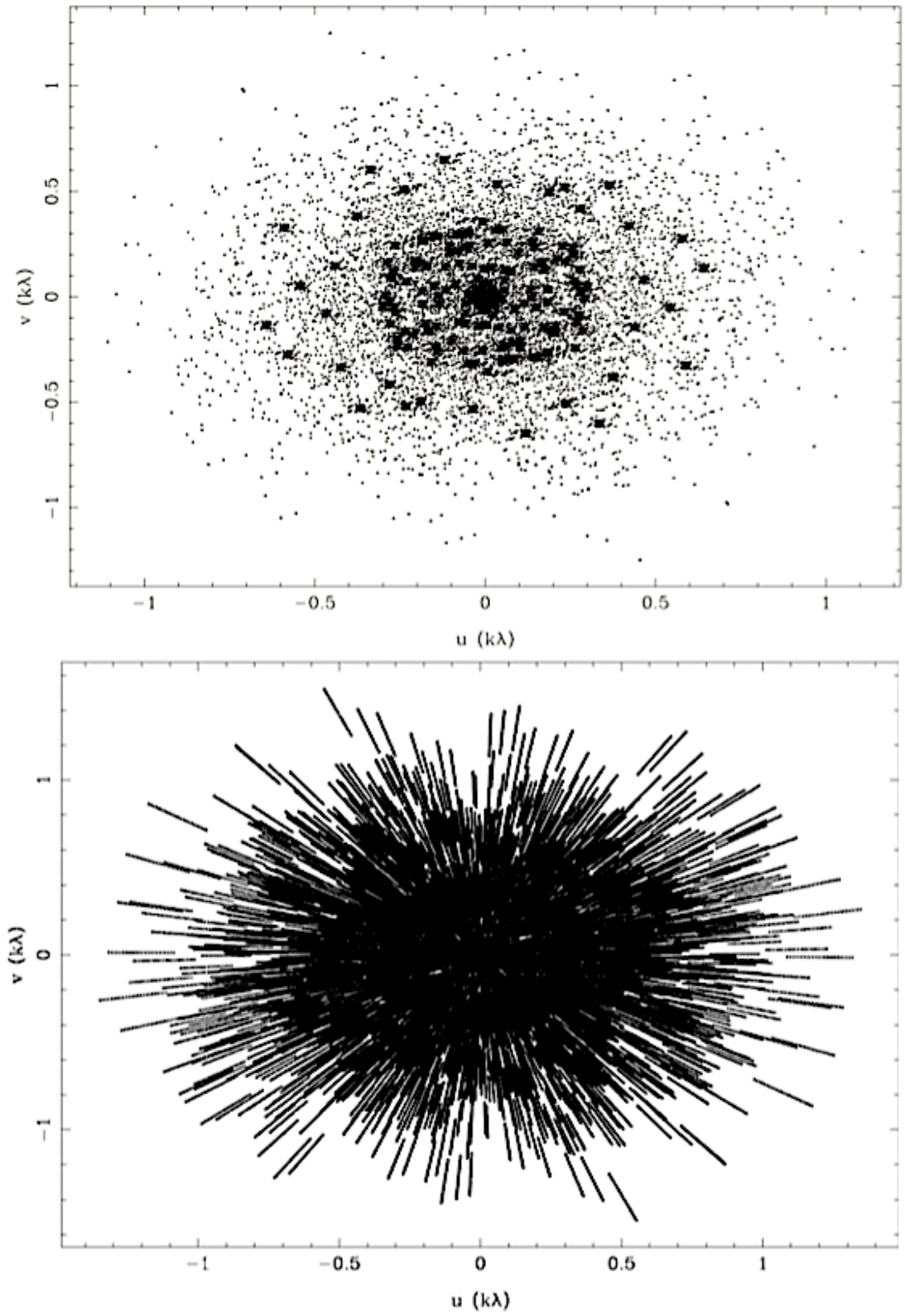

Figure 1.6: The u, v-coverage for a two minute snapshot with the MWA Phase I pointed to zenith with a centre frequency of 154 MHz from Wayth et al. (2015). The top panel shows the monochromatic case, and the bottom panel shows the results of multi-frequency synthesis over 30MHz.

Table 1.3: Key parameters of the MWA and the GLEAM survey.

Parameters	Values
Number of tiles	128
Minimum baseline	7.7 m
Maximum baseline	2864 m
Field-of-view	610 $\deg^2$ at 150 MHz
Sky coverage	Declination <+30°
Frequency	80 - 230 MHz
Resolution	$\sim 7' \times 6'$ at 87 MHz
Estimated confusion limit	10 mJy at 150 MHz
Instantaneous Bandwidth	30.72 MHz

A complementary objective is to investigate the properties of the HII regions themselves at low radio frequencies from 72 to 231 MHz (Chapter 4).

The measured synchrotron emissivities will

- provide new information on the strength of the Galactic magnetic field and the density of cosmic-ray electrons, especially their distributions along the line of sight.
- aid attempts to better remove the Galactic synchrotron foreground emission in order to improve the detection of background radio signals, especially the CMB and the EoR.
- help resolve kinematic distance ambiguities of HII regions. HII regions with weaker associated absorption features are more likely further away due to the fact that distant HII regions absorb less synchrotron emission.

In this thesis, Chapter 2 shows the initial synchrotron emissivity measurements based on absorption measurements towards 47 HII regions. Chapter 3 presents emis-

sivity measurements of 152 HII regions observed in the full area of the GLEAM survey and interprets this in the context of the overall synchrotron emission distribution of our Galaxy. Finally, Chapter 4 presents a large catalogue of Galactic HII regions, and presents a set of their spectral energy distributions, derived from the GLEAM survey data.

Chapter 2

Initial measurements of Galactic synchrotron emissivity

I conducted all work for this chapter under the guidance of my supervisory panel.

This chapter is adapted from:

Su, H., N. Hurley-Walker, C. A. Jackson, N. M. McClure-Griffiths, S. J. Tingay, L. Hindson, P. Hancock, R. B. Wayth, B. M. Gaensler, L. Staveley-Smith, J. Morgan, M. Johnston-Hollitt, E. Lenc, M. E. Bell, J. R. Callingham, K. S. Dwarkanath, B.-Q. For, A. D. Kapińska, B. McKinley, A. R. Offringa, P. Procopio, C. Wu, and Q. Zheng (2017a, March). Galactic synchrotron emissivity measurements between $250^\circ < l < 355^\circ$ from the GLEAM survey with the MWA. MNRAS 465, 3163–3174.

and

Su, H., N. Hurley-Walker, C. A. Jackson, N. M. McClure-Griffiths, S. J. Tingay, L. Hindson, P. Hancock, R. B. Wayth, B. M. Gaensler, L. Staveley-Smith, J. Morgan, M. Johnston-Hollitt, E. Lenc, M. E. Bell, J. R. Callingham, K. S. Dwarkanath, B.-Q. For, A. D. Kapińska, B. McKinley, A. R. Offringa, P. Procopio, C. Wu, and Q. Zheng

(2017b, November). Erratum: Galactic synchrotron emissivity measurements between $250^\circ < l < 355^\circ$ from the GLEAM survey with the MWA. MNRAS 472, 828–834.

In this Chapter, we measure the free-free absorption of this Galactic synchrotron emission by intervening HII regions along the line of sight. These absorption measurements allow us to calculate the Galactic cosmic-ray electron emissivity behind and in front of 47 detected HII regions in the region $250^\circ < l < 355^\circ$, $|b| < 2^\circ$. We find that all average emissivities between the HII regions and the Galactic edge along the line of sight (ϵ_b) are in the range of 0.24 $\sim$ 0.70 K pc^{-1} with a mean of 0.40 K pc^{-1} and a variance of 0.10 K pc^{-1} at 88 MHz. Our best model, the Two-circle model, divides the Galactic disk into three regions using two circles centring on the Galactic centre. It shows a high emissivity region near the Galactic centre, a low emissivity region near the Galactic edge, and a medium emissivity region between these two regions, contrary to the trend found by previous studies.

2.1 Observations

We use data from the GLEAM survey: the GaLactic and Extragalactic All-sky MWA survey (Wayth et al., 2015). The observations used in this study were performed for 10 hours on 17 March, 2014. The data reduction follows the method described in the MWA commissioning survey (Hurley-Walker et al., 2014) with more specific details discussed in Hindson et al. (2016). The main steps of data reduction include flagging, calibrating, and imaging individual snapshots. The calibrated Stokes XX and YY snapshots were imaged with a robust weighting of 0.0. To correct the astrometric changes in source position generated by the ionosphere (Loi et al., 2015), we cross-matched the position of compact sources with MRC sources (Large et al., 1981, 1991) to determine an average astrometric correction and shifted each snapshot accordingly.

The GLEAM data span 72 to 231 MHz divided into five bands. The shortest baseline ($D_{\rm min}$) is 7.7 metres corresponding to an angular scale of 25° at 88 MHz (Tingay et al., 2013). The surface brightness sensitivity ranges from 50 to 100 mJy beam^{-1} for the range of angular sizes from 5° to 15° (Hindson et al., 2016). In this paper, we use the data at the lowest frequency of 88 MHz with a bandwidth of 30.72 MHz to maximize HII region absorption detections. These data have a 1σ sensitivity of 99 mJy beam^{-1} with an angular resolution of $5\farcm6 \times 5\farcm6$ (1 Jy beam^{-1} = 1413.8 K). The noise level is the lowest at Galactic longitude $\sim$300° and increases towards lower and higher Galactic longitudes shown in Fig. 2.1.

Most previous single dish surveys at frequencies of several hundred MHz can recover the total power of the sky but their angular resolutions of continuum images are in the order of degrees. By contrast, the excellent angular resolution of the GLEAM survey enables the detection of HII regions with minimum sizes from 2 to 33 pc for distances from 1 to 20 kpc (Hindson et al., 2016). However, as an interferometer, the MWA is insensitive to power from large scale structures. The MWA consists of 128 aperture arrays distributed in a dense core $<$1.5 km in diameter with a maximum baseline of about 2.5 km. Thus, MWA has excellent (u, v) coverage and surface brightness sensitivity to structures on angular scale from $5\farcm6$ to 31° at 88 MHz, which is sufficient for our emissivity measurements with HII regions of typical angular scale sizes of several arcminutes. The observations of Nord et al. (2006) are only sensitive to structures with angular sizes from $\sim$10′ to 40′, resulting in negative temperature measurements for their observed absorption regions. Our observations also differ from Nord et al. (2006) in spatial coverage. Our current measurements cover the southern sky in the range $250^\circ < l < 355^\circ$, $|b| < 2^\circ$, whereas Nord et al. (2006) mainly covers the northern sky in the range $-15^\circ < l < 26^\circ$, $|b| < 5^\circ$, furthermore the work of Nord et al. (2006) was conducted at 74 MHz, whereas the work in this paper is based on

88 MHz.

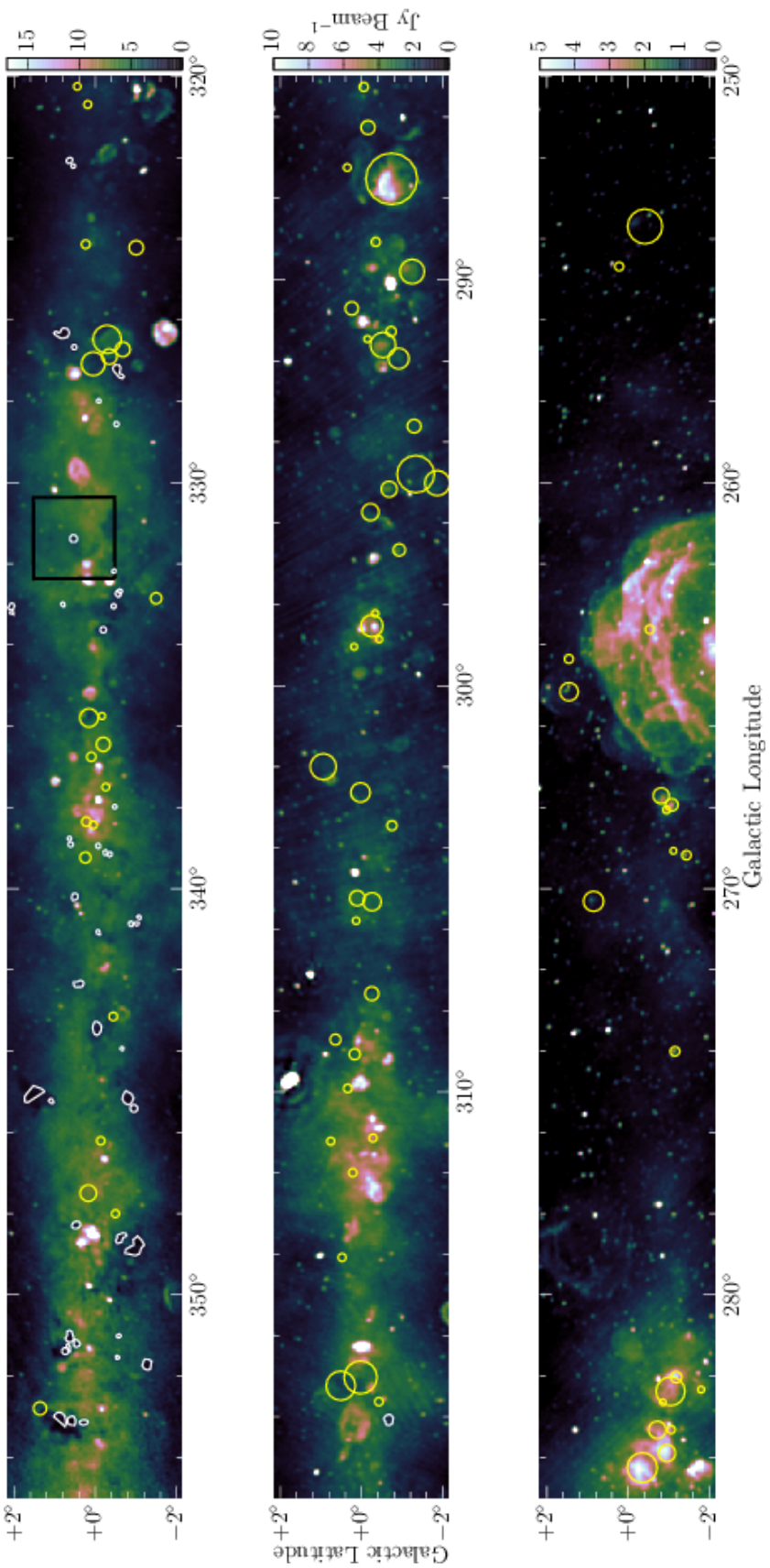

Figure 2.1: A portion of the Galactic plane at 88 MHz with a bandwidth of 30.72 MHz observed by the MWA (Hindson et al., 2016). The angular resolution is $5'.6 \times 5'.6$. The white polygons and yellow circles show the HII regions with detected and undetected absorption features, respectively. Several absorption regions near the top-left corner in the top panel are detected but not measured due to the overlapped HII regions with different distances. The striations in the middle of the second panel is caused by the bright Centaurus A. The black boxed region is enlarged in Fig. 2.3 to show an example absorption feature. Throughout we use the "cubehelix" colour map (Green, 2011). The colour scale is adapted to ensure the Galactic features are highlighted.

2.2 Emissivity calculations with the simplified method

As discussed above, HII regions become optically thick at low frequencies, absorbing the diffuse synchrotron radiation emitted behind them. An HII region whose distance is known is a valuable probe of the synchrotron emission behind and in front of it. Here we introduce the formalism for using HII regions to determine the average emissivity along the line of sight. The quantities of foreground and background emissivity are shown in Fig. 2.2.

Similar to a single dish telescope (Kassim, 1987), we observe the HII region with a brightness temperature of

$$T_o = T_e(1 - e^{-\tau}) + T_b e^{-\tau} + T_f, \tag{2.1}$$

where T_e is the electron temperature of the HII region, T_b is the brightness temperature of the synchrotron emission from the HII region to the Galactic edge along the line of sight, T_f is the brightness temperature of the synchrotron emission from the HII region to the Sun, and τ is the optical depth of the HII region.

Usually, HII regions become optically thick ($\tau \gg 1$) at frequencies below approximately 200 MHz (Mezger and Henderson, 1967). So the observed brightness temperature of the HII region becomes

$$T_o \simeq T_e + T_f. \tag{2.2}$$

The brightness temperature of the sky neighbouring the HII region T_t is

$$T_t = T_f + T_b. \tag{2.3}$$

Defining the average emissivity as the brightness temperature per unit length, the average emissivities behind (ϵ_b) and in front (ϵ_f) of HII regions are

$$\begin{aligned} \epsilon_f &= T_f/D_f = (T_o - T_e)/D_f, \\ \epsilon_b &= T_b/D_b = (T_t - T_o + T_e)/D_b \end{aligned} \tag{2.4}$$

where D_f is the distance between the HII region and the Sun and D_b is the distance between the HII region and the edge of the Galactic plane. T_e and D_f are from the literature (see the references in Table 3.2). T_e is mainly measured from radio recombination lines at about 9 GHz (Balser et al. 2015 and reference therein). For HII regions without measured T_e, we estimate from the relation between the electron temperature and the Galactocentric radius $T_e = (4928 \pm 277) + (385 \pm 29)\ R_{\rm gal}$ from Balser et al. 2015 (a similar relation is derived in Alves et al. 2012). When estimating the electron temperature using the relation in Balser et al. (2015) and Alves et al. (2012) respectively, the differences are 1-8% on ϵ_b, depending on the distance of HII regions. The small differences do not change our modelling results. D_f is mainly measured using kinematics and parallax methods, which are summarised in Anderson et al. (2014). We calculate D_b assuming a Galactocentric radius of 20 kpc (Ferrière 2001 and references therein). Note that our ϵ_b depends on this assumed Galactocentric radius. T_o and T_t are from our observations.

Unlike a single-dish telescope, an interferometer is incapable of measuring the total power of the Galactic plane emission. The data misses an unknown background offset across a large sky area, resulting in $\sim$20% error in the absolute level of the measurements, statistically derived by comparing with the predicted results in Zheng et al. (2017) who shows diffuse Galactic radio emission from 10 MHz to 5 THz. As a result our measurements of ϵ_f have an additive offset or a scaling error and are not absolutely correct (Equation 2.4). However, they are relatively correct because the missing power on scales less than a few degrees is absent equally from T_t and T_o, so the difference $T_t - T_o$ in ϵ_b (Equation 2.4) is correct. However, because ϵ_f relies only on T_o, which is not absolutely calibrated, we will not use ϵ_f in our modelling.

It should be noted that the above formulae differ from those used by Nord et al. (2006) because the MWA recovers the large-scale background emission to a scale of

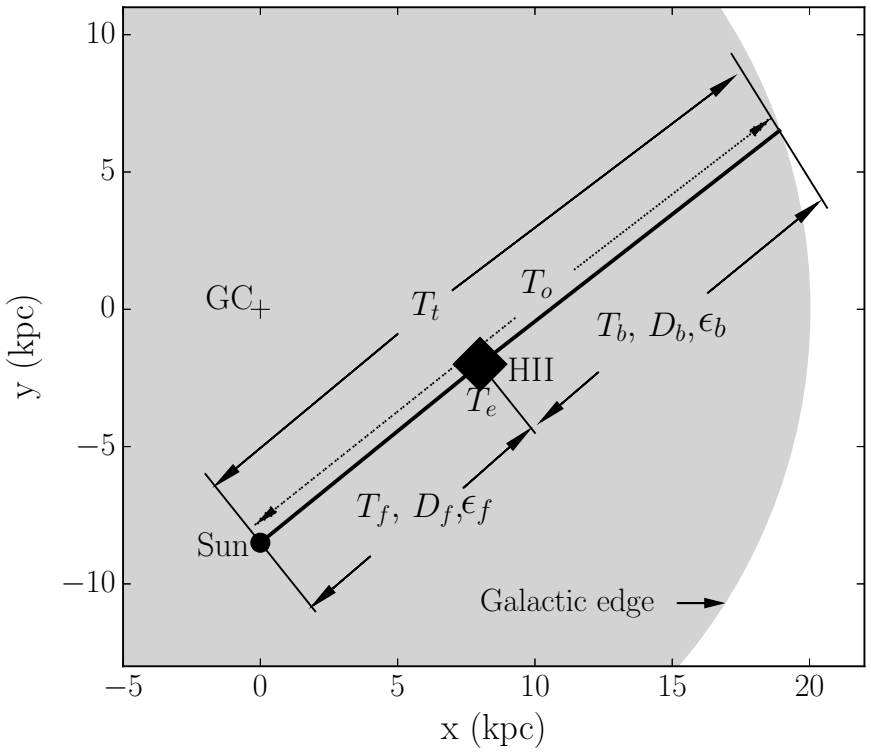

Figure 2.2: A schematic diagram showing a portion of the Galactic disk (grey), the Galactic centre (GC), an HII region, the Sun, the temperatures ($T_t,\ T_o,\ T_f,\ T_b,\ T_e$), the path lengths ($D_f,\ D_b$), and the emissivities ($\epsilon_f,\ \epsilon_b$).

$\sim \lambda/D_{\rm min} = 25^{\circ}$ surrounding the HII regions, whereas the observations of Nord et al. (2006) do not.

2.2.1 HII region selection criteria

In this paper we work with a sample of HII regions with known distances and obvious absorption features to measure the average emissivities along a path. Using the 12 and 22 μm data with high angular resolutions of $6\farcs5$ and $12''$ respectively from the Wide-field Infrared Survey Explorer (*WISE*, Wright et al. 2010), Anderson et al. (2014) constructed a catalogue of $\sim$8000 Galactic HII regions. This *WISE* HII region catalogue uses circles to show the locations of HII regions. To select our sample, we search for absorption regions within these radii. We omitted overlapping HII regions with different distances in our sample due to the complexity in obtaining reliable average emissivities. Note that Hindson et al. (2016) have presented a catalogue of 306 HII regions using the data with all the frequencies between 72 and 231 MHz from the MWA GLEAM. We do not use this catalogue because most of their measurements do not show obvious absorption features, and they did not publish the part of the sky closer to the Galactic Centre.

We define absorption regions such that they are each:

1. inside the radius defined in the *WISE* HII region catalogue;

2. lower than the nearby T_t by at least 3σ in surface brightness;

3. larger than the beam size to avoid beam dilution;

4. coincident with 12 μm emission features in *WISE* observations (Wright et al., 2010) given the 12 μm emission is mainly from polycyclic aromatic hydrocarbon (PAH) molecules, which traces ionization fronts. The 22 μm emission

traces small dust grains composing the inner core of an HII region (see Deharveng et al. 2010; Anderson et al. 2014 and reference therein). Thus, we expect the 12 μm emission region to be coincident with the absorption feature caused by free electrons from ionisation, whereas the 22 μm emission region is much smaller than the absorption feature.

For each absorption feature, we choose a nearby, non-absorbed area to estimate T_t such that the area:

1. is located in the similar Galactic latitude as the absorption region given the brightness temperature decreases rapidly with latitude;

2. does not overlap with any HII region in the *WISE* HII region catalogue;

3. does not overlap with any supernova remnants listed by Green et al. (2015) to avoid contamination from bright non-thermal emission in our observations;

4. does not have an obvious coherent structure, in order to avoid the effects caused by unknown sources, such as the undetected HII regions and supernova remnants.

We show an example of an absorption region and a neighbouring region in Fig. 2.3. We confirm that the low surface brightness region in the centre of the MWA image (Fig. 2.3 left) is from HII region absorption by comparing with the *WISE* image (Fig. 2.3 right). The *WISE* image is constructed by stacking 15 facets and then cropped to the same size as the MWA image. The line-like features are edges of image facets. These features do not have an effect on determining the location of the HII region.

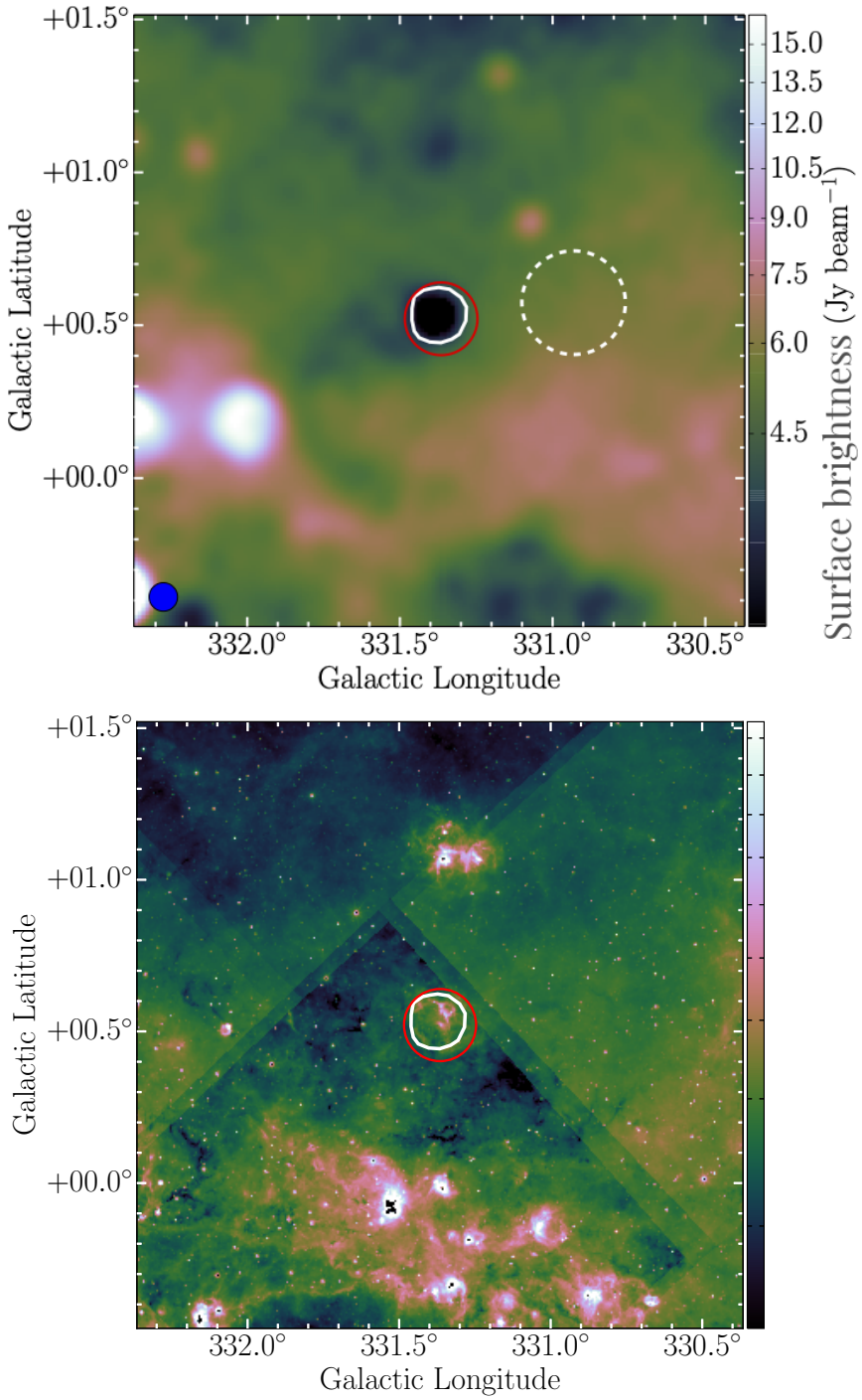

Figure 2.3: An example of an HII region (G331.365+00.521) absorption feature at 88 MHz from the MWA (top) and an emission feature at 12 μm from *WISE* (bottom). The white solid and dashed lines show our defined absorption and neighbouring regions respectively. See section 2.2.1 for the rules for selecting the absorbed and neighbouring regions. The red circle shows this HII region defined in the *WISE* HII region catalogue. The blue circle in the left corner shows the FWHM of the synthesised beam. The root-mean-square of this HII region in this MWA image is about 0.26 Jy beam^{-1}. This entire field is marked by a square in Fig. 2.1.

2.3 Results

2.3.1 The emissivity distribution

We use Equation 2.4 and the MWA measurements of T_t and T_o to estimate the average emissivities both behind and in front of 47 HII regions (see Table 3.2). We find that all average emissivities between the HII regions and the Galactic edge along the line of sight (ϵ_b) are in the range of 0.24 $\sim$ 0.70 K pc^{-1} with an average of 0.40 K pc^{-1} and a variance of 0.10 K pc^{-1}. The average emissivities between the HII regions and the Sun (ϵ_f) have a large range of -12.72 $\sim$ 0.50 K pc^{-1} with a mean of -1.56 K pc^{-1} and a variance of 2.2 K pc^{-1}, although these are subject to an uncertainty in total power affecting ϵ_f.

We estimate the local root-mean-square (RMS) noise for the measured surface brightness (I_o and I_t) using the standard deviation of pixel values in a representative neighbouring region. To incorporate the uncertainty in the distance measurement used in each HII region we proceed as follows (i) where an error is explicitly stated in the literature this is used verbatim. Where no error has been quoted, then (ii) HII regions with parallax distance measurements are assigned a 10% error, (iii) HII regions with a kinematic distance measurement are assigned a 50% error and (iv) for all other cases, including HII regions without a specified distance measurement method (e.g. HII regions listed in Table 6 in Anderson et al. 2014, which are derived from the kinematic measurements), we assign an error of 100%. The errors of the electron temperature (T_e) of HII regions are from the literature. Each above error is propagated to the average emissivities (ϵ_f and ϵ_b). All the quoted errors are 1σ.

The magnitude of any extragalactic synchrotron emission is negligible compared with Galactic synchrotron since its brightness temperature is in the range from 195 to 585 K at 88 MHz which is only $\sim$ 2% of the Galactic component (Guzmán et al.

2011 and references therein). Its effect ($\sim$ 0.03 K pc^{-1}) on our measurements is smaller than our minimum error (0.05 K pc^{-1}) and smaller than our average error (0.06 K pc^{-1}). This effect is derived using the maximum extragalactic brightness temperature of 585 K divided by Galactocentric radius of 20 kpc.

We give an indicative quality number to each measurement as a means of judging reliability (Table 3.2 Col. 10). The quality number is the number of matched conditions below, maximum value of 6 means all conditions met.

1. The HII region is isolated and does not overlap with other HII regions.

2. The HII region belongs to a "known" HII region group, as defined in the *WISE* HII region catalogue (Anderson et al., 2014). "Known" HII regions are associated with radio recombination lines or Hα emission; they are confirmed HII regions, unlike "group" and "candidate" HII regions.

3. The area of the absorption region is at least two times larger than the beam size.

4. The location of the absorption feature corresponds well with that of the *WISE* 12 μm emission feature. We use this criterion because the lowest temperature region in some absorption features has a positional or dimensional offset compared with the brightest emission feature in *WISE*.

5. The distance of the particular HII region is measured rather than assuming it has the same distance as any other associated HII regions.

6. The electron temperature of the HII region is measured rather than calculated from the statistical relation in Balser et al. (2015).

Fig. 2.4 shows the emissivity (ϵ_b) distribution along different lines of sight. Our measured emissivities increase with respect to Galactic longitude (Fig. 2.5, left). This

is coincident with the total line-of-sight emissivity distribution, which can be seen in Fig. 2.6. The emissivity over the line of sight excluding point sources and supernova remnants decreases obviously with respect to Galactic longitude from 355° to 250°. Our measured emissivities are relatively high measured from HII regions with high Galactic latitude and relatively low derived from HII regions with low Galactic latitude (Fig. 2.5, right). This plot possibly reflects the decreasing of emissivity with the distance to the Galactic plane (Peterson and Webber, 2002), although our detections are limited in the range of the Galactic latitude from -1° to 2°.

Similar variations are also found in other surveys, e.g. the 408 MHz Haslam map (Fig. 4 in Haslam et al. 1982). The intensity profiles along Galactic longitude and latitude are well fitted by three magnetic field models in Sun et al. (2008) and Sun and Reich (2010).

2.3.2 Comparison with the literature

According to the brightness temperature spectrum $T(\nu) \propto \nu^{-2.3}$ (Guzmán et al., 2011) and the typical emissivity of 0.01 K pc^{-1} (Beuermann et al., 1985) at 408 MHz (Haslam et al., 1982), the typical emissivity at 88 MHz is expected to be 0.34 K pc^{-1}. The mean of our measured emissivity (ϵ_b) of 0.40 K pc^{-1} with a variance of 0.10 K pc^{-1} agrees within 1σ with this estimation.

To check for any systematic differences between the samples, we compare the measurements for two HII regions that appear both in our sample and Nord et al. (2006), in Table 2.2. Using the same distances and electron temperatures as listed in Nord et al. (2006), and scaling our measurements from 88 to 74 MHz using a brightness temperature spectral index of 2.3 ($T_\nu \propto \nu^{-2.3}$, Guzmán et al. 2011), our measurements agree within 1.5σ with those in Nord et al. (2006).

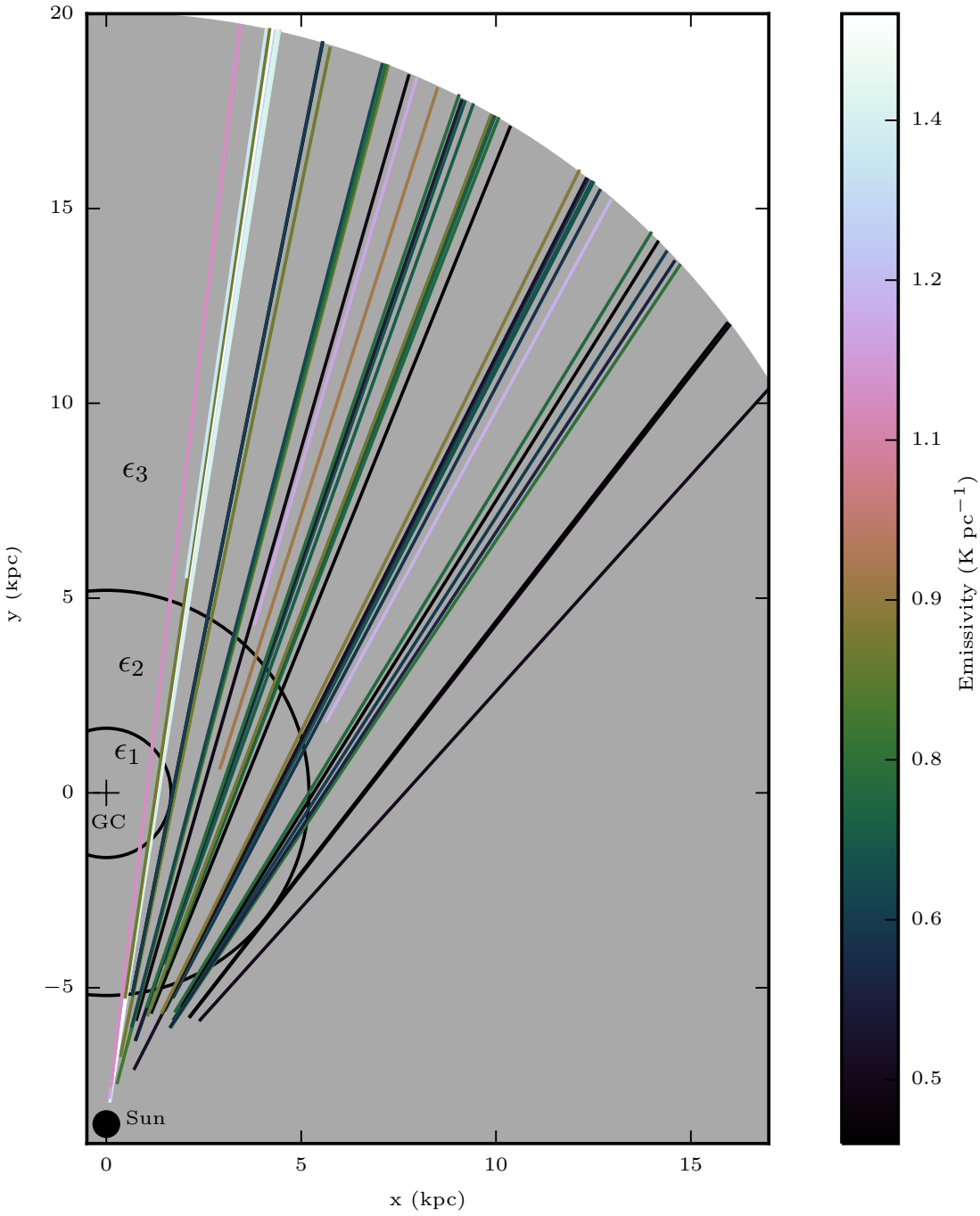

Figure 2.4: Distribution of emissivities (ϵ_b) on lines of sight and the Two-circle model. Each colour represents a path over which the emissivities are averaged. The colours of the lines indicate the value of emissivities along different paths. The Galactic non-thermal emission is assumed to lie in a disk with a Galactocentric radius of 20 kpc shown by the grey circle segment. The two circles near the Galactic centre divide the Galactic plane into three regions with emissivities of ϵ_1, ϵ_2, and ϵ_3 respectively. The Galactocentric radius of the Sun is 8.5 kpc. The Sun and Galactic centre (GC) are marked as a black dot and plus respectively.

Table 2.1: Emissivity measurements for HII regions with absorption features. *Notes.* Notes: Col. (1): The name of HII regions from the *WISE* HII region catalogue. Cols. (2) and (3): The MWA surface brightness measurements of the absorbing HII region and the neighbouring region, respectively. Cols. (4) and (5): The brightness temperatures of the absorbing HII region and the neighbouring region, respectively. Col. (6): The distance from HII regions to the Sun found in the literature. Col. (7): The electron temperature of HII regions from the literature. Col. (8): The average emissivity from HII regions to the Sun. Col. (9): The average emissivity from HII regions to the Galactic edge. Col. (10): The indicative quality of emissivity measurements: a higher value means higher quality (see Section 2.3.1). Col. (11): The references for the distances and electron temperatures. The first and second number indicate the reference for the distance in Col. (6) and the electron temperature in Col. (7) respectively. The reference list: 1. Anderson et al. (2014); 2. Balser et al. (2015); 3. Caswell and Haynes (1987); 4. García et al. (2014); 5. Hou and Han (2014); 6. Nord et al. (2006); 7. Paladini et al. (2004); 8. Quireza et al. (2006); 9. Reid et al. (2014). [a] The electron temperature of this HII region is derived from the statistical relation $T_e = (4928 \pm 277) + (385 \pm 29)\ R_{\rm gal}$ from Balser et al. (2015).

WISE name	$I_{\rm o}$	$I_{\rm t}$	$T_{\rm o}$	$T_{\rm t}$	$D_{\rm f}$	$T_{\rm e}$	$\epsilon_{\rm f}$	$\epsilon_{\rm b}$	Q	Ref.
	Jy beam^{-1}	Jy beam^{-1}	$\times 10^4$ K	$\times 10^4$ K	kpc	$\times 10^3$ K	K pc^{-1}	K pc^{-1}		
(1)	(2)	(3)	(4)	(5)	(6)	(7)	(8)	(9)	(10)	(11)
G317.988−00.754	1.86±0.14	2.80±0.14	1.05±0.08	1.58±0.08	3.6±1.1	4.60±0.37	-0.55±0.20	0.27±0.03	6	5;5
G322.036+00.625	1.30±0.11	1.67±0.11	0.73±0.06	0.94±0.06	3.5±3.5	7.29±0.33[a]	-1.56±1.56	0.35±0.06	2	1;2

Continued on next page

WISE name	$I_{\rm o}$	$I_{\rm t}$	$T_{\rm o}$	$T_{\rm t}$	$D_{\rm f}$	$T_{\rm e}$	$\epsilon_{\rm f}$	$\epsilon_{\rm b}$	Q	Ref.
	Jy beam^{-1}	Jy beam^{-1}	$\times10^4$ K	$\times10^4$ K	kpc	$\times10^3$ K	K pc^{-1}	K pc^{-1}		
(1)	(2)	(3)	(4)	(5)	(6)	(7)	(8)	(9)	(10)	(11)
G322.220+00.504	1.45±0.14	1.72±0.14	0.82±0.08	0.97±0.08	3.5±3.5	7.29±0.33[a]	-1.50±1.50	0.34±0.06	1	1;2
G326.270+00.783	1.49±0.29	3.30±0.29	0.84±0.16	1.87±0.16	3.0±0.4	7.33±0.33[a]	-1.74±0.29	0.42±0.03	5	1;2
G326.643+00.514	2.35±0.29	3.30±0.29	1.33±0.16	1.87±0.16	3.0±0.4	7.32±0.33[a]	-1.33±0.25	0.37±0.03	4	1;2
G327.300−00.548	1.32±0.21	2.73±0.21	0.75±0.12	1.54±0.12	3.2±0.4	6.10±0.36	-1.32±0.22	0.35±0.02	6	1,7;5
G327.991−00.087	5.12±0.18	5.68±0.18	2.89±0.10	3.21±0.10	3.6±1.8	6.00±0.36	0.34±0.21	0.29±0.03	5	5;5
G328.572−00.527	4.29±0.19	5.98±0.19	2.42±0.11	3.38±0.11	3.4±0.4	7.19±0.33[a]	-0.33±0.13	0.41±0.02	4	1;2
G331.365+00.521	3.32±0.26	5.65±0.26	1.88±0.15	3.19±0.15	11.8±5.9	4.80±0.34	-0.01±0.04	0.53±0.21	6	5;5
G332.145−00.452	3.44±0.14	4.60±0.14	1.94±0.08	2.60±0.08	3.7±0.4	7.05±0.32[a]	-0.59±0.12	0.37±0.02	4	1;2
G332.657−00.622	2.19±0.39	3.68±0.39	1.24±0.22	2.08±0.22	3.3±0.4	7.15±0.32[a]	-1.23±0.24	0.39±0.04	3	1;2
G332.762−00.595	2.18±0.39	3.68±0.39	1.23±0.22	2.08±0.22	3.8±0.4	7.01±0.32[a]	-1.03±0.20	0.39±0.04	3	1;2
G332.978+00.773	4.16±0.16	5.75±0.16	2.35±0.09	3.25±0.09	3.8±0.5	4.00±0.35	0.50±0.13	0.27±0.02	5	5;5

Continued on next page

WISE name	$I_{\rm o}$	$I_{\rm t}$	$T_{\rm o}$	$T_{\rm t}$	$D_{\rm f}$	$T_{\rm e}$	$\epsilon_{\rm f}$	$\epsilon_{\rm b}$	Q	Ref.
	Jy beam^{-1}	Jy beam^{-1}	$\times10^4$ K	$\times10^4$ K	kpc	$\times10^3$ K	K pc^{-1}	K pc^{-1}		
(1)	(2)	(3)	(4)	(5)	(6)	(7)	(8)	(9)	(10)	(11)
G333.011−00.441	2.09±0.23	3.42±0.23	1.18±0.13	1.93±0.13	3.6±0.4	7.06±0.32[a]	-1.14±0.18	0.38±0.02	5	1;2
G333.093+01.966	1.77±0.24	2.57±0.24	1.00±0.14	1.45±0.14	1.6±0.6	7.67±0.35[a]	-3.23±1.25	0.34±0.02	5	1;2
G333.627−00.199	2.42±0.27	4.90±0.27	1.37±0.15	2.77±0.15	3.2±0.4	7.16±0.32[a]	-1.17±0.21	0.44±0.03	4	1;2
G337.957−00.474	4.66±0.19	5.46±0.19	2.63±0.11	3.09±0.11	3.1±1.6	5.60±0.35	0.32±0.22	0.27±0.03	4	5;5
G338.706+00.645	3.87±0.30	5.64±0.30	2.19±0.17	3.19±0.17	4.3±0.4	6.76±0.31[a]	-0.30±0.13	0.40±0.03	4	1;2
G338.911+00.615	3.75±0.30	5.64±0.30	2.12±0.17	3.19±0.17	4.4±0.4	6.73±0.31[a]	-0.32±0.12	0.40±0.03	4	1;2
G338.934−00.067	4.62±0.21	6.29±0.21	2.61±0.12	3.56±0.12	3.2±0.4	7.10±0.32[a]	-0.18±0.14	0.39±0.02	4	1;2
G339.109−00.233	4.25±0.29	5.70±0.29	2.40±0.16	3.22±0.16	6.5±3.3	4.20±0.32	0.28±0.16	0.29±0.06	4	5;5
G339.134−00.377	3.25±0.29	5.70±0.29	1.84±0.16	3.22±0.16	3.0±0.4	7.16±0.32[a]	-0.86±0.21	0.43±0.03	3	1;2
G340.216+00.424	2.75±0.30	4.71±0.30	1.55±0.17	2.66±0.17	4.4±2.2	4.80±0.33	-0.21±0.16	0.32±0.04	6	5;5
G340.678−01.049	2.22±0.28	3.81±0.28	1.25±0.16	2.15±0.16	2.3±2.3	7.38±0.33[a]	-1.84±1.86	0.38±0.04	1	1;2

Continued on next page

WISE name	$I_{\rm o}$	$I_{\rm t}$	$T_{\rm o}$	$T_{\rm t}$	$D_{\rm f}$	$T_{\rm e}$	$\epsilon_{\rm f}$	$\epsilon_{\rm b}$	Q	Ref.
	Jy beam^{-1}	Jy beam^{-1}	$\times10^4$ K	$\times10^4$ K	kpc	$\times10^3$ K	K pc^{-1}	K pc^{-1}		
(1)	(2)	(3)	(4)	(5)	(6)	(7)	(8)	(9)	(10)	(11)
G340.780−01.022	1.89±0.28	3.82±0.28	1.12±0.16	2.16±0.16	2.3±0.6	7.38±0.33[a]	-1.99±0.57	0.39±0.03	2	1;2
G340.862−00.870	3.22±0.23	4.26±0.23	1.82±0.13	2.41±0.13	2.3±2.3	7.38±0.33[a]	-1.23±1.25	0.35±0.04	1	1;2
G341.090−00.017	3.22±0.15	5.16±0.15	1.82±0.08	2.92±0.08	3.2±3.2	7.07±0.32[a]	-0.79±0.80	0.40±0.05	3	1;2
G342.277+00.311	2.97±0.33	5.25±0.33	1.68±0.19	2.97±0.19	9.6±4.8	3.90±0.32	0.03±0.06	0.39±0.11	4	5;5
G343.480−00.043	2.46±0.21	4.03±0.21	1.39±0.12	2.28±0.12	13.4±7.4	8.10±0.35	-0.34±0.19	0.71±0.36	6	5;5
G343.914−00.646	3.71±0.16	4.38±0.16	2.10±0.09	2.48±0.09	2.8±1.4	7.20±0.35	-0.70±0.38	0.32±0.03	5	5;5
G345.094−00.779	1.72±0.29	4.26±0.33	0.97±0.19	2.41±0.19	2.1±2.1	7.43±0.33[a]	-2.38±2.39	0.42±0.04	4	1;2
G345.202+01.027	1.18±0.61	4.10±0.61	0.67±0.34	2.32±0.34	1.1±0.6	4.80±0.12	-2.85±1.74	0.33±0.05	4	4;5
G345.235+01.408	1.12±0.34	2.59±0.34	0.69±0.19	1.46±0.19	8.0±4.0	6.00±0.35	-0.64±0.33	0.44±0.09	5	2;2
G345.410−00.953	2.00±0.40	3.60±0.40	1.13±0.23	2.03±0.23	2.6±0.6	6.96±0.05	-1.59±0.43	0.36±0.03	6	1;2
G348.261+00.485	3.40±0.32	6.05±0.32	1.92±0.18	3.42±0.18	1.8±1.8	7.53±0.34[a]	-1.51±1.55	0.43±0.04	4	1;2

Continued on next page

WISE name	$I_{\rm o}$	$I_{\rm t}$	$T_{\rm o}$	$T_{\rm t}$	$D_{\rm f}$	$T_{\rm e}$	$\epsilon_{\rm f}$	$\epsilon_{\rm b}$	Q	Ref.
	Jy beam^{-1}	Jy beam^{-1}	$\times10^4$ K	$\times10^4$ K	kpc	$\times10^3$ K	K pc^{-1}	K pc^{-1}		
(1)	(2)	(3)	(4)	(5)	(6)	(7)	(8)	(9)	(10)	(11)
G348.691−00.826	2.15±0.33	3.03±0.33	1.22±0.19	1.71±0.14	3.4±0.3	4.80±1.00	-0.52±0.33	0.24±0.05	6	1;6
G348.710−01.044	1.27±0.28	2.67±0.28	0.72±0.16	1.51±0.16	3.4±0.3	6.20±1.00	-1.57±0.18	0.37±0.02	6	1;8
G350.991−00.532	3.16±0.31	4.31±0.31	1.79±0.18	2.44±0.18	13.7±6.9	6.10±0.35	-0.12±0.07	0.53±0.25	5	5;5
G350.995+00.654	2.08±0.67	6.86±0.67	1.18±0.38	3.88±0.38	0.6±0.3	10.57±0.34	-12.72±6.58	0.62±0.05	5	8;8
G351.130+00.449	2.85±0.82	8.24±0.82	1.61±0.46	4.66±0.46	1.4±0.7	6.65±0.07	-1.87±1.25	0.53±0.06	5	8;8
G351.311+00.663	2.12±0.35	6.96±0.35	1.20±0.20	3.93±0.20	1.3±0.1	7.71±0.35[a]	-3.63±0.54	0.54±0.03	3	9;2
G351.383+00.737	1.77±0.34	7.02±0.34	1.00±0.19	3.97±0.19	1.3±0.1	9.70±0.09	-5.54±0.57	0.63±0.03	5	9;2
G351.516−00.540	3.28±0.30	6.04±0.38	1.85±0.17	3.41±0.21	3.3±3.3	5.70±1.00	-0.32±0.46	0.38±0.07	3	6;3
G351.688−01.169	1.71±0.25	3.87±0.25	0.97±0.14	2.19±0.14	14.2±1.0	6.49±0.21	-0.29±0.04	0.67±0.06	6	2;2
G353.038+00.581	1.52±0.56	5.33±0.56	0.86±0.32	3.01±0.32	1.1±1.1	7.78±0.35[a]	-5.12±5.18	0.48±0.05	3	1;2
G353.076+00.287	2.06±0.75	6.81±0.75	1.16±0.42	3.85±0.42	0.7±1.5	5.39±0.10	-3.54±7.74	0.44±0.06	5	2;2

Continued on next page

WISE name	I_o	I_t	T_o	T_t	D_f	T_e	ϵ_f	ϵ_b	Q	Ref.
	Jy beam^{-1}	Jy beam^{-1}	$\times 10^4$ K	$\times 10^4$ K	kpc	$\times 10^3$ K	K pc^{-1}	K pc^{-1}		
(1)	(2)	(3)	(4)	(5)	(6)	(7)	(8)	(9)	(10)	(11)
G353.092+00.857	1.29±0.56	5.33±0.56	0.73±0.32	3.01±0.32	1.0±2.0	7.10±0.40	-5.28±10.59	0.47±0.06	5	2;2

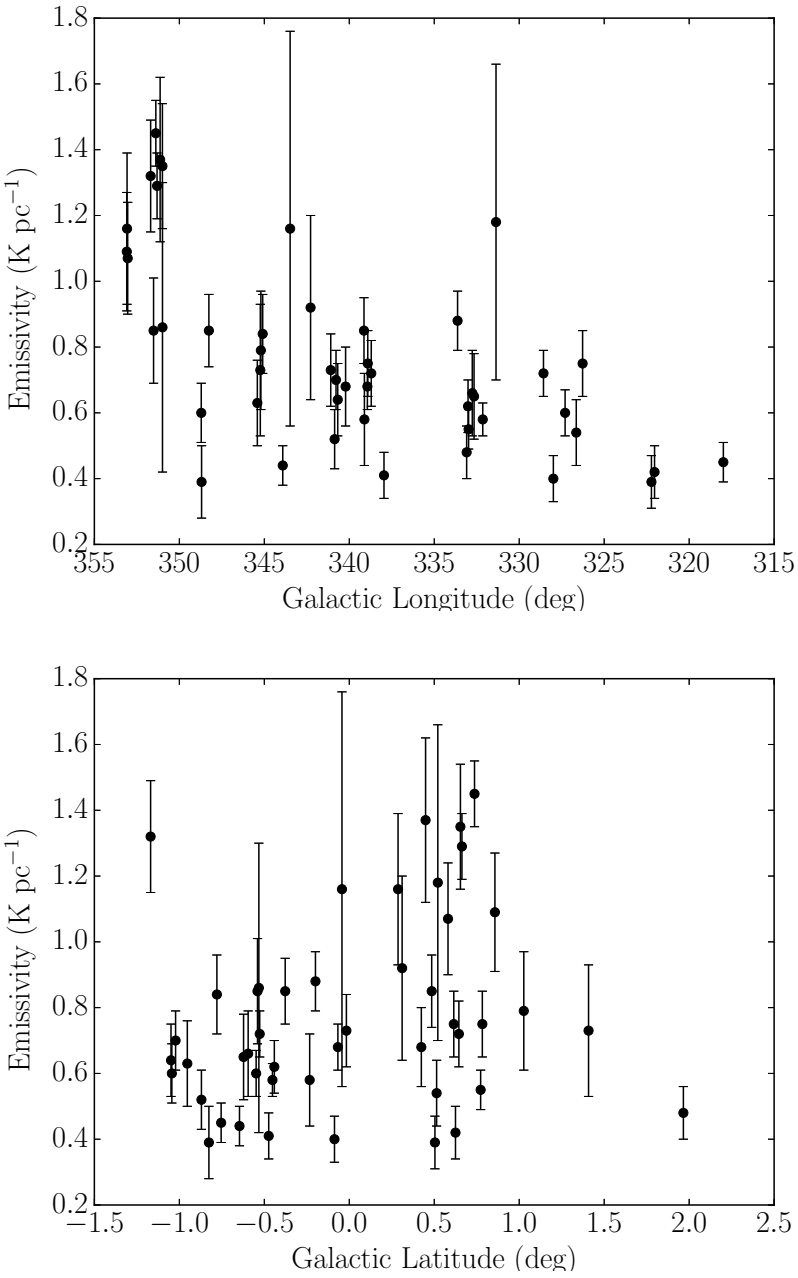

Figure 2.5: Distributions of emissivities (ϵ_b) with respect to Galactic longitude (top) and latitude (bottom). Some measurements have large errors due to the uncertainty of the distances of HII regions.

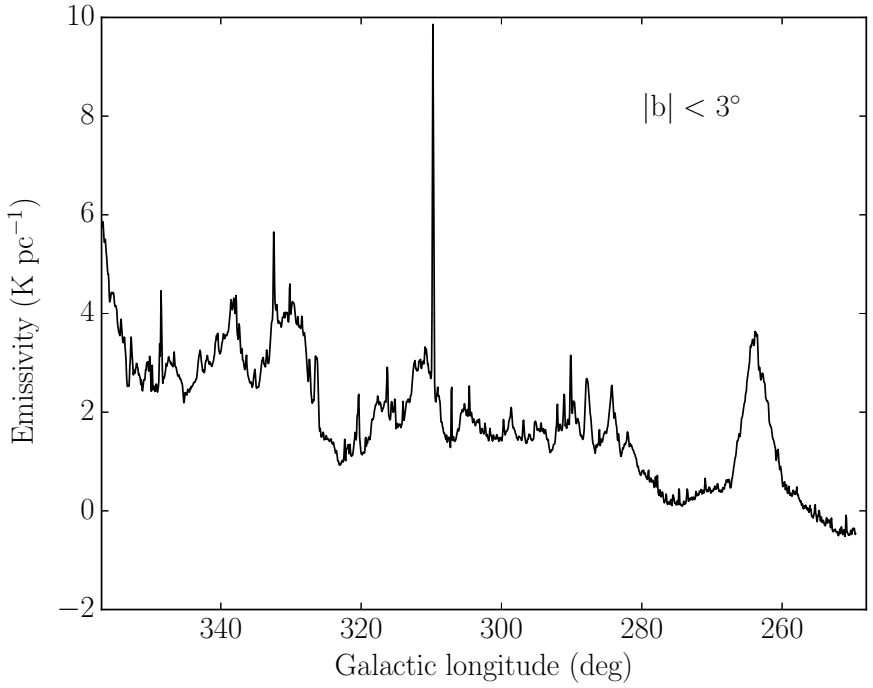

Figure 2.6: Distributions of emissivity from the Sun to the Galactic edge over the line of sight with respect to the Galactic longitude in the range $250^\circ < l < 355^\circ, |b| < 3^\circ$: this includes the contributions from point sources and supernova remnants. The bin size in Galactic longitude is $3\farcm75$. There is a trend of increasing emissivity with longitude. The high emissivity near the Galactic longitude 264° is contributed by the Vela supernova remnant. Note that we do not recover the total power of the Galaxy due to the interferometric nature of the measurements.

Table 2.2: Comparison of three emissivities measured in Nord et al., (2006) and this work.

HII region (this work)	G351.516−00.540	G348.710−01.044	G348.691−00.826
HII region (Nord et al., 2006)	G351.5−0.5	G348.7−1.0	G348.6−0.6
Distance (kpc, used in Nord et al., 2006)	3.3	2.0	2.7
T_e ($\times 10^3$ K, used in Nord et al., 2006)	5.7 ± 1.0	6.2 ± 1.0	4.8 ± 1.0
Angular diameter (arcmin, used in Nord et al., 2006)	3.46	4.47	13.27
ϵ_b(K pc^{-1}, at 74 MHz, Nord et al., 2006)	0.36 ± 0.06	0.36 ± 0.05	0.51 ± 0.05
ϵ_b(K pc^{-1}, scaled at 74 MHz, this work)[1]	0.45 ± 0.06	0.35 ± 0.05	0.26 ± 0.05

[1] To compare our measurements with those in Nord et al. (2006), we re-calculate our emissivities for the two HII regions using the distances and electron temperatures from Nord et al. (2006) and scale our measurements from 88 to 74 MHz using a brightness temperature spectral index of 2.3.

2.3.3 Non-detections and Detection Bias

About 80 HII regions with radii larger than the beam size and smaller than the maximum angular scale sensitivity are not detected as absorption regions in the region we analyse (Fig. 2.1). A possible reason is that not enough synchrotron emission exists behind these HII regions; an absorption feature is only apparent when the integrated brightness temperature blocked by an HII region is larger than its electron temperature (see Equations 2.2 and 2.3). Another possible reason is that these HII regions are optically thin at the observed frequency. As shown in Fig. 2.1, all of our 47 detections are in the range of $315^\circ < l < 355^\circ$ whereas only 25 non-detections are in this range. The other 55 non-detections are in the low brightness temperature region with the range of $250^\circ < l < 315^\circ$, which might be detectable in emission at higher frequencies and these will be followed up in future. Two other possibilities of non-detections are a high electron temperature and/or a low optical depth for these HII regions.

Note that we assume HII regions associated with absorption features have an optical depth much larger than one. In the future, the work will use the MWA GLEAM survey coverage 72–231 MHz to measure the optical depth and confirm this hypothesis.

Finally, our emissivity measurements do not sample the whole Galactic disk uniformly mainly due to the non-uniform distribution of HII regions. Most of the observed HII regions are nearby, with distances of several kiloparsecs. The HII regions with large distances usually have large distance uncertainties, resulting in large emissivity uncertainties.

2.4 Modelling the emissivity distribution

The measured emissivities need modelling to show the emissivity distribution with respect to the Galactic radius. We build four simple models to probe this complex problem.

The synchrotron emissivity is the power per unit volume per unit frequency per unit solid angle produced by cosmic-ray electrons interacting with the magnetic field. Since we can only measure the average emissivity along paths, we adopt four simple models: Uniform; Gaussian; Exponential; and Two-circle to fit the emissivity distribution of the Galaxy. We fit our measured ϵ_b using these models. We test a Uniform model given that Nord et al. (2006) found a constant emissivity outside of a circular region centred at the Galactic centre with a radius of 3 kpc. The Exponential model is motivated by the exponential cosmic-ray electron distribution used in Sun et al. (2008). The Gaussian model is an alternative form to express a decreasing emissivity profile from the Galactic centre. The two-circle model is constructed with more free parameters and to specifically account for the high emissivities found for regions with paths close to the Galactic centre.

Before showing details of each model, we define R_0 to be the Galactocentric radius of the Sun, R to be the Galactocentric radius of any point on the Galactic plane, d to be the distance from an HII region to the Sun, l to be the Galactic longitude, α and β to be free parameters related to Gaussian and Exponential models.

The Uniform model assumes a constant emissivity distribution across the Galactic disk.

In the Gaussian model, the emissivity is assumed to have a distribution $\epsilon(R) = \alpha_1 \exp(-R^2/2\beta_1^2)$. We assume the emissivity peaks at the Galactic centre. R is a function of the distance d, so the emissivity ϵ is also a function of d. The average

emissivity from the HII region to the Galactic edge is the integration of $\epsilon(d)$ for d and then divided by the corresponding path length.

The Exponential model has an emissivity distribution in the form of a natural exponential function $\epsilon(R) = \alpha_2 \exp(-\beta_2 R)$. The method of calculating the average emissivities along the line of sight from this model is the same as that in the Gaussian model.

We also develop a simple Two-circle model motivated by the data. In this model, we divide the Galactic plane into three regions using two circles centring on the Galactic centre. R_1 and R_2 ($R_1 < R_2$) are the radii of circles 1 and 2, respectively. ϵ_1 is the emissivity in circle 1. ϵ_2 is the emissivity in the region between circle 1 and circle 2. ϵ_3 is the emissivity in the region outside circle 2 and within the Galactic edge (see Fig 2.4).

With the assumptions in each model, we determine the free parameters by fitting the observed emissivities (ϵ_b) and those from the model using the (reduced) chi-squared test (e.g. Andrae et al. 2010) to compare the goodness of fit of the models. We did not fit the average emissivities from HII regions to the Sun since they are not absolutely reliable as mentioned in Section 2.1. We sample the whole parameter spaces and find the minimum of chi-squares for each model. We use the boundary of fixed $\Delta\chi^2$ (2σ) to estimate the quoted errors. We project the full M-dimensional (M = 2, 5) confidence region on the one-dimensional confidence interval for each parameter.

The results of modelling are shown in Table 2.3. The Uniform model shows an average emissivity of $0.38^{+0.04}_{-0.02}$ K pc^{-1} with a poor reduced chi-square ($\chi^2_{\rm red} = 6.51$). The Gaussian and Exponential models have similarly poor fits ($\chi^2_{\rm red} \sim 6.03$ and 5.77). The Two-circle model has the best performance compared with the other three models ($\chi^2_{\rm red} = 3.74$). It shows a high emissivity ($2.0^{+1.8}_{-1.7}$ K pc^{-1}) region near the Galactic centre within a radius of $1.7^{+0.1}_{-0.4}$ kpc, a low emissivity ($0.30^{+0.13}_{-0.17}$ K pc^{-1}) region outside

of a radius of $7.5^{+5.5}_{-2.9}$ kpc, a medium emissivity ($0.59^{+0.32}_{-0.49}$ K pc^{-1}) region between the two. In Fig. 2.7 we show the correlations between the parameters for the Two-Circle model. We see that in the 2σ contour of chi-square, a lower R_1 corresponds to a higher ϵ_1, but when R_1 is lower than about 1.3 kpc, ϵ_1 does not increase further. Similarly, a higher R_2 cannot give a lower ϵ_2 when R_2 exceeds about 10 kpc. In the sub-plot R_2:ϵ_3, R_2 is fixed to be higher than 1 kpc since it cannot be less than R_1. The 2σ errors for each parameter in the Two-circle model are large due to the correlations between the parameters, and fundamentally due to the limited number of measurements, and because most of the HII regions are nearby; those that are more distant have large error bars on their distance measurements, reducing their importance during the fitting process. Our best fitted R_1 of the innermost circle includes the brightest Galactic centre region. Potentially showing a physical correlation, the region between the best fitted R_1 and R_2 includes several spiral arms, e.g., the 3-kpc ring, the Sagittarius arm, and the Norma arm. The large region outside of the outer most circle only contains the Scutum-Centaurus arm and the McClure-Griffiths arm (McClure-Griffiths et al., 2004).

Fig. 2.8 compares the models in more detail where it can be seen that none provide a good fit to the four measurements with short path lengths ($14-16$ kpc). However, all models similarly account for the measurements with longer path lengths ($18-26$ kpc). The main differences among models appear at the path length above 26 kpc, where there are several high average emissivities. These high emissivities pass the region near the Galactic centre. Only the Two-circle model, which has additional free parameters, can recover these high emissivities ($2.0^{+1.8}_{-1.7}$ K pc^{-1}) near the Galactic centre.

Furthermore, the Two-circle model can explain the low emissivity along the total lines of sight towards Galactic longitude between 270° and 320° (Fig. 2.6). The brightness temperature in these directions is significantly lower compared with that in other

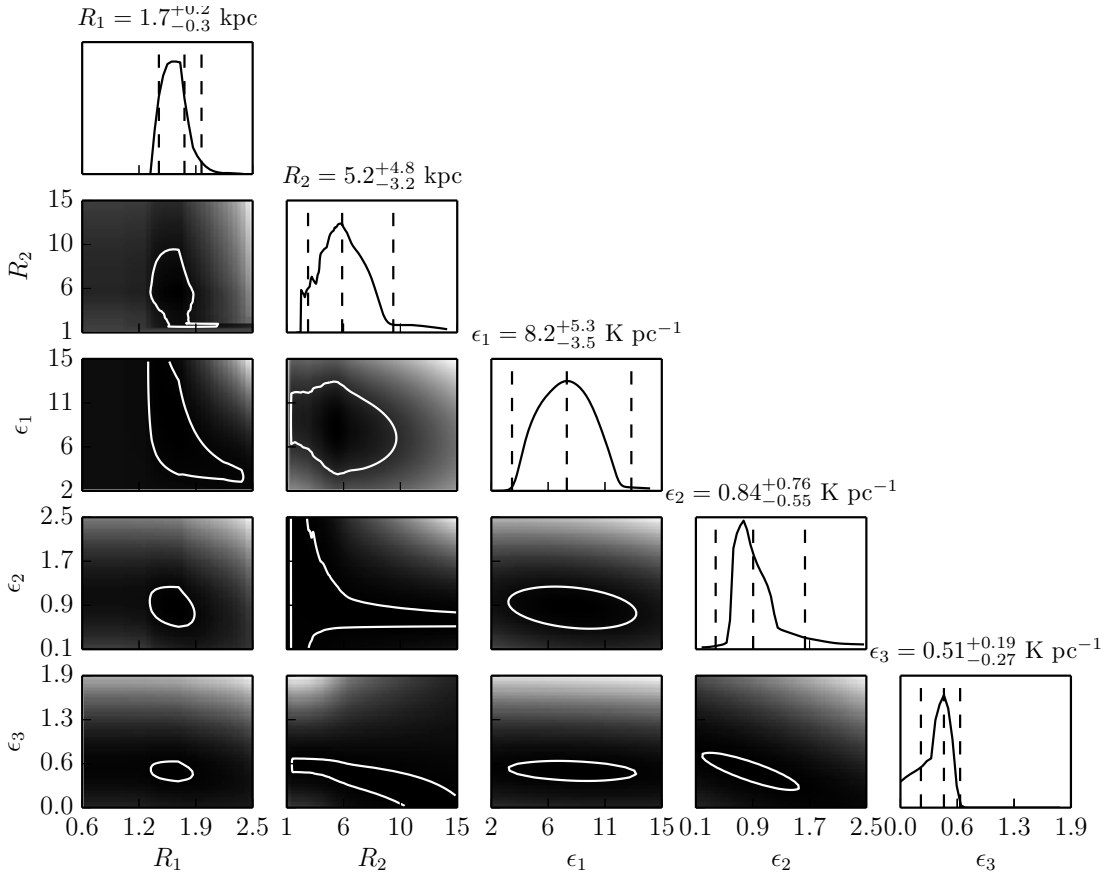

Figure 2.7: Triangle plot showing the correlations between the two-circle model parameters: the grey scale traces the distributions of chi-square with darker regions indicating lower values. The 2σ boundaries of chi-square are shown by white contours. The black solid lines show the relative likelihood distributions with dashed lines showing the best values and 2σ limits of the parameters.

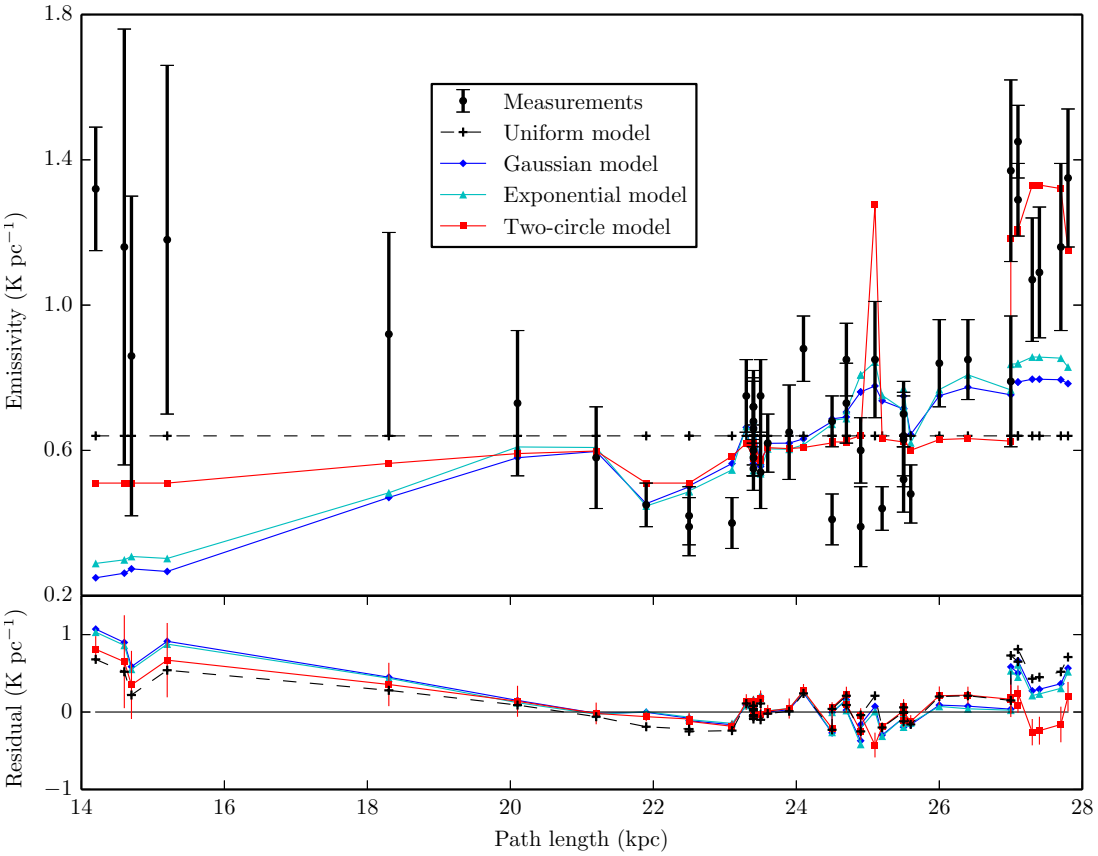

Figure 2.8: Distributions of emissivities (ϵ_b) from our measurements and models with the path length from HII regions to the Galactic edge along the line of sight.

Table 2.3: Parameters from fitting the measured emissivities with four models: Uniform, Gaussian, Exponential, and Two-circle model.

Model	Free parameters	$\chi^2_{\rm red}$	Degrees of freedom
Uniform	$\epsilon = 0.38^{+0.04}_{-0.02}$	6.51	46
Gaussian	$\alpha_1 = 0.71^{+0.29}_{-0.22}$, $\beta_1 = 8.2^{+5.8}_{-2.7}$	6.03	45
Exponential	$\alpha_2 = 0.94^{+0.46}_{-0.43}$, $\beta_2 = 0.11^{+0.06}_{-0.07}$	5.77	45
Two-circle	$R_1 = 1.7^{+0.1}_{-0.4}$, $R_2 = 7.5^{+5.5}_{-2.9}$	3.74	42
	$\epsilon_1 = 2.0^{+1.8}_{-1.7}$, $\epsilon_2 = 0.59^{+0.32}_{-0.49}$, $\epsilon_3 = 0.30^{+0.13}_{-0.17}$		

Note: The unit of ϵ, ϵ_1, ϵ_2, ϵ_3, α_1, and α_2 are K pc^{-1}. The unit of R_1, R_2, and β_1 are kiloparsecs. The unit of β_2 is kpc^{-1}. All the quoted errors are at 2σ level. The Gaussian model tends to the Uniform model when β_1 tends to infinity. The formula for Degrees of Freedom equals the size of the data sample minus the number of parameters in a model.

directions in Fig. 2.1.

Nord et al. (2006) determined a best-fit model with uniform emissivity between 3 and 20 kpc and zero within 3 kpc of the Galactic centre. However, this model does not fit our data better than any of our models. Our best-fit Two-circle model shows the highest emissivity near the Galactic centre, contrary to Nord et al. (2006) but quite likely due to sampling bias: our work samples regions in the fourth quadrant whereas the sample of Nord et al. (2006) is mainly in the first quadrant; two of their measurements overlap with ours. Their measured emissivities are lower when the paths are closer to the Galactic centre, whereas ours are opposite, driving our model fits to increase the emissivity near the Galactic centre. Note that both of these two observations probe 2–3 kpc nearby the Galactic centre but no detection is closer to the Galactic centre. The modelling in Sun et al. (2008) suggested a high magnetic field strength and the free electron model in NE2001 (Cordes and Lazio, 2002) suggested a high free electron density near 2-3 kpc of the Galactic centre. These results support our

conclusions.

Note that our four simplified models are only initial tests for the complex emissivity distribution. Our models have limited power to fully describe our measurements, not to mention other surveys at different frequencies. To understand the Galactic physical structures, we need to analysis our measurements and other survey data coherently using comprehensive models developed by Sun et al. (2008); Sun and Reich (2010); Orlando and Strong (2013), etc.

2.5 Summary

We measured emissivities from 47 HII regions in the region $250^\circ < l < 355^\circ$, $|b| < 2^\circ$ along the two paths behind and in front of HII regions. We find that all average emissivities between the HII regions and the Galactic edge along the line of sight (ϵ_b) are in the range of 0.24 $\sim$ 0.70 K pc^{-1} with a mean of 0.40 K pc^{-1} and a variance of 0.10 K pc^{-1} at 88 MHz. These measurements show the radial dependence of emissivity distribution. The modelling of these measurements shows a high emissivity region near the Galactic centre and low emissivities near the Galactic edge. In specific, the Two-circle model, divides the Galactic disk into three regions using two circles centring on the Galactic centre. It shows a high emissivity region near the Galactic centre, a low emissivity region near the Galactic edge, and a medium emissivity region between these two regions, contrary to the trend found by previous studies.

Chapter 3

Improved measurements of Galactic synchrotron emissivity

I conducted all work for this chapter under the guidance of my supervisory panel.

This chapter is adapted from:

Su, H., J. P. Macquart, N. Hurley-Walker, N. M. McClure-Griffiths, C. A. Jackson, S. J. Tingay, W. W. Tian, B. M. Gaensler, B. McKinley, A. D. Kapińska, L. Hindson, P. Hancock, R. B. Wayth, L. Staveley-Smith, J. Morgan, M. Johnston-Hollitt, E. Lenc, M. E. Bell, J. R. Callingham, K. S. Dwarkanath, B.-Q. For, A. R. Offringa, P. Procopio, C. Wu, and Q. Zheng (2018, September). Galactic synchrotron distribution derived from 152 HII region absorption features in the full GLEAM survey. MNRAS 479, 4041–4055.

In this Chapter, we derive the synchrotron distribution in the Milky Way disk from HII region absorption observations over $-40^\circ < l < 40^\circ$ at six frequencies of 76.2, 83.8, 91.5, 99.2, 106.9, and 114.6 MHz with the GLEAM survey. We develop a new method of emissivity calculation by taking advantage of the Haslam et al., (1981) map

and known spectral indices, which enable us to simultaneously derive the emissivity and the optical depth of HII regions at each frequency. We show our derived synchrotron emissivities based on 152 absorption features of HII regions using both the method previously adopted in the literature and our improved method. We derive the synchrotron emissivity from HII regions to the Galactic edge along the line of sight and, for the first time, derive the emissivity from HII regions to the Sun. These results provide direct information on the distribution of the Galactic magnetic field and cosmic-ray electrons for future modelling.

In this chapter, section 3.1 introduces the observational data used in this work. Section 3.2 discusses the previous simplified method and the new method we developed. Section 3.3 presents our newly-derived emissivities. Section 3.4 discusses our results and compare them to previous work. We summarise our findings in Section 2.5.

3.1 Observations

Specifically, we use data obtained by the MWA as part of the GLEAM (Wayth et al., 2015). The data in this work was collected in four weeks within the first year of the GLEAM between 2013 June and 2014 July.

In this GLEAM data, the flux density is rescaled by comparing the flux densities of well-observed point sources measured by other surveys, such as the NRAO VLA Sky Survey (NVSS, Condon et al. 1998) at a frequency of 1420 MHz, the Sydney University Molonglo Sky Survey (SUMSS, Mauch et al. 2003) at a frequency of 843 MHz, and the VLA Low-Frequency Sky Survey (VLSS, Cohen et al. 2007) at a frequency of 74 MHz. The flux density scale of sources at the frequencies of the GLEAM can be determined by fitting with these flux densities.

The above method works well for point sources but has problems when applying

the same correction factor to the whole image, where extended sources exist. One reason is the interferometer is not sensitive to large scales because of lacking of the short spacings. Thus the correction factor for extended sources is complex since it varies with the scale.

We use the all-sky 408 MHz map of Haslam et al. (1981, 1982) reprocessed by (Remazeilles et al., 2015) to estimate the total power of Galactic synchrotron emission along the line of sight towards the HII regions at the GLEAM frequencies. The Haslam map is a combination of four different surveys from the Jodrell Bank MkI, Bonn 100 meter, Parkes 64 meter and Jodrell Bank MkIA telescopes. This map is dominated by the Galactic synchrotron emission with 6% free-free emission (Dickinson et al., 2003) as neglectable contamination for this work. We also neglect the free-free absorption due to the unresolved HII regions and the warm interstellar medium. The reprocessed Haslam map removed the strong point sources in the destriped/desourced (dsds) version. Thus, the contamination of the extra-galactic sources is minimized.

3.2 Improved method of emissivity calculations

Two methods are available for calculations of the emissivity using HII region absorption observations. One is the simplified method adopted by Nord et al. (2006) and Su et al. (2017a). This method is particularly suitable for observations without large scale structures resolved out and requires that the HII region is opaque. The other is an improved method developed in Su et al. (2018) which is suitable both for interferometer observations with some structures resolved out and single dish observations with total power recovered. It does not require the HII region is opaque, instead, it can solve out the value of optical depth of the HII region.

A simplified method of calculating the Galactic synchrotron emissivity was adopted

by Nord et al. (2006) and slightly modified to include the contribution of the measured background by Su et al. (2017a,b). We believe this approach can be improved in two ways.

Firstly, it assumes the optical depths of HII regions are much larger than 1. However, this assumption may not be correct for some HII regions because they show only mild absorption ($\tau \sim 1$) at the frequencies used to separate the foreground and background emission.

Secondly, the method underestimates the emissivity behind HII regions when some flux density is resolved out by an interferometric observation, especially when the all-sky "zero-spacing" component is omitted (see Fig. 3.1). The shortest spacing of the MWA tiles is about 7 metres, corresponding to an angular scale of about 30 degrees, indicating that the MWA is sensitive to the whole sky emission with fluctuations on scales smaller than 30 degrees. Structures on larger angular scales are resolved out by the MWA. This undetected emission has the effect that the derived emissivities are under-estimated. The surface brightness of the Galactic synchrotron emission increases towards lower frequencies, making its contribution large at the $\approx$100 MHz frequencies relevant to the detection of HII regions compared to 408 MHz at which the Haslam map was obtained.

To improve this method, we have developed a procedure that attempts to solve for both the optical depth of the HII regions and the brightness temperature of the emission associated with the missing interferometric spacings. We scale the 408 MHz all-sky image to the frequency of interest by a global brightness temperature spectral index (α: $S_\nu \propto \nu^\alpha$) to estimate the total power along the line of sight and then use it to deduce the brightness temperature on scales resolved out by our interferometer. We use two data sets from the GLEAM with each one containing three frequencies (76.2, 83.8, 91.5 MHz; and 99.2, 106.9, 114.6 MHz) to perform calculations and assume

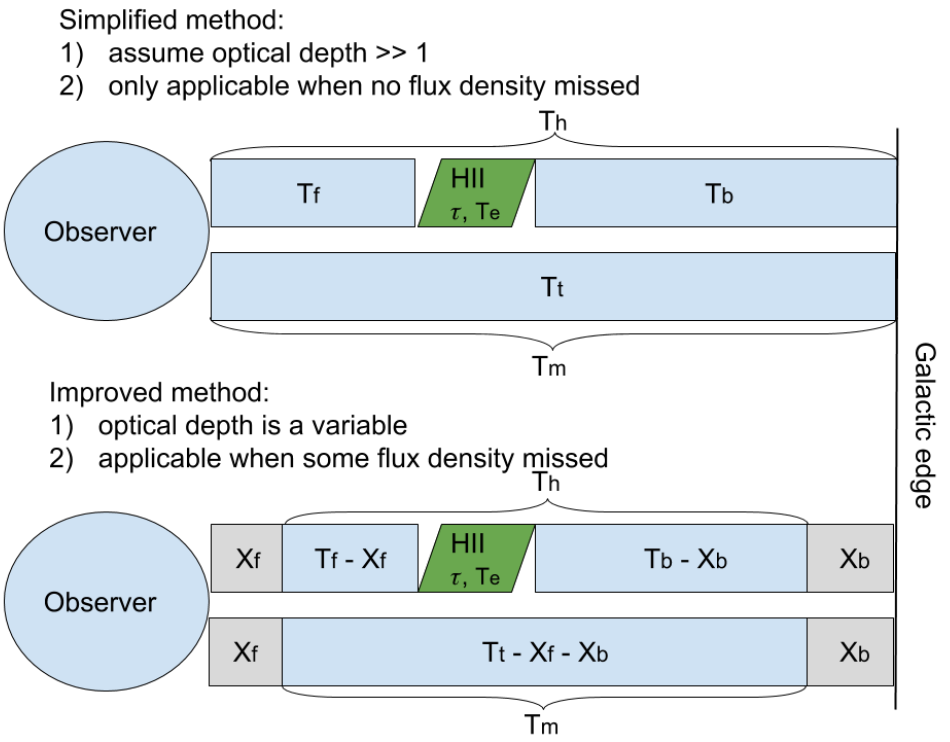

Figure 3.1: A schematic of how the missing flux density affects the derived emissivities in the simplified method (top) and in the improved method (bottom).

that synchrotron and optical depths have a power law scaling with the frequency. More details of this new method are described in what follows.

3.2.1 Definition of parameters

Fig. 3.1 shows a schematic of the absorption process, indicating the variables needed to solve for the emissivity. As usual, we assume the Galactic synchrotron emission is confined to an axisymmetric cylinder with a radius of 20 kpc and a height of several kpc. Note that this assumption is only for the definition of the emissivity in Section 3.2. We can avoid making this assumption if we are only interested in the brightness temperature instead of the emissivity.

The measured or known parameters are the measured brightness temperature in the direction of the absorbed region $T_{\rm h}$, the measured brightness temperature from the

Sun to the Galactic edge in the absence of HII region emission $T_{\rm m}$ (i.e. as derived from a region near the line of sight to the HII region), the observation frequency ν, the spectral index of the synchrotron brightness temperature α, the spectral index of the HII region optical depth β, the total brightness temperature (without missing flux density) from the Sun to the Galactic edge in the absence of HII region absorption $T_{\rm t}$, and the electron temperature of the HII region $T_{\rm e}$. α is taken to be $-2.7\ \pm\ 0.1$ for the Milky Way (Guzmán et al., 2011; Zheng et al., 2017). Note that this spectral index varies between -2.1 and -2.7 depending on the sky regions (Guzmán et al., 2011). We use a low spectral index of -2.7 for the synchrotron emission in this work because the high spectral index is due to the thermal free-free absorption of both the HII regions and warm interstellar medium. β is taken to be -2.1 for frequencies $\nu \ll 10^{10}\ T_{\rm e}$ (ν is in GHz and $T_{\rm e}$ is in K) and $T_{\rm e} < 9 \times 10^5$ K derived on page 47 of Lang (1980), which is always true for HII regions at the GLEAM frequencies. Note that β is a constant does not mean the HII region must be optically thick; it can be optically thin. The errors caused by these two spectral indices are discussed in Section 3.3.2. $T_{\rm t}$ is derived from the improved Haslam map (Remazeilles et al., 2015), scaled from 408 MHz to the GLEAM frequencies using the spectral index of α. $T_{\rm e}$ is from Balser et al. (2015); Hou and Han (2014) and references therein.

The unknown variables are the optical depth of the HII region τ, the total (the sum of the measured and missed) brightness temperature of the synchrotron emission from the HII region to the Galactic edge along the line of sight $T_{\rm b}$, and the corresponding brightness temperature of the synchrotron emission from the HII region to the Sun $T_{\rm f}$, the brightness temperature of the emission on the missing short interferometric spacings respectively between an HII region and the Sun $X_{\rm f}$, and between the Galactic edge and the Sun $X_{\rm b}$.

The selection criteria of the absorbed region and its nearby background region are

the same as those in Su et al. (2017a). We define these regions at the lowest frequency of 76.2 MHz and then apply them to all other five frequencies to get the brightness temperatures within these regions. HII regions overlapped with supernova remnants are not selected (e.g. HII region G35.6−0.5 with distance measured by Zhu et al. 2013). Note that our selected background regions are about one degree away from the absorbed regions, the supernova remnants in Green (2014) catalogue, and obvious point-like sources in the GLEAM. Therefore, the contamination of these sources is negligible, although the Haslam map has a low angular resolution of 51′.

3.2.2 Equations to solve for the optical depth and brightness temperature

A single-dish observation can recover the total power along the line of sight in the case that the HII region fills the beam. The brightness temperature is a result of the contributions from three components: the electron temperature of the HII region, and the brightness temperature of the synchrotron emission behind and in front of the HII region as shown in Equation 2.1.

An interferometer observation does not sample the large angular scale structures corresponding to visibility measurements at small u-v distances. Thus Equation 2.1 should be revised by subtracting the missing term from the brightness temperature both behind and in front of the HII region,

$$T_{\rm h} = T_{\rm e}(1 - {\rm e}^{-\tau}) + (T_{\rm b} - X_{\rm b}){\rm e}^{-\tau} + T_{\rm f} - X_{\rm f}. \tag{3.1}$$

Note that this equation does not require the u-v coverage to be identical at different frequencies because we do not assume the brightness temperature of the missing term follows the same spectral index. We allow the value of the X terms to float with frequency, as X depends on the angular scale at which emission is being missed, which

varies with frequency. The filtering out of large-scale structure on the sky happens in the telescope. However, there is indeed missing large-scale structure in the background emission if we further examine the origin of such large-scale structure: one component from the contribution of T_f and the other from the contribution of T_b. For the missing terms, there is no difference between on and off source directions because it is large scale structures, therefore X_b exists for T_b in the HII region direction. In the formula, we can use one parameter X_f to do the calculation, but we can also use two parameters X_f and X_b to calculate the two components simultaneously. Both methods are correct for uniform distribution of large scale synchrotron emission, however, the later gives more information if the large scale emission is not uniform along the line of sight and it can get more information, such as how much is measured in the foreground and how much is measured in the background.

The total brightness temperature from the Sun to the Galactic edge in the absence of HII region absorption is simply the sum of the brightness temperatures behind and in front of the HII region as stated in Equation 2.3.

The measured brightness temperature on the source-free region (i.e. immediately adjacent to the HII region) becomes the difference between the total brightness temperature and that of the brightness temperatures of the emission associated with the missing interferometric u-v spacings,

$$T_{\rm m} = T_{\rm t} - X_{\rm f} - X_{\rm b}. \tag{3.2}$$

As well as the above three relations, we have supplementary information that encodes the scaling of the brightness temperature and the optical depth with frequency. The total brightness temperature both behind and in front of the HII region should

follow a power law distribution,

$$\begin{aligned} T_{\rm b} &\propto \nu^{\alpha}, \\ T_{\rm f} &\propto \nu^{\alpha}, \\ \tau &\propto \nu^{\beta}. \end{aligned} \tag{3.3}$$

We apply Equations (2)-(5) to our measurements at different frequencies to solve for the optical depth of HII regions and the brightness temperatures behind and in front of each HII region. In summary, we have:

$$\begin{aligned} T_{\rm h_i} &= T_{\rm e}(1-{\rm e}^{-\tau_{\rm i}}) + (T_{\rm b_i} - X_{\rm b_i}){\rm e}^{-\tau_{\rm i}} + T_{\rm f_i} - X_{\rm f_i}, \\ T_{\rm t_i} &= T_{\rm f_i} + T_{\rm b_i}, \\ T_{\rm m_i} &= T_{\rm t_i} - X_{\rm f_i} - X_{\rm b_i}, \\ T_{\rm b_i} &= T_{\rm b_1}\left(\frac{\nu_{\rm i}}{\nu_1}\right)^{\alpha}, \\ T_{\rm f_i} &= T_{\rm f_1}\left(\frac{\nu_{\rm i}}{\nu_1}\right)^{\alpha}, \\ \tau_{\rm i} &= \tau_1\left(\frac{\nu_{\rm i}}{\nu_1}\right)^{\beta}, \end{aligned} \tag{3.4}$$

where the subscript $i = (1, 2, 3)$ indexes the frequencies from low to high. A minimum of three frequencies is required to solve for the unknown variables.

We derive the value of τ, $T_{\rm b}$, $T_{\rm f}$, $X_{\rm b}$, $X_{\rm f}$ using Equation 3.4. Using two sets of three frequencies data, we obtain emissivities at the six frequencies listed in Table 3.1. We use data at 76.2, 83.8, and 91.5 MHz to derive the emissivities at these three frequencies. And then use another three frequencies of 99.2, 106.9, and 114.6 MHz to perform the same analysis. So we derive the emissivities at six different frequencies. We did not use other combinations of data to derive emissivities. Table 3.2 lists the emissivities at 76.2 MHz only. We can derive $X_{\rm b}$ and $X_{\rm f}$ using the Haslam map to estimate the total emission along the line of sight. We then compare this total emission with that measured. Therefore, our equations can find out how much emission is

Table 3.1: Parameters of the GLEAM data with a bandwidth of 7.68 MHz each. The resolution element is described by the beam major axis (BMAJ) and beam minor axis (BMIN).

Frequency MHz	BMAJ arcmin	BMIN arcmin	Conversion factor Jy beam^{-1} to K
76.2	5.41	4.43	2445.01
83.8	4.78	3.89	2598.84
91.5	4.35	3.54	2633.47
99.2	4.03	3.30	2596.70
106.9	3.99	3.22	2310.85
114.6	3.63	2.89	2467.46

undetected in our observations.

The definition of the absorption and background regions is the same as that in Chapter 2.

3.3 Results of measurements

3.3.1 Measured emissivities

Emissivities from the simplified method

We calculate the synchrotron emissivities behind HII regions using the 152 HII region absorption features detected in the GLEAM using the previous simplified method (Col. 11 in Table 3.2). The last column in Table 3.2 shows the emissivities derived from the simplified method described in Su et al. (2017a). The measurements are made at six frequencies from 76.2 to 114.6 MHz. The emissivities behind HII regions at 76.2 MHz are plotted in Fig. 3.2. The derived emissivities in the fourth Galactic quadrant are consistent with our previous results in Su et al. (2017a,b). The emissivities in

the first quadrant are consistent with those in Nord et al. (2006) within three standard deviations.

We check the spectral index of the emissivities at six frequencies derived from each HII region. The average index is about -1.5, which is higher than the expected synchrotron emission spectral index of -2.7 (see Fig. 3.3). The difference between these observed two spectral indexes is most likely caused by the missing flux density mentioned in Section 3.2. To produce a flat spectrum with a spectral index of -1.5, the brightness temperature of the emission on scales that are resolved out should be frequency-dependent, with brightness temperatures under-estimated at lower frequencies in our observations, even though our lower frequencies recover more of the extended emission than the high frequencies: this demonstrates that we need to improve this simplified method to derive more accurate emissivities.

Emissivities from the improved method

Using the improved method described in Section 3.2, we obtained the synchrotron emissivities and HII region optical depths at six frequencies simultaneously (see Table 3.2). Col. (1): the name of HII regions from the *WISE* HII region catalogue. Cols (2) and (3): the distance from the HII region to the Sun and the electron temperature of the HII regions found in the literature (Anderson et al., 2014; Balser et al., 2015; Hou and Han, 2014) and the online *WISE* HII region catalogue (in priority). For an HII region with radial velocity but no distance given in the literature, a kinematic distance is derived from the radial velocity assuming a near distance with Galactic parameters of $R_{\odot} = 8.5$ kpc, $\Theta_{\odot} = 220$ km s^{-1}. HII regions with absorption features are unlikely in the far kinematic distance because nearly no synchrotron emission behind far HII regions can be absorbed to generate observable absorption features. We use $T_{\rm e}$ = (4928 $\pm$ 277) + (385 $\pm$ 29) $R_{\rm gal}$ from Balser et al. (2015) if no electron temperature is given

in the literature. Col. (4): the measured brightness temperature in the direction of the absorbed region. Col. (5): the measured brightness temperature from the Sun to the Galactic edge in the absence of HII region emission (i.e. as derived from a region near the line of sight to the HII region) from the GLEAM map. Col. (6): the total brightness temperature (without missing flux density) from the Sun to the Galactic edge in the absence of HII region absorption derived from the Haslam map. Cols (7) and (8): the brightness temperature of the emission on the missing short interferometric spacings respectively between the Galactic edge and the Sun ($X_{\rm b}$), and between an HII region and the Sun ($X_{\rm f}$). Col. (9): the optical depth of the HII region. Col. (10): the average emissivity between the HII region and the Galactic edge. Col. (11): the average emissivity between the HII region and the Sun. Note that for Cols (10) and (11), the emissivities will be $\sim$15% lower if you accept a synchrotron spectral index of -2.6 instead of -2.7 we used. Col. (12): the emissivity between the HII region and the Galactic edge derived from the simplified method.

Fig. 3.4 shows the emissivities at 76.2 MHz and the paths over which these emissivities are averaged. The electronic version of the full tables with our derived emissivities at all six frequencies is in the appendix of the online paper (Su et al., 2018). Figs. 3.5 and 3.6 show our derived emissivities at 76.2 MHz both behind and in front of HII regions using the improved method.

Table 3.2: The derived synchrotron emissivities and optical depths of HII regions at 76.2 MHz.

HII region	Dis	$T_{\rm e}$	$T_{\rm h}$	$T_{\rm m}$	$T_{\rm t}$	$X_{\rm b}$	$X_{\rm f}$	τ	$\epsilon_{\rm b}$	$\epsilon_{\rm f}$	$\epsilon_{\rm b\_sim}$
	kpc	$\times10^3$ K	$\times10^3$ K	$\times10^3$ K	$\times10^3$ K	$\times10^3$ K	$\times10^3$ K		K pc^{-1}	K pc^{-1}	K pc^{-1}
(1)	(2)	(3)	(4)	(5)	(6)	(7)	(8)	(9)	(10)	(11)	(12)
G000.003+00.127	1.5 ± 0.3	7.62 ± 0.30	17.0 ± 1.0	36.7 ± 4.7	124.9 ± 10.6	$18.2^{+50.8}_{-5.5}$	$70.0^{+21.0}_{-49.7}$	36.3	$1.7^{+2.0}_{-0.5}$	$52.9^{+19.1}_{-35.1}$	1.10 ± 0.20
G000.120−00.556	1.5 ± 0.3	7.62 ± 0.30	23.5 ± 2.3	34.5 ± 3.3	87.4 ± 20.0	$41.8^{+13.7}_{-33.5}$	$11.0^{+26.0}_{-3.4}$	30.0	$2.2^{+0.5}_{-1.2}$	$17.9^{+16.7}_{-4.6}$	0.74 ± 0.17
G005.887−00.443	3.0 ± 0.2	11.13 ± 0.20	7.5 ± 3.1	19.1 ± 0.8	40.3 ± 2.2	$5.9^{+9.5}_{-2.3}$	$15.4^{+4.6}_{-8.8}$	39.2	$1.1^{+0.3}_{-0.3}$	$2.6^{+1.3}_{-1.4}$	0.95 ± 0.14
G006.100−01.263	1.0 ± 0.2	7.70 ± 0.80	1.6 ± 0.7	10.4 ± 2.2	30.3 ± 2.6	$10.4^{+1.9}_{-7.2}$	$9.5^{+5.0}_{-2.8}$	45.6	$1.0^{+0.3}_{-0.2}$	$3.4^{+5.3}_{-1.1}$	0.64 ± 0.10
G007.015−00.271	2.7 ± 0.5	7.50 ± 0.80	7.9 ± 1.9	14.8 ± 1.2	39.2 ± 3.8	$16.7^{+2.3}_{-9.6}$	$7.8^{+9.6}_{-2.2}$	23.2	$1.2^{+0.4}_{-0.3}$	$3.0^{+3.4}_{-1.1}$	0.59 ± 0.10
G007.303−00.125	2.7 ± 0.5	7.17 ± 0.30	8.2 ± 0.7	14.9 ± 1.2	40.8 ± 4.7	$8.4^{+11.9}_{-3.7}$	$17.5^{+4.1}_{-11.9}$	6.3	$0.9^{+0.5}_{-0.1}$	$6.8^{+1.9}_{-4.9}$	0.57 ± 0.06
G008.137+00.232	3.4 ± 0.8	7.09 ± 0.10	11.6 ± 0.5	14.7 ± 0.9	40.5 ± 2.5	$9.7^{+9.1}_{-5.3}$	$15.9^{+5.2}_{-8.6}$	>99	$0.8^{+0.3}_{-0.3}$	$5.9^{+2.1}_{-2.8}$	0.42 ± 0.05
G009.725−00.840	5.2 ± 1.0	6.27 ± 0.30	10.2 ± 0.5	15.1 ± 1.5	37.5 ± 3.6	$9.8^{+9.8}_{-4.3}$	$12.6^{+3.3}_{-9.0}$	>99	$0.9^{+0.4}_{-0.2}$	$3.2^{+0.9}_{-1.9}$	0.51 ± 0.08
G009.942−00.761	5.2 ± 1.0	3.70 ± 0.40	10.4 ± 0.5	15.8 ± 1.6	38.7 ± 3.3	$10.7^{+7.7}_{-6.5}$	$11.6^{+6.3}_{-7.3}$	7.4	$0.9^{+0.3}_{-0.3}$	$3.5^{+1.5}_{-1.6}$	0.42 ± 0.08
G010.160−00.350	14.5 ± 0.9	6.83 ± 0.00	7.8 ± 0.9	16.9 ± 1.4	41.2 ± 1.3	$10.6^{+7.6}_{-5.8}$	$13.7^{+5.8}_{-7.0}$	6.3	$2.5^{+0.8}_{-1.0}$	$1.0^{+0.4}_{-0.5}$	1.23 ± 0.16
G010.308−00.150	15.0 ± 1.1	6.80 ± 0.00	10.0 ± 0.4	21.3 ± 2.9	45.4 ± 0.6	$15.4^{+5.2}_{-9.0}$	$8.7^{+8.3}_{-3.7}$	58.7	$2.5^{+0.4}_{-0.7}$	$0.8^{+0.6}_{-0.3}$	1.46 ± 0.27
G010.769−00.487	5.0 ± 1.0	5.30 ± 0.50	8.6 ± 0.7	17.1 ± 1.3	41.6 ± 2.5	$17.5^{+5.3}_{-11.8}$	$7.0^{+11.5}_{-2.1}$	15.8	$1.3^{+0.4}_{-0.5}$	$2.1^{+2.2}_{-0.5}$	0.63 ± 0.08
G011.662−01.692	1.2 ± 0.1	7.75 ± 0.30	4.7 ± 0.2	7.3 ± 1.1	24.0 ± 1.5	$10.0^{+1.1}_{-6.0}$	$6.7^{+5.5}_{-2.0}$	12.4	$0.8^{+0.2}_{-0.2}$	$3.0^{+4.4}_{-0.6}$	0.39 ± 0.05
G012.742+00.390	2.6 ± 0.7	7.23 ± 0.30	11.0 ± 0.8	15.8 ± 1.2	38.3 ± 2.8	$5.3^{+13.8}_{-0.9}$	$17.2^{+5.2}_{-13.9}$	>99	$0.8^{+0.4}_{-0.1}$	$6.8^{+2.0}_{-4.5}$	0.49 ± 0.07
G012.761−00.133	2.9 ± 0.3	7.62 ± 0.10	2.6 ± 1.0	12.5 ± 1.6	42.5 ± 1.1	$11.2^{+7.1}_{-4.8}$	$18.3^{+5.2}_{-6.3}$	9.8	$1.2^{+0.3}_{-0.2}$	$4.6^{+1.7}_{-2.4}$	0.74 ± 0.08
G013.776−00.795	2.0 ± 0.4	8.60 ± 0.90	6.0 ± 0.6	11.4 ± 2.2	33.4 ± 3.5	$9.9^{+7.4}_{-4.8}$	$12.0^{+4.0}_{-6.0}$	>99	$0.9^{+0.3}_{-0.1}$	$4.7^{+1.7}_{-3.1}$	0.56 ± 0.11

Continued on next page

HII region	Dis	$T_{\rm e}$	$T_{\rm h}$	$T_{\rm m}$	$T_{\rm t}$	$X_{\rm b}$	$X_{\rm f}$	τ	$\epsilon_{\rm b\_com}$	$\epsilon_{\rm f\_com}$	$\epsilon_{\rm b\_sim}$
	kpc	$\times10^3$ K	$\times10^3$ K	$\times10^3$ K	$\times10^3$ K	$\times10^3$ K	$\times10^3$ K		K pc^{-1}	K pc^{-1}	K pc^{-1}
(1)	(2)	(3)	(4)	(5)	(6)	(7)	(8)	(9)	(10)	(11)	(12)
G014.060−00.521	2.0 ± 0.4	7.46 ± 0.30	7.2 ± 0.4	10.4 ± 1.0	34.6 ± 3.9	$16.1^{+3.0}_{-10.4}$	$8.0^{+9.8}_{-2.9}$	>99	$1.0^{+0.3}_{-0.4}$	$3.9^{+5.1}_{-1.5}$	0.42 ± 0.05
G014.207−00.193	3.6 ± 0.5	6.89 ± 0.30	4.3 ± 0.9	13.0 ± 1.1	46.9 ± 2.5	$13.9^{+11.7}_{-8.1}$	$19.8^{+8.2}_{-10.9}$	15.6	$1.2^{+0.5}_{-0.4}$	$4.5^{+2.6}_{-3.1}$	0.67 ± 0.07
G014.481−00.662	2.0 ± 0.4	10.40 ± 1.00	6.9 ± 0.5	9.6 ± 0.9	28.5 ± 2.2	$11.8^{+1.5}_{-6.8}$	$7.1^{+5.9}_{-2.1}$	79.6	$1.0^{+0.3}_{-0.3}$	$1.8^{+3.3}_{-0.6}$	0.51 ± 0.06
G014.576+00.091	3.6 ± 0.5	5.51 ± 0.10	3.1 ± 1.5	12.6 ± 0.7	36.4 ± 2.4	$14.1^{+3.0}_{-10.2}$	$9.7^{+9.2}_{-2.0}$	66.2	$1.2^{+0.1}_{-0.4}$	$2.0^{+2.5}_{-0.8}$	0.66 ± 0.08
G015.097−00.729	2.0 ± 0.1	9.77 ± 0.10	4.6 ± 1.6	8.7 ± 1.3	28.1 ± 4.8	$6.8^{+6.3}_{-2.9}$	$12.6^{+3.1}_{-4.9}$	>99	$0.8^{+0.2}_{-0.1}$	$3.7^{+1.1}_{-2.5}$	0.55 ± 0.09
G015.676−00.288	11.6 ± 0.4	6.51 ± 0.30	8.4 ± 0.2	11.1 ± 0.9	36.8 ± 0.3	$17.8^{+2.2}_{-10.6}$	$7.9^{+10.2}_{-2.8}$	15.0	$1.6^{+0.2}_{-0.6}$	$0.8^{+0.9}_{-0.2}$	0.58 ± 0.06
G016.648−00.357	3.9 ± 0.4	6.81 ± 0.30	4.6 ± 1.0	12.7 ± 0.9	33.1 ± 0.8	$5.2^{+7.3}_{-1.5}$	$15.2^{+4.6}_{-7.7}$	>99	$0.9^{+0.3}_{-0.1}$	$3.0^{+0.8}_{-1.8}$	0.66 ± 0.06
G016.993+00.873	2.6 ± 0.5	6.97 ± 0.10	1.5 ± 0.5	7.8 ± 1.5	25.7 ± 3.1	$6.7^{+4.8}_{-3.4}$	$11.2^{+2.5}_{-3.8}$	19.4	$0.8^{+0.2}_{-0.1}$	$2.2^{+1.0}_{-1.5}$	0.55 ± 0.07
G018.187−00.415	3.6 ± 0.4	6.93 ± 0.30	8.0 ± 0.4	12.5 ± 0.8	33.9 ± 0.9	$9.7^{+6.0}_{-4.3}$	$11.6^{+4.3}_{-5.9}$	10.8	$0.9^{+0.3}_{-0.2}$	$3.5^{+1.1}_{-1.8}$	0.50 ± 0.04
G018.253−00.298	4.1 ± 0.4	7.18 ± 0.10	6.9 ± 1.2	12.3 ± 0.9	34.3 ± 0.4	$13.7^{+2.4}_{-8.6}$	$8.3^{+8.7}_{-2.1}$	24.0	$1.1^{+0.1}_{-0.4}$	$2.0^{+2.1}_{-0.8}$	0.56 ± 0.07
G018.669+01.965	2.6 ± 0.5	7.21 ± 0.10	1.2 ± 0.8	5.8 ± 1.2	21.0 ± 2.8	$5.0^{+3.7}_{-2.8}$	$10.3^{+1.9}_{-2.5}$	32.6	$0.7^{+0.1}_{-0.1}$	$1.5^{+1.1}_{-1.0}$	0.49 ± 0.06
G018.914−00.329	3.4 ± 0.7	5.44 ± 0.10	5.7 ± 0.8	11.0 ± 1.1	38.9 ± 1.2	$7.5^{+11.4}_{-2.7}$	$20.4^{+2.8}_{-11.4}$	39.8	$0.7^{+0.5}_{-0.1}$	$6.1^{+1.5}_{-4.0}$	0.47 ± 0.06
G018.978+00.030	4.0 ± 0.4	6.81 ± 0.30	7.8 ± 1.1	11.8 ± 0.7	33.9 ± 0.4	$15.0^{+2.0}_{-8.5}$	$7.1^{+8.0}_{-2.5}$	18.0	$1.1^{+0.3}_{-0.3}$	$2.0^{+2.0}_{-0.6}$	0.47 ± 0.06
G019.629−00.095	11.7 ± 0.4	6.48 ± 0.10	10.9 ± 0.1	11.1 ± 1.0	39.5 ± 1.0	$10.5^{+11.7}_{-4.4}$	$17.9^{+4.9}_{-11.0}$	78.6	$1.1^{+0.7}_{-0.3}$	$1.9^{+0.4}_{-0.9}$	0.42 ± 0.07
G022.478−00.015	6.2 ± 1.2	6.33 ± 0.30	8.6 ± 0.7	11.9 ± 0.9	31.9 ± 1.8	$11.0^{+6.3}_{-5.7}$	$9.4^{+5.2}_{-6.6}$	75.5	$1.0^{+0.3}_{-0.3}$	$1.7^{+1.1}_{-1.0}$	0.47 ± 0.07
G022.761−00.492	4.8 ± 0.4	6.65 ± 0.30	6.8 ± 0.3	11.6 ± 0.7	37.9 ± 1.7	$7.1^{+12.7}_{-2.3}$	$19.2^{+2.2}_{-13.1}$	62.6	$0.9^{+0.5}_{-0.1}$	$3.8^{+0.7}_{-2.6}$	0.53 ± 0.04
G022.780−00.401	11.1 ± 0.4	6.71 ± 0.30	6.8 ± 0.3	11.6 ± 0.7	37.9 ± 1.7	$7.7^{+10.5}_{-5.1}$	$18.6^{+4.5}_{-10.6}$	7.0	$1.2^{+0.6}_{-0.3}$	$1.7^{+0.4}_{-1.0}$	0.73 ± 0.06
G022.879+00.645	2.5 ± 0.5	7.34 ± 0.30	9.8 ± 0.3	11.1 ± 0.9	28.0 ± 2.0	$13.1^{+3.9}_{-8.7}$	$3.8^{+8.2}_{-1.3}$	>99	$0.9^{+0.3}_{-0.4}$	$2.4^{+3.3}_{-0.7}$	0.35 ± 0.05

Continued on next page

HII region	Dis	T_e	T_h	T_m	T_t	X_b	X_f	τ	ϵ_{b_com}	ϵ_{f_com}	ϵ_{b_sim}
	kpc	$\times 10^3$ K	$\times 10^3$ K	$\times 10^3$ K	$\times 10^3$ K	$\times 10^3$ K	$\times 10^3$ K		K pc^{-1}	K pc^{-1}	K pc^{-1}
(1)	(2)	(3)	(4)	(5)	(6)	(7)	(8)	(9)	(10)	(11)	(12)
G022.987−00.155	2.5 ± 0.5	5.10 ± 0.50	9.9 ± 0.3	17.0 ± 1.0	40.2 ± 2.1	$11.8^{+6.3}_{-7.4}$	$11.4^{+6.2}_{-6.1}$	44.2	$1.0^{+0.3}_{-0.3}$	$6.5^{+2.8}_{-3.1}$	0.52 ± 0.05
G022.988−00.360	4.8 ± 0.4	6.66 ± 0.30	6.1 ± 0.8	11.7 ± 0.8	39.1 ± 1.8	$11.9^{+6.6}_{-7.5}$	$15.4^{+6.6}_{-6.3}$	13.0	$1.1^{+0.3}_{-0.3}$	$3.0^{+1.4}_{-1.2}$	0.57 ± 0.06
G023.097+00.527	2.4 ± 0.5	7.38 ± 0.30	7.3 ± 0.4	11.2 ± 1.1	27.9 ± 2.0	$8.1^{+4.7}_{-4.0}$	$8.5^{+4.1}_{-4.7}$	11.9	$0.8^{+0.2}_{-0.1}$	$3.5^{+1.6}_{-2.1}$	0.47 ± 0.05
G023.240−00.240	4.8 ± 0.4	6.66 ± 0.30	10.7 ± 0.8	17.0 ± 1.0	40.2 ± 2.1	$14.2^{+4.9}_{-7.2}$	$9.0^{+6.9}_{-5.7}$	52.6	$1.2^{+0.2}_{-0.3}$	$2.7^{+1.5}_{-1.2}$	0.60 ± 0.07
G023.572−00.020	5.5 ± 0.4	6.51 ± 0.30	6.7 ± 0.4	9.0 ± 0.7	36.3 ± 1.1	$10.5^{+9.4}_{-4.7}$	$16.8^{+4.9}_{-9.3}$	>99	$1.3^{+0.4}_{-0.6}$	$1.4^{+2.6}_{-0.4}$	0.41 ± 0.04
G023.581−00.400	5.4 ± 0.4	6.53 ± 0.30	8.1 ± 0.3	12.6 ± 1.5	40.3 ± 1.9	$14.9^{+8.0}_{-7.5}$	$13.1^{+7.3}_{-7.7}$	13.8	$1.2^{+0.4}_{-0.3}$	$2.7^{+1.4}_{-1.5}$	0.52 ± 0.08
G023.957+00.149	4.9 ± 0.4	6.66 ± 0.30	7.3 ± 0.3	12.6 ± 1.5	40.3 ± 1.9	$21.4^{+6.4}_{-13.9}$	$6.3^{+13.6}_{-0.9}$	60.3	$1.5^{+0.4}_{-0.6}$	$1.4^{+2.7}_{-0.3}$	0.56 ± 0.08
G024.139+00.432	5.8 ± 0.5	6.46 ± 0.30	8.0 ± 0.2	9.8 ± 0.6	37.3 ± 1.0	$11.8^{+9.8}_{-5.4}$	$15.7^{+5.0}_{-8.9}$	11.0	$0.9^{+0.4}_{-0.2}$	$3.0^{+0.9}_{-1.6}$	0.39 ± 0.04
G024.185+00.211	9.1 ± 0.7	6.37 ± 0.30	8.2 ± 0.1	9.8 ± 0.6	37.3 ± 1.0	$10.0^{+12.5}_{-3.8}$	$17.6^{+3.4}_{-12.2}$	11.7	$1.0^{+0.7}_{-0.2}$	$2.1^{+0.4}_{-1.4}$	0.45 ± 0.05
G024.347+00.088	8.5 ± 0.9	6.31 ± 0.30	6.4 ± 0.2	7.4 ± 0.9	42.3 ± 0.2	$16.4^{+9.8}_{-7.8}$	$18.5^{+7.7}_{-9.2}$	>99	$1.3^{+0.5}_{-0.4}$	$2.2^{+0.9}_{-1.1}$	0.39 ± 0.06
G024.493−00.219	9.7 ± 0.5	6.48 ± 0.30	2.9 ± 0.4	10.3 ± 0.8	39.2 ± 1.0	$10.9^{+6.2}_{-6.5}$	$17.9^{+6.4}_{-5.7}$	64.8	$1.4^{+0.4}_{-0.4}$	$1.4^{+0.7}_{-0.6}$	0.84 ± 0.06
G024.498−00.039	9.2 ± 0.6	6.40 ± 0.30	5.8 ± 0.2	12.6 ± 1.4	40.2 ± 1.9	$12.9^{+7.4}_{-7.2}$	$14.7^{+6.4}_{-8.2}$	34.2	$1.4^{+0.5}_{-0.4}$	$1.5^{+0.7}_{-0.9}$	0.77 ± 0.09
G024.507+00.239	8.8 ± 2.8	6.36 ± 0.10	5.3 ± 0.1	9.4 ± 0.8	37.4 ± 1.3	$11.7^{+8.9}_{-7.6}$	$15.7^{+7.7}_{-9.0}$	20.5	$1.2^{+0.5}_{-0.4}$	$1.6^{+1.0}_{-1.2}$	0.59 ± 0.10
G024.724−00.084	9.1 ± 0.7	6.40 ± 0.30	2.8 ± 0.5	9.9 ± 1.1	39.4 ± 1.3	$3.3^{+14.3}_{-0.4}$	$26.1^{+7.8}_{-13.0}$	6.0	$1.3^{+0.5}_{-0.4}$	$1.8^{+0.7}_{-0.9}$	0.78 ± 0.08
G024.743−00.210	5.1 ± 0.4	6.63 ± 0.30	3.0 ± 0.3	10.4 ± 0.8	39.2 ± 1.0	$9.2^{+8.0}_{-5.9}$	$19.5^{+5.7}_{-8.5}$	29.7	$1.4^{+0.4}_{-0.6}$	$1.4^{+2.7}_{-0.4}$	0.67 ± 0.05
G024.844+00.093	6.3 ± 0.6	5.86 ± 0.10	6.3 ± 0.4	10.1 ± 1.2	39.5 ± 1.3	$11.9^{+8.5}_{-7.2}$	$17.1^{+7.2}_{-8.0}$	39.4	$1.4^{+0.4}_{-0.7}$	$1.5^{+2.4}_{-0.5}$	0.48 ± 0.07
G025.291−00.303	11.2 ± 0.4	6.87 ± 0.30	4.5 ± 0.5	10.3 ± 0.8	39.2 ± 1.0	$12.3^{+7.5}_{-6.2}$	$16.0^{+6.7}_{-6.5}$	7.5	$1.6^{+0.4}_{-0.4}$	$1.2^{+0.6}_{-0.6}$	0.83 ± 0.07
G025.382−00.151	4.0 ± 0.4	9.28 ± 0.10	4.1 ± 0.7	11.0 ± 1.5	32.3 ± 2.1	$13.4^{+4.0}_{-7.9}$	$12.0^{+3.6}_{-2.9}$	12.0	$1.3^{+0.4}_{-0.3}$	$1.7^{+0.9}_{-0.8}$	0.73 ± 0.08

Continued on next page

HII region	Dis	T_e	T_h	T_m	T_t	X_b	X_f	τ	ϵ_{b_com}	ϵ_{f_com}	ϵ_{b_sim}
	kpc	$\times 10^3$ K	$\times 10^3$ K	$\times 10^3$ K	$\times 10^3$ K	$\times 10^3$ K	$\times 10^3$ K		K pc^{-1}	K pc^{-1}	K pc^{-1}
(1)	(2)	(3)	(4)	(5)	(6)	(7)	(8)	(9)	(10)	(11)	(12)
G025.386−00.347	11.2 ± 0.4	6.88 ± 0.30	4.6 ± 0.4	11.0 ± 1.5	32.3 ± 2.1	$8.7^{+6.9}_{-3.6}$	$12.6^{+2.6}_{-5.9}$	17.5	$1.4^{+0.5}_{-0.2}$	$0.9^{+0.2}_{-0.6}$	0.87 ± 0.11
G025.867+00.118	6.5 ± 0.9	6.12 ± 0.10	7.2 ± 0.5	9.5 ± 0.7	36.1 ± 1.3	$9.4^{+12.4}_{-4.0}$	$17.3^{+4.3}_{-12.2}$	50.1	$0.9^{+0.6}_{-0.2}$	$2.8^{+0.7}_{-1.9}$	0.42 ± 0.05
G026.521−00.317	9.1 ± 0.6	6.50 ± 0.30	7.0 ± 0.2	11.0 ± 1.2	33.8 ± 1.7	$7.0^{+11.2}_{-1.3}$	$15.8^{+4.7}_{-11.0}$	15.1	$1.0^{+0.6}_{-0.3}$	$1.8^{+0.5}_{-1.3}$	0.61 ± 0.08
G026.797−00.113	10.8 ± 0.4	6.85 ± 0.30	6.9 ± 0.7	9.2 ± 1.1	35.2 ± 1.1	$12.6^{+6.6}_{-7.1}$	$12.9^{+7.6}_{-6.1}$	>99	$1.3^{+0.4}_{-0.5}$	$1.2^{+0.7}_{-0.6}$	0.57 ± 0.09
G027.281−00.132	5.5 ± 0.5	6.62 ± 0.30	7.4 ± 0.2	8.8 ± 0.6	28.3 ± 1.7	$8.9^{+6.4}_{-5.0}$	$9.8^{+5.1}_{-5.2}$	67.8	$0.8^{+0.3}_{-0.2}$	$1.9^{+0.9}_{-1.0}$	0.38 ± 0.04
G028.022−00.043	9.0 ± 0.6	6.57 ± 0.30	6.4 ± 0.7	8.8 ± 0.6	28.3 ± 1.7	$8.8^{+4.5}_{-4.2}$	$10.8^{+3.8}_{-5.3}$	8.5	$1.0^{+0.3}_{-0.3}$	$1.1^{+0.5}_{-0.6}$	0.52 ± 0.06
G028.246+00.013	7.5 ± 1.5	6.48 ± 0.30	7.8 ± 0.3	9.9 ± 0.9	30.9 ± 1.6	$9.2^{+7.8}_{-5.0}$	$11.9^{+4.6}_{-7.9}$	91.0	$1.0^{+0.3}_{-0.3}$	$1.5^{+0.9}_{-0.9}$	0.45 ± 0.06
G028.638+00.194	7.5 ± 1.5	6.50 ± 0.30	7.7 ± 0.4	9.9 ± 0.9	30.9 ± 1.6	$14.5^{+1.8}_{-9.9}$	$6.5^{+9.0}_{-2.1}$	15.8	$1.2^{+0.4}_{-0.5}$	$1.0^{+1.2}_{-0.4}$	0.46 ± 0.07
G028.679+00.044	7.5 ± 1.6	6.50 ± 0.30	8.0 ± 0.1	9.9 ± 0.9	30.9 ± 1.6	$14.3^{+2.7}_{-8.8}$	$6.7^{+9.0}_{-2.8}$	14.4	$1.2^{+0.2}_{-0.5}$	$1.1^{+1.2}_{-0.4}$	0.44 ± 0.06
G028.746+03.458	15.2 ± 0.8	8.30 ± 0.40	0.1 ± 0.8	1.9 ± 0.8	12.5 ± 0.8	$2.3^{+0.6}_{-1.6}$	$8.3^{+2.1}_{-2.5}$	18.1	$1.0^{+0.3}_{-0.2}$	$0.1^{+0.1}_{-0.1}$	0.87 ± 0.13
G028.774+00.285	7.4 ± 1.5	6.50 ± 0.30	7.5 ± 0.2	10.0 ± 0.9	30.4 ± 1.7	$4.8^{+11.2}_{-1.4}$	$15.5^{+4.7}_{-10.7}$	14.2	$1.0^{+0.3}_{-0.3}$	$1.5^{+0.8}_{-0.8}$	0.48 ± 0.06
G028.983−00.604	3.5 ± 0.4	7.12 ± 0.30	5.3 ± 0.3	10.0 ± 0.6	28.2 ± 1.5	$8.1^{+4.5}_{-4.6}$	$10.4^{+3.6}_{-4.1}$	>99	$0.9^{+0.2}_{-0.2}$	$2.4^{+1.1}_{-1.2}$	0.53 ± 0.04
G029.165−00.035	11.2 ± 0.4	7.09 ± 0.30	8.5 ± 0.2	10.0 ± 0.9	30.4 ± 1.7	$9.9^{+5.0}_{-4.6}$	$9.9^{+5.1}_{-4.6}$	16.7	$1.2^{+0.3}_{-0.3}$	$1.0^{+0.5}_{-0.4}$	0.56 ± 0.07
G029.816+02.225	2.7 ± 0.4	7.35 ± 0.30	2.8 ± 0.2	5.3 ± 0.8	17.0 ± 1.1	$2.9^{+3.2}_{-1.0}$	$8.8^{+2.6}_{-3.1}$	29.9	$0.5^{+0.1}_{-0.2}$	$1.6^{+0.5}_{-1.3}$	0.42 ± 0.04
G029.956−00.020	5.3 ± 0.5	6.75 ± 0.30	5.6 ± 0.2	10.0 ± 0.9	30.4 ± 1.7	$9.5^{+5.5}_{-4.9}$	$11.0^{+4.2}_{-5.4}$	23.2	$1.2^{+0.4}_{-0.5}$	$0.7^{+1.9}_{-0.2}$	0.54 ± 0.05
G030.036−00.167	8.7 ± 0.8	6.65 ± 0.30	5.7 ± 0.1	9.8 ± 0.6	35.3 ± 0.3	$9.9^{+8.4}_{-4.6}$	$15.6^{+4.6}_{-8.5}$	17.4	$1.2^{+0.4}_{-0.3}$	$1.6^{+0.6}_{-0.9}$	0.62 ± 0.05
G030.055−00.339	7.4 ± 1.5	6.57 ± 0.30	5.5 ± 0.1	9.9 ± 0.7	28.3 ± 2.3	$8.1^{+5.7}_{-4.5}$	$10.7^{+3.3}_{-4.7}$	23.6	$1.0^{+0.3}_{-0.3}$	$1.2^{+0.5}_{-0.6}$	0.59 ± 0.06
G030.338−00.252	8.2 ± 2.8	6.61 ± 0.30	4.6 ± 0.2	9.9 ± 0.7	28.3 ± 2.3	$12.6^{+3.8}_{-8.3}$	$5.8^{+8.3}_{-1.7}$	19.5	$1.3^{+0.4}_{-0.5}$	$0.5^{+1.0}_{-0.2}$	0.67 ± 0.11

Continued on next page

HII region	Dis	$T_{\rm e}$	$T_{\rm h}$	$T_{\rm m}$	$T_{\rm t}$	$X_{\rm b}$	$X_{\rm f}$	τ	$\epsilon_{\rm b\_com}$	$\epsilon_{\rm f\_com}$	$\epsilon_{\rm b\_sim}$
	kpc	$\times10^3$ K	$\times10^3$ K	$\times10^3$ K	$\times10^3$ K	$\times10^3$ K	$\times10^3$ K		K pc^{-1}	K pc^{-1}	K pc^{-1}
(1)	(2)	(3)	(4)	(5)	(6)	(7)	(8)	(9)	(10)	(11)	(12)
G030.468+00.394	3.3 ± 0.7	7.20 ± 0.30	7.2 ± 0.3	9.3 ± 0.9	27.9 ± 2.4	$11.4^{+5.1}_{-4.5}$	$7.1^{+4.8}_{-3.5}$	14.7	$0.9^{+0.2}_{-0.2}$	$2.2^{+1.5}_{-1.3}$	0.40 ± 0.05
G030.599−00.344	7.3 ± 0.1	6.59 ± 0.30	4.8 ± 0.1	9.9 ± 0.7	28.3 ± 2.3	$11.9^{+1.2}_{-7.8}$	$6.5^{+7.8}_{-0.8}$	67.1	$1.2^{+0.4}_{-0.4}$	$0.6^{+1.1}_{-0.2}$	0.63 ± 0.05
G030.758−00.047	6.5 ± 0.7	7.03 ± 0.00	4.5 ± 0.2	8.6 ± 0.5	36.4 ± 0.6	$10.5^{+6.0}_{-5.6}$	$17.6^{+5.0}_{-6.2}$	13.3	$1.1^{+0.3}_{-0.3}$	$2.3^{+0.8}_{-1.0}$	0.57 ± 0.04
G030.795−00.275	7.3 ± 0.5	6.60 ± 0.30	5.6 ± 0.2	8.1 ± 0.7	33.5 ± 3.5	$9.0^{+11.6}_{-4.1}$	$16.4^{+4.3}_{-10.1}$	15.8	$0.9^{+0.6}_{-0.2}$	$2.1^{+0.6}_{-1.5}$	0.48 ± 0.05
G030.796+00.183	7.3 ± 0.7	6.60 ± 0.30	5.6 ± 0.1	9.3 ± 0.9	27.9 ± 2.4	$9.2^{+4.8}_{-5.2}$	$9.6^{+4.1}_{-4.5}$	67.5	$1.0^{+0.3}_{-0.2}$	$1.2^{+0.5}_{-0.7}$	0.55 ± 0.06
G031.016−00.039	8.0 ± 2.8	6.64 ± 0.30	5.8 ± 0.1	9.0 ± 0.4	37.4 ± 0.9	$12.5^{+8.8}_{-5.7}$	$15.9^{+6.0}_{-8.4}$	11.9	$1.2^{+0.5}_{-0.4}$	$1.9^{+1.0}_{-1.3}$	0.54 ± 0.09
G031.065+00.045	5.5 ± 1.1	6.75 ± 0.30	5.7 ± 0.1	8.4 ± 0.7	40.4 ± 2.0	$21.7^{+6.5}_{-15.5}$	$10.3^{+15.8}_{-3.1}$	>99	$1.5^{+0.4}_{-0.8}$	$1.7^{+2.9}_{-0.6}$	0.46 ± 0.05
G031.138+00.285	7.3 ± 0.1	6.62 ± 0.30	7.4 ± 0.2	9.3 ± 0.9	27.9 ± 2.4	$8.6^{+6.1}_{-5.0}$	$10.0^{+4.3}_{-5.8}$	17.8	$0.9^{+0.3}_{-0.2}$	$1.5^{+0.6}_{-0.8}$	0.45 ± 0.05
G031.677+00.179	7.2 ± 0.1	6.65 ± 0.30	6.5 ± 0.2	8.9 ± 0.4	36.9 ± 0.9	$18.8^{+2.1}_{-12.0}$	$9.2^{+12.3}_{-1.8}$	>99	$1.4^{+0.4}_{-0.6}$	$1.2^{+1.7}_{-0.2}$	0.48 ± 0.03
G031.881+01.417	3.6 ± 0.4	7.15 ± 0.30	5.0 ± 0.3	7.9 ± 0.8	20.6 ± 1.2	$6.7^{+2.7}_{-2.2}$	$6.0^{+2.7}_{-2.2}$	16.3	$0.7^{+0.1}_{-0.1}$	$1.0^{+0.7}_{-0.6}$	0.45 ± 0.04
G032.181+00.015	6.8 ± 0.7	6.68 ± 0.30	6.6 ± 0.1	9.6 ± 1.0	26.9 ± 1.8	$7.3^{+6.7}_{-1.4}$	$10.0^{+1.9}_{-6.0}$	20.8	$0.9^{+0.3}_{-0.3}$	$1.5^{+0.3}_{-0.9}$	0.50 ± 0.06
G032.870−00.427	10.9 ± 0.4	6.07 ± 0.20	5.5 ± 0.0	6.7 ± 0.6	22.7 ± 1.5	$8.1^{+4.3}_{-4.5}$	$7.9^{+4.1}_{-4.4}$	27.8	$1.0^{+0.3}_{-0.3}$	$0.7^{+0.4}_{-0.4}$	0.47 ± 0.05
G033.051−00.078	7.1 ± 1.0	6.71 ± 0.30	5.6 ± 0.3	9.1 ± 0.8	25.4 ± 1.4	$8.7^{+4.2}_{-5.3}$	$7.5^{+4.7}_{-3.9}$	17.0	$1.0^{+0.2}_{-0.2}$	$0.9^{+0.7}_{-0.6}$	0.55 ± 0.06
G036.192−00.171	6.9 ± 1.7	6.86 ± 0.30	7.7 ± 0.2	11.1 ± 0.8	27.7 ± 0.4	$12.3^{+3.7}_{-7.2}$	$4.3^{+7.3}_{-0.6}$	25.1	$1.2^{+0.4}_{-0.4}$	$0.7^{+1.1}_{-0.2}$	0.55 ± 0.07
G036.459−00.183	8.9 ± 0.6	7.03 ± 0.30	7.8 ± 0.2	10.3 ± 0.9	26.6 ± 0.2	$4.5^{+7.0}_{-1.3}$	$11.8^{+3.5}_{-7.0}$	2.4	$1.0^{+0.2}_{-0.2}$	$1.0^{+0.4}_{-0.4}$	0.57 ± 0.06
G037.028−00.202	6.8 ± 1.2	6.90 ± 0.30	7.5 ± 0.2	9.7 ± 1.1	26.4 ± 0.3	$10.0^{+2.7}_{-5.4}$	$6.6^{+5.0}_{-2.4}$	29.0	$1.0^{+0.2}_{-0.3}$	$1.1^{+0.7}_{-0.4}$	0.48 ± 0.08
G037.677+00.155	6.7 ± 0.1	6.93 ± 0.30	6.5 ± 0.5	10.0 ± 0.8	28.5 ± 0.8	$5.1^{+7.8}_{-1.1}$	$13.4^{+4.0}_{-7.9}$	52.5	$0.8^{+0.4}_{-0.2}$	$1.9^{+0.6}_{-1.2}$	0.56 ± 0.06
G317.628−00.425	3.6 ± 0.7	4.50 ± 0.50	6.4 ± 0.3	9.7 ± 0.8	18.3 ± 1.6	$4.2^{+2.0}_{-2.8}$	$4.4^{+3.0}_{-2.0}$	41.8	$0.5^{+0.1}_{-0.1}$	$1.8^{+0.9}_{-0.6}$	0.37 ± 0.05

Continued on next page

HII region	Dis	$T_{\rm e}$	$T_{\rm h}$	$T_{\rm m}$	$T_{\rm t}$	$X_{\rm b}$	$X_{\rm f}$	τ	$\epsilon_{\rm b\_com}$	$\epsilon_{\rm f\_com}$	$\epsilon_{\rm b\_sim}$
	kpc	$\times10^3$ K	$\times10^3$ K	$\times10^3$ K	$\times10^3$ K	$\times10^3$ K	$\times10^3$ K		K pc^{-1}	K pc^{-1}	K pc^{-1}
(1)	(2)	(3)	(4)	(5)	(6)	(7)	(8)	(9)	(10)	(11)	(12)
G319.164−00.421	11.4 ± 0.6	7.80 ± 0.40	4.1 ± 0.5	9.0 ± 0.5	18.9 ± 1.0	$3.6^{+2.1}_{-1.4}$	$6.3^{+1.3}_{-1.7}$	12.4	$1.1^{+0.1}_{-0.3}$	$0.2^{+0.1}_{-0.2}$	0.93 ± 0.07
G320.692+00.185	12.8 ± 0.7	8.10 ± 0.40	5.4 ± 0.2	7.2 ± 1.0	17.6 ± 0.8	$6.0^{+1.8}_{-4.0}$	$4.4^{+3.3}_{-1.3}$	>99	$1.2^{+0.4}_{-0.3}$	$0.1^{+0.2}_{-0.0}$	0.78 ± 0.10
G321.115−00.546	4.0 ± 0.6	7.22 ± 0.30	5.2 ± 0.3	7.7 ± 0.6	20.1 ± 0.6	$7.2^{+2.2}_{-4.2}$	$5.1^{+4.1}_{-1.5}$	32.1	$0.8^{+0.2}_{-0.2}$	$0.7^{+1.0}_{-0.1}$	0.46 ± 0.04
G322.162+00.625	3.5 ± 0.5	7.29 ± 0.30	3.4 ± 0.5	6.8 ± 1.2	15.7 ± 0.8	$3.7^{+1.0}_{-1.8}$	$5.2^{+1.7}_{-0.7}$	19.8	$0.6^{+0.2}_{-0.1}$	$0.4^{+0.5}_{-0.3}$	0.49 ± 0.07
G326.270+00.783	3.0 ± 0.4	7.33 ± 0.30	3.3 ± 0.6	9.2 ± 0.6	19.1 ± 0.9	$5.6^{+1.7}_{-3.1}$	$5.7^{+1.4}_{-1.4}$	9.2	$0.8^{+0.2}_{-0.1}$	$0.5^{+0.5}_{-0.4}$	0.59 ± 0.04
G326.643+00.514	3.0 ± 0.4	7.32 ± 0.30	3.8 ± 1.0	9.3 ± 0.7	19.4 ± 1.1	$5.6^{+0.7}_{-3.4}$	$4.4^{+2.9}_{-1.3}$	>99	$0.8^{+0.2}_{-0.1}$	$0.3^{+0.9}_{-0.1}$	0.57 ± 0.06
G327.300−00.548	3.5 ± 0.7	4.70 ± 0.50	4.5 ± 0.8	16.5 ± 1.1	30.7 ± 1.8	$8.1^{+2.5}_{-5.4}$	$6.2^{+4.6}_{-2.1}$	5.8	$1.1^{+0.1}_{-0.2}$	$1.7^{+1.4}_{-0.7}$	0.78 ± 0.07
G327.555−00.829	2.6 ± 0.5	7.41 ± 0.30	5.4 ± 0.3	13.0 ± 1.0	26.6 ± 1.8	$5.1^{+3.8}_{-3.0}$	$8.5^{+2.9}_{-3.5}$	17.8	$0.8^{+0.1}_{-0.1}$	$2.2^{+1.3}_{-1.2}$	0.66 ± 0.05
G327.889−00.045	3.6 ± 0.7	6.00 ± 0.60	11.7 ± 0.3	14.3 ± 1.6	37.0 ± 0.2	$15.5^{+2.2}_{-10.6}$	$7.2^{+10.3}_{-2.1}$	>99	$1.0^{+0.1}_{-0.4}$	$3.6^{+2.8}_{-1.0}$	0.39 ± 0.09
G328.572−00.527	3.4 ± 0.4	7.19 ± 0.30	12.6 ± 0.5	16.5 ± 1.1	30.7 ± 1.8	$9.4^{+3.6}_{-4.4}$	$5.0^{+3.9}_{-3.4}$	41.1	$0.9^{+0.1}_{-0.2}$	$3.0^{+1.2}_{-1.1}$	0.49 ± 0.06
G330.873−00.369	3.7 ± 0.4	7.07 ± 0.30	10.7 ± 0.3	16.1 ± 1.5	32.2 ± 1.5	$8.4^{+4.5}_{-4.7}$	$7.7^{+4.1}_{-4.2}$	75.2	$0.9^{+0.2}_{-0.2}$	$2.9^{+1.3}_{-1.2}$	0.56 ± 0.07
G331.123−00.530	4.3 ± 0.4	6.92 ± 0.30	10.7 ± 0.4	16.1 ± 1.5	32.2 ± 1.5	$5.0^{+7.6}_{-1.5}$	$7.5^{+3.4}_{-4.1}$	>99	$1.0^{+0.2}_{-0.2}$	$2.6^{+0.9}_{-1.1}$	0.57 ± 0.08
G331.156−00.391	4.3 ± 0.4	6.92 ± 0.30	10.6 ± 0.5	16.1 ± 1.5	32.2 ± 1.5	$10.2^{+3.1}_{-5.3}$	$5.9^{+5.1}_{-2.6}$	24.2	$1.0^{+0.1}_{-0.2}$	$2.2^{+1.2}_{-0.7}$	0.57 ± 0.08
G331.338−00.365	4.1 ± 0.4	6.96 ± 0.30	12.1 ± 0.4	15.9 ± 1.4	31.8 ± 1.5	$10.5^{+3.8}_{-5.4}$	$5.4^{+4.9}_{-3.8}$	17.6	$0.9^{+0.2}_{-0.2}$	$2.6^{+1.1}_{-1.0}$	0.49 ± 0.07
G331.520−00.076	5.4 ± 0.5	6.68 ± 0.30	13.6 ± 0.2	19.6 ± 0.3	40.4 ± 0.7	$11.0^{+6.4}_{-6.2}$	$10.1^{+6.0}_{-6.9}$	45.2	$1.1^{+0.3}_{-0.3}$	$2.9^{+1.3}_{-1.2}$	0.62 ± 0.03
G332.145−00.452	3.7 ± 0.4	7.05 ± 0.30	9.8 ± 0.5	14.5 ± 1.0	32.6 ± 2.3	$8.6^{+5.6}_{-5.5}$	$9.3^{+4.9}_{-6.0}$	9.2	$0.9^{+0.2}_{-0.2}$	$3.1^{+1.4}_{-1.7}$	0.52 ± 0.06
G332.762−00.595	3.6 ± 0.4	7.06 ± 0.30	7.5 ± 0.8	12.1 ± 0.7	39.1 ± 3.6	$12.7^{+8.0}_{-8.9}$	$14.3^{+8.2}_{-7.6}$	>99	$1.0^{+0.3}_{-0.4}$	$4.1^{+2.4}_{-2.2}$	0.52 ± 0.05
G332.978+00.773	3.5 ± 0.4	7.09 ± 0.30	11.6 ± 0.6	17.3 ± 0.9	33.8 ± 1.6	$10.4^{+3.3}_{-4.4}$	$6.0^{+4.5}_{-3.1}$	22.5	$1.0^{+0.2}_{-0.2}$	$3.0^{+1.3}_{-1.0}$	0.57 ± 0.06

Continued on next page

HII region	Dis	T_e	T_h	T_m	T_t	X_b	X_f	τ	ϵ_{b_com}	ϵ_{f_com}	ϵ_{b_sim}
	kpc	$\times 10^3$ K	$\times 10^3$ K	$\times 10^3$ K	$\times 10^3$ K	$\times 10^3$ K	$\times 10^3$ K		K pc^{-1}	K pc^{-1}	K pc^{-1}
(1)	(2)	(3)	(4)	(5)	(6)	(7)	(8)	(9)	(10)	(11)	(12)
G333.011−00.441	3.6 ± 0.4	7.06 ± 0.30	8.0 ± 0.2	12.1 ± 0.7	39.0 ± 3.7	$11.0^{+9.5}_{-5.1}$	$15.9^{+4.1}_{-10.5}$	18.8	$0.9^{+0.4}_{-0.2}$	$4.7^{+1.2}_{-2.9}$	0.49 ± 0.04
G333.093+01.966	1.6 ± 0.6	7.67 ± 0.30	7.0 ± 0.3	11.1 ± 1.3	21.7 ± 1.4	$6.4^{+3.0}_{-3.1}$	$4.2^{+2.2}_{-2.4}$	29.0	$0.7^{+0.1}_{-0.1}$	$2.2^{+1.6}_{-1.8}$	0.48 ± 0.06
G333.129−00.439	3.5 ± 0.4	7.09 ± 0.30	6.7 ± 0.6	12.1 ± 0.7	39.0 ± 3.7	$15.7^{+4.8}_{-10.1}$	$11.2^{+10.0}_{-4.7}$	>99	$1.2^{+0.2}_{-0.4}$	$3.1^{+2.8}_{-1.7}$	0.55 ± 0.05
G333.215−00.298	3.4 ± 0.4	7.11 ± 0.30	8.4 ± 0.5	12.1 ± 0.7	39.0 ± 3.7	$12.9^{+7.8}_{-9.3}$	$14.0^{+8.2}_{-8.0}$	18.7	$1.0^{+0.3}_{-0.4}$	$4.5^{+2.5}_{-2.5}$	0.47 ± 0.04
G333.245−00.487	3.4 ± 0.4	7.11 ± 0.30	7.6 ± 1.0	12.0 ± 0.8	40.0 ± 3.5	$18.7^{+5.7}_{-13.7}$	$9.3^{+12.5}_{-5.0}$	16.4	$1.3^{+0.2}_{-0.6}$	$2.9^{+3.6}_{-1.4}$	0.50 ± 0.06
G333.593−00.090	3.2 ± 0.4	7.17 ± 0.30	7.1 ± 0.4	15.3 ± 2.1	39.7 ± 1.2	$13.2^{+5.5}_{-5.8}$	$11.2^{+5.2}_{-5.8}$	>99	$1.2^{+0.2}_{-0.2}$	$3.3^{+1.8}_{-1.7}$	0.68 ± 0.10
G333.594−00.291	3.2 ± 0.4	7.17 ± 0.30	6.2 ± 0.7	12.7 ± 0.5	41.2 ± 1.2	$12.5^{+8.9}_{-6.4}$	$15.9^{+6.2}_{-8.4}$	14.8	$1.1^{+0.3}_{-0.3}$	$4.5^{+2.1}_{-2.7}$	0.60 ± 0.04
G333.627−00.199	3.2 ± 0.4	7.16 ± 0.30	6.2 ± 0.8	14.7 ± 1.8	40.0 ± 1.1	$9.8^{+6.9}_{-4.5}$	$15.3^{+3.9}_{-6.1}$	20.3	$1.1^{+0.3}_{-0.2}$	$4.4^{+1.4}_{-1.9}$	0.69 ± 0.09
G333.683−00.512	11.8 ± 0.4	7.10 ± 0.30	8.5 ± 0.2	12.1 ± 0.7	39.0 ± 3.7	$13.3^{+8.6}_{-8.7}$	$13.6^{+8.6}_{-8.7}$	32.5	$1.6^{+0.5}_{-0.5}$	$1.3^{+0.7}_{-0.8}$	0.72 ± 0.06
G336.446−00.198	10.3 ± 0.4	6.55 ± 0.30	12.5 ± 1.1	14.3 ± 1.0	41.6 ± 1.4	$14.6^{+6.1}_{-9.3}$	$12.8^{+9.6}_{-6.3}$	55.7	$1.3^{+0.4}_{-0.6}$	$1.8^{+0.9}_{-0.6}$	0.50 ± 0.10
G336.455+00.042	11.4 ± 0.4	6.84 ± 0.30	13.0 ± 0.5	14.3 ± 1.0	41.6 ± 1.4	$11.0^{+10.9}_{-6.4}$	$16.2^{+6.6}_{-9.7}$	>99	$1.2^{+0.6}_{-0.4}$	$1.9^{+0.6}_{-0.9}$	0.51 ± 0.08
G337.957−00.474	3.1 ± 0.4	7.14 ± 0.30	11.7 ± 1.0	17.1 ± 1.3	48.7 ± 2.1	$14.3^{+9.0}_{-7.9}$	$17.3^{+7.7}_{-10.9}$	30.4	$1.1^{+0.4}_{-0.3}$	$6.9^{+2.7}_{-3.2}$	0.54 ± 0.07
G338.706+00.645	4.3 ± 0.4	6.76 ± 0.30	9.5 ± 0.3	14.0 ± 0.7	32.6 ± 1.4	$15.0^{+4.5}_{-10.3}$	$9.6^{+4.0}_{-5.6}$	13.2	$1.1^{+0.3}_{-0.4}$	$1.5^{+2.2}_{-0.5}$	0.51 ± 0.04
G338.911+00.615	4.4 ± 0.4	6.73 ± 0.30	8.5 ± 0.7	14.1 ± 0.7	33.2 ± 1.5	$9.9^{+5.9}_{-5.8}$	$9.2^{+5.6}_{-5.9}$	>99	$1.0^{+0.3}_{-0.3}$	$2.4^{+1.3}_{-1.4}$	0.56 ± 0.05
G338.934−00.067	3.2 ± 0.4	7.10 ± 0.30	11.3 ± 0.5	17.8 ± 1.5	45.2 ± 1.7	$13.3^{+7.6}_{-7.7}$	$14.1^{+6.8}_{-7.4}$	25.4	$1.1^{+0.3}_{-0.3}$	$5.7^{+2.3}_{-2.5}$	0.59 ± 0.07
G339.233+00.243	11.2 ± 0.4	6.64 ± 0.30	12.9 ± 0.3	17.0 ± 0.8	43.3 ± 1.3	$12.1^{+7.9}_{-6.8}$	$13.7^{+7.2}_{-7.2}$	76.8	$1.4^{+0.5}_{-0.4}$	$1.8^{+0.7}_{-0.7}$	0.68 ± 0.06
G340.051−00.231	3.9 ± 0.4	6.86 ± 0.30	8.9 ± 0.3	14.5 ± 0.7	36.0 ± 0.6	$6.0^{+8.8}_{-2.6}$	$15.5^{+2.3}_{-8.6}$	5.2	$0.8^{+0.4}_{-0.1}$	$4.5^{+0.7}_{-2.6}$	0.55 ± 0.04
G340.294−00.193	3.5 ± 0.4	6.98 ± 0.30	10.5 ± 1.0	14.6 ± 0.7	36.1 ± 0.6	$6.2^{+11.3}_{-1.9}$	$15.2^{+4.6}_{-11.5}$	>99	$0.9^{+0.3}_{-0.2}$	$4.0^{+1.4}_{-2.0}$	0.48 ± 0.06

Continued on next page

HII region	Dis	$T_{\rm e}$	$T_{\rm h}$	$T_{\rm m}$	$T_{\rm t}$	$X_{\rm b}$	$X_{\rm f}$	τ	$\epsilon_{\rm b\_com}$	$\epsilon_{\rm f\_com}$	$\epsilon_{\rm b\_sim}$
	kpc	$\times10^3$ K	$\times10^3$ K	$\times10^3$ K	$\times10^3$ K	$\times10^3$ K	$\times10^3$ K		K pc^{-1}	K pc^{-1}	K pc^{-1}
(1)	(2)	(3)	(4)	(5)	(6)	(7)	(8)	(9)	(10)	(11)	(12)
G341.090−00.017	3.4 ± 0.7	4.30 ± 0.40	8.5 ± 0.9	17.0 ± 1.5	36.4 ± 0.3	$7.6^{+6.7}_{-4.7}$	$11.6^{+4.7}_{-6.5}$	29.8	$0.9^{+0.3}_{-0.2}$	$4.6^{+1.6}_{-2.2}$	0.56 ± 0.08
G341.283−00.353	3.4 ± 0.7	6.00 ± 0.60	9.3 ± 0.4	17.0 ± 1.5	36.4 ± 0.3	$5.1^{+9.4}_{-1.5}$	$9.4^{+4.6}_{-4.2}$	16.0	$1.0^{+0.2}_{-0.2}$	$3.7^{+1.6}_{-1.4}$	0.60 ± 0.08
G345.235+01.408	2.4 ± 0.5	6.00 ± 0.60	4.2 ± 0.9	9.9 ± 2.2	25.4 ± 2.7	$8.9^{+3.6}_{-5.1}$	$6.7^{+4.7}_{-2.1}$	57.4	$0.9^{+0.3}_{-0.3}$	$1.4^{+2.6}_{-0.5}$	0.48 ± 0.10
G345.410−00.953	2.6 ± 0.6	6.96 ± 0.00	6.4 ± 0.5	12.4 ± 0.6	31.0 ± 1.0	$9.6^{+4.5}_{-3.6}$	$9.1^{+3.9}_{-4.2}$	>99	$1.0^{+0.1}_{-0.2}$	$2.6^{+2.1}_{-1.2}$	0.54 ± 0.04
G345.491+00.354	2.0 ± 0.4	7.20 ± 0.70	10.0 ± 0.3	14.8 ± 0.7	34.2 ± 0.5	$5.3^{+9.2}_{-0.5}$	$14.0^{+4.2}_{-9.2}$	4.2	$0.7^{+0.4}_{-0.2}$	$8.4^{+3.0}_{-5.1}$	0.48 ± 0.04
G348.249−00.971	2.5 ± 0.8	7.27 ± 0.30	7.6 ± 0.2	13.4 ± 1.1	35.7 ± 3.2	$10.7^{+7.5}_{-5.3}$	$11.6^{+5.0}_{-7.3}$	>99	$0.9^{+0.3}_{-0.2}$	$4.8^{+2.5}_{-3.3}$	0.53 ± 0.05
G348.261+00.485	1.3 ± 0.3	7.30 ± 0.70	8.1 ± 1.8	13.6 ± 1.1	36.5 ± 3.0	$16.2^{+3.8}_{-9.3}$	$6.8^{+9.0}_{-3.1}$	28.8	$1.1^{+0.1}_{-0.3}$	$5.9^{+7.3}_{-2.4}$	0.50 ± 0.09
G348.691−00.826	3.4 ± 0.3	6.93 ± 0.30	3.4 ± 0.9	8.0 ± 0.8	27.4 ± 2.0	$8.4^{+3.7}_{-4.3}$	$11.5^{+2.7}_{-4.0}$	84.3	$0.8^{+0.1}_{-0.2}$	$2.2^{+0.9}_{-1.2}$	0.48 ± 0.06
G348.710−01.044	3.4 ± 0.3	7.15 ± 0.10	3.3 ± 0.8	8.0 ± 0.8	27.4 ± 2.0	$11.7^{+3.5}_{-6.5}$	$7.7^{+6.5}_{-2.3}$	20.3	$0.9^{+0.3}_{-0.3}$	$1.1^{+1.9}_{-0.2}$	0.50 ± 0.05
G349.814−00.625	2.2 ± 0.4	6.30 ± 0.60	3.6 ± 0.9	9.9 ± 0.5	29.8 ± 1.0	$7.1^{+5.8}_{-3.5}$	$12.7^{+3.5}_{-5.6}$	58.9	$0.8^{+0.2}_{-0.1}$	$4.2^{+2.0}_{-2.2}$	0.51 ± 0.05
G350.617+00.984	1.4 ± 0.3	9.00 ± 0.90	5.9 ± 1.1	10.5 ± 1.3	27.0 ± 2.5	$7.9^{+4.7}_{-4.0}$	$8.9^{+2.6}_{-3.2}$	5.9	$0.8^{+0.1}_{-0.1}$	$3.8^{+2.2}_{-1.9}$	0.52 ± 0.08
G350.995+00.654	1.4 ± 0.3	7.67 ± 0.30	4.2 ± 2.1	12.1 ± 1.0	31.8 ± 2.1	$8.1^{+5.4}_{-3.6}$	$11.1^{+3.5}_{-4.3}$	81.4	$0.9^{+0.2}_{-0.1}$	$4.9^{+2.7}_{-2.7}$	0.61 ± 0.10
G351.130+00.449	1.6 ± 1.3	6.65 ± 0.10	5.4 ± 2.5	12.1 ± 1.0	31.9 ± 2.1	$12.9^{+1.3}_{-9.8}$	$6.9^{+9.3}_{-1.7}$	29.0	$1.0^{+0.3}_{-0.3}$	$5.5^{+5.4}_{-5.0}$	0.53 ± 0.12
G351.170+00.704	17.1 ± 2.1	5.61 ± 0.00	5.9 ± 1.6	2.9 ± 1.9	46.5 ± 1.7	$20.8^{+11.9}_{-10.6}$	$22.6^{+10.4}_{-13.5}$	>99	$2.1^{+1.2}_{-1.0}$	$1.4^{+0.6}_{-0.8}$	0.20 ± 0.25
G351.246+00.673	1.3 ± 0.1	8.56 ± 0.10	4.1 ± 1.5	11.9 ± 1.2	31.3 ± 2.7	$8.5^{+5.1}_{-2.7}$	$11.0^{+3.2}_{-4.1}$	17.1	$0.9^{+0.2}_{-0.3}$	$5.0^{+1.7}_{-3.3}$	0.64 ± 0.08
G351.311+00.663	1.3 ± 0.1	7.71 ± 0.30	2.6 ± 0.3	11.0 ± 0.9	34.2 ± 2.5	$7.3^{+8.3}_{-1.2}$	$15.9^{+4.8}_{-7.6}$	28.7	$0.9^{+0.3}_{-0.3}$	$8.2^{+2.6}_{-5.9}$	0.63 ± 0.04
G351.348+00.593	1.4 ± 0.3	7.67 ± 0.30	4.4 ± 1.9	11.0 ± 0.9	34.2 ± 2.5	$10.5^{+6.1}_{-4.9}$	$12.6^{+4.5}_{-6.1}$	54.2	$0.9^{+0.2}_{-0.1}$	$6.7^{+3.2}_{-4.1}$	0.56 ± 0.09
G351.367+00.640	1.3 ± 0.1	9.70 ± 0.10	4.5 ± 1.4	11.9 ± 1.2	31.3 ± 2.7	$8.8^{+3.7}_{-4.2}$	$10.6^{+3.2}_{-3.3}$	22.7	$1.0^{+0.2}_{-0.1}$	$4.2^{+2.2}_{-2.8}$	0.66 ± 0.08

Continued on next page

HII region	Dis	$T_{\rm e}$	$T_{\rm h}$	$T_{\rm m}$	$T_{\rm t}$	$X_{\rm b}$	$X_{\rm f}$	τ	$\epsilon_{\rm b\_com}$	$\epsilon_{\rm f\_com}$	$\epsilon_{\rm b\_sim}$
	kpc	$\times 10^3$ K	$\times 10^3$ K	$\times 10^3$ K	$\times 10^3$ K	$\times 10^3$ K	$\times 10^3$ K		K pc^{-1}	K pc^{-1}	K pc^{-1}
(1)	(2)	(3)	(4)	(5)	(6)	(7)	(8)	(9)	(10)	(11)	(12)
G351.383+00.737	1.3 ± 0.1	7.71 ± 0.30	2.1 ± 1.6	11.1 ± 0.7	31.9 ± 1.7	$12.1^{+3.6}_{-7.3}$	$12.3^{+3.5}_{-3.2}$	27.2	$0.9^{+0.1}_{-0.1}$	$2.5^{+4.9}_{-0.8}$	0.65 ± 0.07
G351.472−00.458	3.5 ± 0.7	7.46 ± 0.10	6.2 ± 0.7	10.9 ± 0.7	28.0 ± 1.0	$9.1^{+3.7}_{-5.8}$	$8.0^{+5.8}_{-3.4}$	11.1	$0.9^{+0.1}_{-0.2}$	$1.9^{+1.6}_{-1.1}$	0.51 ± 0.05
G351.651+00.510	1.4 ± 0.3	5.60 ± 0.60	9.2 ± 1.1	14.2 ± 0.5	44.0 ± 0.9	$22.1^{+6.6}_{-15.7}$	$7.7^{+15.4}_{-1.1}$	50.8	$1.2^{+0.4}_{-0.6}$	$8.1^{+11.2}_{-3.0}$	0.41 ± 0.05
G351.688−01.169	14.5 ± 1.1	7.56 ± 0.10	2.6 ± 0.7	8.0 ± 1.0	25.1 ± 1.5	$9.2^{+2.8}_{-5.2}$	$7.9^{+4.8}_{-2.4}$	34.4	$1.6^{+0.5}_{-0.4}$	$0.2^{+0.3}_{-0.1}$	0.98 ± 0.13
G352.597−00.188	6.6 ± 0.3	7.56 ± 0.20	10.2 ± 0.6	14.0 ± 0.6	36.5 ± 0.6	$14.8^{+4.4}_{-9.8}$	$7.7^{+9.8}_{-0.8}$	10.5	$1.2^{+0.4}_{-0.4}$	$1.6^{+1.4}_{-0.3}$	0.54 ± 0.05
G353.038+00.581	1.8 ± 0.4	6.40 ± 0.60	4.2 ± 2.3	15.9 ± 1.2	47.3 ± 4.2	$15.3^{+6.1}_{-10.1}$	$16.1^{+8.9}_{-6.6}$	56.6	$1.3^{+0.3}_{-0.4}$	$7.7^{+5.3}_{-4.1}$	0.73 ± 0.11
G353.076+00.287	1.8 ± 0.4	5.00 ± 0.50	3.6 ± 1.4	16.1 ± 1.2	46.7 ± 3.5	$13.5^{+8.9}_{-7.3}$	$17.0^{+6.5}_{-9.2}$	>99	$1.2^{+0.3}_{-0.3}$	$8.0^{+4.6}_{-4.4}$	0.72 ± 0.08
G353.092+00.857	1.8 ± 0.4	5.50 ± 0.60	2.3 ± 1.0	14.6 ± 1.7	35.9 ± 4.1	$14.2^{+4.3}_{-10.2}$	$7.2^{+9.6}_{-2.2}$	14.1	$1.2^{+0.4}_{-0.4}$	$2.2^{+5.3}_{-0.5}$	0.72 ± 0.08
G353.408−00.381	3.3 ± 0.9	8.48 ± 0.10	12.0 ± 0.5	13.4 ± 0.5	43.7 ± 1.4	$17.3^{+5.8}_{-9.9}$	$12.9^{+9.4}_{-5.2}$	93.2	$1.1^{+0.3}_{-0.4}$	$5.0^{+3.1}_{-2.1}$	0.40 ± 0.03
G359.740−00.412	1.5 ± 0.3	8.60 ± 0.90	13.4 ± 2.8	33.9 ± 3.4	80.6 ± 18.0	$41.0^{+12.3}_{-35.0}$	$22.2^{+15.4}_{-9.7}$	21.4	$2.6^{+0.8}_{-1.3}$	$17.4^{+12.2}_{-7.7}$	1.17 ± 0.19

3.3.2 Error estimation

For the emissivities derived from simplified equations, we propagate the error throughout the simple equations to estimate their errors. For our improved method, the equations are too complex to permit directly calculating the uncertainty of each solution caused by the variance of the known parameters from the measurements. The sources of the error include

- the error of the HII region electron temperature,
- the error of the distance from HII region to us,
- the RMS of the brightness temperature for the absorbed region in the GLEAM map,
- the RMS of the brightness temperature for the background region in the GLEAM map,
- the RMS of the brightness temperature for the background region in the Haslam map,
- the variation of the spectral indices of the synchrotron brightness temperature and the HII region optical depth.

We use a Monte Carlo method to statistically estimate the error of these solutions caused by the first five error sources. Specifically, we use the values of known parameters to calculate the solutions and then sample around these parameters. We set each input parameter to be a random number following a Gaussian distribution with a mean from the best input value and a standard derivation from our one-sigma measurement error. Using these new input parameters, we can find new solutions. By repeating the

calculation, we get a distribution of each solution and then calculate the one-sigma upper and lower limits. The estimated errors are about 10-90% of the emissivity values (see Table 3.2). Note that we do not include the contribution of the spectral indices of the synchrotron brightness temperature and the HII region optical depth because the solutions finding becomes computationally expensive with these two spectral indices included. The spectral index of the brightness temperature cause a difference of about 15% of the emissivity values, estimated from the variance of the Haslam map scaling, when this spectral index changes from -2.7 to -2.6. Although causing this extra error to the measured emissivities, it is still necessary to use the Haslam map; otherwise, the measured emissivities behind HII regions will be under-estimated due to the missing flux density, and the emissivities in front of HII regions cannot be calculated. The error contributed by the spectral index of the HII region optical depth is small ($< 1\%$ of the emissivity) because the term $e^{-\tau}$ in Equation 3.4 is small when the optical depth is much larger than one.

We check which input parameter dominates the errors of the final emissivities. We set only one input parameter to be a random number while setting all other parameters to be constants. Then similarly with the above error estimation, we calculate the one-sigma upper and lower limits of the emissivities. The error contribution of each input parameter is shown in Fig. 3.7. We find the RMS of the brightness temperature of the Haslam map contributes the most to the final errors of the measured emissivities.

In the future, new maps from new data processing techniques may be able to recover the total power along the line of sight, which will avoid extrapolating the Halam map from 408 MHz to the GLEAM frequencies. For example, Eastwood et al. (2018) use a new widefield imaging technique named the Tikhonov-regularized m-mode analysis imaging to map the northern sky with most of the large-scale structures recovered. Lunar occultation technique enables measuring the Galactic synchrotron emission in-

tegrated along the line of sight where the Moon occults the sky (e.g. Shaver et al. 1999; McKinley et al. 2013 and McKinley et al. submitted). Future large single-dishes observing at around 150 MHz will assist further.

3.4 Discussion of the derived emissivities

We compare the emissivities from the simplified method and our improved method in Fig. 3.2 (left). The emissivities from the old method are systematically lower than those from the new method, which indicates the old method underestimates the emissivities due to the missing flux density.

We compare the total and missing brightness temperatures behind the HII region in Fig. 3.2 (right). The unrecovered brightness temperature behind HII regions ($X_{\rm b}$) is about 50% of the total brightness temperature behind HII regions ($T_{\rm b}$), indicating that about 50% of the large-scale structure behind HII regions has not been recovered in our observations. The brightness temperature in front of HII regions that was not recovered ($X_{\rm f}$) is comparable with the total brightness temperature in front of HII regions ($T_{\rm f}$) indicating that nearly all the large-scale structures in front of HII regions have not been recovered. Thus, the missing structures must be considered in the emissivity calculation. Note that the $X_{\rm b}$ and $X_{\rm f}$ are comparable, while $T_{\rm f}$ is about 50% of $T_{\rm b}$. It is reasonable that most of $T_{\rm f}$ are not detected because an interferometer measures the difference along the HII region direction and its nearby direction, and also because most HII regions are nearby so that accumulated $T_{\rm f}$ is small compared to $T_{\rm b}$. The emission from the HII region to us is nearly the same for both directions, therefore, is not easily detected. However, $T_{\rm b}$ is 'different' on the HII region direction and its nearby direction because most of the $T_{\rm b}$ is absorbed by the HII region on its direction, so the MWA detects a portion of $T_{\rm b}$.

To confirm that our non-detections are reasonable, we compare the GLEAM map and the Haslam map at the visibility plane. We use nine square regions with size of 10°, 30°, and 60° centred at $l = 0°$, 20°, and 340°, $b = 0°$. We use the GLEAM map at the frequency of 76.2 MHz. The Haslam map is scaled from 408 MHz to the same frequency of 76.2 MHz using a spectral index of -2.7. The GLEAM map is smoothed to the same angular resolution of the Haslam map (51 arcmin), and the two maps are made with the same pixel size. For each region, we convert the two images to the visibility plane using Fast Fourier Transform (FFT) and then plot the amplitude against u-v distance to compare the difference between the two visibilities (see Fig. 3.8). The difference varies with the region size and location. On average, about 60% of the amplitude in the visibility of the Haslam map is not detected in the GLEAM. Our absorption analysis shows that 50% of the large-scale structures are not recovered for the emission behind HII regions, and nearly all emission from the column between the HII region and the Sun is not detected. These two results are generally consistent.

The most apparent feature in the derived emissivities is that they increase towards the Galactic centre. Both the emissivity and the brightness temperature peak near the Galactic centre and decrease as the line-of-sight goes far away from the Galactic centre (Fig. 3.2). To further confirm this trend, we check the average emissivity measured in the GLEAM map from the Sun to the Galactic edge (Fig. 3.9). It is evident that the emissivity along the path from the Sun to the Galactic edge peaks at the Galactic centre direction. This trend indicates the emissivity decreases with Galactocentric radius, which is modelled in Su et al. (2017a,b). This is consistent with the lowest order of disk component of the Galactic magnetic field, which is usually assumed to be exponentially distributed in the previous models (e.g. Beuermann et al. 1985; Sun et al. 2008). Face-on galaxies with spiral arms directly observed also show a similar profile as the one in Fig. 3.9, e.g. the LOw Frequency ARray (LOFAR; van Haarlem

et al. 2013) observation of the Whirlpool Galaxy (also known as M51) at the frequency of 150 MHz (see Fig. 13 in Mulcahy et al. 2014).

The average emissivities along the paths near the line of sight to the Sun are much higher than those far away from the Sun, though they have large errors. Several reasons can explain this effect. Firstly, the emissivity near the Galactic edge is much lower than that near the Galactic centre, which makes our average emissivities along the path high near the Galactic centre and low near the Galactic edge. Secondly, it may simply indicate that all distances from the HII region to the Galactic edge along the line of sight are over-estimated, which makes the emissivities behind HII regions decrease fractionally with distance. Thirdly, it may indicate the region near the Sun is not a representative region of the whole Milky Way because previous studies show that we are in a local bubble created by two or three supernovae (Maíz-Apellániz, 2001), which may increase the density of cosmic-ray electrons within several kpc of the Sun.

No obvious spiral arm structures can be visually seen from our observed emissivities because the emissivity is averaged along different path lengths. Further modelling work in the future will help to reveal that whether the emissivity distribution is correlated with the spiral arms or not, because this information is embedded in our derived emissivities. From an observational aspect, we can see the spiral arms as peaks in emissivity and brightness temperature along the total paths from the Sun to the Galactic edge as a function of Galactic longitude (see Fig. 6 in Su et al. 2017a and Fig. 1 in Beuermann et al. 1985).

We estimate the number density of relativistic electrons in the Galactic disk to confirm that our derived emissivities are consistent with existing electron models. Specifically, we get the relativistic electron density by using the total power of the synchrotron emission in the Galactic disk divided by the total power of one relativistic electron and then divided by the volume of the Galactic disk. In the above calcula-

tions, we use an average Galactic magnetic field strength of 5 ± 1 μG (Sun et al., 2008) and an average emissivity of 1 $\pm$ 0.5 K pc^{-1} at 76.2 MHz where 1 K pc^{-1} is equal to 5.75 $\times$ 10^{-41} W m^{-3} Hz^{-1} sr^{-1}. We use a typical energy of relativistic electrons of 10 $\pm$ 1 GeV (Stephens, 2001), a radius of the Galactic disk of 20 kpc (Nord et al., 2006), and scale height of the Galactic disk of 1 kpc. We integrate the power of synchrotron emission in the frequency range 10 MHz to 1000 GHz. We derive a number density of relativistic electrons of 168 $\pm$ 108 cm^{-3}. The relativistic electrons follow a power law distribution with energy, $n_e(E) = k\, E^{-3.152}$ (Adriani et al., 2017). Using this distribution, we derive the average density of 10 GeV electrons to be (5.6 $\pm$ 3.6) $\times$ 10^{-5} cm^{-3}, which is similar to the value of $(4 \pm 3) \times 10^{-5}$ cm^{-3} from the literature (see Fig. 4 in Jansson and Farrar 2012a, cited from GALPROP in Strong et al. 2010). Note that the estimated electron density has large errors due to the above typical values adopted. To further investigate the electron distribution, future work should use comprehensive Galactic magnetic field models (Han et al., 2006; Brown et al., 2007; Sun et al., 2008; Sun and Reich, 2010; Van Eck et al., 2011).

3.5 Summary of this chapter

We develop a new method of emissivity calculation by improving upon the previous simplified method. Using this new method, we calculate the synchrotron emissivities both behind and in front of 152 HII regions at six frequencies of 76.2, 83.8, 91.5, 99.2, 106.9, and 114.6 MHz. This new method enables us to derive the HII region optical depth and estimate the amount of flux density missing from our observations at each frequency. We find that the emissivities increase towards the Galactic centre. This lowest order of emissivity variation is consistent with the current Galactic magnetic field and relativistic electron distributions because both the magnetic field strength

and the relativistic electron density increase towards the Galactic centre. The high emissivities nearby the Sun (if actually real) might be caused by the local bubble.

The number of line-of-sight measurements will increase in the MWA phase II stage (Wayth et al., in prep.) because both the number of antenna and the maximum baselines are increased, and in the future, we will have better knowledge of the distance and electron temperature of HII regions. The lack of HII regions with larger distances is a key factor holding back the modelling at present because most HII regions are located near the Sun with distances less than several kpc. Future total power surveys at similar frequencies can improve the accuracy of the emissivity measurements. The derived emissivities may help to recover the 3D distribution of synchrotron emission in the Milky Way. Furthermore, they provide direct information on the spatial distribution of the Galactic magnetic field and the relativistic electrons for the future modelling.

In future, we expect to derive new measurements from about 150 HII regions. We will take advantage of the data in all five frequency bands of the GLEAM to derive the emissivity spectrum. A 3D emissivity map, combining these discrete measurements and the total line-of-sight emissivity distributions, will show more details of the Galactic structures with the help of existed comprehensive 3D models. We may set a length scale on cosmic ray electron propagation by comparing the possible cosmic ray source distribution and emissivity distribution. Possibly, we can derive the cosmic ray electron distribution with an assumed Galactic magnetic field distribution, and vice versa.

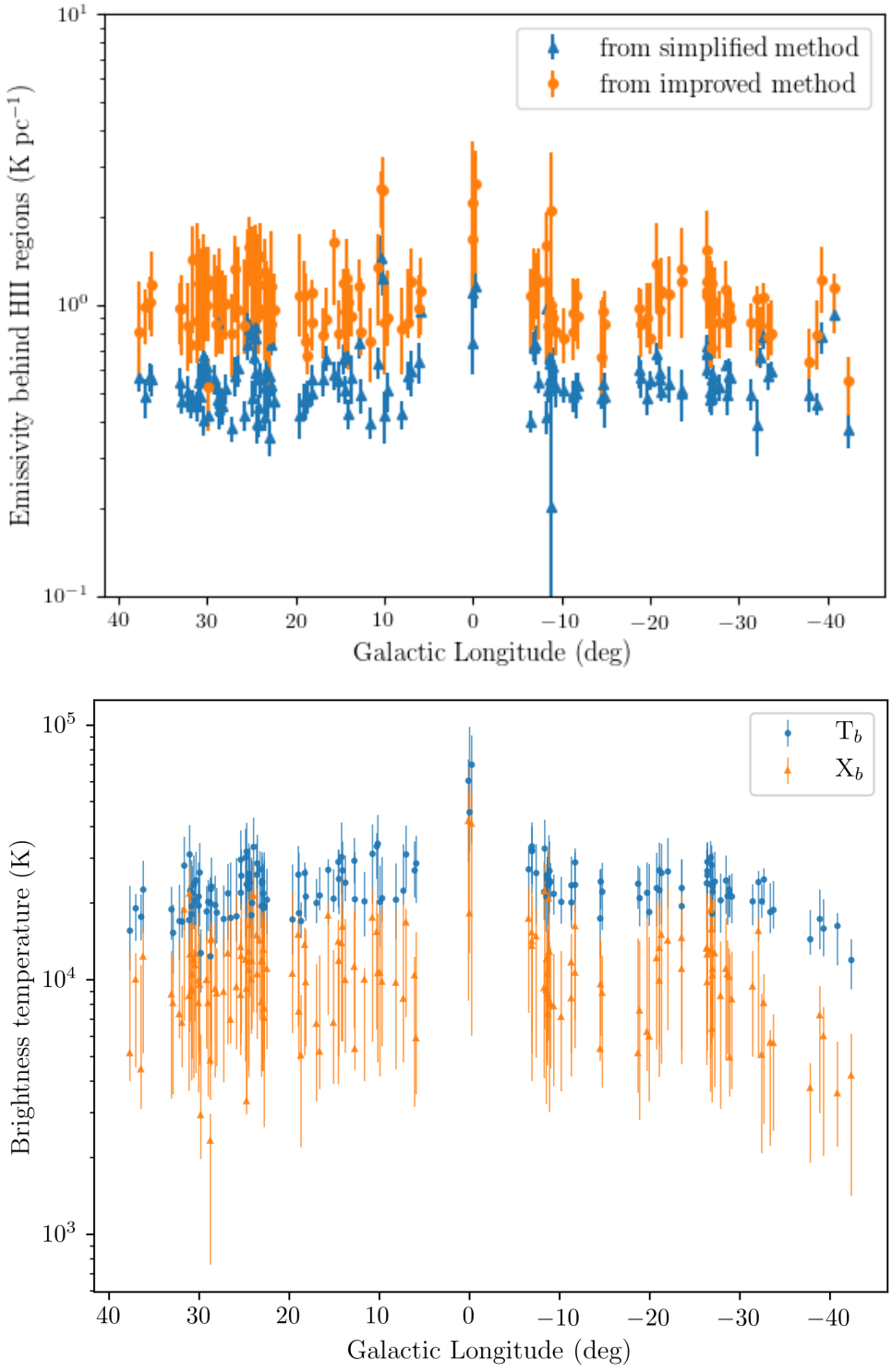

Figure 3.2: The effect of missing short interferometric spacings on the derived emissivities at 76.2 MHz. Top: Emissivities behind HII regions from the simplified and improved methods. Bottom: the brightness temperature from HII regions to the Galactic edge and the brightness temperature of its missing term.

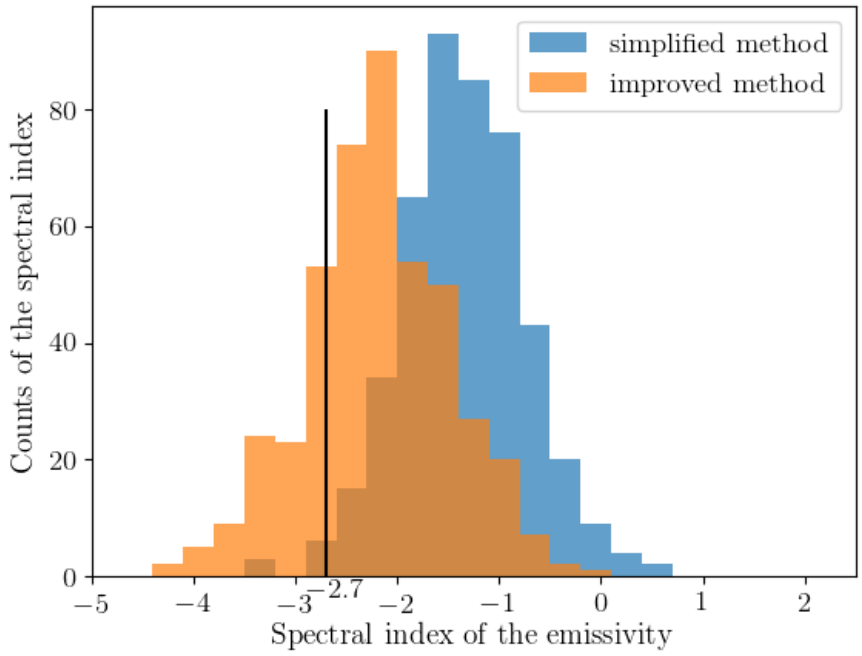

Figure 3.3: The spectral index distribution of the derived emissivity from the simplified method and improved method. The spectral index is calculated from the emissivity (behind the HII region) at the frequency from 76.2 to 99.2 MHz, from 83.8 to 106.9 MHz, and from 91.5 to 114.6 MHz. The bin width is 0.3. Most of the spectral indices from the simplified method are far away from the expected value of -2.7 shown by the black vertical line, indicating the missing flux density is affecting the simplified method. However, the emissivity from the improved method gives a spectral index close to -2.7. Note that emissivity is defined by the brightness temperature divided by a distance. For each HII regions, its distance is a constant, so the emissivity behind that HII region and the corresponding brightness temperature should follow the same spectral index of -2.7.

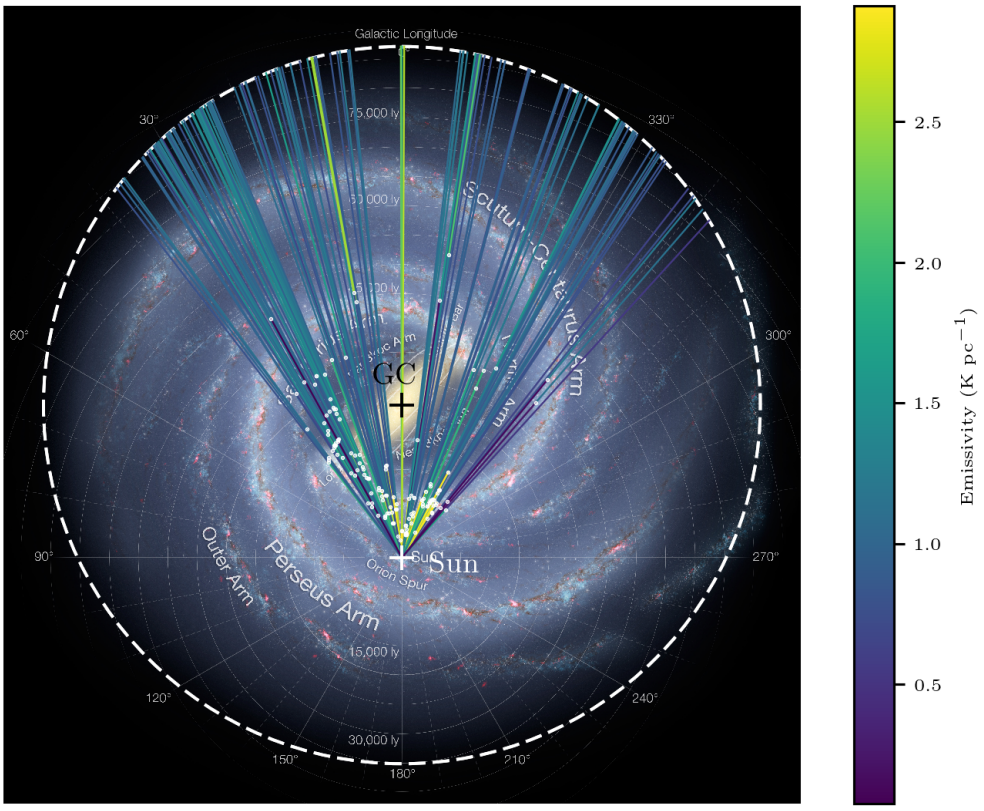

Figure 3.4: Our new derived emissivities at 76.2 MHz both behind and in front of HII regions. Each line indicates a path over which the emissivity is averaged with a white dot on it indicating the location of the HII region. The background image is an artist's concept with the up-to-date information about the structures of the Milky Way. We adjusted its colour to avoid obscuring the colour of emissivities. Background image credit: NASA / JPL-Caltech / R. Hurt (SSC-Caltech) with this link: https://www.nasa.gov/jpl/charting-the-milky-way-from-the-inside-out.

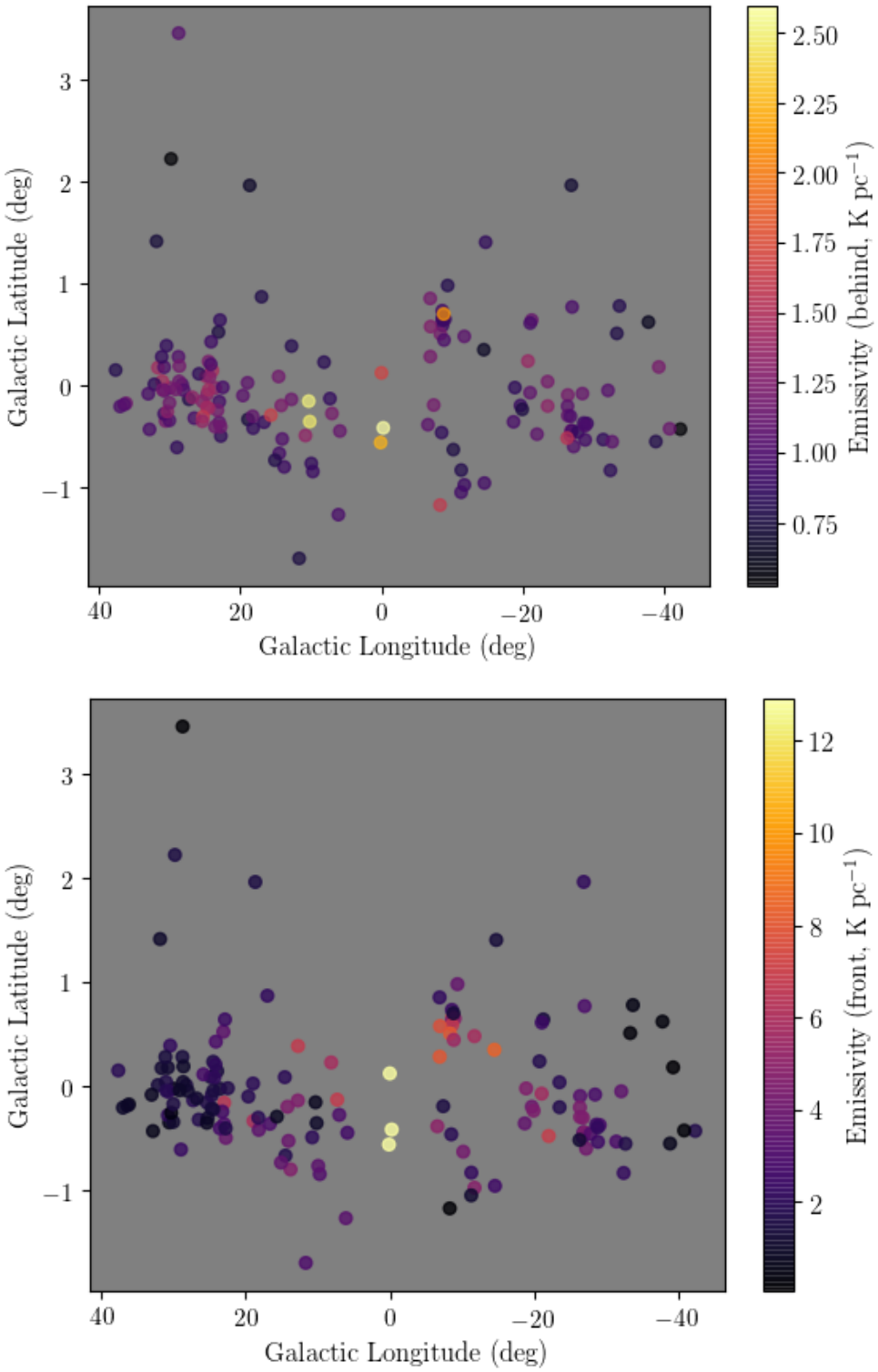

Figure 3.5: Correctly-calculated emissivities derived from our new method from HII regions to the Galactic edge (top) and from HII regions to the Sun (bottom) along the line of sight.

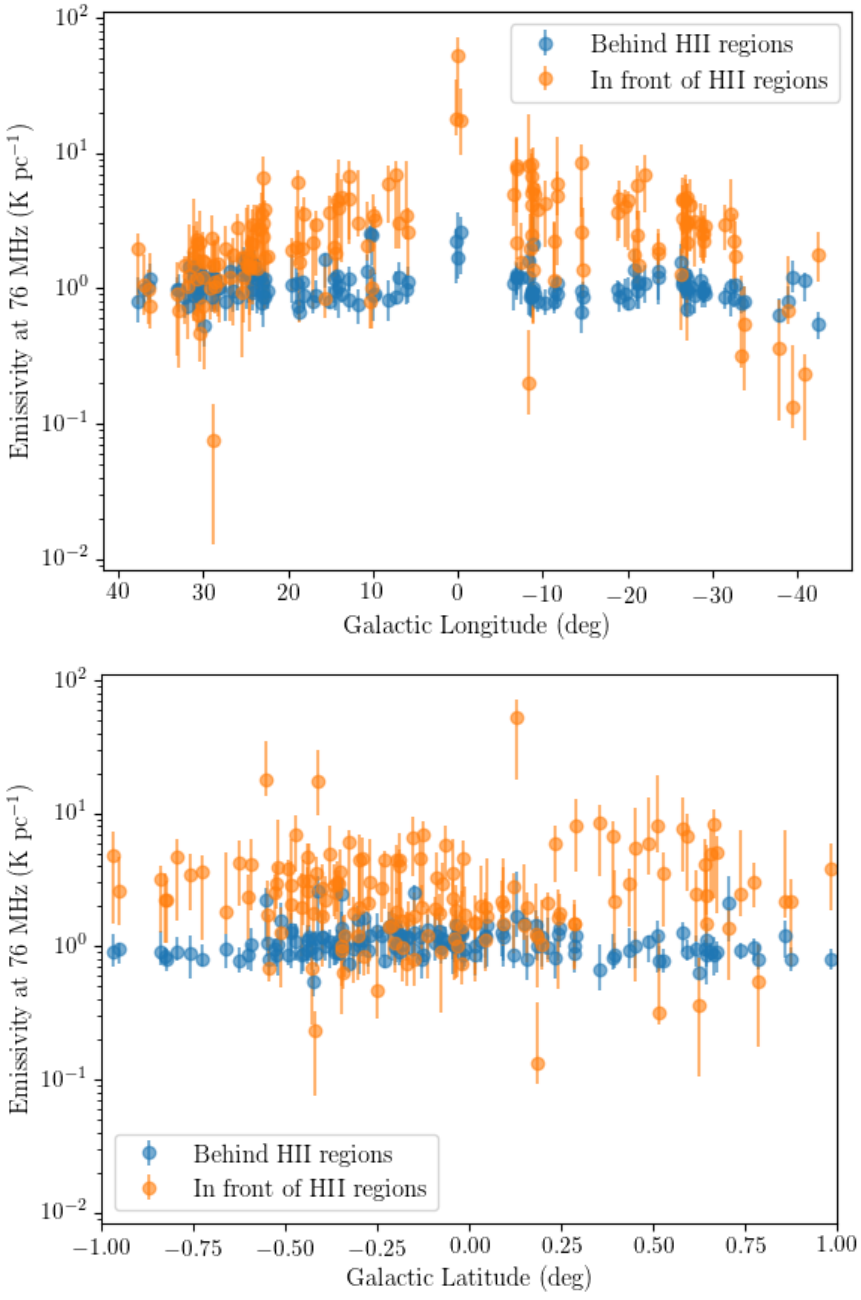

Figure 3.6: Emissivity distribution as a function of Galactic longitude (top) and Galactic latitude (bottom) at 76.2 MHz. For the distribution with Galactic latitude, we only plot the emissivities derived from HII regions in the latitude range from -1 to 1 degree.

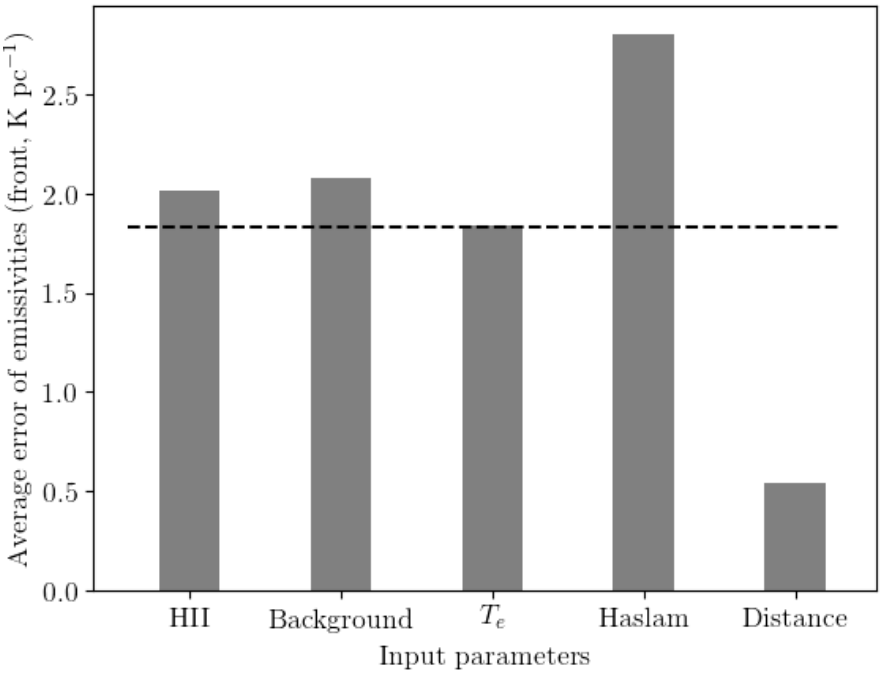

Figure 3.7: The contribution of different input parameters to the error of the emissivities at 76.2 MHz from HII regions to the Sun. The total error of the emissivity is from different input parameters which are the rms of the absorbed region (HII), the rms of the nearby region (Background), the error of the electron temperature ($T_{\rm e}$), the rms of the background region in the Haslam map (Haslam), and the error of the distance from HII region to us (Distance). Each error here is an average of all the 152 absorption measurements. "front" on the y-axis means the emissivities are averaged along the path from HII region to the Sun (in front of HII region). The error from the rms of the Haslam map contributes the most to the final error of the derived emissivities. The horizontal line indicates the average uncertainties of all the derived emissivities between the HII region and the Sun. Note that the error involved in scaling the Haslam map to our frequencies is not included here.

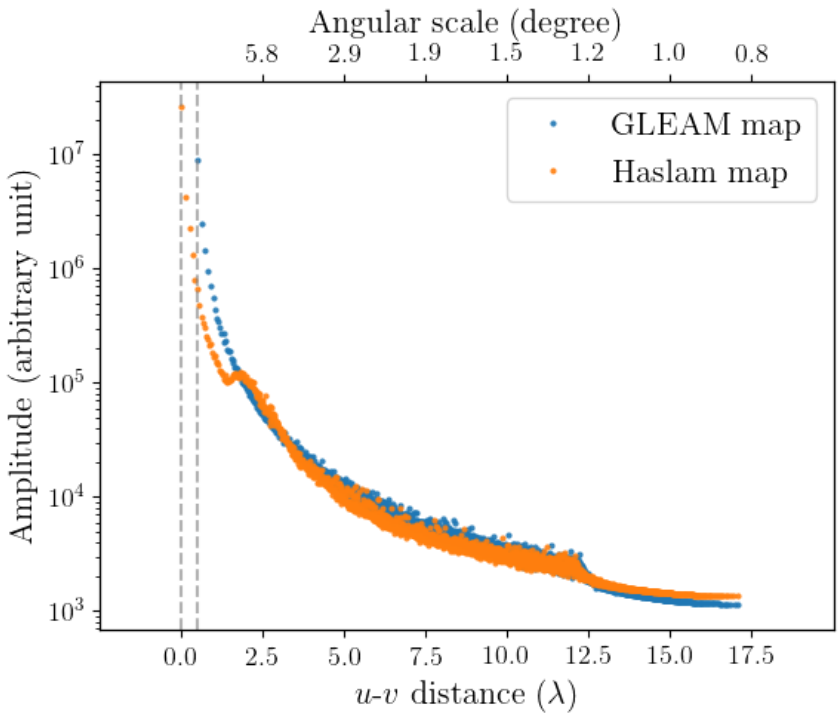

Figure 3.8: Comparison of the visibility of the GLEAM and Haslam maps in the square region centring at $l = 340°$, $b = 0°$ with a box size of 10°. The unit of the u-v distance is λ rather than kλ, because of the long wavelength of about 4 meters. The visibility data is binned (2000 bins) to show the differences clearly. The x-axis on top of the plot shows the angular size corresponding to the u-v distance. The y-axis has an arbitrary unit, but this does not affect our comparison because they should use the same factor to make it as a physical unit. The y-axis is in log scale, so the amplitude with u-v distance close to zero dominate the total difference of the two amplitudes. The minimum u-v distance of the GLEAM map is small (about 0.5λ, corresponding to an angular scale of about 30°). The u-v distance between the two vertical lines is included in the Haslam map but is not included in the GLEAM map because of the shortest baseline of 7.7 metres. The maximum u-v distance is the same for both maps because we smoothed them to the same resolution. The integrated amplitude with the u-v distance of the GLEAM map is 40% lower than that of the Haslam map in this region. This percentage varies with regions on the Galactic plane. The average percentage of all the nine regions we checked is about 60%.

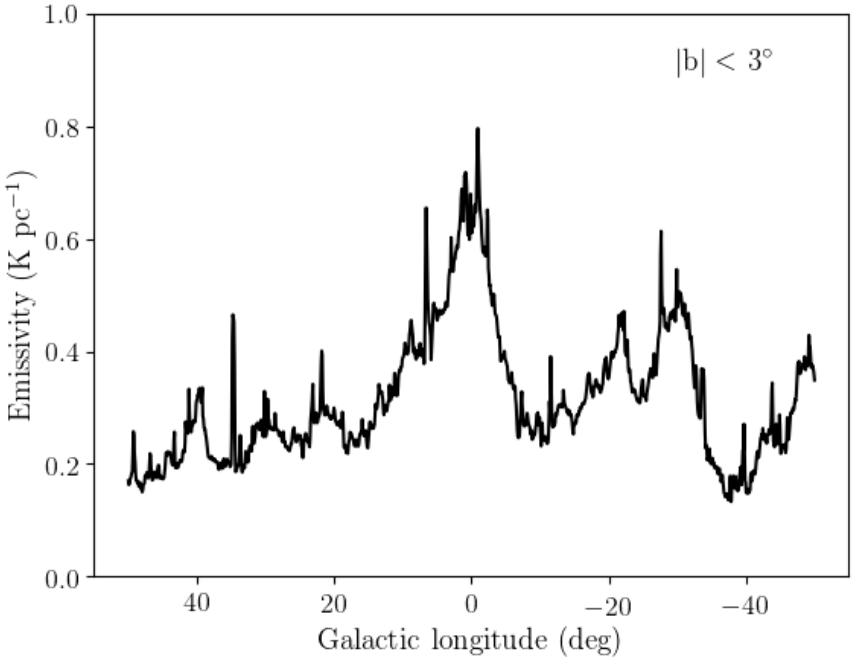

Figure 3.9: Distribution of the measured average emissivity in the GLEAM along the path from the Sun to the Galactic edge with Galactic longitude from 50° to -50° and latitude $|b| < 3^\circ$. All detected sources and diffuse emission are included in this plot. The bin size in Galactic longitude is $4\farcm85$ and in Galactic latitude is $-3^\circ < b < 3^\circ$. The Galactic centre direction has higher average emissivity compared with other directions. The existence of spiral arms possibly causes other low peaks. Note that these emissivities are directly from the GLEAM map without any correction using the Haslam map.

Chapter 4

GLEAM catalogue of Galactic HII regions

I conducted all work for this Chapter under the guidance of my supervisory panel based on the following publication in preparation.
Su, H., N. Hurley-Walker, J. P. Macquart, N. M. McClure-Griffiths, C. A. Jackson, L. Hindson, B. M. Gaensler, W. W. Tian, C. H. Jordan, A. R. Offringa, P. Hancock, S. J. Tingay, B. McKinley, A. D. Kapińska, R. B. Wayth, L. Staveley-Smith, J. Morgan, M. Johnston-Hollitt, E. Lenc, M. E. Bell, J. R. Callingham, K. S. Dwarkanath, B.-Q. For, P. Procopio, C. Wu, and Q. Zheng. Galactic HII regions catalogue in GLEAM. In preparation.

In this Chapter, we identify 588 HII regions from GLEAM data in the sky region $-50^\circ < l < 50^\circ$, $|b| < 5^\circ$ by performing HII region finding both from emission features at 215 MHz and from absorption features at 88 MHz. For each HII region, we extract its spectrum over 20 separate frequencies ranging from 72 to 231 MHz with bandwidth of 8 MHz each. These spectra help identify HII regions and obtain their spectral indices. We compare our detections with those in the *WISE* HII region catalogue. We derive the electron density, ionised gas mass, and ionising photon flux

of 66 HII regions which have turnover frequencies in the GLEAM band. We find 21 HII region candidates from the absorption features, which have similar spectra to the well-confirmed HII regions.

4.1 Data

The data used in this work is the same as those used in Chapter 3. These data products have both narrowband channels of 8 MHz bandwidth and wideband channels of 30 MHz bandwidth. The wideband data has lower rms noise level, therefore, is suitable for searching HII regions, especially those with low surface brightness. The narrowband images contain unique information at each frequency for the detected HII regions which are valuable for the spectral analysis. In this Chapter, we use the wideband 216 MHz (the highest frequency) data to find HII regions with emission features and the wideband 88 MHz (the lowest frequency) data to search for HII regions showing absorption features. After finding HII regions, we extract their spectra using the narrowband data to study their properties.

Before source finding, we estimate the background and rms of the GLEAM images using the software package named the Background and Noise Estimation tool (BANE) from the Aegean package. BANE can measure the background and rms of an image efficiently and accurately. It does this in two steps. First, for a certain given pixel, it chooses a boxcar surrounding that pixel and removes pixels with values higher than a threshold (3σ) in that box. Second, it calculates the mean and standard deviation of pixel values with the non-masked pixels in that box. Note that it does not repeat these two steps for each pixel; instead, it uses a sparse grid of pixels and then interpolates to improve the speed of calculation.

The most important parameter using BANE is the box size over which the back-

ground and rms are calculated. We set the box size to be 1.°5, which is comparable to HII regions with the largest angular scale. This choice of box size can help to calculate the background properly over the whole survey area. Fig. 4.1 shows the image, background and rms at 216 MHz in the sky region where we find HII regions. We check the derived background and rms maps by comparing to the results from several typical regions in DS9. The maps from BANE have consistent background and rms with those from source-free regions.

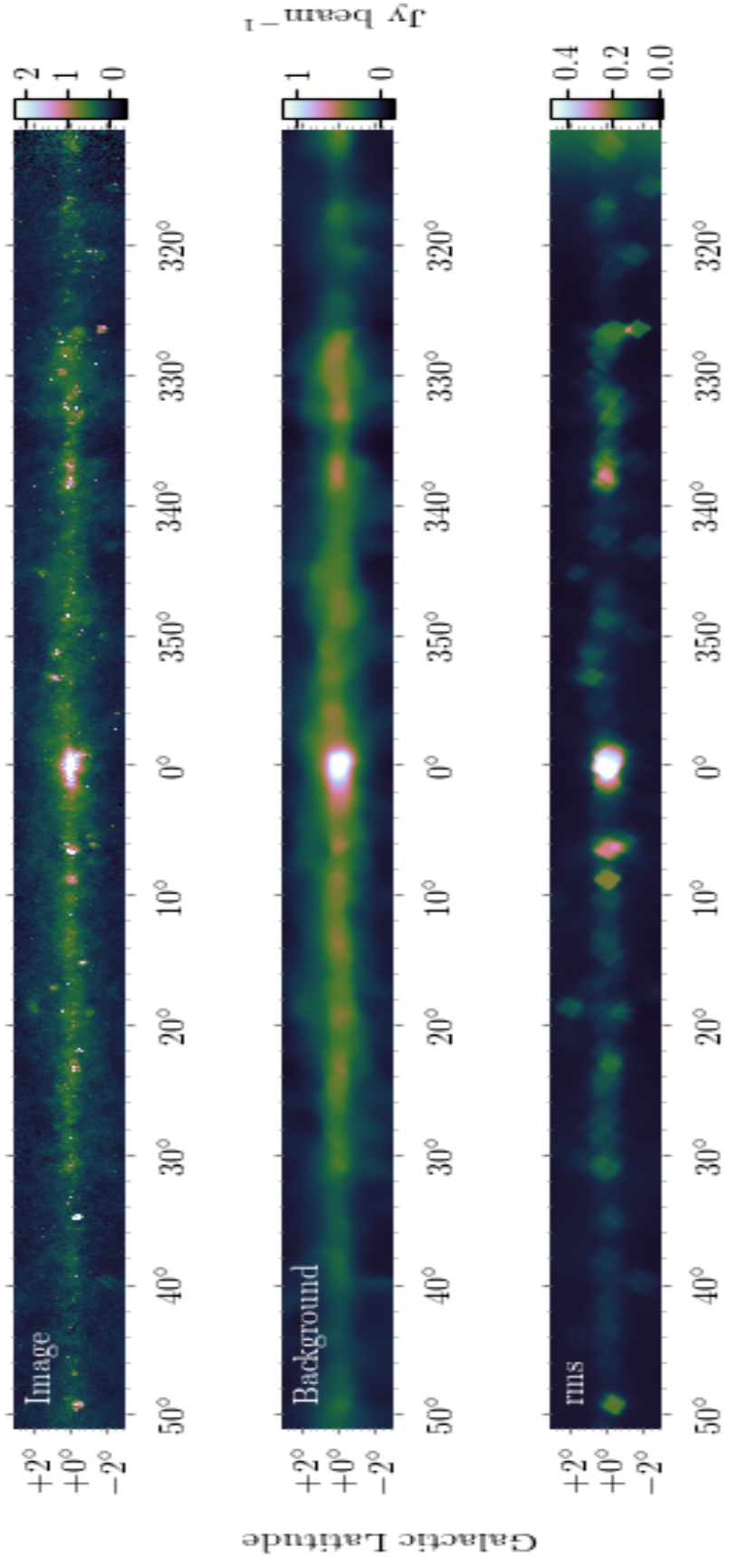

Figure 4.1: The sky brightness map of the Galactic plane from the GLEAM survey (top) and its background map (middle) and rms map. The sky map is at the frequency of 216 MHz with a bandwidth of 30 MHz. This map is adopted to find HII regions with emission features. The background and rms are calculated using BANE with a box size of 1°.5.

4.2 HII region finding

We do blind source finding in the GLEAM images for both emission and absorption features, and selecting HII regions matching sources in the *WISE* HII region catalogue. Below is a description of each step in the flowchart of our HII region finding procedure shown in Fig. 4.3.

In step 1, we estimate the background and rms for our GLEAM maps at each frequency using BANE in the Aegean package. An important parameter in BANE is the box size, above which the emission structures are thought to be background. We set the box size to be 1°.5 degrees (225 pixels in 215 MHz data) which is close to the angular size of the largest HII regions. An example of the background and rms maps is in Fig. 4.1.

In step 2, we remove the detected background maps in step 1 from the GLEAM maps. Usually, our target sources have no clear boundaries with the diffuse background emission. This step generates maps with the average background subtracted, making the source finding straightforward.

In step 3, we divide the background-removed maps generated in step 2 by their rms maps generated in step 1. This step produces signal-to-noise ratio maps for our target sky region. We use these maps to do source finding in the following steps. Doing source finding with these maps can find more reasonable boundaries for our target sources than by using the original maps, especially for extended sources with low surface brightness. The ratio maps show significant difference between the dark source region and its surrounding non-source region. Therefore, we do this step to enhance our source finding in the following steps.

In step 4, we find all sources with emission features at 231 MHz with bandwidth

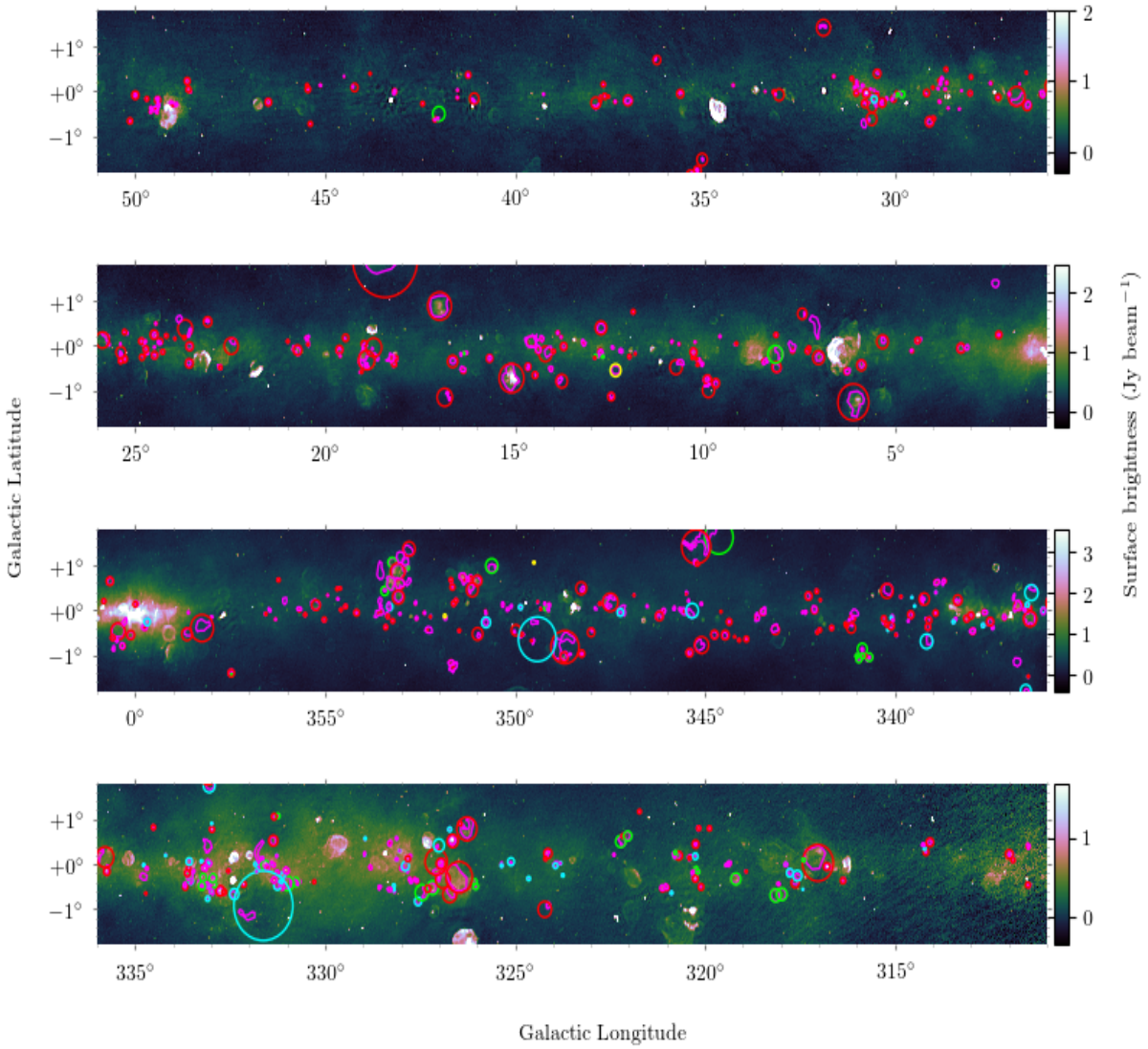

Figure 4.2: Image of the Galactic plane observed in the GLEAM in the range of $-50° < l < 50°$, $|b| < 2°$. Identified HII regions are marked by pink polygons and the cross-matched sources in the *WISE* HII region catalogue are in circles. The red, green, and cyan circles show the locations of the known, group, and candidate HII regions, respectively.

of 30 MHz using Findclumps from the Starlink[1] package. We choose the wide-band data because it has higher signal-to-noise ratio compared with narrow-band data. The shape of output sources and the method of source finding are two important parameters in Findclumps. We set the source shape to be polygonal for accurately describing the boundary of sources with irregular shapes. We set the method of source finding in the Findclumps algorithm to be FellWalker[2]. The FellWalker method is designed to find sources of irregular shape, which is suitable for finding the extended sources with complex shapes on the Galactic plane. FellWalker perform source finding by searching for peaks along the line of greatest gradient and have pixels along the route to the clump associate with the peak (Berry, 2015). We note that, although Aegean is also a powerful and efficient tool for source finding, it can only fit elliptical Gaussian shapes to sources, and can not match irregular shapes for sources with complex structures. We therefore rely only on the Findclumps algorithm to extract HII region boundaries from our image data.

In step 5, we find all sources with absorption features using the 88 MHz wideband data. Some HII regions are optically thick and only show absorption features at all the GLEAM frequencies. We aim to find such HII regions not found in step 4 in this step. The low frequency map of 88 MHz shows more absorption features than those in the high frequency map at 218 MHz. These absorbed regions have pixels with negative values in our signal-to-noise ratio map because they have lower surface brightness than that of their local background. To find sources with absorption features, firstly, we remove all emission features in the background subtracted image by setting positive pixel values to be NaN. Secondly, we set negative pixel values to be their additive inverse. Then, we can perform normal source finding using Findclumps. All

[1]http://starlink.eao.hawaii.edu/starlink

[2]http://starlink.eao.hawaii.edu/starlink/fellwalker.html

absorption features are found in this step. However, we also include absorption features caused by other types of sources, such as pulsar wind nebulae. We will select our target HII regions in the following steps.

In step 6, we cross-match our detected sources from step 4 and 5 with the *WISE* HII region catalogue. HII regions are extended sources and have irregular shapes, which need a complex algorithm for cross-matching, so we do the cross-matching by eye. We remove those sources with no corresponding counterpart in the *WISE* HII region catalogue. HII regions with high surface brightness temperature can match well with those in the *WISE* catalogue. Other sources did not match well mainly because different sources are not well separated in space, i.e., multiple sources are identified as one source in our source finding due to the fact that many sources are connected with each other. We separate these sources by hand using the *WISE* catalogue as a prior. Nearly half of the sources have their edges redefined as a result. Some source regions are defined by absorption features only, because of the lack of emission features or because the emission region is polluted by synchrotron emission. For extended HII regions with their absorption region and emission region not perfectly match, we join these two regions as our final HII region. In this case, the defined region may not perfectly match the emission feature at 215 MHz.

In step 7, we extract spectra of the sources from step 6 using our 8 MHz narrow-band data. We use narrow band data to maximise the spectrum information for our detected sources.

In step 8, we remove sources with non-power-law spectra to obtain our HII region catalogue. HII regions are thermal sources possibly having turnover frequencies in the GLEAM band. An HII region has optical depth $\tau = 1$ at its turnover frequency, below which frequency it is optically thick and above that frequency it is optically thin (Mezger and Henderson, 1967). Therefore, we only select source with integrated flux

density increasing with frequency or increasing first and then decreasing. We use the following broken power law spectrum to fit with the spectra of all cross-matched HII regions

$$\begin{aligned} S &= S_0 + S_1(\nu/\nu_0)^{\alpha},\ (\nu \leq \nu_0) \\ S &= S_0 + S_1(\nu/\nu_0)^{\beta},\ (\nu > \nu_0) \end{aligned} \tag{4.1}$$

where S is the integrated flux density at frequency ν, and ν_0 is the turnover frequency of the HII region (Kurtz, 2005). If the deduced value of ν_0 is outside of the GLEAM frequency range (i.e. $\nu_0 < 91.5$ MHz or $\nu_0 > 211.8$ MHz), we designate it as having no detected turnover frequency. Sources whose spectra do not fit well with this power-law equation are removed in our catalogue. These removed sources may still be HII regions, but they are excluded because they are not good detections in our current observations because they are possibly affected by the overlapping supernova remnant or diffuse synchrotron emission. In this final step, we find 588 HII regions cross-matched with the *WISE* HII region catalogue which have a power law spectrum.

4.3 Results

We identified 588 HII regions listed in Table A.1 using the GLEAM data. We extracted their parameters including their coordinates, flux densities, spectral indices and turnover frequencies. Fig. 4.2 shows their shapes and position on the Galactic plane. Fig. 4.4 shows the images and spectra of two typical HII regions detected in our observations.

For the 66 HII regions whose turnover frequencies are able to be detected, we further calculated their EM, electron density (n_e), the mass of the ionized gas in the HII region, and the total ionizing photon flux of the Lyman continuum (see Table. 4.1). The distance and the electron temperature of the HII region in Table. 4.1 are found in

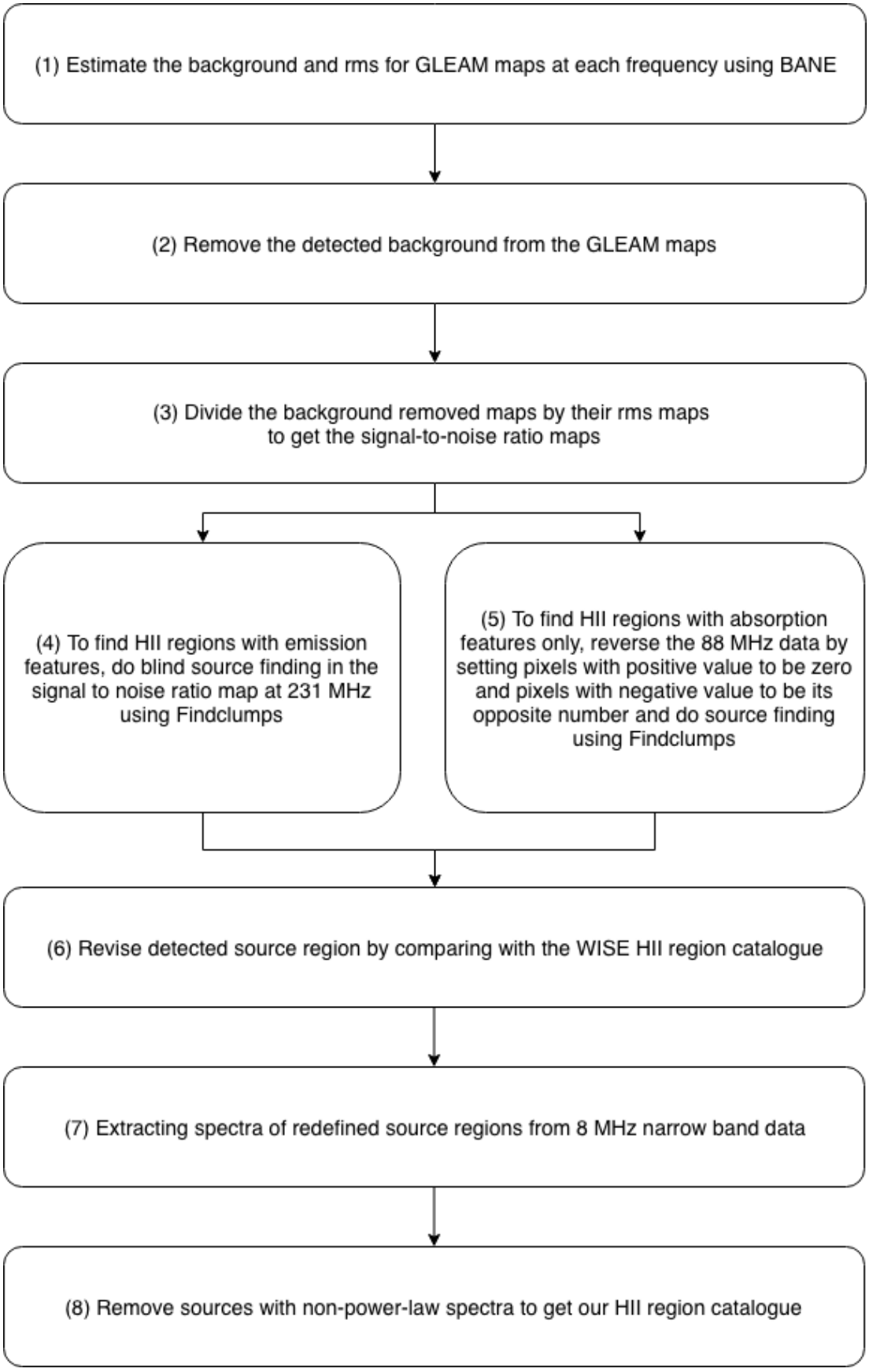

Figure 4.3: Steps of HII region finding.

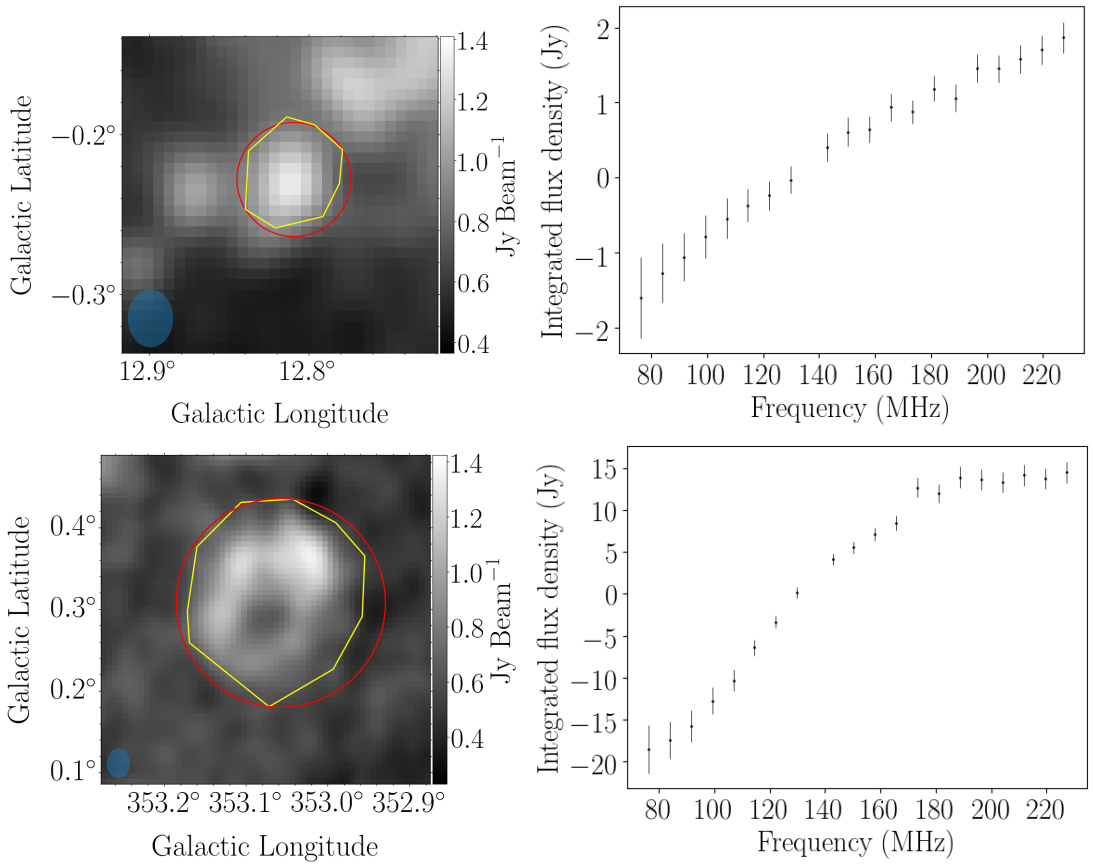

Figure 4.4: Images and spectra of two typical HII region G012.820−00.238 (top two panels) and G353.076+00.287 (bottom two panels). Images are at 216 MHz with a beam size of $2\overset{\circ}{.}2 \times 1\overset{\circ}{.}7$ indicated by blue ellipses. The yellow polygon shows the HII region in our detection and the red circle indicates the matched HII region in the *WISE* catalogue. Spectra are extracted from the polygon regions. The spectra on the right shows how the flux density varies for each of the identified HII regions; the lower panel indicates that G353.076+00.287 has a turnover frequency of ~ 170 MHz.

the literature (Anderson et al., 2014; Balser et al., 2015; Hou and Han, 2014) and the online *WISE* HII region catalogue (in priority). Table 4.1 contains HII regions with turnover frequencies detected in the GLEAM survey, and Table 4.2 contains the HII regions newly found the GLEAM survey using their spectra.

HII regions would not be detected in the GLEAM survey if their angular sizes are smaller than 2 arcmin or their brightness temperature is less than 1000 Kelvin at the frequency of near 100 MHz. Future surveys with improved angular resolutions and surface brightness sensitivities may find more HII regions with absorption features.

The histograms of the derived parameters are shown in Fig. 4.5. The spectral indices derived in this work are consistent with those in Hindson et al. (2016); both are in the range of -0.2$\sim$2.0. Hindson et al. (2016) find turnover frequencies of 61 HII regions using the GLEAM 30 MHz wideband data from 88 to 216 MHz, the Molonglo Galactic Plane Survey (MGPS, Green et al. 1999; Murphy et al. 2007) at 843 MHz, and the SGPS at 1420 MHz. The turnover frequencies in their sample are higher than those in this work by a factor of $\sim$5. The HII regions in Hindson et al. (2016) are in the Galactic longitude range from 284 to 340 degrees, while the HII regions in our sample are in wider ranges from 5 to 50 degrees and from 311 to 349 degrees. The overlapped range is from 311 to 349 degrees, with only five overlapped HII regions as below: G316.796-00.056 (172.5 MHz) vs. G316.81-0.05 (680 MHz); G320.248+00.442 (159.2 MHz) vs. G320.28+0.43 (410 MHz); G333.093+01.966 (143.2 MHz) vs. G333.04+2.03 (820 MHz); G337.652-00.050 (153.7 MHz) vs. G337.63-0.07 (290 MHz); G338.934-00.067 (174.0 MHz) vs. G338.95-0.08 (1100 MHz).

Fig. 4.6 shows the background subtracted spectra of the cross-matched HII region G333.093+01.966 with turnover frequency of 143.2 MHz in this work and HII region G333.04+2.03 with turnover frequency of 820 MHz in Hindson et al. (2016). The main reason for the difference is that Hindson et al. (2016) used data from a first-pass

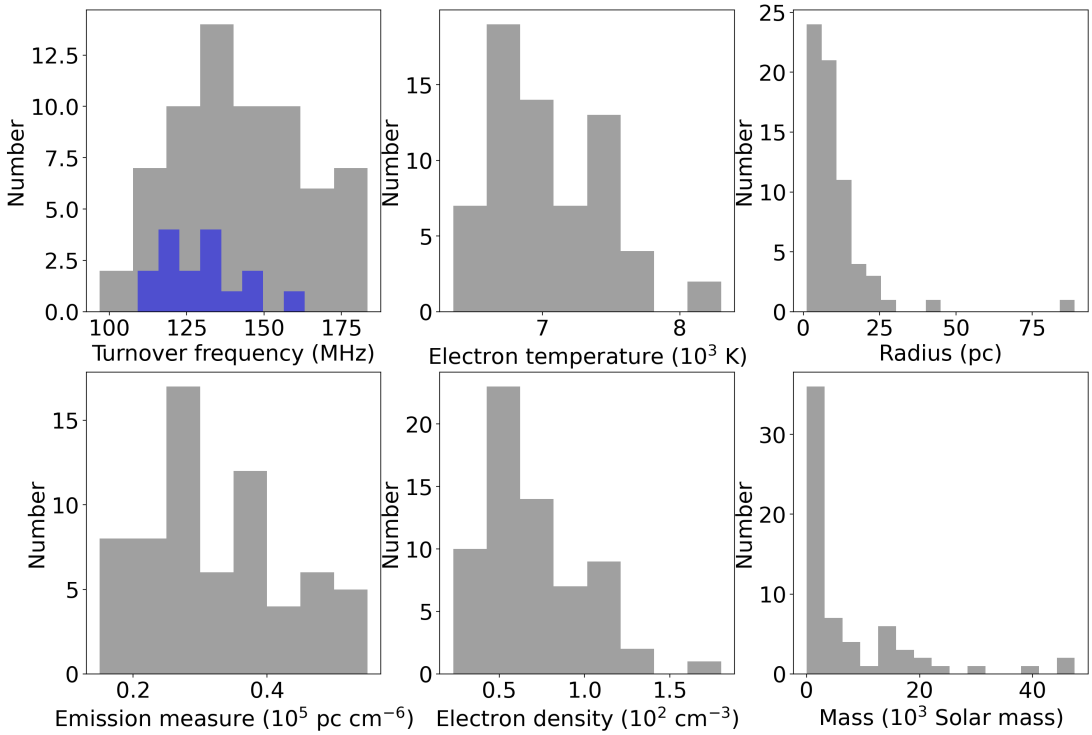

Figure 4.5: The histograms of the turnover frequency, electron temperature, radius, emission measure, electron density, mass of HII regions with turnover frequency detected in this work crossmatched with the *WISE* HII regions (grays); the histogram of the turnover frequency of HII regions detected in GLEAM only without crossmatched with *WISE* HII regions (blue). The mass of HII region G028.746+03.458 and G026.797-00.113 are filtered because they are larger than those of others by a factor of about two.

processing of GLEAM without multi-scale clean, while the data used in this work is from Hurley-Walker et al. (2019) and that had more thorough multi-scale cleaning and flux density scale calibration. The different background subtraction methods also contribute to the spectrum difference. We use the source-surrounding region to estimated the background when we do the background subtraction of HII region spectrum, while Hindson et al. (2016) used BANE (Hancock et al., 2012). HII region G333.093+01.966 is visible at high frequencies in the GLEAM survey, through its surface brightness is close to that of its background region. Calculating background using BANE may not be accurate over the Galactic plane with different scales of structures. Re-assessing the background for HII region spectra could be future work. If the turnover frequency is at frequencies outside of the GLEAM frequency range, the GLEAM data only is not going to constrain the turnover frequency because of missing the higher frequency data. If it is within the band then the GLEAM produce give a better result with improved spectral resolution.

We find 21 HII region candidates in the GLEAM survey (see Table 4.2). These candidates have similar spectra to the well confirmed HII regions in Table 4.1. We derive their flux densities, turnover frequencies, and spectral indices. These candidates show obvious absorption features, but nearly no emission features in the GLEAM survey. They do not show emission features in the *WISE* and Spitzer observations either. RRL observations are required to identify them to be HII regions. The background determination is described in step 1 of HII region finding steps. We use the (reduced) chi-squared test to compare the goodness of absorption spectrum fitting.

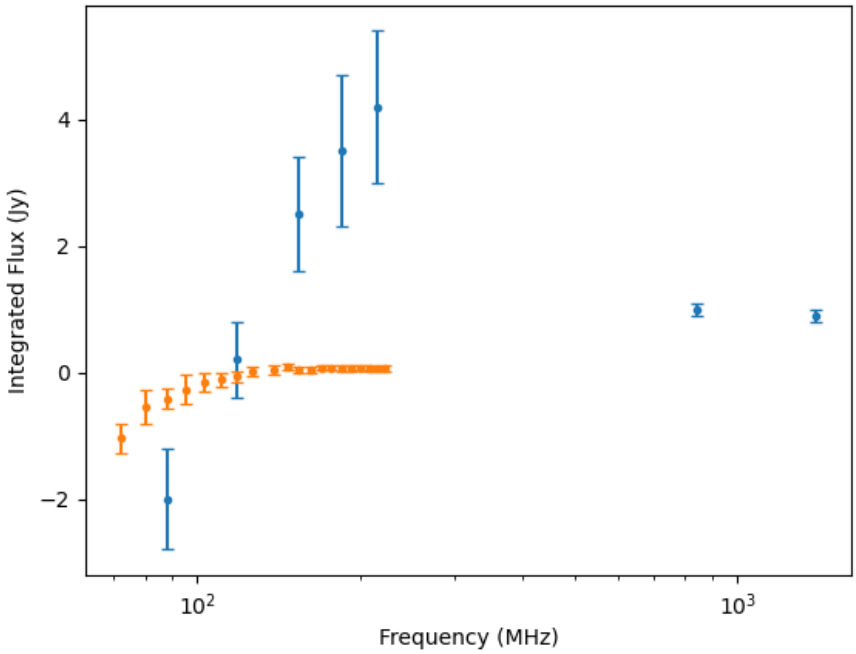

Figure 4.6: The background-subtracted spectra of the matched HII region G333.093+01.966 with turnover frequency of 143.2 MHz in this work (orange) and HII region G333.04+2.03 with turnover frequency of 820 MHz in Hindson et al. (2016) (blue).

Table 4.1: Physical properties of HII regions with turnover frequencies detected. *Notes*. Col. (1): the name of the HII region from the *WISE* HII region catalogue. Col. (2): the turnover frequency of the HII region. Col. (3): the distance to the HII region. Col. (4): the electron temperature of the HII region estimated from the relation between the electron temperature and the Galactocentric radius $T_e = (4928 \pm 277) + (385 \pm 29)\ R_{\rm gal}$ from Balser et al. (2015). Col. (5): the radius of the HII region in unit of pc. Col. (6): the emission measure of the HII region. Col. (7): the electron density in the HII region. Col. (8): the mass of the ionized gas in the HII region. Col. (9): the total ionizing photon flux of the Lyman continuum.

HII region	$\nu_{\rm t}$	Distance	$T_{\rm e}$	Radius	EM	$n_{\rm e}$	Mass	$N_{\rm Ly}$
	MHz	kpc	$\times 10^3$ K	pc	10^5 pc cm^{-6}	10^2 cm^{-3}	10^3 M$_\odot$	$10^{48} s^{-1}$
(1)	(2)	(3)	(4)	(5)	(6)	(7)	(8)	(9)
G005.887−00.443	144.39±9.19	3.0±0.2	7.05±0.32	6.34±0.42	0.33±0.05	0.72±0.08	1.90±0.25	0.31±0.02
G012.474−01.140	139.34±26.10	4.2±0.4	6.66±0.31	6.70±0.64	0.28±0.11	0.65±0.05	2.02±0.26	0.12±0.01
G012.742+00.390	121.78±10.42	2.6±0.7	7.23±0.33	6.77±1.82	0.24±0.05	0.59±0.03	1.90±0.52	0.10±0.03
G014.207−00.193	158.27±4.98	3.6±0.5	6.89±0.31	10.61±1.47	0.39±0.03	0.60±0.07	7.46±1.32	0.40±0.06
G015.097−00.729	167.94±13.86	2.0±0.1	7.47±0.34	11.36±0.57	0.49±0.09	0.65±0.10	9.94±1.65	3.33±0.17
G016.285−00.171	137.16±54.47	4.1±0.4	6.74±0.31	2.25±0.22	0.28±0.23	1.11±0.05	0.13±0.01	0.09±0.01

Continued on next page

HII region	$\nu_{\rm t}$	Distance	$T_{\rm e}$	Radius	EM	$n_{\rm e}$	Mass	$N_{\rm Ly}$
	MHz	kpc	$\times 10^3$ K	pc	10^5 pc cm^{-6}	10^2 cm^{-3}	10^3 M$_\odot$	$10^{48} s^{-1}$
(1)	(2)	(3)	(4)	(5)	(6)	(7)	(8)	
G016.424−00.201	155.70±47.01	3.9±0.4	6.81±0.31	1.13±0.12	0.37±0.23	1.80±0.05	0.03±0.00	0.08±0.01
G016.648−00.357	162.10±6.15	3.9±0.4	6.81±0.31	9.17±0.94	0.40±0.04	0.66±0.07	5.27±0.78	0.14±0.02
G016.856−01.156	171.99±10.69	2.2±0.6	7.40±0.33	7.66±2.09	0.51±0.07	0.81±0.04	3.78±1.05	0.10±0.03
G016.993+00.873	150.92±9.49	2.6±0.5	7.26±0.33	14.17±2.72	0.37±0.05	0.51±0.04	15.14±3.18	3.06±0.59
G018.144−00.281	108.91±66.14	4.2±0.4	6.74±0.31	3.73±0.35	0.17±0.22	0.68±0.05	0.36±0.04	0.37±0.04
G018.187−00.415	123.07±60.90	3.6±0.4	6.93±0.32	3.94±0.44	0.23±0.24	0.76±0.05	0.48±0.06	0.27±0.03
G018.253−00.298	130.30±14.03	4.0±0.4	6.80±0.31	3.98±0.40	0.25±0.06	0.80±0.05	0.52±0.06	0.65±0.07
G018.881−00.493	149.53±15.12	4.6±0.4	6.62±0.31	2.43±0.21	0.32±0.07	1.16±0.06	0.17±0.02	0.45±0.04
G018.978+00.030	153.25±9.71	4.0±0.4	6.81±0.31	5.33±0.53	0.35±0.05	0.82±0.06	1.28±0.16	0.26±0.03
G019.629−00.095	111.75±23.58	11.7±0.4	6.73±0.31	18.55±0.63	0.18±0.08	0.31±0.15	20.56±9.72	3.18±0.13
G020.457+00.021	113.84±17.08	11.1±0.4	6.59±0.30	5.60±0.20	0.18±0.06	0.57±0.14	1.03±0.26	0.95±0.07

Continued on next page

HII region	$\nu_{\rm t}$	Distance	$T_{\rm e}$	Radius	EM	$n_{\rm e}$	Mass	$N_{\rm Ly}$
	MHz	kpc	$\times 10^3$ K	pc	10^5 pc cm^{-6}	10^2 cm^{-3}	10^3 M$_\odot$	$10^{48} s^{-1}$
(1)	(2)	(3)	(4)	(5)	(6)	(7)	(8)	
G020.481+00.168	124.44±17.55	13.7±0.5	7.42±0.33	10.30±0.38	0.26±0.08	0.50±0.14	5.64±1.57	1.77±0.11
G020.728−00.105	129.36±10.02	11.8±0.4	6.81±0.31	22.71±0.77	0.25±0.04	0.33±0.15	40.12±18.28	9.57±0.33
G023.097+00.527	176.20±11.55	2.4±0.5	7.38±0.33	4.58±0.96	0.53±0.08	1.07±0.04	1.07±0.23	0.04±0.01
G023.572−00.020	129.41±14.88	5.5±0.4	6.51±0.30	9.36±0.68	0.23±0.06	0.50±0.07	4.24±0.68	0.83±0.06
G023.581−00.400	134.96±18.58	5.4±0.4	6.53±0.30	9.56±0.71	0.26±0.08	0.52±0.07	4.68±0.72	0.28±0.03
G024.347+00.088	167.85±27.46	9.2±0.7	6.39±0.30	11.06±0.84	0.39±0.14	0.60±0.07	8.36±1.14	0.53±0.07
G024.493−00.219	179.67±19.77	9.7±0.5	6.48±0.30	13.87±0.72	0.46±0.11	0.58±0.10	15.98±2.86	2.17±0.13
G024.507+00.239	182.63±18.20	8.8±2.8	6.35±0.30	15.74±5.01	0.47±0.10	0.54±0.03	21.98±7.08	2.27±0.72
G026.521−00.317	120.13±44.92	9.1±0.6	6.50±0.30	17.51±1.15	0.20±0.16	0.34±0.08	18.78±4.41	0.91±0.08
G026.797−00.113	138.52±11.35	10.8±0.4	6.85±0.31	41.00±1.52	0.29±0.05	0.27±0.14	189.54±98.56	5.89±0.23
G026.984−00.062	125.64±64.01	10.2±0.4	6.72±0.31	7.66±0.30	0.23±0.25	0.55±0.13	2.55±0.60	0.79±0.07

Continued on next page

HII region	$\nu_{\rm t}$	Distance	$T_{\rm e}$	Radius	EM	$n_{\rm e}$	Mass	$N_{\rm Ly}$
	MHz	kpc	$\times 10^3$ K	pc	10^5 pc cm^{-6}	10^2 cm^{-3}	10^3 M$_\odot$	$10^{48} s^{-1}$
(1)	(2)	(3)	(4)	(5)	(6)	(7)	(8)	
G027.281−00.132	114.61±46.70	5.5±0.5	6.62±0.31	6.53±0.59	0.19±0.16	0.53±0.06	1.54±0.21	0.35±0.04
G028.746+03.458	154.89±8.33	15.2±0.8	8.30±0.38	88.87±4.68	0.47±0.06	0.23±0.10	1678.18±751.56	22.15±1.17
G030.338−00.252	142.47±44.48	8.2±2.8	6.61±0.30	14.75±5.04	0.29±0.19	0.45±0.02	14.80±5.08	1.05±0.36
G030.795−00.275	162.95±21.21	7.3±0.5	6.60±0.30	10.76±0.74	0.39±0.11	0.60±0.08	7.73±1.10	1.16±0.09
G031.016−00.039	157.20±17.67	8.0±2.8	6.64±0.31	8.73±3.05	0.36±0.09	0.64±0.02	4.43±1.56	0.44±0.16
G033.051−00.078	138.39±31.27	7.1±1.0	6.71±0.31	16.04±2.26	0.28±0.13	0.42±0.04	17.88±2.97	0.37±0.06
G037.028−00.202	139.58±21.08	6.8±1.2	6.90±0.31	13.85±2.44	0.30±0.10	0.46±0.03	12.72±2.41	0.29±0.06
G037.677+00.155	157.91±20.47	6.7±0.1	6.93±0.32	6.33±0.09	0.39±0.11	0.78±0.34	2.06±0.88	0.18±0.03
G046.495−00.241	176.59±20.78	4.8±0.1	7.34±0.33	6.93±0.14	0.53±0.13	0.87±0.24	3.01±0.83	0.50±0.02
G048.922−00.285	134.37±22.52	5.3±0.2	7.40±0.33	2.57±0.10	0.30±0.11	1.08±0.13	0.19±0.02	1.10±0.05
G049.002−00.303	150.70±18.24	5.3±0.2	7.40±0.33	2.88±0.11	0.38±0.10	1.15±0.13	0.28±0.03	1.10±0.05

Continued on next page

HII region	$\nu_{\rm t}$	Distance	$T_{\rm e}$	Radius	EM	$n_{\rm e}$	Mass	$N_{\rm Ly}$
	MHz	kpc	$\times 10^3$ K	pc	10^5 pc cm^{-6}	10^2 cm^{-3}	10^3 M$_\odot$	$10^{48} s^{-1}$
(1)	(2)	(3)	(4)	(5)	(6)	(7)	(8)	
G049.051−00.255	116.88±25.12	5.3±0.2	7.40±0.33	3.39±0.13	0.22±0.10	0.81±0.13	0.33±0.06	0.99±0.04
G049.407−00.193	127.56±59.11	5.3±0.2	7.41±0.33	7.40±0.28	0.27±0.26	0.60±0.13	2.54±0.56	0.55±0.03
G049.997−00.087	133.13±17.99	5.5±0.1	7.43±0.34	8.80±0.16	0.30±0.09	0.58±0.28	4.10±1.95	0.21±0.02
G311.489+00.394	142.60±19.87	5.6±0.1	7.38±0.33	5.02±0.09	0.34±0.10	0.82±0.28	1.08±0.37	0.58±0.06
G316.796−00.056	172.50±22.47	2.5±0.6	7.58±0.34	3.77±0.90	0.53±0.15	1.18±0.03	0.65±0.16	0.55±0.13
G320.248+00.442	159.23±67.93	2.1±0.6	7.63±0.34	3.30±0.94	0.45±0.40	1.17±0.02	0.43±0.12	0.04±0.01
G320.692+00.185	101.57±8.13	12.8±0.7	8.10±0.37	21.16±1.16	0.19±0.03	0.30±0.10	29.31±9.52	5.56±0.31
G324.135+00.236	175.80±101.10	6.9±0.1	6.85±0.31	12.91±0.19	0.48±0.58	0.61±0.35	13.54±7.70	1.11±0.02
G326.270+00.783	138.89±3.71	3.0±0.4	7.33±0.33	13.80±1.84	0.32±0.03	0.48±0.07	13.08±2.60	1.07±0.14
G326.643+00.514	126.78±13.18	3.0±0.4	7.32±0.33	7.62±1.02	0.26±0.06	0.59±0.04	2.69±0.41	1.32±0.18
G330.673−00.388	158.52±74.92	4.0±0.4	7.00±0.32	2.19±0.22	0.39±0.39	1.34±0.05	0.15±0.02	0.14±0.02

Continued on next page

HII region	$\nu_{\rm t}$	Distance	$T_{\rm e}$	Radius	EM	$n_{\rm e}$	Mass	$N_{\rm Ly}$
	MHz	kpc	$\times 10^3$ K	pc	10^5 pc cm^{-6}	10^2 cm^{-3}	10^3 M$_\odot$	$10^{48} s^{-1}$
(1)	(2)	(3)	(4)	(5)	(6)	(7)	(8)	
G331.338−00.365	143.44±20.70	4.1±0.4	6.96±0.32	4.13±0.40	0.32±0.10	0.88±0.05	0.64±0.07	0.73±0.07
G332.657−00.622	183.43±14.93	3.3±0.4	7.15±0.32	3.49±0.42	0.55±0.10	1.26±0.05	0.55±0.07	0.47±0.06
G332.762−00.595	124.23±10.09	3.8±0.4	7.01±0.32	7.57±0.80	0.24±0.04	0.56±0.05	2.52±0.36	1.41±0.15
G333.093+01.966	143.16±9.01	1.6±0.6	7.67±0.35	5.73±2.15	0.36±0.05	0.79±0.04	1.55±0.58	0.05±0.02
G337.652−00.050	153.66±16.01	11.8±0.4	6.89±0.31	11.27±0.38	0.36±0.08	0.57±0.15	8.40±2.23	5.79±0.21
G338.114−00.193	121.79±21.21	11.9±0.4	6.90±0.31	15.63±0.53	0.22±0.08	0.38±0.15	14.93±5.93	8.63±0.30
G338.706+00.645	130.81±26.79	4.3±0.4	6.76±0.31	3.77±0.35	0.25±0.11	0.82±0.05	0.45±0.05	0.26±0.03
G338.911+00.615	148.72±22.16	4.4±0.4	6.73±0.31	4.82±0.44	0.33±0.10	0.82±0.06	0.96±0.11	0.73±0.07
G338.934−00.067	174.03±29.77	3.2±0.4	7.10±0.32	3.74±0.47	0.49±0.18	1.14±0.04	0.62±0.08	0.13±0.02
G339.134−00.377	126.72±8.25	3.0±0.4	7.16±0.32	3.74±0.50	0.25±0.04	0.82±0.05	0.45±0.07	0.13±0.02
G339.233+00.243	109.00±39.22	11.2±0.4	6.64±0.31	26.28±0.94	0.17±0.13	0.25±0.14	47.43±26.40	2.06±0.09

Continued on next page

HII region	ν_t	Distance	T_e	Radius	EM	n_e	Mass	N_{Ly}
	MHz	kpc	$\times 10^3$ K	pc	10^5 pc cm^{-6}	10^2 cm^{-3}	10^3 M$_\odot$	$10^{48} s^{-1}$
(1)	(2)	(3)	(4)	(5)	(6)	(7)	(8)	
G339.585−00.104	109.67±96.57	13.3±0.5	7.28±0.33	19.34±0.73	0.19±0.36	0.32±0.13	23.62±10.01	1.93±0.11
G340.780−01.022	96.90±62.20	2.3±0.6	7.38±0.33	1.43±0.37	0.15±0.20	1.03±0.02	0.03±0.01	0.03±0.01
G345.651+00.015	150.38±58.65	15.2±0.9	7.73±0.35	7.22±0.43	0.40±0.33	0.75±0.08	2.92±0.37	1.56±0.13
G348.691−00.826	160.70±15.65	3.4±0.3	6.93±0.32	21.89±1.93	0.40±0.09	0.43±0.06	46.52±7.82	0.85±0.07
G348.710−01.044	132.59±5.04	3.4±0.3	6.93±0.32	6.40±0.56	0.27±0.03	0.65±0.08	1.75±0.26	0.85±0.08

Table 4.2: HII region candidates in the GLEAM survey. *Notes*. Col. (1): the name of the HII region candidate. Col. (2): the right ascension of the source centre. Col (3): the declination of the source centre. Col. (4): the radius of the HII region candidate. Col. (5): the integrated flux density of the HII region candidate including background at the frequency of 227.2 MHz. Col. (7): the integrated flux density of the background near the HII region candidate at 227.2 MHz. Col. (8): the turnover frequency of the HII region candidate. Col. (9): the spectral index α. Col. (10): the spectral index β. Col. (11): the goodness of fitting.

Name	RA	DEC	Radius	flux_img	flux_bkg	ν_0	α	β	Goodness
	deg	deg	arcmin	Jy	Jy	MHz			
(1)	(2)	(3)	(4)	(5)	(6)	(7)	(8)	(9)	(10)
G000.283−00.253	266.82	-28.83	3.2	7.20 ± 0.36	8.97 ± 0.36	$147.7^{+11.9}_{-11.5}$	$2.2^{+1.6}_{-1.2}$	$0.2^{+0.2}_{-0.2}$	2.2
G002.359+01.384	266.46	-26.20	1.3	0.16 ± 0.06	2.70 ± 0.06	$136.3^{+7.8}_{-12.2}$	$1.2^{+1.5}_{-0.7}$	$0.0^{+0.1}_{-0.1}$	20.5
G003.105−00.045	268.25	-26.30	3.8	0.92 ± 0.07	2.80 ± 0.07	$121.9^{+25.7}_{-28.6}$	$1.8^{+2.0}_{-1.3}$	$0.0^{+0.1}_{-0.3}$	9.8
G007.164+00.425	270.05	-22.55	5.9	0.16 ± 0.10	10.33 ± 0.10	$109.2^{+10.6}_{-11.5}$	$2.3^{+1.7}_{-1.4}$	$0.1^{+0.2}_{-0.1}$	13.1
G023.850+00.588	278.16	-7.80	3.5	0.71 ± 0.09	2.85 ± 0.09	-	$0.7^{+1.6}_{-0.6}$	-	11.9
G030.823−00.715	282.53	-2.20	13.0	0.86 ± 0.10	2.37 ± 0.10	$120.4^{+25.9}_{-16.4}$	$1.9^{+1.9}_{-1.3}$	$0.1^{+0.2}_{-0.2}$	16.4

Continued on next page

Name	RA	DEC	Radius	flux_img	flux_bkg	ν_0	α	β	Goodness
	deg	deg	arcmin	Jy	Jy	MHz			
(1)	(2)	(3)	(4)	(5)	(6)	(7)	(8)	(9)	(10)
G331.600+00.247	242.76	-51.16	2.2	4.11 ± 0.09	10.16 ± 0.09	$127.6^{+33.4}_{-47.1}$	$1.8^{+1.9}_{-1.1}$	$0.3^{+0.3}_{-0.2}$	8.6
G333.108+00.411	244.31	-50.00	1.7	0.41 ± 0.08	8.56 ± 0.08	-	$0.2^{+0.3}_{-0.1}$	-	12.2
G334.780−00.280	246.89	-49.31	4.1	4.14 ± 0.08	3.73 ± 0.08	$118.6^{+9.1}_{-9.0}$	$2.0^{+1.7}_{-1.1}$	$0.2^{+0.1}_{-0.1}$	4.7
G336.789−01.152	249.93	-48.43	4.0	1.00 ± 0.07	3.79 ± 0.07	$130.9^{+18.3}_{-18.4}$	$2.2^{+1.7}_{-1.3}$	$0.3^{+0.3}_{-0.2}$	8.9
G336.875+00.282	248.44	-47.40	5.3	1.07 ± 0.09	1.37 ± 0.09	$131.8^{+37.0}_{-76.2}$	$1.6^{+2.0}_{-1.2}$	$0.1^{+0.2}_{-0.4}$	9.1
G339.192−00.192	251.20	-45.98	5.1	0.28 ± 0.07	0.30 ± 0.07	-	$0.1^{+0.4}_{-0.1}$	-	4.8
G339.653−00.240	251.68	-45.67	5.2	1.06 ± 0.07	0.44 ± 0.07	-	$0.1^{+0.5}_{-0.1}$	-	7.9
G341.070−00.065	252.78	-44.47	2.7	1.89 ± 0.07	4.81 ± 0.07	$126.4^{+10.7}_{-9.0}$	$1.3^{+1.3}_{-0.7}$	$0.2^{+0.1}_{-0.1}$	7.2
G352.810+00.626	261.21	-34.65	2.6	1.45 ± 0.08	3.18 ± 0.08	$110.2^{+32.9}_{-59.1}$	$1.7^{+2.1}_{-1.3}$	$0.3^{+0.4}_{-0.2}$	17.9
G352.886+01.078	260.81	-34.33	9.5	5.08 ± 0.08	3.18 ± 0.08	$163.2^{+12.5}_{-14.4}$	$1.1^{+0.9}_{-0.5}$	$0.1^{+0.2}_{-0.2}$	5.7
G353.026+01.179	260.80	-34.16	3.7	8.64 ± 0.08	4.90 ± 0.08	$145.7^{+11.7}_{-9.5}$	$1.8^{+1.5}_{-0.8}$	$0.3^{+0.2}_{-0.2}$	10.0

Continued on next page

Name	RA	DEC	Radius	flux_img	flux_bkg	ν_0	α	β	Goodness
	deg	deg	arcmin	Jy	Jy	MHz			
(1)	(2)	(3)	(4)	(5)	(6)	(7)	(8)	(9)	(10)
G353.545+00.091	262.24	-34.33	4.5	0.72 ± 0.08	0.86 ± 0.08	$116.2^{+221.3}_{-72.0}$	$1.7^{+2.2}_{-1.5}$	$0.0^{+0.4}_{-0.4}$	17.2
G353.557+00.886	261.45	-33.88	2.3	2.74 ± 0.08	9.83 ± 0.08	$132.2^{+6.3}_{-5.0}$	$2.1^{+1.7}_{-1.1}$	$0.4^{+0.2}_{-0.1}$	8.0
G353.561+00.207	262.14	-34.26	3.0	0.72 ± 0.08	2.40 ± 0.08	$134.5^{+27.9}_{-30.5}$	$1.7^{+2.0}_{-1.2}$	$0.0^{+0.2}_{-0.3}$	6.8
G356.067+00.211	263.77	-32.16	1.6	0.53 ± 0.07	3.85 ± 0.07	-	$0.1^{+0.6}_{-0.1}$	-	9.1

Chapter 5

Summary

The diffuse synchrotron emission in the Milky Way is of interest in understanding our Galaxy and to clean out foreground contamination from EoR and CMB. A large number of sky surveys have mapped the synchrotron emission and other components (such as HI emission, the free-free emission, etc) in the frequency range from tens of MHz to GHz. The synchrotron emission shows higher surface brightness than those of other components at frequencies below several hundreds of MHz, which makes investigating its distribution especially important. However, observations are limited to map the 2D sky with information on the integrated line of sight. Therefore, we need special techniques to probe the distribution of the synchrotron emission in the radial direction of the Galactic disk. Models fitting with these 2D maps revealed spiral-arm structures of the synchrotron emission distribution. Thus, modelling is a powerful tool, but it urgently needs observational constraints to explore the complex radial distributions. In this regard, HII region absorption is a useful phenomenon for splitting the total line of sight emission into two columns: the one from the HII region to us and the one from the HII region to the Galactic edge. HII regions can be seen across the entireăGalactic disk, therefore, many HII region absorption measurements provide valuable radial distribution of diffuse synchrotron emission for understanding the Milky Way.

This thesis has presented the results of Galactic synchrotron emission tomography taking advantage of the information from HII region absorption observations. These observational results have provided the largest sample of the synchrotron distribution along 152 different lines of sight, revealing new insights into the 3D spatial distribution of the diffuse synchrotron emission in the disk of the Milky Way. We further extracted an HII region catalogue containing 588 HII regions in the GLEAM survey.

5.1 Results

We have calculated the synchrotron emissivities using the absorption of 152 HII regions at six frequencies of 76.2, 83.8, 91.5, 99.2, 106.9, and 114.6 MHz. For the first time, we derived emissivities from these HII regions to the Sun, which are especially important for studying the distribution of the synchrotron emission near the Sun within a distance of several kiloparsecs. When calculating the emissivities, we derived the optical depths of these HII regions at these six frequencies. Nearly all of these HII regions have optical depths much larger than one, indicating that they are optically thick. We also obtained the amount of missing flux density in the GLEAM observations assuming that the scaled Haslam map probes the total power of the synchrotron emission along the line of sight. About half of the synchrotron emission between the HII region to the Galactic edge along the line of sight is not recovered in the current GLEAM maps according to our HII region absorption analysis. Before accounting for this missing component, the spectral index of the brightness temperature of the diffuse synchrotron emission in the GLEAM map is about -1.5 (Su et al., 2017a), which is lower than the expected -2.7. After including this component, the spectral index becomes about -2.5 (Su et al., 2018), which is acceptable compared with the expected -2.7.

We have improved previous emissivity calculation methods. The previous simplified method of emissivity calculation assumes the optical depth of the HII region is much larger than one, i.e., the HII region is opaque to the synchrotron emission. And this method is only applicable when no flux density is missing in the observed sky maps. Our improved method takes advantage of the multi-frequency measurements of the GLEAM survey and a total power observation along the line of sight (Haslam map). Observations at three frequencies of the GLEAM survey help to solve the optical depth of the HII region and the synchrotron emissivities of both behind and in front of the HII region. The scaled Haslam map is adopted to estimate the brightness temperature integrated from the Sun to the Galactic edge along the line of sight of the HII region. Therefore, this improved method enables us to derive the optical depth of the HII region and estimate the amount of flux density missing from our observations at each frequency.

We have built four simplified models to investigate the first order of the synchrotron distribution. These models are named Uniform, Gaussian, Exponential, and Two-circle models to study the synchrotron emission distribution with the Galactocentric radius. The Two-circle model divides the Galactic disk using two circles centred at the Galactic centre with different radii. It fits our initial measurements best compared with the other three models. It shows the emissivity in the region near the Galactic centre with a Galactocentric radius of less than 1.7 kpc is the highest ($8.2^{+5.3}_{-3.5}$ K pc^{-1}). The emissivity in the region with a radius larger than 5.2 kpc is the lowest ($0.51^{+0.19}_{-0.27}$ K pc^{-1}). The emissivity in the region between the above two is medium ($0.84^{+0.76}_{-0.55}$ K pc^{-1}). Note that these emissivities are at the frequency of 88 MHz. More information on the synchrotron distribution contained in our absorption analysis will be shown in future models.

We have extracted an HII region catalogue using data in the whole GLEAM survey.

We found these HII regions from their emission and absorption features at the highest and the lowest GLEAM frequencies, respectively. Our catalogue contains information of the coordinates, flux density, and spectral index of 588 HII regions, all of which matched sources in the *WISE* HII region catalogue. For each HII region, we extracted its spectrum using 20 separate frequencies ranging from 72 to 231 MHz with a bandwidth of 8 MHz each. Our spectral index range of -0.2$\sim$2.0 is consistent with those in Hindson et al. (2016). We studied 66 HII regions with turnover frequencies determined in the frequency of the GLEAM survey and derived their physical parameters, such as the emission measure, the electron density, the mass of the ionized gas, and the total ionizing photon flux of the Lyman continuum. This catalogue contributes useful information for studying HII regions at metre wavelengths. HII regions are expected to have optical depths larger than one at frequencies below 1 GHz in theory. The turnover frequency is a probe of the emission measure and electron density of HII regions. The parameters measured in this work are important for understanding the physics of HII regions. We found 21 HII region candidates from the absorption features whose spectra are similar to those of the well-studied HII regions.

5.2 Future work

Next-generation telescopes, such as the "Phase II" of the MWA (Wayth et al., 2018) and the SKA, will observe more HII regions with absorption features because of their improved angular resolutions and surface brightness sensitivities. The number of observed HII region absorption features will increase from the current 152 to several thousands if the angular resolution improves from several arcminutes to several arcseconds, estimated from the angular size distribution for *WISE* HII region catalogue sources in Anderson et al. (2014).

The distance of an HII region is an important parameter for HII region absorption analysis. However, nearly half of the HII regions are still waiting to have reliable distance estimations. The parallax measurement of the HII region distance is accurate but rare, therefore, kinematic distances are widely adopted. Future research measuring more HII region distances is essential for the HII region tomography.

A single-dish survey at the frequency of $\sim$100 MHz will significantly improve the absolute scale of measured emissivities. In lieu of such a survey, we scale the Haslam map from 408 MHz to this frequency with a brightness temperature spectral index of -2.7. The systematic error introduced by this scaling will disappear if we do a single-dish survey or recover the total power along the line of sight using some special techniques, such as the Tikhonov-regularized m-mode analysis imaging (Eastwood et al., 2018).

Future models with our measured synchrotron emissivities included will reveal more information about the Galactic synchrotron distribution. For example, the GALPROP code can calculate the propagation of the relativistic electrons/positrons based on the 2D synchrotron emission maps. The line-of-sight information in our measurements are expected to further constrain the spatial distribution of the relativistic electron in global models such as the GALPROP.

Appendix A

Catalogue of HII regions in GLEAM

Table A.1: Catalogue of HII regions in the GLEAM. *Notes*. Col. (1): the name of the HII region in this GLEAM HII region catalogue. Col. (2): the name of the matched HII region in the *WISE* HII region catalogue. Col. (3): the right ascension of the source centre in our catalogue. Col (4): the declination of the source centre in our catalogue. Col. (5): the radius of the HII regions in our catalogue. Col. (6): the integrated flux density of the HII region including background. Both the errors for Col. (5) and (6) are the rms in the HII region. Col. (7): the integrated flux density of the background near the HII region. Col. (8): the turnover frequency of the HII region. Col. (9): the spectral index α. Col. (10): the spectral index β. Col. (11): the goodness of fitting.

Name	*WISE*	RA	DEC	Radius	flux_img	flux_bkg	ν_0	α	β	Goodness
		deg	deg	arcmin	Jy	Jy	MHz			
(1)	(2)	(3)	(4)	(5)	(6)	(7)	(8)	(9)	(10)	(11)
G359.965+00.147	G000.003+00.12	266.24	-28.89	215.4	3.19 ± 0.40	7.07 ± 0.40	$150.7^{+22.4}_{-32.8}$	$2.1^{+1.8}_{-1.3}$	$0.0^{+0.3}_{-0.5}$	2.6
G000.124−00.564	G000.120−00.55	267.03	-29.12	323.2	7.72 ± 0.27	10.61 ± 0.27	$136.7^{+10.9}_{-10.4}$	$1.9^{+1.8}_{-1.2}$	$-0.4^{+0.2}_{-0.3}$	3.1
G000.349−00.793	G000.328−00.80	267.39	-29.05	248.6	4.05 ± 0.13	3.28 ± 0.13	$126.8^{+18.1}_{-21.9}$	$2.1^{+1.8}_{-1.3}$	$0.3^{+0.2}_{-0.2}$	3.9
G000.461−00.474	G000.455−00.47	267.14	-28.79	632.1	22.34 ± 0.26	36.38 ± 0.26	$133.6^{+8.9}_{-7.9}$	$1.8^{+1.5}_{-0.9}$	$0.2^{+0.1}_{-0.1}$	8.5
G000.489−00.674	G000.498−00.67	267.35	-28.87	171.3	1.79 ± 0.14	1.36 ± 0.14	-	$0.2^{+0.6}_{-0.2}$	-	2.6
G000.575−00.851	G000.583−00.87	267.58	-28.88	218.7	0.87 ± 0.12	1.33 ± 0.12	-	$0.2^{+0.9}_{-0.2}$	-	3.1

Continued on next page

Name	*WISE*	RA	DEC	Radius	flux_img	flux_bkg	ν_0	α	β	Goodness
		deg	deg	arcmin	Jy	Jy	MHz			
(1)	(2)	(3)	(4)	(5)	(6)	(7)	(8)	(9)	(10)	(11)
G000.593−00.612	G000.595−00.61	267.35	-28.75	208.8	2.22 ± 0.16	2.45 ± 0.16	$169.3^{+14.6}_{-31.8}$	$2.0^{+1.8}_{-1.2}$	$0.2^{+0.3}_{-0.4}$	5.1
G000.666+00.646	G000.668+00.64	266.17	-28.03	300.5	4.28 ± 0.10	4.62 ± 0.10	-	$-0.0^{+0.1}_{-0.4}$	-	9.2
G000.823+00.197	G000.829+00.19	266.70	-28.13	149.3	2.94 ± 0.25	2.15 ± 0.25	-	$-0.2^{+0.2}_{-0.6}$	-	2.2
G002.266+00.224	G002.272+00.23	267.51	-26.88	259.4	2.72 ± 0.08	2.94 ± 0.08	-	$0.1^{+0.4}_{-0.1}$	-	10.0
G003.296−00.056	G003.266−00.06	268.37	-26.14	368.9	6.24 ± 0.07	8.06 ± 0.07	$132.4^{+16.1}_{-16.8}$	$0.9^{+1.3}_{-0.6}$	$-0.5^{+0.3}_{-0.3}$	12.7
G004.395+00.115	G004.409+00.11	268.82	-25.10	337.2	4.30 ± 0.07	3.78 ± 0.07	$165.7^{+14.0}_{-15.8}$	$1.3^{+1.6}_{-0.8}$	$-0.2^{+0.3}_{-0.4}$	2.9
G004.566−00.116	G004.557−00.12	269.14	-25.07	113.7	0.57 ± 0.07	0.59 ± 0.07	-	$0.1^{+0.9}_{-0.1}$	-	4.9
G005.316+00.126	G005.332+00.08	269.32	-24.30	298.3	1.33 ± 0.09	3.35 ± 0.09	$128.5^{+9.7}_{-10.6}$	$2.6^{+1.6}_{-1.6}$	$0.0^{+0.2}_{-0.2}$	4.0
G005.895−00.412	G005.887−00.44	270.15	-24.07	317.8	5.14 ± 0.12	3.98 ± 0.12	$144.4^{+8.3}_{-10.1}$	$1.9^{+1.6}_{-1.0}$	$0.3^{+0.2}_{-0.2}$	27.9
G005.997−01.304	G006.100−01.26	271.06	-24.42	1022.0	68.15 ± 0.10	17.86 ± 0.10	$166.1^{+9.2}_{-14.0}$	$0.9^{+0.6}_{-0.3}$	$0.3^{+0.3}_{-0.1}$	13.7
G006.243−00.576	G006.270−00.57	270.50	-23.85	261.2	2.47 ± 0.13	2.12 ± 0.13	$110.6^{+19.7}_{-69.8}$	$2.1^{+2.0}_{-1.6}$	$0.2^{+0.3}_{-0.1}$	17.6

Continued on next page

Name	*WISE*	RA	DEC	Radius	flux_img	flux_bkg	ν_0	α	β	Goodness
		deg	deg	arcmin	Jy	Jy	MHz			
(1)	(2)	(3)	(4)	(5)	(6)	(7)	(8)	(9)	(10)	(11)
G006.929−02.125	G006.930−02.13	272.34	-24.01	458.4	1.36 ± 0.07	-0.20 ± 0.07	$159.7^{+15.0}_{-9.4}$	$1.3^{+1.5}_{-0.7}$	$-0.3^{+0.2}_{-0.3}$	24.1
G006.992−00.276	G007.015−00.27	270.61	-23.05	358.3	6.19 ± 0.11	4.85 ± 0.11	$164.2^{+5.4}_{-9.0}$	$1.0^{+0.6}_{-0.3}$	$-0.0^{+0.1}_{-0.1}$	14.4
G007.039+00.173	G007.039+00.17	270.22	-22.78	80.5	0.34 ± 0.11	0.32 ± 0.11	-	$0.1^{+0.8}_{-0.1}$	-	3.5
G007.264−00.062	G007.268−00.06	270.56	-22.71	131.7	0.50 ± 0.11	0.58 ± 0.11	-	$0.2^{+0.5}_{-0.1}$	-	4.3
G007.299−00.125	G007.303−00.12	270.64	-22.71	192.0	1.25 ± 0.11	1.40 ± 0.11	$141.3^{+8.7}_{-7.2}$	$2.0^{+1.7}_{-1.2}$	$0.2^{+0.2}_{-0.1}$	4.6
G007.394+00.690	G007.443+00.70	269.92	-22.22	174.4	0.37 ± 0.09	0.64 ± 0.09	-	$0.1^{+0.4}_{-0.1}$	-	4.4
G007.728−00.022	G007.700−00.12	270.77	-22.28	432.3	3.65 ± 0.10	6.31 ± 0.10	$132.6^{+5.8}_{-5.9}$	$1.6^{+1.4}_{-0.7}$	$0.1^{+0.1}_{-0.1}$	10.9
G008.107−00.479	G008.123−00.48	271.40	-22.18	395.2	2.97 ± 0.09	6.04 ± 0.09	$105.4^{+5.6}_{-5.6}$	$2.6^{+1.6}_{-1.5}$	$0.2^{+0.1}_{-0.1}$	14.8
G008.128+00.231	G008.137+00.23	270.74	-21.81	150.2	1.29 ± 0.10	0.98 ± 0.10	-	$0.3^{+0.5}_{-0.2}$	-	8.0
G008.068−00.169	G008.153−00.19	271.09	-22.06	576.0	6.39 ± 0.10	8.84 ± 0.10	$132.3^{+6.2}_{-7.2}$	$1.6^{+1.3}_{-0.7}$	$0.2^{+0.1}_{-0.1}$	14.6
G008.355−00.326	G008.358−00.29	271.39	-21.89	209.5	2.99 ± 0.10	1.48 ± 0.10	$145.9^{+20.0}_{-9.2}$	$1.7^{+1.8}_{-1.0}$	$0.1^{+0.2}_{-0.2}$	10.0

Continued on next page

Name	*WISE*	RA	DEC	Radius	flux_img	flux_bkg	ν_0	α	β	Goodness
		deg	deg	arcmin	Jy	Jy	MHz			
(1)	(2)	(3)	(4)	(5)	(6)	(7)	(8)	(9)	(10)	(11)
G008.443−00.361	G008.456−00.35	271.46	-21.83	241.5	3.26 ± 0.10	1.83 ± 0.10	$155.3^{+9.1}_{-8.3}$	$1.2^{+0.9}_{-0.5}$	$-0.2^{+0.1}_{-0.2}$	8.9
G009.197+00.027	G009.178+00.04	271.50	-20.98	149.9	0.73 ± 0.09	0.90 ± 0.09	-	$0.1^{+0.5}_{-0.1}$	-	5.3
G009.607+00.201	G009.613+00.20	271.55	-20.54	104.6	0.28 ± 0.09	0.53 ± 0.09	-	$0.1^{+1.1}_{-0.1}$	-	2.7
G009.706−00.853	G009.725−00.84	272.59	-20.96	288.0	1.13 ± 0.08	1.90 ± 0.08	$139.4^{+15.9}_{-47.6}$	$1.6^{+1.9}_{-1.0}$	$0.1^{+0.2}_{-0.3}$	8.5
G009.945−00.882	G009.913−01.00	272.74	-20.77	314.6	1.01 ± 0.08	0.69 ± 0.08	-	$0.0^{+0.5}_{-0.0}$	-	6.9
G009.964−00.733	G009.942−00.76	272.61	-20.68	361.7	2.75 ± 0.09	2.11 ± 0.09	$150.3^{+21.2}_{-13.1}$	$0.9^{+1.1}_{-0.5}$	$-0.1^{+0.2}_{-0.2}$	7.2
G010.075−00.421	G010.083−00.41	272.37	-20.43	156.9	0.94 ± 0.09	0.84 ± 0.09	-	$0.2^{+0.3}_{-0.1}$	-	3.3
G010.156−00.342	G010.160−00.35	272.34	-20.32	212.4	5.22 ± 0.09	1.65 ± 0.09	-	$0.6^{+0.3}_{-0.2}$	-	5.5
G010.193−00.428	G010.197−00.43	272.44	-20.33	122.3	0.99 ± 0.09	0.67 ± 0.09	-	$0.2^{+0.3}_{-0.1}$	-	6.6
G010.225−00.307	G010.227−00.30	272.34	-20.24	101.7	0.56 ± 0.09	0.53 ± 0.09	-	$0.1^{+0.4}_{-0.1}$	-	5.5
G010.266+00.080	G010.266+00.07	272.00	-20.02	76.3	0.25 ± 0.09	0.35 ± 0.09	-	$0.0^{+0.5}_{-0.0}$	-	5.5

Continued on next page

Name	*WISE*	RA	DEC	Radius	flux_img	flux_bkg	ν_0	α	β	Goodness
		deg	deg	arcmin	Jy	Jy	MHz			
(1)	(2)	(3)	(4)	(5)	(6)	(7)	(8)	(9)	(10)	(11)
G010.296−00.142	G010.308−00.15	272.23	-20.10	297.8	4.19 ± 0.09	3.28 ± 0.09	$149.0^{+38.8}_{-12.4}$	$1.1^{+1.2}_{-0.5}$	$0.4^{+0.3}_{-0.4}$	16.4
G010.322−00.276	G010.331−00.27	272.36	-20.14	106.7	0.50 ± 0.09	0.63 ± 0.09	-	$0.1^{+0.5}_{-0.1}$	-	6.5
G010.696+00.033	G010.689+00.03	272.27	-19.67	71.3	0.29 ± 0.09	0.23 ± 0.09	-	$0.1^{+0.6}_{-0.1}$	-	3.5
G010.653−00.405	G010.769−00.48	272.65	-19.91	344.0	3.01 ± 0.09	3.45 ± 0.09	$157.3^{+16.8}_{-14.9}$	$1.6^{+1.6}_{-0.9}$	$0.1^{+0.3}_{-0.3}$	9.4
G010.876+00.084	G010.877+00.08	272.31	-19.48	102.2	0.36 ± 0.09	0.39 ± 0.09	-	$0.1^{+0.5}_{-0.0}$	-	7.2
G011.845−00.175	G011.840−00.19	273.05	-18.76	113.0	0.58 ± 0.09	0.43 ± 0.09	-	$0.0^{+0.4}_{-0.0}$	-	9.1
G011.905+00.744	G011.893+00.74	272.23	-18.26	136.9	1.07 ± 0.08	0.71 ± 0.08	-	$0.4^{+0.5}_{-0.2}$	-	11.9
G011.989−00.261	G011.995−00.24	273.20	-18.67	122.0	0.57 ± 0.09	0.54 ± 0.09	-	$0.4^{+2.0}_{-0.4}$	-	6.8
G012.215−00.121	G012.217−00.13	273.19	-18.41	200.4	2.00 ± 0.08	1.86 ± 0.08	$149.0^{+37.0}_{-34.6}$	$1.1^{+1.8}_{-0.8}$	$0.2^{+0.4}_{-0.3}$	4.6
G012.345−00.544	G012.359−00.55	273.64	-18.50	419.5	1.19 ± 0.08	6.38 ± 0.08	$111.6^{+23.6}_{-21.9}$	$1.8^{+1.9}_{-1.2}$	$0.3^{+0.2}_{-0.2}$	12.8
G012.437−00.045	G012.429−00.04	273.23	-18.18	139.1	0.95 ± 0.08	0.93 ± 0.08	-	$0.1^{+0.6}_{-0.1}$	-	3.1

Continued on next page

Name	*WISE*	RA	DEC	Radius	flux_img	flux_bkg	ν_0	α	β	Goodness
		deg	deg	arcmin	Jy	Jy	MHz			
(1)	(2)	(3)	(4)	(5)	(6)	(7)	(8)	(9)	(10)	(11)
G012.465−01.124	G012.474−01.14	274.24	-18.67	253.4	1.05 ± 0.07	0.86 ± 0.07	$139.3^{+41.3}_{-10.9}$	$1.2^{+2.1}_{-0.9}$	$-0.0^{+0.2}_{-0.2}$	14.7
G012.698−00.251	G012.692−00.25	273.55	-18.05	108.9	0.88 ± 0.08	0.57 ± 0.08	-	$0.2^{+0.3}_{-0.1}$	-	9.3
G012.735+00.367	G012.742+00.39	273.00	-17.72	393.3	2.25 ± 0.08	8.32 ± 0.08	$121.8^{+9.2}_{-11.6}$	$2.0^{+1.8}_{-1.2}$	$0.0^{+0.1}_{-0.1}$	14.2
G012.745−00.157	G012.761−00.13	273.49	-17.96	253.4	5.45 ± 0.08	2.69 ± 0.08	-	$0.2^{+0.1}_{-0.1}$	-	12.2
G012.816−00.235	G012.820−00.23	273.59	-17.94	128.5	1.87 ± 0.08	0.85 ± 0.08	$145.0^{+75.6}_{-51.0}$	$1.1^{+1.8}_{-0.7}$	$0.7^{+0.5}_{-0.4}$	7.5
G012.880−00.232	G012.884−00.23	273.62	-17.88	108.6	0.75 ± 0.08	0.50 ± 0.08	$147.1^{+52.9}_{-38.2}$	$1.1^{+1.9}_{-0.8}$	$0.4^{+0.4}_{-0.3}$	3.5
G012.902−00.289	G012.907−00.27	273.69	-17.89	80.5	0.39 ± 0.08	0.33 ± 0.08	-	$0.1^{+0.4}_{-0.1}$	-	2.5
G013.198+00.059	G013.186+00.04	273.52	-17.46	262.9	4.11 ± 0.08	3.02 ± 0.08	$92.2^{+54.0}_{-49.6}$	$1.5^{+2.1}_{-1.2}$	$0.3^{+0.4}_{-0.2}$	11.5
G013.729−00.023	G013.725−00.02	273.86	-17.03	232.3	1.67 ± 0.09	2.98 ± 0.09	$138.3^{+10.8}_{-14.5}$	$1.6^{+1.7}_{-0.9}$	$-0.1^{+0.1}_{-0.2}$	6.2
G013.827−00.782	G013.776−00.79	274.60	-17.31	344.5	2.95 ± 0.08	2.50 ± 0.08	$143.5^{+28.9}_{-11.6}$	$1.2^{+1.3}_{-0.6}$	$0.2^{+0.2}_{-0.2}$	16.7
G013.796+00.181	G013.789+00.18	273.70	-16.88	80.7	0.33 ± 0.09	0.34 ± 0.09	-	$0.0^{+0.3}_{-0.0}$	-	3.1

Continued on next page

Name	*WISE*	RA	DEC	Radius	flux_img	flux_bkg	ν_0	α	β	Goodness
		deg	deg	arcmin	Jy	Jy	MHz			
(1)	(2)	(3)	(4)	(5)	(6)	(7)	(8)	(9)	(10)	(11)
G013.887+00.282	G013.880+00.28	273.66	-16.75	108.4	0.71 ± 0.09	0.56 ± 0.09	-	$0.2^{+1.2}_{-0.2}$	-	5.5
G013.996−00.131	G013.992−00.13	274.09	-16.85	141.8	0.92 ± 0.09	1.29 ± 0.09	$164.1^{+17.3}_{-13.6}$	$1.4^{+1.6}_{-0.8}$	$0.1^{+0.3}_{-0.3}$	3.9
G014.055−00.525	G014.060−00.52	274.48	-16.98	220.3	1.40 ± 0.08	2.15 ± 0.08	$153.7^{+25.5}_{-57.7}$	$1.0^{+1.6}_{-0.7}$	$0.2^{+0.4}_{-0.2}$	6.5
G014.108−00.145	G014.207−00.19	274.16	-16.76	482.3	4.63 ± 0.09	9.10 ± 0.09	$158.3^{+4.9}_{-5.1}$	$0.9^{+0.5}_{-0.4}$	$0.1^{+0.1}_{-0.1}$	6.5
G014.313+00.151	G014.303+00.14	273.99	-16.44	260.6	1.76 ± 0.09	2.67 ± 0.09	$156.0^{+14.8}_{-16.9}$	$1.2^{+1.7}_{-0.8}$	$-0.3^{+0.3}_{-0.4}$	4.9
G014.389−00.083	G014.392−00.10	274.24	-16.48	312.3	3.96 ± 0.09	4.70 ± 0.09	$127.2^{+39.3}_{-23.7}$	$1.2^{+1.6}_{-0.7}$	$0.3^{+0.3}_{-0.2}$	12.6
G014.454−00.647	G014.481−00.66	274.79	-16.69	173.3	0.93 ± 0.09	1.07 ± 0.09	$148.7^{+50.8}_{-62.8}$	$1.0^{+1.7}_{-0.7}$	$0.3^{+0.4}_{-0.4}$	12.1
G014.556+00.113	G014.576+00.09	274.14	-16.24	635.0	14.89 ± 0.09	16.93 ± 0.09	$143.5^{+5.1}_{-4.3}$	$1.1^{+0.7}_{-0.4}$	$0.4^{+0.2}_{-0.1}$	15.6
G014.658−00.481	G014.667−00.47	274.74	-16.43	188.0	0.34 ± 0.09	0.92 ± 0.09	-	$0.0^{+0.5}_{-0.0}$	-	5.1
G015.114−00.720	G015.097−00.72	275.18	-16.14	1125.2	126.00 ± 0.08	27.68 ± 0.08	$167.9^{+12.0}_{-15.7}$	$1.6^{+0.6}_{-0.3}$	$0.6^{+0.3}_{-0.3}$	14.9
G015.683−00.281	G015.676−00.28	275.06	-15.43	181.3	0.11 ± 0.08	1.45 ± 0.08	-	$0.1^{+0.4}_{-0.1}$	-	9.4

Continued on next page

Name	*WISE*	RA	DEC	Radius	flux_img	flux_bkg	ν_0	α	β	Goodness
		deg	deg	arcmin	Jy	Jy	MHz			
(1)	(2)	(3)	(4)	(5)	(6)	(7)	(8)	(9)	(10)	(11)
G016.286−00.170	G016.285−00.17	275.25	-14.85	141.7	0.82 ± 0.08	0.89 ± 0.08	$137.2^{+76.8}_{-32.1}$	$1.1^{+1.9}_{-0.8}$	$0.1^{+0.4}_{-0.3}$	13.7
G016.359−00.174	G016.352−00.17	275.29	-14.79	84.6	0.25 ± 0.08	0.30 ± 0.08	-	$0.1^{+0.3}_{-0.0}$	-	7.2
G016.382−00.527	G016.363−00.55	275.62	-14.93	273.4	1.59 ± 0.07	2.59 ± 0.07	$129.7^{+19.8}_{-14.3}$	$1.2^{+1.9}_{-0.9}$	$0.2^{+0.2}_{-0.2}$	5.2
G016.442−00.202	G016.424−00.20	275.36	-14.73	146.1	0.79 ± 0.08	0.72 ± 0.08	$155.7^{+63.2}_{-30.8}$	$0.8^{+1.7}_{-0.6}$	$0.2^{+0.4}_{-0.3}$	5.5
G016.637−00.330	G016.648−00.35	275.57	-14.62	260.4	1.35 ± 0.07	3.48 ± 0.07	$162.1^{+6.1}_{-6.2}$	$0.9^{+0.7}_{-0.4}$	$0.0^{+0.1}_{-0.1}$	18.0
G016.767−01.123	G016.856−01.15	276.36	-14.87	393.5	3.25 ± 0.06	0.84 ± 0.06	$172.0^{+10.2}_{-11.2}$	$0.4^{+0.4}_{-0.2}$	$-0.5^{+0.2}_{-0.3}$	6.7
G016.948+00.849	G016.993+00.87	274.65	-13.79	1010.9	68.50 ± 0.07	28.42 ± 0.07	$150.9^{+10.3}_{-8.7}$	$1.0^{+0.6}_{-0.3}$	$0.3^{+0.2}_{-0.1}$	14.6
G018.145−00.300	G018.144−00.28	276.27	-13.27	209.9	3.18 ± 0.07	1.81 ± 0.07	$108.9^{+74.0}_{-58.3}$	$1.2^{+2.0}_{-0.9}$	$0.6^{+0.5}_{-0.3}$	13.1
G018.207−00.411	G018.187−00.41	276.40	-13.27	253.7	3.19 ± 0.07	2.58 ± 0.07	$123.1^{+58.3}_{-63.5}$	$1.1^{+1.8}_{-0.8}$	$0.5^{+0.4}_{-0.2}$	7.6
G018.296−00.290	G018.253−00.29	276.33	-13.13	428.3	6.14 ± 0.07	5.13 ± 0.07	$130.3^{+15.7}_{-12.3}$	$1.3^{+1.3}_{-0.6}$	$0.4^{+0.2}_{-0.2}$	9.2
G018.475+01.979	G018.426+01.92	274.37	-11.91	1850.6	69.99 ± 0.10	42.05 ± 0.10	$148.2^{+5.5}_{-5.7}$	$0.9^{+0.5}_{-0.3}$	$0.2^{+0.1}_{-0.1}$	20.1

Continued on next page

Name	*WISE*	RA	DEC	Radius	flux_img	flux_bkg	ν_0	α	β	Goodness
		deg	deg	arcmin	Jy	Jy	MHz			
(1)	(2)	(3)	(4)	(5)	(6)	(7)	(8)	(9)	(10)	(11)
G018.671+01.982	G018.669+01.96	274.46	-11.73	273.4	5.62 ± 0.10	1.22 ± 0.10	-	$0.3^{+0.2}_{-0.1}$	-	10.1
G018.675−00.259	G018.677−00.23	276.49	-12.78	353.4	1.76 ± 0.08	3.53 ± 0.08	-	$0.2^{+0.2}_{-0.1}$	-	13.0
G018.763−00.073	G018.725−00.04	276.36	-12.62	88.1	0.59 ± 0.08	0.35 ± 0.08	$115.2^{+54.6}_{-75.7}$	$1.3^{+2.2}_{-1.2}$	$0.0^{+0.2}_{-0.2}$	13.0
G018.910−00.451	G018.881−00.49	276.77	-12.66	302.1	3.25 ± 0.08	2.97 ± 0.08	$149.5^{+14.2}_{-16.0}$	$1.6^{+1.5}_{-0.9}$	$0.5^{+0.3}_{-0.2}$	8.7
G019.022−00.262	G018.914−00.32	276.65	-12.48	740.1	15.32 ± 0.08	14.41 ± 0.08	$173.8^{+13.0}_{-25.8}$	$0.8^{+0.5}_{-0.3}$	$0.3^{+0.3}_{-0.2}$	7.7
G018.958−00.014	G018.978+00.03	276.40	-12.42	217.3	2.43 ± 0.08	2.57 ± 0.08	$153.3^{+10.1}_{-9.3}$	$1.2^{+1.3}_{-0.7}$	$0.2^{+0.2}_{-0.1}$	4.4
G019.072−00.599	G019.045−00.58	276.98	-12.59	136.4	0.39 ± 0.08	0.75 ± 0.08	-	$0.2^{+0.7}_{-0.1}$	-	3.8
G019.486+00.141	G019.466+00.16	276.51	-11.88	125.1	0.78 ± 0.08	0.54 ± 0.08	-	$0.1^{+0.5}_{-0.1}$	-	2.3
G019.611−00.239	G019.609−00.23	276.91	-11.94	70.4	0.50 ± 0.08	0.28 ± 0.08	-	$0.3^{+1.0}_{-0.2}$	-	1.6
G019.631−00.126	G019.629−00.09	276.82	-11.87	301.4	3.52 ± 0.08	4.02 ± 0.08	$111.8^{+19.7}_{-27.5}$	$2.0^{+1.9}_{-1.3}$	$0.4^{+0.3}_{-0.2}$	9.1
G020.453+00.042	G020.457+00.02	277.06	-11.07	238.8	1.17 ± 0.07	1.22 ± 0.07	$113.8^{+17.5}_{-16.6}$	$1.7^{+2.1}_{-1.3}$	$-0.1^{+0.1}_{-0.3}$	5.5

Continued on next page

Name	*WISE*	RA	DEC	Radius	flux_img	flux_bkg	ν_0	α	β	Goodness
		deg	deg	arcmin	Jy	Jy	MHz			
(1)	(2)	(3)	(4)	(5)	(6)	(7)	(8)	(9)	(10)	(11)
G020.470+00.177	G020.481+00.16	276.95	-10.99	231.8	1.42 ± 0.07	1.66 ± 0.07	$124.4^{+16.4}_{-18.7}$	$1.8^{+2.0}_{-1.4}$	$-0.1^{+0.2}_{-0.4}$	4.6
G020.772−00.114	G020.728−00.10	277.35	-10.86	466.3	10.40 ± 0.08	7.15 ± 0.08	$129.4^{+10.7}_{-9.4}$	$2.0^{+1.5}_{-0.9}$	$0.3^{+0.2}_{-0.2}$	9.6
G020.989+00.086	G020.988+00.09	277.27	-10.57	99.1	0.63 ± 0.08	0.40 ± 0.08	-	$0.3^{+1.1}_{-0.3}$	-	4.3
G022.444+00.074	G022.478−00.01	277.97	-9.29	317.2	0.96 ± 0.09	4.13 ± 0.09	$127.2^{+23.8}_{-29.5}$	$1.8^{+1.9}_{-1.2}$	$0.2^{+0.3}_{-0.2}$	9.7
G022.790−00.488	G022.761−00.49	278.63	-9.24	230.8	2.46 ± 0.09	1.84 ± 0.09	-	$0.3^{+0.4}_{-0.2}$	-	4.6
G023.112+00.542	G023.097+00.52	277.86	-8.48	220.3	1.11 ± 0.08	1.25 ± 0.08	$176.2^{+11.0}_{-12.1}$	$0.9^{+1.3}_{-0.6}$	$-0.3^{+0.3}_{-0.4}$	2.6
G023.577−00.022	G023.572−00.02	278.58	-8.33	317.8	4.17 ± 0.10	5.37 ± 0.10	$129.4^{+16.1}_{-13.7}$	$1.7^{+1.7}_{-1.0}$	$0.2^{+0.2}_{-0.2}$	5.6
G023.581−00.384	G023.581−00.40	278.91	-8.49	273.1	1.48 ± 0.09	3.51 ± 0.09	$135.0^{+22.3}_{-14.8}$	$1.8^{+2.0}_{-1.3}$	$-0.1^{+0.3}_{-0.4}$	6.0
G023.580+00.285	G023.689+00.37	278.31	-8.18	376.6	1.35 ± 0.10	2.64 ± 0.10	$184.2^{+90.5}_{-62.1}$	$0.8^{+1.4}_{-0.5}$	$0.2^{+0.6}_{-0.6}$	14.3
G023.700+00.170	G023.708+00.17	278.47	-8.13	109.9	0.55 ± 0.10	0.61 ± 0.10	-	$0.1^{+0.6}_{-0.1}$	-	2.4
G023.959+00.159	G023.957+00.14	278.60	-7.91	95.0	0.34 ± 0.10	0.41 ± 0.10	-	$0.1^{+0.8}_{-0.1}$	-	2.9

Continued on next page

Name	*WISE*	RA	DEC	Radius	flux_img	flux_bkg	ν_0	α	β	Goodness
		deg	deg	arcmin	Jy	Jy	MHz			
(1)	(2)	(3)	(4)	(5)	(6)	(7)	(8)	(9)	(10)	(11)
G024.194+00.219	G024.185+00.21	278.65	-7.67	131.1	0.15 ± 0.09	0.41 ± 0.09	-	$0.1^{+0.9}_{-0.1}$	-	2.1
G024.284−00.138	G024.280−00.14	279.02	-7.75	186.3	2.02 ± 0.10	1.86 ± 0.10	-	$0.1^{+0.6}_{-0.1}$	-	6.2
G024.365+00.063	G024.347+00.08	278.87	-7.59	203.0	0.94 ± 0.09	1.82 ± 0.09	$167.9^{+16.7}_{-38.2}$	$1.2^{+1.7}_{-0.8}$	$-0.1^{+0.3}_{-0.5}$	7.9
G024.464+00.487	G024.456+00.48	278.54	-7.31	91.6	0.80 ± 0.09	0.28 ± 0.09	-	$1.0^{+1.4}_{-0.9}$	-	4.8
G024.491−00.228	G024.493−00.21	279.19	-7.61	289.8	3.50 ± 0.09	3.19 ± 0.09	$179.7^{+20.1}_{-19.4}$	$1.0^{+1.0}_{-0.5}$	$0.2^{+0.4}_{-0.4}$	2.5
G024.501−00.041	G024.498−00.03	279.03	-7.52	91.7	0.43 ± 0.09	0.45 ± 0.09	-	$0.2^{+0.6}_{-0.1}$	-	4.0
G024.491+00.242	G024.507+00.23	278.77	-7.40	280.5	4.44 ± 0.09	3.23 ± 0.09	$182.6^{+15.7}_{-20.7}$	$1.1^{+1.2}_{-0.6}$	$-0.0^{+0.4}_{-0.5}$	4.6
G024.681−00.168	G024.678−00.16	279.23	-7.42	123.2	1.07 ± 0.09	0.81 ± 0.09	-	$0.3^{+0.6}_{-0.2}$	-	2.6
G024.722−00.091	G024.724−00.08	279.18	-7.34	206.3	2.06 ± 0.09	2.00 ± 0.09	-	$0.2^{+0.3}_{-0.2}$	-	6.7
G024.728+00.079	G024.734+00.08	279.03	-7.26	129.6	0.58 ± 0.09	0.67 ± 0.09	-	$0.2^{+0.9}_{-0.1}$	-	2.6
G024.741−00.213	G024.743−00.21	279.30	-7.38	99.4	0.36 ± 0.09	0.47 ± 0.09	-	$0.2^{+0.7}_{-0.1}$	-	2.4

Continued on next page

Name	*WISE*	RA	DEC	Radius	flux_img	flux_bkg	ν_0	α	β	Goodness
		deg	deg	arcmin	Jy	Jy	MHz			
(1)	(2)	(3)	(4)	(5)	(6)	(7)	(8)	(9)	(10)	(11)
G024.814−00.226	G024.826−00.26	279.34	-7.32	94.5	0.39 ± 0.09	0.42 ± 0.09	-	$0.0^{+0.4}_{-0.0}$	-	2.9
G024.821+00.082	G024.844+00.09	279.07	-7.18	270.8	3.84 ± 0.09	2.78 ± 0.09	-	$0.3^{+0.4}_{-0.2}$	-	7.3
G025.212+00.275	G025.220+00.28	279.08	-6.74	111.8	0.48 ± 0.09	0.55 ± 0.09	-	$0.1^{+0.7}_{-0.1}$	-	2.3
G025.302+00.305	G025.286+00.29	279.09	-6.65	103.1	0.49 ± 0.09	0.43 ± 0.09	-	$0.1^{+0.6}_{-0.1}$	-	5.5
G025.273−00.311	G025.291−00.30	279.63	-6.95	150.2	0.70 ± 0.08	0.80 ± 0.08	-	$0.3^{+0.7}_{-0.2}$	-	3.1
G025.377−00.169	G025.382−00.15	279.55	-6.80	182.9	3.47 ± 0.09	1.31 ± 0.09	-	$0.9^{+0.4}_{-0.3}$	-	4.4
G025.387−00.345	G025.386−00.34	279.71	-6.87	164.1	0.57 ± 0.08	0.59 ± 0.08	-	$0.1^{+0.2}_{-0.1}$	-	11.4
G025.399+00.032	G025.397+00.03	279.38	-6.69	81.0	0.46 ± 0.09	0.30 ± 0.09	-	$0.1^{+0.5}_{-0.1}$	-	2.5
G025.708+00.027	G025.700+00.02	279.53	-6.41	159.1	1.53 ± 0.09	1.07 ± 0.09	-	$0.2^{+0.4}_{-0.2}$	-	5.4
G025.804+00.187	G025.867+00.11	279.43	-6.25	472.0	6.11 ± 0.09	4.65 ± 0.09	-	$0.3^{+0.2}_{-0.1}$	-	11.2
G026.124−00.058	G026.117−00.06	279.80	-6.08	286.6	3.54 ± 0.09	2.78 ± 0.09	$151.0^{+18.3}_{-17.3}$	$1.5^{+1.7}_{-0.8}$	$0.1^{+0.2}_{-0.3}$	7.0

Continued on next page

Name	*WISE*	RA	DEC	Radius	flux_img	flux_bkg	ν_0	α	β	Goodness
		deg	deg	arcmin	Jy	Jy	MHz			
(1)	(2)	(3)	(4)	(5)	(6)	(7)	(8)	(9)	(10)	(11)
G026.499−00.299	G026.521−00.31	280.18	-5.86	268.1	1.67 ± 0.09	2.71 ± 0.09	$120.1^{+38.2}_{-51.6}$	$1.4^{+2.1}_{-1.0}$	$0.2^{+0.3}_{-0.1}$	17.8
G026.534+00.414	G026.542+00.41	279.56	-5.50	84.2	0.44 ± 0.09	0.22 ± 0.09	-	$0.2^{+0.6}_{-0.1}$	-	2.5
G026.714+00.166	G026.721+00.16	279.87	-5.46	48.3	0.11 ± 0.09	0.07 ± 0.09	-	$0.0^{+0.7}_{-0.0}$	-	1.9
G026.776−00.157	G026.797−00.11	280.18	-5.55	744.3	7.65 ± 0.09	10.27 ± 0.09	$138.5^{+10.9}_{-11.8}$	$1.7^{+1.4}_{-0.8}$	$0.4^{+0.2}_{-0.2}$	6.3
G026.982−00.059	G026.984−00.06	280.19	-5.32	132.3	1.15 ± 0.09	0.54 ± 0.09	$125.6^{+43.8}_{-84.2}$	$1.2^{+2.2}_{-1.1}$	$0.1^{+0.3}_{-0.2}$	12.1
G027.294−00.161	G027.281−00.13	280.43	-5.09	158.8	1.74 ± 0.09	0.69 ± 0.09	$114.6^{+41.9}_{-51.5}$	$1.0^{+2.0}_{-0.7}$	$0.2^{+0.3}_{-0.1}$	4.7
G027.485+00.183	G027.476+00.17	280.21	-4.76	86.3	0.84 ± 0.10	0.25 ± 0.10	-	$0.1^{+0.3}_{-0.1}$	-	3.1
G028.005+00.320	G027.997+00.31	280.32	-4.24	88.5	0.29 ± 0.10	0.28 ± 0.10	-	$0.1^{+0.9}_{-0.1}$	-	1.5
G028.020−00.042	G028.022−00.04	280.65	-4.39	182.3	0.79 ± 0.10	1.25 ± 0.10	-	$0.2^{+0.4}_{-0.1}$	-	5.4
G028.248+00.015	G028.246+00.01	280.71	-4.16	66.2	0.16 ± 0.10	0.17 ± 0.10	-	$0.1^{+0.8}_{-0.1}$	-	2.7
G028.301−00.399	G028.305−00.39	281.10	-4.30	70.0	0.21 ± 0.09	0.16 ± 0.09	-	$0.1^{+0.9}_{-0.1}$	-	2.5

Continued on next page

Name	*WISE*	RA	DEC	Radius	flux_img	flux_bkg	ν_0	α	β	Goodness
		deg	deg	arcmin	Jy	Jy	MHz			
(1)	(2)	(3)	(4)	(5)	(6)	(7)	(8)	(9)	(10)	(11)
G028.595−00.371	G028.600−00.37	281.21	-4.03	68.1	0.23 ± 0.09	0.17 ± 0.09	-	$0.1^{+0.9}_{-0.1}$	-	4.2
G028.642+00.191	G028.638+00.19	280.73	-3.73	84.6	0.34 ± 0.10	0.26 ± 0.10	-	$0.1^{+0.6}_{-0.1}$	-	2.6
G028.633+00.470	G028.656+00.49	280.48	-3.61	82.2	0.34 ± 0.10	0.24 ± 0.10	-	$0.2^{+1.4}_{-0.2}$	-	2.2
G028.676+00.046	G028.679+00.04	280.88	-3.77	93.8	0.70 ± 0.10	0.33 ± 0.10	-	$0.2^{+0.5}_{-0.1}$	-	5.0
G028.804+03.466	G028.746+03.45	277.89	-2.08	415.0	14.51 ± 0.09	-0.17 ± 0.09	$154.9^{+9.4}_{-7.3}$	$0.8^{+0.5}_{-0.3}$	$0.0^{+0.1}_{-0.1}$	18.2
G028.755+00.288	G028.774+00.28	280.70	-3.59	130.0	0.74 ± 0.10	0.66 ± 0.10	-	$0.1^{+0.5}_{-0.1}$	-	4.2
G028.797+00.169	G028.801+00.17	280.82	-3.60	130.0	0.95 ± 0.10	0.63 ± 0.10	-	$0.3^{+0.7}_{-0.2}$	-	3.9
G028.793+00.236	G028.823+00.23	280.76	-3.58	87.7	0.22 ± 0.10	0.27 ± 0.10	-	$0.1^{+0.6}_{-0.1}$	-	3.0
G028.825−00.229	G028.823−00.22	281.19	-3.76	111.3	0.38 ± 0.09	0.41 ± 0.09	-	$0.1^{+0.7}_{-0.1}$	-	4.4
G028.867+00.054	G028.861+00.06	280.96	-3.59	100.0	0.42 ± 0.10	0.39 ± 0.10	-	$0.1^{+0.6}_{-0.1}$	-	4.2
G028.975−00.593	G028.983−00.60	281.58	-3.79	162.3	0.32 ± 0.09	0.61 ± 0.09	-	$0.1^{+0.4}_{-0.1}$	-	8.5

Continued on next page

Name	*WISE*	RA	DEC	Radius	flux_img	flux_bkg	ν_0	α	β	Goodness
		deg	deg	arcmin	Jy	Jy	MHz			
(1)	(2)	(3)	(4)	(5)	(6)	(7)	(8)	(9)	(10)	(11)
G029.007+00.080	G029.000+00.08	281.00	-3.46	88.3	0.30 ± 0.10	0.25 ± 0.10	-	$0.1^{+0.7}_{-0.1}$	-	3.1
G029.103−00.672	G029.088−00.67	281.71	-3.71	281.5	0.34 ± 0.09	1.92 ± 0.09	$118.5^{+13.7}_{-13.6}$	$1.9^{+1.9}_{-1.2}$	$0.3^{+0.2}_{-0.2}$	6.0
G029.191−00.047	G029.165−00.03	281.19	-3.35	212.1	0.64 ± 0.10	0.65 ± 0.10	-	$0.1^{+0.3}_{-0.1}$	-	4.9
G029.850−00.086	G029.814−00.06	281.53	-2.78	194.6	0.84 ± 0.11	0.86 ± 0.11	$162.7^{+29.5}_{-23.7}$	$1.3^{+2.0}_{-0.9}$	$0.2^{+0.5}_{-0.4}$	4.1
G029.899−00.022	G029.901−00.02	281.50	-2.71	86.6	0.63 ± 0.11	0.26 ± 0.11	-	$0.2^{+0.7}_{-0.2}$	-	3.0
G029.929−00.059	G029.928−00.05	281.54	-2.70	110.0	1.67 ± 0.11	0.47 ± 0.11	-	$1.0^{+0.6}_{-0.7}$	-	2.7
G029.955−00.095	G029.955−00.09	281.59	-2.69	123.3	0.72 ± 0.11	0.56 ± 0.11	-	$0.2^{+0.8}_{-0.2}$	-	4.4
G029.954−00.029	G029.956−00.02	281.53	-2.66	73.2	0.48 ± 0.11	0.19 ± 0.11	-	$0.2^{+0.5}_{-0.1}$	-	8.3
G030.004−00.070	G030.007−00.08	281.59	-2.64	79.8	0.37 ± 0.11	0.27 ± 0.11	-	$0.3^{+1.2}_{-0.3}$	-	6.5
G030.061−00.167	G030.036−00.16	281.70	-2.63	177.2	0.82 ± 0.11	0.66 ± 0.11	-	$0.2^{+0.7}_{-0.2}$	-	4.9
G030.211−00.157	G030.212−00.15	281.76	-2.49	141.9	1.29 ± 0.12	0.56 ± 0.12	-	$0.2^{+0.3}_{-0.1}$	-	10.4

Continued on next page

Name	*WISE*	RA	DEC	Radius	flux_img	flux_bkg	ν_0	α	β	Goodness
		deg	deg	arcmin	Jy	Jy	MHz			
(1)	(2)	(3)	(4)	(5)	(6)	(7)	(8)	(9)	(10)	(11)
G030.329−00.210	G030.321−00.21	281.86	-2.41	83.5	0.41 ± 0.12	0.32 ± 0.12	-	$0.1^{+0.3}_{-0.1}$	-	4.5
G030.368−00.263	G030.338−00.25	281.92	-2.40	278.2	2.35 ± 0.11	1.90 ± 0.11	$142.5^{+13.9}_{-75.1}$	$1.8^{+1.7}_{-1.3}$	$0.3^{+0.2}_{-0.2}$	16.8
G030.440+00.426	G030.468+00.39	281.34	-2.02	200.9	0.17 ± 0.12	1.23 ± 0.12	-	$0.1^{+0.5}_{-0.1}$	-	7.0
G030.469−00.033	G030.470−00.03	281.77	-2.21	103.1	0.65 ± 0.12	0.48 ± 0.12	$157.5^{+98.1}_{-30.2}$	$1.0^{+2.2}_{-0.8}$	$0.1^{+0.6}_{-0.4}$	11.0
G030.485−00.099	G030.478−00.09	281.83	-2.22	68.3	0.28 ± 0.12	0.25 ± 0.12	-	$0.1^{+0.5}_{-0.1}$	-	2.4
G030.567−00.216	G030.546−00.17	281.97	-2.20	66.9	0.32 ± 0.12	0.23 ± 0.12	-	$0.1^{+1.1}_{-0.1}$	-	5.6
G030.542+00.027	G030.547+00.01	281.75	-2.11	85.9	0.48 ± 0.12	0.32 ± 0.12	-	$0.1^{+0.7}_{-0.1}$	-	1.4
G030.602−00.100	G030.585−00.09	281.89	-2.12	60.3	0.38 ± 0.12	0.18 ± 0.12	-	$0.2^{+0.6}_{-0.1}$	-	3.3
G030.525−00.305	G030.599−00.34	282.03	-2.28	193.4	1.19 ± 0.11	0.86 ± 0.11	-	$0.2^{+0.5}_{-0.1}$	-	5.6
G030.700−00.634	G030.613−00.61	282.41	-2.28	140.2	1.68 ± 0.11	0.56 ± 0.11	$134.9^{+27.3}_{-16.1}$	$0.9^{+1.8}_{-0.7}$	$-0.1^{+0.1}_{-0.3}$	5.6
G030.644+00.049	G030.642+00.05	281.77	-2.01	75.2	0.35 ± 0.12	0.28 ± 0.12	-	$0.1^{+0.5}_{-0.1}$	-	3.2

Continued on next page

Name	*WISE*	RA	DEC	Radius	flux_img	flux_bkg	ν_0	α	β	Goodness
		deg	deg	arcmin	Jy	Jy	MHz			
(1)	(2)	(3)	(4)	(5)	(6)	(7)	(8)	(9)	(10)	(11)
G030.736−00.029	G030.758−00.04	281.88	-1.97	305.6	13.50 ± 0.12	3.59 ± 0.12	-	$0.9^{+0.2}_{-0.2}$	-	14.0
G030.771−00.260	G030.795−00.27	282.11	-2.04	348.8	3.30 ± 0.11	2.85 ± 0.11	$163.0^{+19.0}_{-23.4}$	$1.0^{+1.0}_{-0.5}$	$0.2^{+0.3}_{-0.3}$	8.3
G030.848+00.129	G030.847+00.14	281.79	-1.80	137.9	1.38 ± 0.12	0.73 ± 0.12	$177.9^{+46.7}_{-26.0}$	$0.9^{+1.6}_{-0.6}$	$0.0^{+0.7}_{-0.5}$	7.4
G030.903+00.011	G030.905+00.01	281.92	-1.80	99.4	0.80 ± 0.12	0.38 ± 0.12	-	$0.2^{+0.6}_{-0.2}$	-	2.3
G030.994−00.018	G031.016−00.03	281.99	-1.73	148.4	1.04 ± 0.12	0.79 ± 0.12	$157.2^{+20.4}_{-14.9}$	$1.0^{+1.6}_{-0.7}$	$-0.0^{+0.3}_{-0.3}$	4.0
G030.992+00.173	G031.020+00.16	281.82	-1.65	285.4	1.41 ± 0.12	1.18 ± 0.12	$147.2^{+58.8}_{-45.8}$	$1.1^{+2.0}_{-0.8}$	$0.2^{+0.5}_{-0.3}$	11.8
G031.059+00.072	G031.051+00.08	281.94	-1.63	174.7	1.96 ± 0.12	0.91 ± 0.12	$142.1^{+15.3}_{-14.2}$	$1.2^{+1.6}_{-0.8}$	$0.2^{+0.3}_{-0.2}$	2.7
G031.138+00.272	G031.138+00.28	281.80	-1.47	96.9	0.72 ± 0.12	0.41 ± 0.12	-	$0.2^{+0.7}_{-0.1}$	-	2.8
G031.607+00.332	G031.610+00.33	281.96	-1.03	72.7	0.27 ± 0.10	0.16 ± 0.10	-	$0.1^{+1.4}_{-0.1}$	-	3.4
G031.899+01.437	G031.881+01.41	281.11	-0.26	338.8	0.72 ± 0.08	0.44 ± 0.08	-	$0.1^{+0.3}_{-0.1}$	-	13.0
G033.142−00.066	G033.051−00.07	283.01	0.16	86.4	1.11 ± 0.08	0.15 ± 0.08	$138.4^{+23.8}_{-38.7}$	$0.6^{+1.2}_{-0.4}$	$0.2^{+0.2}_{-0.1}$	11.9

Continued on next page

Name	*WISE*	RA	DEC	Radius	flux_img	flux_bkg	ν_0	α	β	Goodness
		deg	deg	arcmin	Jy	Jy	MHz			
(1)	(2)	(3)	(4)	(5)	(6)	(7)	(8)	(9)	(10)	(11)
G033.201−00.014	G033.176−00.01	282.99	0.23	101.0	0.38 ± 0.08	0.22 ± 0.08	-	$0.1^{+0.7}_{-0.1}$	-	4.5
G033.417−00.003	G033.419−00.00	283.08	0.43	52.7	0.16 ± 0.08	0.06 ± 0.08	-	$0.0^{+0.4}_{-0.0}$	-	1.7
G034.261+00.134	G034.256+00.13	283.35	1.24	80.9	0.89 ± 0.08	0.13 ± 0.08	-	$0.7^{+1.2}_{-0.6}$	-	7.0
G035.063−01.511	G035.075−01.51	285.18	1.21	135.2	0.38 ± 0.07	0.00 ± 0.07	$160.7^{+118.3}_{-40.0}$	$0.3^{+0.7}_{-0.2}$	$-0.0^{+0.3}_{-0.3}$	9.0
G035.215−01.755	G035.197−01.75	285.46	1.23	193.0	2.15 ± 0.06	-0.05 ± 0.06	-	$0.5^{+0.4}_{-0.3}$	-	6.2
G035.345−01.831	G035.380−01.85	285.59	1.31	117.3	0.63 ± 0.06	-0.03 ± 0.06	-	$0.1^{+0.3}_{-0.1}$	-	6.2
G035.645−00.034	G035.649−00.05	284.13	2.40	195.5	1.39 ± 0.08	0.51 ± 0.08	-	$0.1^{+0.4}_{-0.1}$	-	10.8
G036.293+00.716	G036.267+00.69	283.76	3.32	134.2	0.45 ± 0.08	0.19 ± 0.08	-	$0.1^{+0.5}_{-0.1}$	-	5.0
G037.028−00.212	G037.028−00.20	284.92	3.55	306.9	0.94 ± 0.08	1.92 ± 0.08	$139.6^{+24.0}_{-18.2}$	$1.3^{+1.7}_{-0.8}$	$-0.1^{+0.2}_{-0.3}$	8.5
G037.367−00.228	G037.362−00.23	285.09	3.84	81.4	0.41 ± 0.08	0.18 ± 0.08	-	$0.1^{+0.5}_{-0.1}$	-	6.9
G037.539−00.115	G037.544−00.11	285.07	4.05	81.3	0.37 ± 0.09	0.17 ± 0.09	-	$0.1^{+0.5}_{-0.1}$	-	4.7

Continued on next page

Name	*WISE*	RA	DEC	Radius	flux_img	flux_bkg	ν_0	α	β	Goodness
		deg	deg	arcmin	Jy	Jy	MHz			
(1)	(2)	(3)	(4)	(5)	(6)	(7)	(8)	(9)	(10)	(11)
G037.638−00.105	G037.641−00.11	285.10	4.14	63.7	0.34 ± 0.08	0.13 ± 0.08	-	$0.0^{+0.5}_{-0.0}$	-	4.5
G037.667+00.149	G037.677+00.15	284.89	4.28	140.4	0.59 ± 0.09	0.55 ± 0.09	$157.9^{+17.9}_{-23.0}$	$0.8^{+1.4}_{-0.6}$	$-0.0^{+0.2}_{-0.3}$	2.6
G037.751−00.106	G037.750−00.11	285.16	4.24	53.2	0.20 ± 0.08	0.09 ± 0.08	-	$0.1^{+1.0}_{-0.1}$	-	2.8
G037.763−00.215	G037.763−00.21	285.26	4.20	126.1	1.49 ± 0.08	0.50 ± 0.08	-	$0.2^{+0.5}_{-0.2}$	-	3.0
G037.862−00.310	G037.872−00.25	285.39	4.24	314.8	3.04 ± 0.08	1.20 ± 0.08	-	$0.1^{+0.4}_{-0.1}$	-	9.2
G039.250−00.063	G039.248−00.06	285.81	5.59	80.7	0.56 ± 0.09	0.17 ± 0.09	-	$0.3^{+1.6}_{-0.3}$	-	8.2
G040.503+02.539	G040.503+02.53	284.05	7.89	150.2	1.93 ± 0.08	0.13 ± 0.08	-	$0.2^{+0.3}_{-0.2}$	-	6.6
G040.521+02.596	G040.544+02.59	284.01	7.94	116.2	0.25 ± 0.08	0.05 ± 0.08	-	$0.0^{+0.7}_{-0.0}$	-	7.2
G041.096−00.198	G041.074−00.16	286.78	7.17	206.5	1.87 ± 0.09	0.32 ± 0.09	-	$0.4^{+0.5}_{-0.3}$	-	6.4
G041.232+00.360	G041.235+00.36	286.34	7.55	106.4	0.34 ± 0.09	0.11 ± 0.09	-	$0.2^{+0.9}_{-0.1}$	-	5.5
G041.516+00.032	G041.512+00.02	286.77	7.65	69.9	0.40 ± 0.09	0.08 ± 0.09	-	$0.1^{+0.7}_{-0.1}$	-	8.1

Continued on next page

Name	*WISE*	RA	DEC	Radius	flux_img	flux_bkg	ν_0	α	β	Goodness
		deg	deg	arcmin	Jy	Jy	MHz			
(1)	(2)	(3)	(4)	(5)	(6)	(7)	(8)	(9)	(10)	(11)
G041.521−00.136	G041.516−00.14	286.92	7.58	75.1	0.33 ± 0.09	0.07 ± 0.09	-	$0.2^{+1.5}_{-0.2}$	-	5.4
G042.030−00.603	G042.006−00.50	287.58	7.81	99.2	1.87 ± 0.09	0.09 ± 0.09	-	$0.1^{+0.2}_{-0.1}$	-	11.3
G042.114−00.627	G042.103−00.62	287.64	7.88	89.2	0.93 ± 0.08	0.08 ± 0.08	-	$0.2^{+0.7}_{-0.2}$	-	5.3
G042.432−00.264	G042.434−00.27	287.46	8.33	113.6	0.66 ± 0.09	0.15 ± 0.09	-	$0.4^{+1.4}_{-0.4}$	-	4.5
G043.172−00.013	G043.170−00.00	287.58	9.10	208.7	7.31 ± 0.09	0.51 ± 0.09	-	$0.6^{+0.3}_{-0.2}$	-	4.8
G043.817+00.393	G043.818+00.39	287.52	9.86	60.1	0.22 ± 0.09	0.07 ± 0.09	-	$0.1^{+0.5}_{-0.0}$	-	3.6
G044.268+00.103	G044.224+00.08	287.99	10.12	94.7	0.68 ± 0.08	0.14 ± 0.08	-	$0.2^{+0.9}_{-0.2}$	-	4.7
G044.506+00.338	G044.501+00.33	287.89	10.44	52.5	0.21 ± 0.08	0.05 ± 0.08	-	$0.1^{+0.7}_{-0.1}$	-	4.1
G045.124+00.132	G045.121+00.13	288.37	10.89	91.6	0.79 ± 0.08	0.11 ± 0.08	-	$0.7^{+1.8}_{-0.7}$	-	8.5
G045.394−00.716	G045.391−00.72	289.26	10.74	77.2	0.31 ± 0.07	0.07 ± 0.07	-	$0.1^{+0.7}_{-0.1}$	-	5.1
G045.445+00.060	G045.453+00.04	288.58	11.15	171.8	3.57 ± 0.08	0.41 ± 0.08	-	$1.3^{+0.7}_{-0.8}$	-	7.2

Continued on next page

Name	*WISE*	RA	DEC	Radius	flux_img	flux_bkg	ν_0	α	β	Goodness
		deg	deg	arcmin	Jy	Jy	MHz			
(1)	(2)	(3)	(4)	(5)	(6)	(7)	(8)	(9)	(10)	(11)
G045.472+00.125	G045.475+00.13	288.54	11.20	70.7	0.27 ± 0.08	0.08 ± 0.08	-	$0.1^{+0.7}_{-0.1}$	-	3.8
G046.494−00.238	G046.495−00.24	289.35	11.94	256.3	3.28 ± 0.08	1.09 ± 0.08	$176.6^{+15.7}_{-25.9}$	$0.9^{+0.7}_{-0.4}$	$0.2^{+0.3}_{-0.3}$	6.8
G048.550−00.005	G048.547−00.00	290.13	13.86	78.8	0.66 ± 0.10	0.18 ± 0.10	-	$0.1^{+0.5}_{-0.1}$	-	5.8
G048.600+00.048	G048.599+00.04	290.10	13.93	191.8	4.93 ± 0.10	1.08 ± 0.10	-	$0.2^{+0.3}_{-0.1}$	-	5.2
G048.629+00.230	G048.630+00.23	289.95	14.04	208.7	2.45 ± 0.09	1.07 ± 0.09	-	$0.1^{+0.4}_{-0.1}$	-	6.6
G048.924−00.288	G048.922−00.28	290.57	14.06	159.9	5.93 ± 0.10	0.76 ± 0.10	$134.4^{+30.5}_{-14.5}$	$1.0^{+1.2}_{-0.5}$	$0.5^{+0.3}_{-0.2}$	12.0
G049.000−00.304	G049.002−00.30	290.62	14.12	164.4	5.95 ± 0.10	0.71 ± 0.10	$150.7^{+18.5}_{-18.0}$	$1.2^{+1.1}_{-0.6}$	$0.4^{+0.3}_{-0.2}$	4.3
G049.050−00.256	G049.051−00.25	290.60	14.18	167.4	5.34 ± 0.10	0.66 ± 0.10	$116.9^{+14.0}_{-36.2}$	$1.4^{+1.7}_{-0.8}$	$0.5^{+0.3}_{-0.2}$	12.5
G049.393−00.289	G049.384−00.29	290.80	14.47	155.4	7.03 ± 0.10	0.76 ± 0.10	-	$1.1^{+0.4}_{-0.4}$	-	5.1
G049.405−00.186	G049.407−00.19	290.71	14.53	201.5	2.97 ± 0.10	0.99 ± 0.10	$127.6^{+86.0}_{-32.2}$	$1.1^{+1.9}_{-0.8}$	$0.4^{+0.4}_{-0.2}$	15.2
G049.430−00.476	G049.428−00.46	290.98	14.42	89.6	1.33 ± 0.10	0.21 ± 0.10	-	$1.1^{+1.5}_{-1.0}$	-	8.6

Continued on next page

Name	*WISE*	RA	DEC	Radius	flux_img	flux_bkg	ν_0	α	β	Goodness
		deg	deg	arcmin	Jy	Jy	MHz			
(1)	(2)	(3)	(4)	(5)	(6)	(7)	(8)	(9)	(10)	(11)
G049.466−00.392	G049.484−00.39	290.93	14.49	327.5	13.89 ± 0.10	1.72 ± 0.10	-	$0.5^{+0.3}_{-0.2}$	-	5.8
G049.582−00.372	G049.589−00.37	290.96	14.60	110.0	1.88 ± 0.09	0.34 ± 0.09	-	$0.5^{+1.3}_{-0.4}$	-	12.1
G049.588−00.461	G049.592−00.45	291.05	14.56	98.4	1.08 ± 0.09	0.25 ± 0.09	-	$0.7^{+1.7}_{-0.6}$	-	7.4
G049.707−00.175	G049.690−00.16	290.85	14.80	127.3	0.54 ± 0.09	0.40 ± 0.09	-	$0.1^{+0.7}_{-0.1}$	-	6.9
G050.001−00.068	G049.997−00.08	290.89	15.11	238.5	1.07 ± 0.08	1.20 ± 0.08	$133.1^{+23.7}_{-12.3}$	$1.7^{+2.2}_{-1.4}$	$-0.2^{+0.2}_{-0.4}$	9.8
G050.119−00.675	G050.137−00.66	291.50	14.93	108.8	0.75 ± 0.07	0.20 ± 0.07	-	$0.2^{+0.8}_{-0.2}$	-	5.2
G311.502+00.397	G311.489+00.39	210.92	-61.27	228.1	2.80 ± 0.29	1.85 ± 0.29	$142.6^{+20.3}_{-19.5}$	$1.6^{+1.8}_{-1.1}$	$-0.0^{+0.4}_{-0.4}$	10.6
G311.484−00.457	G311.501−00.46	211.38	-62.09	214.4	1.89 ± 0.30	1.58 ± 0.30	-	$0.3^{+0.8}_{-0.3}$	-	9.2
G311.895+00.092	G311.893+00.08	211.88	-61.45	185.3	3.66 ± 0.28	1.55 ± 0.28	-	$0.3^{+0.5}_{-0.2}$	-	6.1
G311.942+00.223	G311.991+00.21	211.90	-61.31	274.2	6.16 ± 0.27	3.47 ± 0.27	-	$0.2^{+0.3}_{-0.1}$	-	14.4
G314.085+00.488	G314.078+00.48	215.89	-60.37	241.2	1.47 ± 0.17	0.62 ± 0.17	-	$0.3^{+0.8}_{-0.2}$	-	17.3

Continued on next page

Name	*WISE*	RA	DEC	Radius	flux_img	flux_bkg	ν_0	α	β	Goodness
		deg	deg	arcmin	Jy	Jy	MHz			
(1)	(2)	(3)	(4)	(5)	(6)	(7)	(8)	(9)	(10)	(11)
G314.188+00.279	G314.184+00.26	216.24	-60.53	156.4	1.32 ± 0.17	0.32 ± 0.17	-	$0.4^{+0.8}_{-0.3}$	-	4.6
G314.216+00.339	G314.219+00.34	216.25	-60.47	107.2	0.63 ± 0.17	0.16 ± 0.17	-	$0.2^{+1.1}_{-0.2}$	-	6.9
G314.253+00.422	G314.239+00.42	216.26	-60.38	190.6	2.69 ± 0.17	0.32 ± 0.17	-	$0.2^{+0.5}_{-0.1}$	-	5.5
G316.352−00.366	G316.369−00.36	220.79	-60.29	236.6	2.72 ± 0.13	1.21 ± 0.13	-	$0.3^{+1.4}_{-0.2}$	-	8.7
G316.762−00.037	G316.796−00.05	221.25	-59.82	321.2	13.28 ± 0.13	3.20 ± 0.13	$172.5^{+21.6}_{-23.3}$	$0.9^{+0.6}_{-0.4}$	$0.2^{+0.4}_{-0.3}$	7.8
G317.090+00.151	G317.030+00.02	221.68	-59.51	1006.5	42.23 ± 0.12	38.90 ± 0.12	$111.4^{+12.6}_{-5.7}$	$1.8^{+1.4}_{-0.8}$	$0.4^{+0.2}_{-0.1}$	17.4
G317.405+00.093	G317.405+00.09	222.29	-59.43	147.9	0.90 ± 0.12	0.73 ± 0.12	-	$0.4^{+1.6}_{-0.3}$	-	3.8
G317.416−00.564	G317.426−00.56	222.89	-60.01	64.4	0.13 ± 0.11	0.10 ± 0.11	-	$0.0^{+0.6}_{-0.0}$	-	4.1
G317.551−00.269	G317.570−00.25	222.87	-59.69	272.0	1.30 ± 0.11	2.77 ± 0.11	-	$0.1^{+0.4}_{-0.1}$	-	13.2
G317.636−00.407	G317.628−00.42	223.14	-59.78	321.5	2.00 ± 0.11	2.79 ± 0.11	$169.8^{+26.1}_{-43.2}$	$1.0^{+1.7}_{-0.6}$	$0.1^{+0.4}_{-0.6}$	9.1
G317.762−00.200	G317.765−00.19	223.18	-59.53	310.4	1.53 ± 0.11	3.04 ± 0.11	-	$0.1^{+0.8}_{-0.1}$	-	6.4

Continued on next page

Name	*WISE*	RA	DEC	Radius	flux_img	flux_bkg	ν_0	α	β	Goodness
		deg	deg	arcmin	Jy	Jy	MHz			
(1)	(2)	(3)	(4)	(5)	(6)	(7)	(8)	(9)	(10)	(11)
G317.870−00.017	G317.870−00.00	223.21	-59.32	184.7	1.29 ± 0.11	1.35 ± 0.11	-	$-0.1^{+0.1}_{-0.6}$	-	12.7
G317.982−00.667	G317.979−00.67	223.99	-59.85	458.7	3.38 ± 0.10	5.38 ± 0.10	$138.6^{+17.5}_{-22.9}$	$1.1^{+1.2}_{-0.5}$	$0.1^{+0.2}_{-0.1}$	13.3
G318.067−00.443	G318.059−00.45	223.93	-59.61	162.2	0.84 ± 0.10	0.78 ± 0.10	-	$0.0^{+0.6}_{-0.0}$	-	13.0
G318.149−00.713	G318.141−00.69	224.32	-59.81	523.3	4.15 ± 0.10	6.03 ± 0.10	$95.8^{+7.3}_{-4.6}$	$2.5^{+1.5}_{-1.3}$	$0.3^{+0.1}_{-0.1}$	22.1
G318.925−00.162	G318.915−00.16	225.16	-58.96	94.4	0.66 ± 0.09	0.24 ± 0.09	-	$0.0^{+0.7}_{-0.0}$	-	5.6
G319.193−00.322	G319.188−00.32	225.77	-58.97	442.1	12.17 ± 0.08	4.78 ± 0.08	$122.7^{+27.7}_{-43.1}$	$1.8^{+1.8}_{-1.1}$	$0.2^{+0.3}_{-0.2}$	11.3
G319.351+00.021	G319.348+00.01	225.71	-58.60	189.6	2.33 ± 0.08	0.79 ± 0.08	-	$0.2^{+0.4}_{-0.1}$	-	8.0
G319.389−00.008	G319.397−00.00	225.80	-58.60	173.8	2.62 ± 0.08	0.67 ± 0.08	-	$0.3^{+0.5}_{-0.2}$	-	6.1
G319.439−00.018	G319.453−00.02	225.90	-58.59	126.4	0.60 ± 0.08	0.39 ± 0.08	-	$0.1^{+0.8}_{-0.1}$	-	7.0
G319.875+00.791	G319.884+00.79	225.88	-57.67	146.6	1.14 ± 0.08	0.34 ± 0.08	-	$0.2^{+0.6}_{-0.2}$	-	5.4
G320.128−00.488	G320.104−00.51	227.49	-58.66	187.1	1.28 ± 0.08	0.81 ± 0.08	-	$0.1^{+0.4}_{-0.1}$	-	6.1

Continued on next page

Name	*WISE*	RA	DEC	Radius	flux_img	flux_bkg	ν_0	α	β	Goodness
		deg	deg	arcmin	Jy	Jy	MHz			
(1)	(2)	(3)	(4)	(5)	(6)	(7)	(8)	(9)	(10)	(11)
G320.166+00.792	G320.163+00.79	226.35	-57.53	201.9	4.34 ± 0.07	0.67 ± 0.07	-	$0.8^{+0.4}_{-0.3}$	-	6.2
G320.190−00.165	G320.190−00.17	227.28	-58.35	152.5	0.61 ± 0.08	0.70 ± 0.08	-	$0.1^{+0.9}_{-0.1}$	-	3.8
G320.244−00.103	G320.236−00.09	227.31	-58.26	138.5	0.79 ± 0.08	0.46 ± 0.08	-	$0.1^{+0.6}_{-0.1}$	-	3.6
G320.245+00.436	G320.248+00.44	226.81	-57.80	153.8	1.51 ± 0.07	0.52 ± 0.07	$159.2^{+71.4}_{-64.4}$	$0.7^{+1.3}_{-0.5}$	$0.3^{+0.5}_{-0.3}$	21.5
G320.241−00.318	G320.255−00.32	227.52	-58.45	296.4	6.78 ± 0.08	2.42 ± 0.08	-	$0.2^{+0.2}_{-0.1}$	-	11.3
G320.253+00.185	G320.257+00.17	227.05	-58.01	88.3	0.28 ± 0.08	0.21 ± 0.08	-	$0.0^{+0.3}_{-0.0}$	-	5.9
G320.318−00.190	G320.311−00.17	227.52	-58.30	187.1	3.26 ± 0.08	0.88 ± 0.08	-	$1.3^{+0.7}_{-0.8}$	-	7.8
G320.394+00.148	G320.407+00.13	227.32	-57.97	244.7	2.43 ± 0.08	1.23 ± 0.08	-	$0.2^{+0.4}_{-0.1}$	-	5.9
G320.696+00.190	G320.692+00.18	227.77	-57.78	296.5	5.14 ± 0.07	1.83 ± 0.07	$101.6^{+9.6}_{-6.7}$	$1.8^{+1.9}_{-1.0}$	$0.4^{+0.2}_{-0.2}$	11.5
G320.784+00.254	G320.782+00.25	227.85	-57.68	145.8	1.87 ± 0.07	0.44 ± 0.07	-	$0.2^{+0.4}_{-0.1}$	-	12.7
G320.821+00.191	G320.799+00.18	227.97	-57.72	259.7	2.17 ± 0.07	0.82 ± 0.07	-	$0.1^{+0.3}_{-0.1}$	-	8.2

Continued on next page

Name	*WISE*	RA	DEC	Radius	flux_img	flux_bkg	ν_0	α	β	Goodness
		deg	deg	arcmin	Jy	Jy	MHz			
(1)	(2)	(3)	(4)	(5)	(6)	(7)	(8)	(9)	(10)	(11)
G320.887−00.639	G320.884−00.64	228.89	-58.39	116.4	0.68 ± 0.08	0.38 ± 0.08	-	$0.0^{+0.6}_{-0.0}$	-	3.7
G321.012−00.494	G321.015−00.52	228.95	-58.21	224.7	4.37 ± 0.08	1.24 ± 0.08	-	$0.5^{+0.4}_{-0.3}$	-	3.2
G321.123−00.526	G321.115−00.54	229.16	-58.17	222.9	6.20 ± 0.08	1.42 ± 0.08	-	$0.3^{+0.2}_{-0.1}$	-	9.3
G321.720+01.174	G321.725+01.16	228.46	-56.41	79.0	0.21 ± 0.06	0.03 ± 0.06	-	$0.1^{+1.0}_{-0.1}$	-	6.0
G322.056+00.627	G322.036+00.62	229.50	-56.70	334.2	2.65 ± 0.06	1.17 ± 0.06	$99.5^{+9.8}_{-20.3}$	$1.9^{+1.8}_{-1.2}$	$0.3^{+0.2}_{-0.2}$	37.9
G322.160+00.641	G322.162+00.62	229.64	-56.64	157.1	2.37 ± 0.06	0.29 ± 0.06	-	$0.4^{+0.4}_{-0.2}$	-	8.9
G322.205+00.499	G322.220+00.50	229.85	-56.73	400.1	3.92 ± 0.06	1.70 ± 0.06	$96.6^{+15.7}_{-8.5}$	$2.0^{+1.7}_{-1.1}$	$0.4^{+0.2}_{-0.1}$	4.9
G322.399+00.211	G322.396+00.20	230.43	-56.87	115.9	0.63 ± 0.06	0.25 ± 0.06	-	$0.1^{+0.5}_{-0.1}$	-	4.6
G323.750−00.242	G323.743−00.24	232.93	-56.49	89.5	0.18 ± 0.06	0.16 ± 0.06	-	$0.0^{+0.6}_{-0.0}$	-	4.1
G323.812+00.018	G323.806+00.02	232.76	-56.24	74.4	0.43 ± 0.06	0.15 ± 0.06	-	$0.1^{+0.6}_{-0.1}$	-	4.3
G323.914−00.015	G323.936−00.03	232.94	-56.21	296.1	2.13 ± 0.06	1.61 ± 0.06	-	$-0.0^{+0.0}_{-0.4}$	-	8.2

Continued on next page

Name	*WISE*	RA	DEC	Radius	flux_img	flux_bkg	ν_0	α	β	Goodness
		deg	deg	arcmin	Jy	Jy	MHz			
(1)	(2)	(3)	(4)	(5)	(6)	(7)	(8)	(9)	(10)	(11)
G324.137+00.241	G324.135+00.23	233.00	-55.87	256.8	3.52 ± 0.06	1.47 ± 0.06	$175.8^{+122.8}_{-79.4}$	$0.6^{+0.9}_{-0.3}$	$0.3^{+0.5}_{-0.4}$	20.8
G324.199+00.115	G324.201+00.11	233.22	-55.94	95.0	0.37 ± 0.06	0.25 ± 0.06	-	$0.1^{+1.9}_{-0.1}$	-	5.8
G324.139−00.919	G324.219−01.00	234.22	-56.82	281.3	1.01 ± 0.05	0.84 ± 0.05	-	$0.2^{+0.4}_{-0.1}$	-	13.3
G324.646−00.320	G324.642−00.32	234.33	-56.03	108.3	0.38 ± 0.05	0.27 ± 0.05	-	$0.2^{+0.9}_{-0.1}$	-	6.6
G325.117+00.025	G325.108+00.05	234.64	-55.48	123.6	0.30 ± 0.05	0.28 ± 0.05	-	$0.1^{+0.5}_{-0.1}$	-	4.4
G325.351−00.011	G325.354−00.03	235.01	-55.37	200.4	0.69 ± 0.05	0.61 ± 0.05	-	$0.2^{+0.9}_{-0.1}$	-	7.0
G326.040−00.500	G326.036−00.49	236.49	-55.34	195.3	0.88 ± 0.10	0.98 ± 0.10	-	$0.1^{+0.5}_{-0.1}$	-	5.3
G326.069−00.406	G326.065−00.39	236.43	-55.25	192.8	1.32 ± 0.10	0.91 ± 0.10	-	$0.2^{+0.7}_{-0.2}$	-	5.4
G326.233+00.795	G326.270+00.78	235.40	-54.19	817.2	17.97 ± 0.06	8.72 ± 0.06	$138.9^{+4.1}_{-3.3}$	$1.3^{+0.6}_{-0.4}$	$0.3^{+0.1}_{-0.1}$	13.5
G326.447+00.899	G326.446+00.90	235.58	-53.98	142.1	1.59 ± 0.06	0.39 ± 0.06	-	$0.7^{+0.5}_{-0.4}$	-	2.4
G326.498−00.288	G326.474−00.29	236.90	-54.89	1165.3	64.77 ± 0.11	45.50 ± 0.11	$109.6^{+11.9}_{-8.0}$	$2.5^{+1.6}_{-1.3}$	$-0.0^{+0.1}_{-0.2}$	2.5

Continued on next page

Name	*WISE*	RA	DEC	Radius	flux_img	flux_bkg	ν_0	α	β	Goodness
		deg	deg	arcmin	Jy	Jy	MHz			
(1)	(2)	(3)	(4)	(5)	(6)	(7)	(8)	(9)	(10)	(11)
G326.683+00.514	G326.643+00.51	236.30	-54.14	428.7	22.15 ± 0.08	5.09 ± 0.08	$126.8^{+9.5}_{-16.9}$	$1.7^{+1.3}_{-0.8}$	$0.9^{+0.3}_{-0.3}$	9.4
G326.717+00.777	G326.721+00.77	236.07	-53.91	153.4	0.42 ± 0.07	0.63 ± 0.07	$134.5^{+99.7}_{-80.0}$	$0.8^{+2.0}_{-0.7}$	$0.1^{+0.5}_{-0.2}$	14.6
G326.701−00.640	G326.722−00.67	237.55	-55.04	512.3	10.47 ± 0.11	7.14 ± 0.11	$124.0^{+29.0}_{-25.0}$	$2.0^{+1.8}_{-1.2}$	$0.1^{+0.2}_{-0.3}$	4.6
G327.002−00.303	G326.900−00.34	237.60	-54.59	292.7	3.77 ± 0.11	3.15 ± 0.11	-	$0.4^{+0.5}_{-0.2}$	-	3.2
G326.953+00.041	G326.951+00.00	237.16	-54.35	380.4	5.78 ± 0.10	4.21 ± 0.10	-	$0.2^{+0.2}_{-0.1}$	-	6.4
G327.049+00.375	G327.006+00.41	236.93	-54.03	192.5	1.16 ± 0.08	0.84 ± 0.08	$97.4^{+28.7}_{-59.1}$	$1.8^{+2.0}_{-1.4}$	$0.1^{+0.2}_{-0.1}$	14.3
G326.999−00.140	G327.078+00.05	237.42	-54.46	650.3	9.94 ± 0.10	10.01 ± 0.10	$119.5^{+38.5}_{-55.8}$	$1.5^{+1.8}_{-0.9}$	$0.6^{+0.3}_{-0.2}$	19.2
G327.180−00.520	G327.172−00.52	238.07	-54.64	463.0	11.99 ± 0.10	10.56 ± 0.10	$91.8^{+59.6}_{-44.4}$	$1.8^{+1.8}_{-1.2}$	$0.7^{+0.4}_{-0.3}$	12.4
G327.304−00.545	G327.300−00.54	238.26	-54.59	157.8	3.36 ± 0.10	1.07 ± 0.10	-	$1.0^{+0.5}_{-0.5}$	-	3.2
G327.401−00.627	G327.454−00.63	238.48	-54.59	502.5	5.08 ± 0.09	5.03 ± 0.09	-	$0.3^{+0.3}_{-0.2}$	-	7.4
G327.571−00.831	G327.555−00.82	238.93	-54.64	258.6	1.04 ± 0.07	2.13 ± 0.07	$159.3^{+14.0}_{-39.4}$	$1.7^{+1.8}_{-1.0}$	$0.1^{+0.3}_{-0.3}$	10.9

Continued on next page

Name	*WISE*	RA	DEC	Radius	flux_img	flux_bkg	ν_0	α	β	Goodness
		deg	deg	arcmin	Jy	Jy	MHz			
(1)	(2)	(3)	(4)	(5)	(6)	(7)	(8)	(9)	(10)	(11)
G327.583−00.371	G327.582−00.37	238.44	-54.27	152.4	1.72 ± 0.09	1.29 ± 0.09	$148.4^{+59.2}_{-100.4}$	$1.1^{+1.9}_{-1.0}$	$0.2^{+0.4}_{-0.3}$	18.4
G327.638−00.342	G327.651−00.33	238.49	-54.22	136.0	1.34 ± 0.08	1.04 ± 0.08	$99.7^{+121.2}_{-55.0}$	$1.1^{+2.1}_{-1.1}$	$0.2^{+0.5}_{-0.2}$	32.3
G327.738−00.393	G327.735−00.39	238.67	-54.19	126.2	0.69 ± 0.08	0.90 ± 0.08	-	$0.1^{+0.7}_{-0.1}$	-	2.8
G327.754+00.174	G327.763+00.16	238.08	-53.74	168.0	1.50 ± 0.07	1.45 ± 0.07	-	$0.0^{+0.6}_{-0.0}$	-	5.3
G327.778−00.340	G327.770−00.34	238.67	-54.13	161.5	1.61 ± 0.08	1.34 ± 0.08	-	$0.4^{+0.8}_{-0.3}$	-	2.1
G327.829+00.116	G327.824+00.11	238.24	-53.74	216.0	4.13 ± 0.07	3.12 ± 0.07	-	$0.1^{+0.4}_{-0.1}$	-	11.5
G327.824−00.153	G327.838−00.14	238.52	-53.95	137.8	1.00 ± 0.08	1.06 ± 0.08	-	$0.1^{+0.6}_{-0.1}$	-	2.2
G327.881−00.045	G327.889−00.04	238.48	-53.83	321.6	4.33 ± 0.07	5.79 ± 0.07	$113.8^{+28.2}_{-13.0}$	$1.9^{+1.9}_{-1.2}$	$0.1^{+0.1}_{-0.1}$	6.1
G327.978−00.094	G327.991−00.08	238.66	-53.81	189.1	3.67 ± 0.07	2.40 ± 0.07	$100.0^{+60.7}_{-40.4}$	$1.4^{+2.2}_{-1.0}$	$0.4^{+0.3}_{-0.2}$	11.8
G328.039+00.301	G328.043+00.29	238.32	-53.46	77.1	0.97 ± 0.07	0.37 ± 0.07	-	$0.0^{+0.7}_{-0.0}$	-	7.1
G328.112+00.111	G328.117+00.10	238.62	-53.57	132.8	1.25 ± 0.07	1.27 ± 0.07	-	$0.0^{+0.4}_{-0.0}$	-	6.9

Continued on next page

Name	*WISE*	RA	DEC	Radius	flux_img	flux_bkg	ν_0	α	β	Goodness
		deg	deg	arcmin	Jy	Jy	MHz			
(1)	(2)	(3)	(4)	(5)	(6)	(7)	(8)	(9)	(10)	(11)
G328.122+00.572	G328.117+00.57	238.14	-53.20	139.4	0.62 ± 0.07	1.00 ± 0.07	-	$0.1^{+1.0}_{-0.1}$	-	3.7
G328.191−00.478	G328.193−00.47	239.36	-53.97	88.2	0.33 ± 0.07	0.38 ± 0.07	-	$0.0^{+0.5}_{-0.0}$	-	5.1
G328.184−00.590	G328.193−00.56	239.47	-54.06	192.7	1.10 ± 0.07	1.12 ± 0.07	$174.3^{+33.0}_{-47.0}$	$1.4^{+1.9}_{-0.9}$	$0.3^{+0.5}_{-0.6}$	7.8
G328.306−00.555	G328.279−00.55	239.59	-53.95	227.2	1.87 ± 0.07	1.77 ± 0.07	$185.3^{+85.9}_{-45.6}$	$1.1^{+1.8}_{-0.7}$	$0.4^{+0.7}_{-0.6}$	7.6
G328.286+00.460	G328.286+00.46	238.47	-53.19	232.0	5.87 ± 0.07	2.88 ± 0.07	-	$0.4^{+0.5}_{-0.2}$	-	1.7
G328.557−00.526	G328.572−00.52	239.88	-53.77	187.6	2.07 ± 0.06	1.37 ± 0.06	-	$0.4^{+0.4}_{-0.2}$	-	4.0
G328.809−00.079	G328.807−00.07	239.72	-53.26	175.2	1.73 ± 0.07	1.96 ± 0.07	-	$0.1^{+0.7}_{-0.1}$	-	7.1
G328.946+00.565	G328.945+00.57	239.20	-52.68	113.6	0.53 ± 0.07	0.61 ± 0.07	-	$0.2^{+0.8}_{-0.2}$	-	4.6
G328.962+00.224	G328.962+00.20	239.58	-52.93	165.1	0.77 ± 0.06	1.11 ± 0.06	-	$0.2^{+1.1}_{-0.2}$	-	6.5
G330.281−00.390	G330.290−00.39	241.89	-52.52	117.9	0.30 ± 0.06	0.54 ± 0.06	-	$0.1^{+0.8}_{-0.1}$	-	5.7
G330.673−00.388	G330.673−00.38	242.36	-52.26	138.4	1.29 ± 0.07	1.04 ± 0.07	$158.5^{+66.2}_{-83.7}$	$0.9^{+1.8}_{-0.8}$	$0.4^{+0.6}_{-0.3}$	44.5

Continued on next page

Name	*WISE*	RA	DEC	Radius	flux_img	flux_bkg	ν_0	α	β	Goodness
		deg	deg	arcmin	Jy	Jy	MHz			
(1)	(2)	(3)	(4)	(5)	(6)	(7)	(8)	(9)	(10)	(11)
G330.724−00.438	G330.738−00.44	242.48	-52.26	138.8	0.88 ± 0.07	0.93 ± 0.07	-	$0.1^{+0.3}_{-0.1}$	-	7.4
G330.802−00.400	G330.775−00.39	242.53	-52.18	262.1	2.91 ± 0.07	2.80 ± 0.07	$128.5^{+20.8}_{-10.3}$	$1.4^{+1.6}_{-0.8}$	$0.4^{+0.2}_{-0.2}$	10.7
G330.872−00.359	G330.873−00.36	242.57	-52.10	153.2	3.24 ± 0.07	1.23 ± 0.07	-	$0.5^{+0.3}_{-0.2}$	-	4.1
G330.994−00.430	G330.986−00.43	242.79	-52.07	516.4	8.23 ± 0.08	10.53 ± 0.08	$104.3^{+8.6}_{-6.3}$	$2.3^{+1.5}_{-1.1}$	$0.4^{+0.1}_{-0.1}$	7.2
G331.020−00.138	G331.020−00.14	242.50	-51.84	281.3	7.36 ± 0.08	4.56 ± 0.08	$147.0^{+18.4}_{-14.6}$	$1.3^{+1.3}_{-0.7}$	$0.4^{+0.3}_{-0.2}$	2.0
G331.112−00.242	G331.120−00.24	242.72	-51.85	314.6	5.67 ± 0.08	4.56 ± 0.08	$142.6^{+13.2}_{-12.2}$	$1.2^{+1.1}_{-0.6}$	$0.4^{+0.2}_{-0.2}$	3.4
G331.131−00.519	G331.123−00.53	243.05	-52.04	178.8	2.78 ± 0.08	1.46 ± 0.08	-	$0.2^{+0.3}_{-0.1}$	-	3.3
G331.154−00.388	G331.156−00.39	242.93	-51.93	174.5	1.81 ± 0.08	1.46 ± 0.08	-	$0.2^{+0.3}_{-0.1}$	-	8.1
G331.175−00.456	G331.172−00.46	243.03	-51.97	130.5	1.02 ± 0.08	0.82 ± 0.08	-	$0.2^{+0.4}_{-0.1}$	-	4.5
G331.238+01.080	G331.249+01.07	241.45	-50.79	135.6	0.68 ± 0.06	0.50 ± 0.06	-	$0.2^{+0.5}_{-0.1}$	-	2.0
G331.263−00.469	G331.256−00.48	243.15	-51.91	267.3	1.90 ± 0.08	3.37 ± 0.08	$144.6^{+12.9}_{-12.5}$	$1.7^{+1.6}_{-0.9}$	$0.0^{+0.2}_{-0.2}$	5.2

Continued on next page

Name	*WISE*	RA	DEC	Radius	flux_img	flux_bkg	ν_0	α	β	Goodness
		deg	deg	arcmin	Jy	Jy	MHz			
(1)	(2)	(3)	(4)	(5)	(6)	(7)	(8)	(9)	(10)	(11)
G331.262−00.186	G331.259−00.18	242.84	-51.71	197.3	3.36 ± 0.09	2.12 ± 0.09	$141.3^{+50.6}_{-62.3}$	$1.1^{+2.0}_{-0.8}$	$0.4^{+0.4}_{-0.3}$	17.0
G331.275+00.181	G331.280+00.19	242.45	-51.43	111.9	0.35 ± 0.09	0.65 ± 0.09	-	$0.1^{+0.9}_{-0.1}$	-	2.9
G331.345−00.342	G331.338−00.36	243.11	-51.77	260.7	6.57 ± 0.09	3.70 ± 0.09	$143.4^{+24.1}_{-17.3}$	$1.2^{+1.3}_{-0.6}$	$0.5^{+0.3}_{-0.2}$	4.2
G331.361+01.066	G331.344+01.05	241.61	-50.72	207.4	1.44 ± 0.06	0.99 ± 0.06	$155.5^{+21.6}_{-16.9}$	$1.1^{+1.3}_{-0.6}$	$0.2^{+0.2}_{-0.2}$	4.9
G331.359−00.017	G331.361−00.01	242.77	-51.52	174.9	3.76 ± 0.09	1.76 ± 0.09	$134.7^{+59.8}_{-62.1}$	$1.1^{+1.9}_{-0.7}$	$0.5^{+0.5}_{-0.3}$	7.2
G331.368+00.523	G331.365+00.52	242.19	-51.12	318.0	0.75 ± 0.08	4.09 ± 0.08	$135.3^{+10.0}_{-8.3}$	$2.3^{+1.6}_{-1.2}$	$0.4^{+0.2}_{-0.2}$	4.0
G331.408+00.023	G331.412+00.01	242.78	-51.46	118.8	1.21 ± 0.09	0.66 ± 0.09	-	$0.1^{+0.4}_{-0.1}$	-	5.8
G331.526−00.081	G331.520−00.07	243.03	-51.45	267.0	12.32 ± 0.09	3.02 ± 0.09	-	$0.7^{+0.3}_{-0.3}$	-	2.7
G331.570−00.015	G331.580−00.02	243.01	-51.37	386.6	11.14 ± 0.09	6.01 ± 0.09	$126.9^{+36.6}_{-40.4}$	$1.5^{+1.8}_{-0.8}$	$0.6^{+0.3}_{-0.2}$	4.1
G332.070−01.124	G331.628−00.92	244.83	-51.83	791.4	0.77 ± 0.07	5.24 ± 0.07	$122.4^{+22.6}_{-10.7}$	$2.1^{+1.8}_{-1.2}$	$0.0^{+0.1}_{-0.2}$	7.7
G331.652+00.132	G331.653+00.12	242.95	-51.21	141.5	1.22 ± 0.09	1.07 ± 0.09	-	$0.2^{+0.9}_{-0.2}$	-	3.4

Continued on next page

Name	*WISE*	RA	DEC	Radius	flux_img	flux_bkg	ν_0	α	β	Goodness
		deg	deg	arcmin	Jy	Jy	MHz			
(1)	(2)	(3)	(4)	(5)	(6)	(7)	(8)	(9)	(10)	(11)
G331.754−00.072	G331.744−00.06	243.29	-51.29	119.0	0.85 ± 0.09	0.72 ± 0.09	-	$0.1^{+1.0}_{-0.1}$	-	2.2
G331.805−00.165	G331.797−00.14	243.45	-51.32	63.5	0.22 ± 0.10	0.18 ± 0.10	-	$-0.0^{+0.2}_{-0.1}$	-	1.4
G331.825−00.003	G331.834−00.00	243.30	-51.19	124.1	0.71 ± 0.09	0.87 ± 0.09	-	$0.0^{+0.7}_{-0.0}$	-	2.5
G332.137−00.441	G332.145−00.45	244.14	-51.29	192.1	3.60 ± 0.10	1.82 ± 0.10	-	$1.0^{+0.6}_{-0.5}$	-	2.6
G332.428−00.675	G332.394−00.66	244.74	-51.26	280.0	1.23 ± 0.09	3.32 ± 0.09	$132.4^{+13.0}_{-15.7}$	$1.9^{+1.8}_{-1.1}$	$0.1^{+0.2}_{-0.2}$	6.0
G332.545−00.154	G332.554−00.15	244.29	-50.80	179.4	1.07 ± 0.09	1.29 ± 0.09	$170.5^{+17.7}_{-31.7}$	$1.2^{+1.7}_{-0.8}$	$-0.1^{+0.4}_{-0.5}$	5.4
G332.663−00.622	G332.657−00.62	244.94	-51.05	232.1	6.54 ± 0.09	2.05 ± 0.09	$183.4^{+16.9}_{-13.0}$	$1.6^{+0.7}_{-0.6}$	$0.6^{+0.4}_{-0.4}$	4.2
G332.768−00.599	G332.762−00.59	245.04	-50.96	399.3	14.77 ± 0.09	6.00 ± 0.09	$124.2^{+11.2}_{-9.0}$	$1.8^{+1.5}_{-0.8}$	$0.9^{+0.3}_{-0.3}$	8.4
G332.923−00.451	G332.918−00.45	245.05	-50.75	241.3	6.71 ± 0.09	3.14 ± 0.09	$157.3^{+8.5}_{-7.5}$	$2.1^{+1.0}_{-0.8}$	$0.5^{+0.2}_{-0.2}$	3.2
G332.943−00.293	G332.956−00.31	244.89	-50.62	404.7	9.25 ± 0.09	7.35 ± 0.09	$132.8^{+6.6}_{-5.3}$	$2.6^{+1.3}_{-1.1}$	$0.5^{+0.2}_{-0.2}$	7.0
G332.983+00.782	G332.978+00.77	243.77	-49.82	193.5	3.36 ± 0.06	1.34 ± 0.06	$129.6^{+56.2}_{-67.6}$	$1.1^{+2.0}_{-0.8}$	$0.7^{+0.5}_{-0.3}$	6.5

Continued on next page

Name	*WISE*	RA	DEC	Radius	flux_img	flux_bkg	ν_0	α	β	Goodness
		deg	deg	arcmin	Jy	Jy	MHz			
(1)	(2)	(3)	(4)	(5)	(6)	(7)	(8)	(9)	(10)	(11)
G332.985+00.905	G332.987+00.90	243.64	-49.73	82.3	0.10 ± 0.06	0.14 ± 0.06	-	$0.1^{+1.1}_{-0.1}$	-	3.0
G332.989−00.631	G332.990−00.61	245.32	-50.83	234.8	3.77 ± 0.09	2.19 ± 0.09	$181.9^{+18.2}_{-15.1}$	$1.1^{+0.8}_{-0.5}$	$0.2^{+0.4}_{-0.4}$	3.8
G333.034−00.440	G333.011−00.44	245.16	-50.66	181.4	5.26 ± 0.09	1.27 ± 0.09	-	$1.2^{+0.3}_{-0.3}$	-	8.4
G333.070+00.030	G333.052+00.03	244.68	-50.30	324.4	2.46 ± 0.09	5.04 ± 0.09	$124.0^{+16.2}_{-9.0}$	$1.5^{+1.7}_{-0.9}$	$0.1^{+0.1}_{-0.1}$	4.5
G333.030+01.770	G333.053+01.74	242.78	-49.07	410.5	2.71 ± 0.05	2.54 ± 0.05	$117.7^{+13.3}_{-15.8}$	$1.3^{+1.7}_{-0.7}$	$0.2^{+0.2}_{-0.1}$	9.3
G333.070−00.483	G333.074−00.48	245.25	-50.67	213.4	8.84 ± 0.09	2.13 ± 0.09	-	$1.3^{+0.3}_{-0.3}$	-	6.1
G333.111+01.992	G333.093+01.96	242.64	-48.85	565.0	3.23 ± 0.05	1.32 ± 0.05	$143.2^{+8.4}_{-9.7}$	$1.0^{+0.9}_{-0.5}$	$0.2^{+0.1}_{-0.1}$	9.2
G333.093−00.759	G333.094−00.77	245.58	-50.85	162.9	0.93 ± 0.08	0.87 ± 0.08	$115.9^{+36.2}_{-53.9}$	$1.0^{+1.9}_{-0.8}$	$0.3^{+0.3}_{-0.2}$	5.3
G333.127−00.435	G333.129−00.43	245.26	-50.59	134.5	3.36 ± 0.09	0.89 ± 0.09	-	$1.3^{+0.4}_{-0.4}$	-	9.1
G333.187−00.069	G333.173−00.06	244.92	-50.29	263.5	4.95 ± 0.09	3.74 ± 0.09	$117.8^{+53.7}_{-43.2}$	$1.2^{+1.6}_{-0.7}$	$0.4^{+0.3}_{-0.2}$	19.9
G333.220−00.302	G333.215−00.29	245.21	-50.43	298.0	7.57 ± 0.09	4.80 ± 0.09	-	$0.3^{+0.2}_{-0.1}$	-	9.6

Continued on next page

Name	*WISE*	RA	DEC	Radius	flux_img	flux_bkg	ν_0	α	β	Goodness
		deg	deg	arcmin	Jy	Jy	MHz			
(1)	(2)	(3)	(4)	(5)	(6)	(7)	(8)	(9)	(10)	(11)
G333.235−00.492	G333.245−00.48	245.44	-50.56	335.8	8.43 ± 0.09	3.31 ± 0.09	-	$0.4^{+0.3}_{-0.2}$	-	3.6
G333.257+00.054	G333.255+00.06	244.86	-50.16	140.5	0.95 ± 0.09	0.76 ± 0.09	-	$0.4^{+1.2}_{-0.3}$	-	3.2
G333.296−00.385	G333.288−00.39	245.39	-50.44	221.0	4.96 ± 0.09	1.59 ± 0.09	-	$0.6^{+0.3}_{-0.3}$	-	7.0
G333.472−00.148	G333.467−00.15	245.32	-50.15	148.9	0.97 ± 0.08	0.91 ± 0.08	-	$0.2^{+0.6}_{-0.1}$	-	4.0
G333.521−00.393	G333.534−00.38	245.65	-50.29	216.5	1.67 ± 0.08	1.20 ± 0.08	-	$0.2^{+0.3}_{-0.1}$	-	7.1
G333.571+00.054	G333.580+00.05	245.21	-49.93	277.8	4.89 ± 0.08	3.07 ± 0.08	$124.2^{+25.9}_{-16.7}$	$2.0^{+1.8}_{-1.3}$	$-0.1^{+0.2}_{-0.4}$	6.9
G333.594−00.083	G333.593−00.09	245.39	-50.02	193.2	4.74 ± 0.08	1.56 ± 0.08	$151.3^{+23.2}_{-20.4}$	$1.0^{+0.8}_{-0.4}$	$0.5^{+0.3}_{-0.2}$	4.3
G333.562−00.290	G333.594−00.29	245.58	-50.18	338.7	6.02 ± 0.08	3.32 ± 0.08	$135.4^{+18.2}_{-9.0}$	$1.4^{+1.2}_{-0.6}$	$0.6^{+0.3}_{-0.2}$	7.9
G333.626−00.211	G333.627−00.19	245.56	-50.08	236.2	10.82 ± 0.08	2.28 ± 0.08	-	$0.9^{+0.2}_{-0.2}$	-	3.0
G333.684−00.467	G333.683−00.51	245.91	-50.22	218.7	2.05 ± 0.08	1.21 ± 0.08	-	$0.2^{+0.4}_{-0.1}$	-	4.0
G334.197+00.199	G334.202+00.19	245.74	-49.39	94.9	0.40 ± 0.07	0.30 ± 0.07	-	$0.1^{+0.9}_{-0.1}$	-	2.2

Continued on next page

Name	*WISE*	RA	DEC	Radius	flux_img	flux_bkg	ν_0	α	β	Goodness
		deg	deg	arcmin	Jy	Jy	MHz			
(1)	(2)	(3)	(4)	(5)	(6)	(7)	(8)	(9)	(10)	(11)
G334.525+00.822	G334.521+00.81	245.42	-48.72	181.1	0.78 ± 0.06	0.41 ± 0.06	-	$0.1^{+0.3}_{-0.1}$	-	9.0
G334.697−00.100	G334.698−00.09	246.60	-49.24	154.3	2.13 ± 0.08	1.01 ± 0.08	-	$0.1^{+0.6}_{-0.1}$	-	4.2
G334.718−00.652	G334.721−00.65	247.23	-49.61	75.5	0.23 ± 0.07	0.11 ± 0.07	-	$0.2^{+1.2}_{-0.2}$	-	3.6
G334.784−00.025	G334.774−00.02	246.61	-49.13	118.4	0.73 ± 0.08	0.45 ± 0.08	-	$0.1^{+0.3}_{-0.0}$	-	4.9
G335.740−00.137	G335.748−00.16	247.74	-48.51	396.7	7.87 ± 0.09	4.72 ± 0.09	$167.7^{+11.2}_{-18.0}$	$1.0^{+0.8}_{-0.4}$	$0.0^{+0.3}_{-0.3}$	7.5
G335.908+00.174	G335.794+00.15	247.57	-48.18	580.2	7.01 ± 0.09	6.11 ± 0.09	$170.6^{+63.7}_{-40.4}$	$1.0^{+1.6}_{-0.6}$	$0.2^{+0.6}_{-0.5}$	12.2
G336.096−00.025	G336.097+00.00	247.98	-48.18	284.7	4.00 ± 0.09	3.45 ± 0.09	$156.8^{+27.4}_{-24.8}$	$1.3^{+2.1}_{-0.9}$	$-0.1^{+0.4}_{-0.5}$	2.1
G336.386+00.478	G336.410+00.38	247.73	-47.62	374.7	1.13 ± 0.09	3.67 ± 0.09	$132.8^{+10.4}_{-10.0}$	$2.0^{+1.7}_{-1.2}$	$-0.2^{+0.2}_{-0.3}$	5.5
G336.456−00.202	G336.446−00.19	248.54	-48.03	577.4	34.06 ± 0.09	16.18 ± 0.09	$110.2^{+25.2}_{-12.0}$	$1.7^{+1.5}_{-0.8}$	$0.4^{+0.2}_{-0.2}$	11.5
G336.455+00.043	G336.455+00.04	248.27	-47.87	182.8	2.96 ± 0.09	1.63 ± 0.09	-	$0.2^{+0.5}_{-0.1}$	-	8.0
G336.495−01.481	G336.491−01.47	250.01	-48.86	93.8	0.53 ± 0.06	0.14 ± 0.06	-	$0.2^{+0.5}_{-0.2}$	-	5.5

Continued on next page

Name	*WISE*	RA	DEC	Radius	flux_img	flux_bkg	ν_0	α	β	Goodness
		deg	deg	arcmin	Jy	Jy	MHz			
(1)	(2)	(3)	(4)	(5)	(6)	(7)	(8)	(9)	(10)	(11)
G336.513+00.117	G336.518+00.11	248.25	-47.78	183.2	3.03 ± 0.09	1.72 ± 0.09	$106.5^{+51.4}_{-31.4}$	$1.5^{+2.0}_{-1.2}$	$0.1^{+0.3}_{-0.1}$	3.3
G336.539−01.794	G336.559−01.79	250.41	-49.04	232.8	0.92 ± 0.06	0.31 ± 0.06	$170.5^{+12.2}_{-32.0}$	$0.6^{+0.7}_{-0.3}$	$-0.2^{+0.3}_{-0.3}$	17.8
G336.584+00.006	G336.585+00.01	248.44	-47.80	154.1	2.09 ± 0.09	1.49 ± 0.09	-	$0.1^{+0.5}_{-0.1}$	-	6.5
G336.807+00.091	G336.753+00.09	248.58	-47.58	486.0	28.85 ± 0.09	9.14 ± 0.09	-	$0.3^{+0.2}_{-0.1}$	-	8.3
G337.134−00.160	G337.120−00.18	249.18	-47.51	195.1	9.02 ± 0.10	1.97 ± 0.10	-	$0.1^{+0.2}_{-0.1}$	-	10.5
G337.435−00.393	G337.428−00.40	249.73	-47.44	153.2	2.64 ± 0.09	1.08 ± 0.09	$96.4^{+81.8}_{-65.6}$	$1.4^{+2.4}_{-1.3}$	$0.0^{+0.1}_{-0.4}$	10.2
G337.529−00.259	G337.496−00.25	249.68	-47.28	321.3	4.06 ± 0.09	4.24 ± 0.09	$165.0^{+10.2}_{-14.7}$	$1.0^{+1.0}_{-0.5}$	$-0.2^{+0.2}_{-0.3}$	4.6
G337.632−00.054	G337.652−00.05	249.55	-47.07	244.5	6.30 ± 0.09	2.53 ± 0.09	$153.7^{+13.3}_{-18.8}$	$1.2^{+1.3}_{-0.7}$	$0.1^{+0.3}_{-0.2}$	4.0
G337.675−00.341	G337.684−00.34	249.91	-47.22	148.4	1.33 ± 0.09	1.07 ± 0.09	-	$0.2^{+0.5}_{-0.1}$	-	4.3
G337.964−00.456	G337.957−00.47	250.32	-47.08	286.6	6.03 ± 0.08	2.70 ± 0.08	-	$0.5^{+0.4}_{-0.3}$	-	1.8
G337.989−00.125	G338.003−00.12	249.98	-46.85	259.5	8.46 ± 0.09	2.49 ± 0.09	$161.9^{+16.4}_{-24.7}$	$0.8^{+0.8}_{-0.4}$	$-0.1^{+0.3}_{-0.3}$	7.8

Continued on next page

Name	*WISE*	RA	DEC	Radius	flux_img	flux_bkg	ν_0	α	β	Goodness
		deg	deg	arcmin	Jy	Jy	MHz			
(1)	(2)	(3)	(4)	(5)	(6)	(7)	(8)	(9)	(10)	(11)
G338.124−00.186	G338.114−00.19	250.18	-46.79	249.3	9.22 ± 0.09	2.93 ± 0.09	$121.8^{+23.1}_{-19.3}$	$1.8^{+2.0}_{-1.2}$	$0.0^{+0.2}_{-0.3}$	4.1
G338.359+00.207	G338.350+00.22	249.98	-46.35	318.2	13.64 ± 0.08	3.54 ± 0.08	$94.5^{+51.2}_{-41.7}$	$1.5^{+2.0}_{-1.0}$	$0.5^{+0.4}_{-0.2}$	6.3
G338.409−00.197	G338.405−00.20	250.46	-46.58	148.9	2.21 ± 0.08	1.12 ± 0.08	-	$0.3^{+0.9}_{-0.2}$	-	3.0
G338.463−00.256	G338.462−00.26	250.58	-46.58	134.8	1.45 ± 0.08	1.01 ± 0.08	-	$0.0^{+0.6}_{-0.0}$	-	3.9
G338.719+00.615	G338.706+00.64	249.88	-45.81	254.4	2.10 ± 0.07	1.50 ± 0.07	$130.8^{+22.7}_{-30.9}$	$1.3^{+1.8}_{-0.8}$	$0.4^{+0.3}_{-0.2}$	6.2
G338.898+00.612	G338.911+00.61	250.05	-45.68	290.3	5.70 ± 0.07	2.41 ± 0.07	$148.7^{+26.6}_{-17.7}$	$1.3^{+1.3}_{-0.6}$	$0.6^{+0.3}_{-0.3}$	4.9
G338.929+00.394	G338.926+00.39	250.32	-45.80	107.0	0.70 ± 0.07	0.52 ± 0.07	-	$0.1^{+0.7}_{-0.1}$	-	2.7
G338.927−00.066	G338.934−00.06	250.81	-46.10	163.1	1.88 ± 0.07	1.40 ± 0.07	$174.0^{+34.1}_{-25.5}$	$1.0^{+1.3}_{-0.5}$	$0.3^{+0.4}_{-0.4}$	2.9
G339.102−00.194	G339.109−00.23	251.12	-46.05	129.0	0.68 ± 0.07	0.76 ± 0.07	-	$0.2^{+0.5}_{-0.1}$	-	5.0
G339.135−00.373	G339.134−00.37	251.35	-46.15	235.9	2.13 ± 0.07	2.64 ± 0.07	$126.7^{+8.8}_{-7.7}$	$1.8^{+1.7}_{-1.0}$	$0.3^{+0.2}_{-0.1}$	4.8
G339.117−00.658	G339.169−00.69	251.64	-46.35	406.0	1.62 ± 0.07	5.17 ± 0.07	$102.0^{+25.5}_{-18.2}$	$2.0^{+1.8}_{-1.2}$	$0.3^{+0.2}_{-0.1}$	12.9

Continued on next page

Name	*WISE*	RA	DEC	Radius	flux_img	flux_bkg	ν_0	α	β	Goodness
		deg	deg	arcmin	Jy	Jy	MHz			
(1)	(2)	(3)	(4)	(5)	(6)	(7)	(8)	(9)	(10)	(11)
G339.290+00.229	G339.233+00.24	250.84	-45.64	394.9	2.49 ± 0.07	2.60 ± 0.07	$109.0^{+30.2}_{-48.3}$	$1.5^{+2.1}_{-1.1}$	$0.2^{+0.3}_{-0.1}$	9.9
G339.486+00.092	G339.486+00.08	251.17	-45.58	71.5	0.22 ± 0.07	0.16 ± 0.07	-	$0.1^{+0.9}_{-0.1}$	-	5.7
G339.559+00.279	G339.556+00.28	251.03	-45.40	68.7	0.20 ± 0.07	0.16 ± 0.07	-	$0.1^{+0.8}_{-0.1}$	-	2.5
G339.585−00.110	G339.585−00.10	251.48	-45.63	226.5	1.65 ± 0.07	2.09 ± 0.07	$109.7^{+126.5}_{-66.6}$	$1.3^{+2.3}_{-1.2}$	$0.1^{+0.6}_{-0.1}$	13.9
G339.843+00.299	G339.845+00.29	251.28	-45.17	117.7	1.03 ± 0.07	0.50 ± 0.07	-	$0.5^{+1.1}_{-0.5}$	-	5.9
G339.957−00.548	G339.977−00.55	252.30	-45.63	128.7	0.56 ± 0.07	0.64 ± 0.07	-	$0.1^{+0.3}_{-0.1}$	-	6.7
G340.052−00.225	G340.051−00.23	252.04	-45.35	105.3	0.58 ± 0.07	0.44 ± 0.07	-	$0.2^{+0.5}_{-0.1}$	-	3.7
G340.073−00.155	G340.097−00.17	251.98	-45.29	179.9	1.53 ± 0.07	1.15 ± 0.07	-	$0.2^{+0.3}_{-0.1}$	-	4.8
G340.114−00.337	G340.106−00.35	252.21	-45.38	244.2	1.90 ± 0.07	2.30 ± 0.07	$127.9^{+17.5}_{-15.6}$	$1.3^{+1.5}_{-0.7}$	$0.3^{+0.2}_{-0.1}$	8.9
G340.191−00.443	G340.186−00.44	252.40	-45.39	95.0	0.16 ± 0.07	0.22 ± 0.07	-	$0.1^{+0.8}_{-0.1}$	-	3.0
G340.208−00.317	G340.211−00.31	252.28	-45.29	167.5	0.94 ± 0.07	0.90 ± 0.07	$187.8^{+64.9}_{-75.2}$	$0.9^{+1.4}_{-0.5}$	$0.3^{+0.5}_{-0.7}$	12.7

Continued on next page

Name	*WISE*	RA	DEC	Radius	flux_img	flux_bkg	ν_0	α	β	Goodness
		deg	deg	arcmin	Jy	Jy	MHz			
(1)	(2)	(3)	(4)	(5)	(6)	(7)	(8)	(9)	(10)	(11)
G340.200+00.449	G340.216+00.42	251.44	-44.80	499.6	0.21 ± 0.07	6.94 ± 0.07	$128.1^{+8.6}_{-5.9}$	$2.1^{+1.6}_{-1.1}$	$0.2^{+0.1}_{-0.1}$	18.0
G340.298−00.197	G340.294−00.19	252.23	-45.15	196.9	3.96 ± 0.07	1.73 ± 0.07	-	$0.3^{+0.2}_{-0.1}$	-	5.2
G340.293−00.286	G340.296−00.27	252.32	-45.21	120.4	0.73 ± 0.07	0.59 ± 0.07	$126.3^{+73.3}_{-61.3}$	$1.0^{+2.1}_{-0.9}$	$0.1^{+0.4}_{-0.2}$	8.8
G340.695−01.084	G340.678−01.04	253.56	-45.40	246.8	1.20 ± 0.06	0.81 ± 0.06	$128.8^{+19.0}_{-16.1}$	$1.2^{+1.7}_{-0.7}$	$0.3^{+0.3}_{-0.2}$	6.4
G340.779−01.018	G340.780−01.02	253.56	-45.30	133.4	0.83 ± 0.06	0.39 ± 0.06	$96.9^{+81.7}_{-42.7}$	$0.8^{+2.1}_{-0.6}$	$0.3^{+0.4}_{-0.2}$	29.5
G340.845−01.017	G340.850−01.02	253.62	-45.25	230.9	3.73 ± 0.06	0.99 ± 0.06	$159.4^{+30.9}_{-28.4}$	$0.7^{+0.6}_{-0.2}$	$0.4^{+0.3}_{-0.2}$	8.0
G340.859−00.876	G340.862−00.87	253.48	-45.15	160.5	0.87 ± 0.06	0.61 ± 0.06	$157.2^{+24.4}_{-23.2}$	$0.8^{+1.2}_{-0.5}$	$0.2^{+0.3}_{-0.2}$	8.0
G340.939−01.088	G340.951−01.09	253.78	-45.22	222.7	1.15 ± 0.06	0.92 ± 0.06	$110.9^{+33.2}_{-14.0}$	$1.5^{+2.0}_{-1.1}$	$0.3^{+0.3}_{-0.2}$	12.4
G341.003−01.025	G341.005−01.02	253.77	-45.13	156.6	0.48 ± 0.06	0.52 ± 0.06	-	$0.1^{+0.4}_{-0.1}$	-	5.6
G341.117−00.180	G341.125−00.18	252.95	-44.51	175.1	0.58 ± 0.07	0.82 ± 0.07	$118.8^{+30.5}_{-49.8}$	$1.2^{+2.2}_{-0.9}$	$0.2^{+0.3}_{-0.2}$	26.8
G341.137−00.334	G341.151−00.40	253.13	-44.59	139.2	0.71 ± 0.06	0.67 ± 0.06	$91.6^{+88.1}_{-46.6}$	$0.8^{+2.3}_{-0.7}$	$0.2^{+0.3}_{-0.1}$	17.1

Continued on next page

Name	*WISE*	RA	DEC	Radius	flux_img	flux_bkg	ν_0	α	β	Goodness
		deg	deg	arcmin	Jy	Jy	MHz			
(1)	(2)	(3)	(4)	(5)	(6)	(7)	(8)	(9)	(10)	(11)
G341.206−00.225	G341.207−00.23	253.08	-44.47	116.0	0.58 ± 0.07	0.48 ± 0.07	-	$0.1^{+0.4}_{-0.1}$	-	4.3
G341.265−00.350	G341.283−00.35	253.27	-44.50	150.1	0.86 ± 0.07	0.75 ± 0.07	-	$0.2^{+0.3}_{-0.1}$	-	6.0
G341.293−00.299	G341.305−00.30	253.24	-44.44	111.6	0.35 ± 0.07	0.35 ± 0.07	-	$0.1^{+0.5}_{-0.1}$	-	1.5
G341.670−00.390	G341.668−00.39	253.67	-44.21	156.7	0.33 ± 0.07	0.81 ± 0.07	$152.8^{+21.5}_{-24.9}$	$1.2^{+2.2}_{-1.0}$	$-0.1^{+0.3}_{-0.4}$	4.3
G341.966+00.221	G341.968+00.22	253.27	-43.59	95.2	0.29 ± 0.08	0.24 ± 0.08	-	$0.1^{+0.7}_{-0.1}$	-	1.2
G341.984−00.432	G341.983−00.44	253.99	-43.99	106.1	0.25 ± 0.08	0.30 ± 0.08	-	$0.0^{+0.3}_{-0.1}$	-	1.8
G342.047−00.483	G342.050−00.50	254.10	-43.97	129.0	0.47 ± 0.08	0.39 ± 0.08	-	$0.0^{+0.5}_{-0.0}$	-	3.1
G342.067+00.423	G342.062+00.41	253.14	-43.39	128.9	1.10 ± 0.08	0.50 ± 0.08	-	$0.3^{+0.5}_{-0.2}$	-	4.6
G342.128+00.019	G342.120+00.00	253.63	-43.60	273.5	2.59 ± 0.08	2.70 ± 0.08	$160.8^{+21.3}_{-53.2}$	$1.1^{+1.6}_{-0.7}$	$0.1^{+0.3}_{-0.4}$	15.5
G342.282+00.321	G342.277+00.31	253.44	-43.29	265.5	3.13 ± 0.08	2.53 ± 0.08	$167.4^{+16.6}_{-27.1}$	$0.8^{+0.8}_{-0.4}$	$0.1^{+0.3}_{-0.2}$	6.8
G342.354−00.051	G342.354−00.04	253.90	-43.47	154.0	1.38 ± 0.08	0.85 ± 0.08	-	$0.1^{+0.4}_{-0.1}$	-	4.4

Continued on next page

Name	*WISE*	RA	DEC	Radius	flux_img	flux_bkg	ν_0	α	β	Goodness
		deg	deg	arcmin	Jy	Jy	MHz			
(1)	(2)	(3)	(4)	(5)	(6)	(7)	(8)	(9)	(10)	(11)
G342.431−00.053	G342.429−00.04	253.97	-43.41	104.7	0.35 ± 0.08	0.44 ± 0.08	-	$0.0^{+0.6}_{-0.0}$	-	3.6
G343.155−00.408	G343.147−00.44	254.97	-43.06	366.9	1.53 ± 0.07	4.38 ± 0.07	$119.1^{+65.4}_{-22.0}$	$1.4^{+1.8}_{-0.8}$	$0.3^{+0.2}_{-0.2}$	17.8
G343.445−00.021	G343.480−00.04	254.80	-42.59	313.6	5.62 ± 0.06	3.46 ± 0.06	$132.2^{+29.2}_{-12.2}$	$1.2^{+1.0}_{-0.5}$	$0.6^{+0.3}_{-0.2}$	19.6
G343.645−00.154	G343.636−00.15	255.11	-42.52	349.7	3.11 ± 0.06	3.28 ± 0.06	$139.6^{+14.7}_{-18.5}$	$1.0^{+1.6}_{-0.6}$	$0.1^{+0.2}_{-0.1}$	7.9
G343.916−00.650	G343.914−00.64	255.86	-42.61	116.4	0.38 ± 0.06	0.44 ± 0.06	-	$0.1^{+0.4}_{-0.1}$	-	4.4
G344.109−00.664	G344.103−00.67	256.04	-42.46	91.2	0.24 ± 0.06	0.24 ± 0.06	-	$0.1^{+0.5}_{-0.1}$	-	6.2
G344.221−00.597	G344.224−00.59	256.06	-42.33	53.5	0.12 ± 0.06	0.09 ± 0.06	-	$0.0^{+1.1}_{-0.0}$	-	6.0
G344.373−00.250	G344.366−00.26	255.81	-42.00	190.9	0.72 ± 0.06	0.83 ± 0.06	-	$0.3^{+0.7}_{-0.2}$	-	2.7
G344.469−00.562	G344.472−00.55	256.22	-42.11	292.0	0.49 ± 0.06	2.91 ± 0.06	$134.8^{+9.1}_{-7.1}$	$1.6^{+1.6}_{-0.9}$	$0.1^{+0.1}_{-0.1}$	10.2
G344.591−00.037	G344.583−00.03	255.76	-41.70	69.0	0.10 ± 0.06	0.13 ± 0.06	-	$0.0^{+0.4}_{-0.0}$	-	6.4
G344.817+01.714	G344.638+01.62	254.12	-40.44	742.9	10.65 ± 0.06	5.37 ± 0.06	$123.9^{+4.8}_{-4.1}$	$1.4^{+1.0}_{-0.6}$	$0.3^{+0.1}_{-0.1}$	13.4

Continued on next page

Name	*WISE*	RA	DEC	Radius	flux_img	flux_bkg	ν_0	α	β	Goodness
		deg	deg	arcmin	Jy	Jy	MHz			
(1)	(2)	(3)	(4)	(5)	(6)	(7)	(8)	(9)	(10)	(11)
G344.756−00.554	G344.753−00.54	256.45	-41.88	305.6	0.68 ± 0.06	3.37 ± 0.06	$120.9^{+8.4}_{-8.0}$	$2.0^{+1.9}_{-1.2}$	$0.3^{+0.2}_{-0.2}$	7.5
G345.181−00.779	G345.094−00.77	257.03	-41.68	480.3	3.40 ± 0.06	5.57 ± 0.06	$135.6^{+15.7}_{-14.1}$	$0.8^{+0.7}_{-0.3}$	$0.2^{+0.1}_{-0.1}$	22.5
G345.104+00.139	G345.095+00.13	255.99	-41.18	126.2	0.29 ± 0.06	0.75 ± 0.06	-	$0.0^{+0.3}_{-0.1}$	-	8.6
G345.243+01.052	G345.202+01.02	255.15	-40.52	284.3	3.82 ± 0.06	2.66 ± 0.06	$124.5^{+6.6}_{-5.2}$	$1.3^{+1.2}_{-0.6}$	$0.5^{+0.2}_{-0.2}$	13.0
G345.046+01.482	G345.235+01.40	254.55	-40.41	958.2	15.66 ± 0.06	8.83 ± 0.06	$132.3^{+4.7}_{-7.0}$	$1.4^{+0.8}_{-0.5}$	$0.4^{+0.2}_{-0.1}$	15.3
G345.291+01.463	G345.284+01.46	254.77	-40.22	234.3	4.94 ± 0.06	1.13 ± 0.06	$178.2^{+35.8}_{-33.1}$	$0.9^{+0.5}_{-0.3}$	$0.5^{+0.4}_{-0.3}$	9.2
G345.339+01.441	G345.338+01.44	254.83	-40.20	159.8	2.24 ± 0.06	0.64 ± 0.06	$178.4^{+20.8}_{-18.9}$	$0.9^{+0.7}_{-0.4}$	$0.4^{+0.3}_{-0.3}$	6.4
G345.371−00.059	G345.340−00.01	256.42	-41.09	414.9	1.74 ± 0.06	5.33 ± 0.06	$147.2^{+14.2}_{-15.3}$	$1.1^{+1.4}_{-0.6}$	$0.2^{+0.2}_{-0.1}$	9.3
G345.372+01.399	G345.391+01.39	254.90	-40.20	230.7	5.48 ± 0.06	1.25 ± 0.06	-	$0.8^{+0.2}_{-0.2}$	-	4.2
G345.410−00.932	G345.410−00.95	257.38	-41.58	306.9	5.22 ± 0.06	1.39 ± 0.06	-	$0.5^{+0.2}_{-0.2}$	-	11.7
G345.435+00.207	G345.432+00.20	256.19	-40.88	116.6	0.76 ± 0.06	0.59 ± 0.06	-	$0.2^{+0.5}_{-0.1}$	-	7.5

Continued on next page

Name	*WISE*	RA	DEC	Radius	flux_img	flux_bkg	ν_0	α	β	Goodness
		deg	deg	arcmin	Jy	Jy	MHz			
(1)	(2)	(3)	(4)	(5)	(6)	(7)	(8)	(9)	(10)	(11)
G345.471+01.458	G345.463+01.45	254.92	-40.09	157.9	1.28 ± 0.06	0.70 ± 0.06	-	$0.1^{+0.2}_{-0.1}$	-	13.0
G345.490+00.375	G345.491+00.35	256.06	-40.73	161.5	0.66 ± 0.06	0.71 ± 0.06	-	$0.1^{+0.2}_{-0.1}$	-	5.6
G345.538+01.496	G345.540+01.49	254.93	-40.01	155.8	1.07 ± 0.06	0.59 ± 0.06	$147.5^{+22.1}_{-45.8}$	$0.7^{+1.0}_{-0.4}$	$0.2^{+0.2}_{-0.1}$	35.3
G345.553−00.028	G345.586−00.04	256.53	-40.93	291.4	6.57 ± 0.06	3.56 ± 0.06	$137.3^{+18.9}_{-10.7}$	$1.4^{+1.6}_{-0.8}$	$0.3^{+0.2}_{-0.2}$	3.1
G345.655+00.010	G345.651+00.01	256.57	-40.82	166.1	1.02 ± 0.06	1.09 ± 0.06	$150.4^{+26.2}_{-91.1}$	$1.0^{+1.9}_{-0.8}$	$0.1^{+0.2}_{-0.3}$	43.9
G345.810+00.039	G345.810+00.04	256.66	-40.68	171.2	0.98 ± 0.06	1.10 ± 0.06	$137.4^{+32.1}_{-59.8}$	$1.1^{+1.8}_{-0.8}$	$0.1^{+0.2}_{-0.3}$	19.6
G346.088−00.027	G346.107−00.01	256.95	-40.50	226.3	1.61 ± 0.07	2.12 ± 0.07	$134.8^{+45.2}_{-32.4}$	$1.1^{+2.3}_{-1.0}$	$-0.2^{+0.3}_{-0.5}$	7.8
G346.209−00.130	G346.206−00.13	257.16	-40.47	368.6	3.86 ± 0.07	4.66 ± 0.07	$122.0^{+13.1}_{-12.1}$	$2.1^{+1.9}_{-1.4}$	$0.1^{+0.2}_{-0.1}$	4.1
G346.530+00.085	G346.521+00.08	257.18	-40.08	107.9	0.56 ± 0.07	0.63 ± 0.07	-	$0.0^{+0.5}_{-0.0}$	-	6.0
G346.867+00.336	G346.873+00.33	257.18	-39.66	80.1	0.31 ± 0.07	0.33 ± 0.07	-	$0.0^{+0.6}_{-0.0}$	-	4.3
G347.194−00.010	G347.230−00.05	257.80	-39.60	511.6	6.03 ± 0.07	8.92 ± 0.07	-	$0.2^{+0.7}_{-0.1}$	-	8.0

Continued on next page

Name	*WISE*	RA	DEC	Radius	flux_img	flux_bkg	ν_0	α	β	Goodness
		deg	deg	arcmin	Jy	Jy	MHz			
(1)	(2)	(3)	(4)	(5)	(6)	(7)	(8)	(9)	(10)	(11)
G347.515+00.209	G347.495+00.17	257.81	-39.21	650.1	14.88 ± 0.07	12.59 ± 0.07	$159.0^{+28.0}_{-54.7}$	$1.3^{+1.3}_{-0.5}$	$0.4^{+0.4}_{-0.5}$	13.6
G347.767+00.138	G347.770+00.14	258.08	-39.05	143.4	0.90 ± 0.07	0.96 ± 0.07	-	$0.4^{+1.8}_{-0.3}$	-	8.2
G347.879+00.037	G347.891+00.04	258.27	-39.02	145.4	0.81 ± 0.07	0.76 ± 0.07	-	$0.1^{+0.3}_{-0.1}$	-	4.4
G347.983−00.452	G348.000−00.49	258.86	-39.22	132.1	0.67 ± 0.07	0.78 ± 0.07	-	$0.2^{+0.3}_{-0.1}$	-	7.1
G348.252−00.987	G348.249−00.97	259.62	-39.31	170.4	2.55 ± 0.07	1.03 ± 0.07	-	$1.0^{+0.5}_{-0.4}$	-	6.1
G348.227+00.466	G348.261+00.48	258.09	-38.49	247.5	2.96 ± 0.07	2.18 ± 0.07	$176.2^{+8.2}_{-30.8}$	$0.9^{+0.6}_{-0.3}$	$0.1^{+0.3}_{-0.2}$	14.8
G348.559−00.990	G348.557−00.98	259.85	-39.06	137.9	0.44 ± 0.07	0.34 ± 0.07	-	$0.2^{+0.5}_{-0.1}$	-	3.2
G348.707−00.830	G348.691−00.82	259.79	-38.85	1201.0	11.09 ± 0.08	24.31 ± 0.08	$160.7^{+9.8}_{-21.5}$	$0.8^{+0.7}_{-0.3}$	$0.2^{+0.2}_{-0.1}$	12.0
G348.725−01.012	G348.710−01.04	260.00	-38.94	397.3	11.11 ± 0.07	4.48 ± 0.07	$132.6^{+5.3}_{-4.8}$	$2.4^{+1.3}_{-0.9}$	$0.8^{+0.2}_{-0.2}$	7.6
G349.101+00.109	G349.109+00.11	259.11	-37.99	162.8	1.85 ± 0.09	1.06 ± 0.09	-	$0.2^{+0.6}_{-0.2}$	-	4.0
G349.126+00.006	G349.126+00.01	259.23	-38.03	130.8	2.52 ± 0.08	0.81 ± 0.08	-	$0.2^{+0.5}_{-0.1}$	-	4.6

Continued on next page

Name	*WISE*	RA	DEC	Radius	flux_img	flux_bkg	ν_0	α	β	Goodness
		deg	deg	arcmin	Jy	Jy	MHz			
(1)	(2)	(3)	(4)	(5)	(6)	(7)	(8)	(9)	(10)	(11)
G349.182+00.049	G349.185+00.04	259.23	-37.96	205.5	1.95 ± 0.09	1.93 ± 0.09	-	$0.1^{+0.7}_{-0.1}$	-	7.1
G349.220+00.140	G349.217+00.13	259.16	-37.87	117.1	0.54 ± 0.08	0.60 ± 0.08	-	$0.0^{+0.3}_{-0.1}$	-	1.9
G349.333+00.029	G349.328+00.02	259.36	-37.84	105.4	0.26 ± 0.09	0.45 ± 0.09	-	$0.0^{+0.6}_{-0.0}$	-	4.5
G349.410+00.179	G349.407+00.18	259.26	-37.69	97.8	0.22 ± 0.08	0.35 ± 0.08	-	$0.0^{+0.5}_{-0.0}$	-	3.6
G349.487−00.266	G349.418−00.64	259.78	-37.89	352.2	-0.20 ± 0.08	3.27 ± 0.08	$127.7^{+43.9}_{-20.9}$	$1.7^{+2.1}_{-1.2}$	$0.2^{+0.3}_{-0.2}$	9.5
G349.507+01.058	G349.507+01.05	258.43	-37.10	68.4	0.17 ± 0.07	0.10 ± 0.07	-	$0.2^{+1.1}_{-0.2}$	-	9.4
G349.518−00.699	G349.578−00.68	260.25	-38.11	208.2	2.59 ± 0.07	0.72 ± 0.07	$123.5^{+118.2}_{-29.2}$	$0.3^{+1.8}_{-0.4}$	$-0.3^{+0.5}_{-0.4}$	8.7
G349.826−00.577	G349.831−00.54	260.34	-37.79	270.2	3.24 ± 0.07	1.49 ± 0.07	$152.0^{+22.5}_{-20.1}$	$1.3^{+1.4}_{-0.6}$	$0.6^{+0.4}_{-0.3}$	10.8
G349.848+00.066	G349.860+00.06	259.70	-37.40	161.1	0.12 ± 0.08	1.13 ± 0.08	$141.3^{+28.1}_{-24.9}$	$1.9^{+1.9}_{-1.4}$	$-0.1^{+0.3}_{-0.4}$	6.2
G350.028−00.487	G349.981−00.45	260.40	-37.57	139.1	1.30 ± 0.07	0.51 ± 0.07	$178.2^{+15.9}_{-38.9}$	$0.7^{+1.1}_{-0.4}$	$-0.1^{+0.4}_{-0.4}$	5.9
G350.105+00.084	G350.105+00.08	259.86	-37.18	146.8	1.37 ± 0.08	0.79 ± 0.08	-	$0.3^{+0.7}_{-0.2}$	-	4.5

Continued on next page

Name	*WISE*	RA	DEC	Radius	flux_img	flux_bkg	ν_0	α	β	Goodness
		deg	deg	arcmin	Jy	Jy	MHz			
(1)	(2)	(3)	(4)	(5)	(6)	(7)	(8)	(9)	(10)	(11)
G350.199+00.007	G350.201+00.01	260.01	-37.15	150.1	0.51 ± 0.08	0.95 ± 0.08	-	$0.1^{+1.0}_{-0.1}$	-	4.5
G350.320+00.149	G350.323+00.14	259.95	-36.97	121.3	0.65 ± 0.08	0.70 ± 0.08	-	$0.1^{+1.0}_{-0.1}$	-	3.9
G350.322+00.090	G350.328+00.09	260.01	-37.00	104.4	0.46 ± 0.08	0.49 ± 0.08	-	$0.1^{+1.0}_{-0.1}$	-	5.9
G350.494+00.947	G350.505+00.95	259.26	-36.37	133.7	0.49 ± 0.08	0.50 ± 0.08	-	$0.1^{+0.5}_{-0.1}$	-	2.9
G350.616+00.932	G350.617+00.98	259.36	-36.27	368.6	4.16 ± 0.08	4.59 ± 0.08	$150.5^{+14.6}_{-16.2}$	$1.0^{+1.0}_{-0.5}$	$0.0^{+0.2}_{-0.2}$	12.5
G350.772−00.278	G350.767−00.27	260.71	-36.84	271.7	0.47 ± 0.08	2.61 ± 0.08	$153.8^{+16.3}_{-76.0}$	$1.6^{+2.0}_{-1.1}$	$-0.1^{+0.2}_{-0.5}$	15.6
G350.769−00.075	G350.769−00.07	260.50	-36.73	101.1	0.16 ± 0.08	0.37 ± 0.08	-	$0.0^{+0.7}_{-0.1}$	-	3.2
G350.776−00.026	G350.781−00.02	260.45	-36.69	56.7	0.05 ± 0.08	0.13 ± 0.08	-	$0.0^{+0.7}_{-0.0}$	-	3.8
G350.960−00.569	G350.991−00.53	261.14	-36.85	214.6	1.17 ± 0.07	1.10 ± 0.07	$121.0^{+41.3}_{-27.7}$	$1.4^{+2.0}_{-0.9}$	$0.4^{+0.3}_{-0.2}$	7.1
G351.004+00.659	G350.995+00.65	259.92	-36.11	385.7	20.38 ± 0.08	7.15 ± 0.08	$150.6^{+19.1}_{-10.3}$	$1.3^{+0.9}_{-0.5}$	$0.7^{+0.3}_{-0.3}$	16.4
G351.156+00.465	G351.130+00.44	260.22	-36.10	402.2	9.30 ± 0.09	4.80 ± 0.09	$170.9^{+7.3}_{-16.0}$	$1.1^{+0.6}_{-0.4}$	$0.3^{+0.3}_{-0.2}$	7.4

Continued on next page

Name	*WISE*	RA	DEC	Radius	flux_img	flux_bkg	ν_0	α	β	Goodness
		deg	deg	arcmin	Jy	Jy	MHz			
(1)	(2)	(3)	(4)	(5)	(6)	(7)	(8)	(9)	(10)	(11)
G351.180+00.700	G351.170+00.70	260.00	-35.95	291.2	6.53 ± 0.09	2.25 ± 0.09	-	$0.5^{+0.3}_{-0.2}$	-	8.7
G351.245+00.690	G351.246+00.67	260.06	-35.90	207.2	4.84 ± 0.09	1.42 ± 0.09	-	$0.4^{+0.3}_{-0.2}$	-	8.9
G351.382+00.692	G351.383+00.73	260.15	-35.79	475.7	31.03 ± 0.09	7.10 ± 0.09	-	$0.7^{+0.1}_{-0.1}$	-	14.4
G351.475−00.462	G351.472−00.45	261.39	-36.36	106.5	0.50 ± 0.07	0.32 ± 0.07	-	$0.3^{+0.6}_{-0.2}$	-	3.3
G351.563+00.209	G351.557+00.21	260.77	-35.91	179.0	2.29 ± 0.08	1.36 ± 0.08	-	$0.3^{+0.9}_{-0.2}$	-	5.7
G351.624+00.156	G351.620+00.14	260.86	-35.89	207.6	2.63 ± 0.08	1.89 ± 0.08	-	$0.3^{+0.5}_{-0.2}$	-	7.0
G351.633−01.251	G351.646−01.25	262.32	-36.67	476.6	6.32 ± 0.07	2.26 ± 0.07	$137.2^{+5.2}_{-14.3}$	$1.0^{+0.8}_{-0.4}$	$0.2^{+0.2}_{-0.1}$	25.3
G351.654+00.510	G351.651+00.51	260.53	-35.67	174.8	1.33 ± 0.08	1.33 ± 0.08	$131.1^{+16.0}_{-12.7}$	$1.7^{+2.0}_{-1.1}$	$0.3^{+0.2}_{-0.2}$	4.4
G351.688−01.165	G351.688−01.16	262.27	-36.58	283.8	5.19 ± 0.07	1.25 ± 0.07	$149.9^{+22.1}_{-11.5}$	$1.0^{+0.7}_{-0.4}$	$0.4^{+0.2}_{-0.2}$	18.4
G351.685+00.644	G351.693+00.67	260.41	-35.56	169.5	0.98 ± 0.08	0.74 ± 0.08	-	$0.3^{+0.6}_{-0.2}$	-	4.3
G351.841−00.182	G351.852−00.13	261.36	-35.90	157.4	0.14 ± 0.07	1.11 ± 0.07	-	$0.1^{+0.6}_{-0.1}$	-	5.7

Continued on next page

Name	*WISE*	RA	DEC	Radius	flux_img	flux_bkg	ν_0	α	β	Goodness
		deg	deg	arcmin	Jy	Jy	MHz			
(1)	(2)	(3)	(4)	(5)	(6)	(7)	(8)	(9)	(10)	(11)
G352.219−00.141	G352.234−00.15	261.58	-35.57	115.1	0.36 ± 0.07	0.49 ± 0.07	-	$0.1^{+0.6}_{-0.1}$	-	2.6
G352.282−00.478	G352.313−00.44	261.97	-35.70	340.8	1.20 ± 0.07	3.73 ± 0.07	-	$0.2^{+0.5}_{-0.1}$	-	25.6
G352.381−00.063	G352.393−00.06	261.61	-35.39	109.1	0.56 ± 0.07	0.59 ± 0.07	-	$0.2^{+0.7}_{-0.2}$	-	2.6
G352.436+02.124	G352.587+02.10	259.46	-34.10	275.0	0.57 ± 0.06	0.34 ± 0.06	$117.6^{+27.7}_{-45.4}$	$1.4^{+2.1}_{-1.1}$	$0.2^{+0.3}_{-0.1}$	12.5
G352.598−00.178	G352.597−00.18	261.88	-35.27	141.8	1.07 ± 0.07	0.92 ± 0.07	-	$0.2^{+0.6}_{-0.2}$	-	5.3
G352.619+00.161	G352.628+00.14	261.55	-35.06	147.9	0.77 ± 0.08	0.95 ± 0.08	-	$0.0^{+0.9}_{-0.0}$	-	5.1
G352.808+01.317	G352.795+01.35	260.51	-34.26	525.2	6.74 ± 0.07	4.56 ± 0.07	$138.6^{+6.6}_{-5.6}$	$1.4^{+1.1}_{-0.7}$	$-0.0^{+0.1}_{-0.1}$	13.1
G352.830+00.947	G352.838+00.93	260.90	-34.45	225.7	2.33 ± 0.08	1.36 ± 0.08	$170.8^{+12.0}_{-16.4}$	$0.8^{+0.7}_{-0.4}$	$0.0^{+0.2}_{-0.2}$	2.1
G353.034−00.082	G353.032−00.08	262.07	-34.86	115.2	0.32 ± 0.08	0.55 ± 0.08	-	$0.1^{+0.7}_{-0.1}$	-	3.1
G353.030+00.628	G353.038+00.58	261.35	-34.46	460.3	26.14 ± 0.08	9.97 ± 0.08	$176.6^{+8.7}_{-11.6}$	$1.2^{+0.4}_{-0.3}$	$0.5^{+0.2}_{-0.2}$	3.4
G353.064+00.301	G353.076+00.28	261.71	-34.62	460.4	14.56 ± 0.08	11.06 ± 0.08	$143.5^{+23.7}_{-7.2}$	$1.6^{+1.2}_{-0.8}$	$0.5^{+0.2}_{-0.3}$	23.4

Continued on next page

Name	*WISE*	RA	DEC	Radius	flux_img	flux_bkg	ν_0	α	β	Goodness
		deg	deg	arcmin	Jy	Jy	MHz			
(1)	(2)	(3)	(4)	(5)	(6)	(7)	(8)	(9)	(10)	(11)
G353.057+00.817	G353.092+00.85	261.18	-34.33	694.9	68.09 ± 0.08	18.05 ± 0.08	$173.4^{+7.1}_{-10.9}$	$1.4^{+0.4}_{-0.3}$	$0.4^{+0.2}_{-0.2}$	6.0
G353.228−00.239	G353.221−00.24	262.36	-34.78	144.4	0.26 ± 0.08	0.73 ± 0.08	$98.8^{+78.1}_{-62.8}$	$1.7^{+2.2}_{-1.6}$	$0.0^{+0.2}_{-0.3}$	9.3
G353.211+01.056	G353.236+01.06	261.05	-34.07	392.0	12.72 ± 0.08	5.26 ± 0.08	-	$0.1^{+0.1}_{-0.0}$	-	47.2
G353.291+00.595	G353.272+00.59	261.56	-34.27	579.6	37.22 ± 0.08	11.94 ± 0.08	$177.0^{+7.7}_{-8.4}$	$1.2^{+0.4}_{-0.3}$	$0.5^{+0.2}_{-0.2}$	8.5
G353.326+00.084	G353.308+00.06	262.10	-34.52	333.6	1.91 ± 0.08	3.58 ± 0.08	$121.6^{+9.3}_{-6.8}$	$2.5^{+1.7}_{-1.4}$	$0.4^{+0.2}_{-0.2}$	2.1
G353.362−00.119	G353.350−00.14	262.33	-34.60	247.8	2.46 ± 0.08	2.03 ± 0.08	$130.0^{+10.6}_{-12.8}$	$1.5^{+1.5}_{-0.8}$	$0.2^{+0.2}_{-0.1}$	8.5
G353.409−00.375	G353.408−00.38	262.62	-34.70	149.3	1.49 ± 0.07	0.64 ± 0.07	-	$0.9^{+0.7}_{-0.6}$	-	7.3
G353.434+00.479	G353.436+00.42	261.78	-34.21	218.7	2.22 ± 0.08	2.06 ± 0.08	-	$0.1^{+0.1}_{-0.1}$	-	31.8
G353.587−00.077	G353.574−00.05	262.44	-34.39	501.9	12.41 ± 0.08	6.10 ± 0.08	$113.6^{+13.8}_{-10.2}$	$1.2^{+1.5}_{-0.7}$	$-0.5^{+0.3}_{-0.3}$	4.3
G354.187−00.057	G354.175−00.06	262.82	-33.88	172.0	2.49 ± 0.07	1.39 ± 0.07	-	$0.3^{+0.5}_{-0.2}$	-	2.0
G354.464+00.080	G354.465+00.07	262.86	-33.57	168.2	1.91 ± 0.07	1.15 ± 0.07	-	$0.2^{+0.5}_{-0.1}$	-	5.3

Continued on next page

Name	*WISE*	RA	DEC	Radius	flux_img	flux_bkg	ν_0	α	β	Goodness
		deg	deg	arcmin	Jy	Jy	MHz			
(1)	(2)	(3)	(4)	(5)	(6)	(7)	(8)	(9)	(10)	(11)
G354.583+00.008	G354.589+00.00	263.01	-33.51	104.3	0.32 ± 0.07	0.52 ± 0.07	-	$0.0^{+0.6}_{-0.0}$	-	3.4
G354.609+00.481	G354.611+00.48	262.56	-33.23	86.0	0.32 ± 0.07	0.30 ± 0.07	-	$0.1^{+0.6}_{-0.1}$	-	1.7
G354.666+00.251	G354.672+00.24	262.83	-33.31	106.0	0.42 ± 0.07	0.53 ± 0.07	-	$0.1^{+0.5}_{-0.0}$	-	1.5
G354.682+00.483	G354.685+00.46	262.60	-33.17	109.5	0.50 ± 0.07	0.52 ± 0.07	-	$0.3^{+1.0}_{-0.2}$	-	2.7
G354.935+00.332	G354.936+00.33	262.92	-33.04	61.3	0.23 ± 0.07	0.22 ± 0.07	-	$0.0^{+0.6}_{-0.0}$	-	2.0
G355.027−00.218	G355.026−00.21	263.53	-33.26	177.6	0.46 ± 0.07	1.40 ± 0.07	-	$0.1^{+0.6}_{-0.1}$	-	2.2
G355.254+00.141	G355.244+00.10	263.32	-32.88	455.4	10.55 ± 0.07	11.27 ± 0.07	$156.6^{+10.6}_{-12.5}$	$0.9^{+1.0}_{-0.4}$	$-0.5^{+0.3}_{-0.3}$	6.4
G355.528−00.103	G355.529−00.10	263.74	-32.78	123.1	0.42 ± 0.07	0.83 ± 0.07	-	$0.1^{+0.4}_{-0.1}$	-	3.0
G355.683+00.018	G355.680+00.00	263.72	-32.58	234.8	0.69 ± 0.07	2.34 ± 0.07	$121.1^{+44.9}_{-70.0}$	$1.5^{+2.2}_{-1.2}$	$0.2^{+0.3}_{-0.1}$	27.2
G356.233+00.677	G356.230+00.67	263.42	-31.77	113.0	0.74 ± 0.07	0.68 ± 0.07	-	$0.2^{+0.5}_{-0.1}$	-	6.4
G356.308−00.205	G356.310−00.20	264.34	-32.18	75.5	0.46 ± 0.07	0.33 ± 0.07	-	$0.1^{+0.9}_{-0.1}$	-	5.8

Continued on next page

Name	*WISE*	RA	DEC	Radius	flux_img	flux_bkg	ν_0	α	β	Goodness
		deg	deg	arcmin	Jy	Jy	MHz			
(1)	(2)	(3)	(4)	(5)	(6)	(7)	(8)	(9)	(10)	(11)
G356.468+00.005	G356.472+00.00	264.23	-31.93	176.4	1.00 ± 0.07	1.45 ± 0.07	-	$-0.0^{+0.0}_{-0.3}$	-	8.0
G356.572−00.087	G356.560−00.08	264.39	-31.89	129.0	0.40 ± 0.07	0.83 ± 0.07	-	$-0.0^{+0.0}_{-0.3}$	-	3.8
G357.467−01.450	G357.465−01.45	266.31	-31.85	92.9	0.29 ± 0.06	0.14 ± 0.06	-	$0.1^{+0.3}_{-0.1}$	-	4.3
G357.488−01.395	G357.475−01.40	266.27	-31.81	285.4	0.71 ± 0.06	1.11 ± 0.06	$124.9^{+10.4}_{-9.9}$	$1.9^{+1.8}_{-1.1}$	$0.2^{+0.2}_{-0.1}$	7.0
G357.988−00.156	G357.985−00.16	265.34	-30.73	123.3	0.39 ± 0.10	0.81 ± 0.10	-	$0.0^{+0.6}_{-0.0}$	-	2.5
G358.211−00.366	G358.243−00.40	265.68	-30.65	693.5	-1.97 ± 0.12	19.78 ± 0.12	$191.2^{+12.5}_{-23.8}$	$0.6^{+1.4}_{-0.3}$	$-0.6^{+0.5}_{-0.3}$	9.3
G358.605−00.058	G358.600−00.05	265.62	-30.15	108.3	1.51 ± 0.18	0.77 ± 0.18	-	$0.1^{+0.9}_{-0.1}$	-	1.2
G358.596−00.489	G358.641−00.53	266.04	-30.39	359.8	1.75 ± 0.15	7.73 ± 0.15	$124.7^{+250.4}_{-51.8}$	$0.2^{+2.3}_{-0.6}$	$-0.3^{+2.1}_{-0.5}$	15.6
G359.708+00.634	G359.558+00.59	265.61	-28.85	1935.9	34.05 ± 0.16	64.10 ± 0.16	$121.1^{+5.6}_{-4.4}$	$1.6^{+1.3}_{-0.8}$	$-0.0^{+0.1}_{-0.1}$	10.9
G359.687−00.263	G359.685−00.26	266.48	-29.34	272.1	9.57 ± 0.33	13.43 ± 0.33	$148.8^{+13.8}_{-13.3}$	$1.9^{+1.6}_{-0.9}$	$0.3^{+0.2}_{-0.2}$	2.1
G359.750−00.375	G359.740−00.41	266.62	-29.34	281.4	5.17 ± 0.32	9.98 ± 0.32	$149.6^{+15.8}_{-12.3}$	$1.9^{+1.6}_{-1.0}$	$-0.1^{+0.2}_{-0.3}$	3.0

Continued on next page

Name	*WISE*	RA	DEC	Radius	flux_img	flux_bkg	ν_0	α	β	Goodness
		deg	deg	arcmin	Jy	Jy	MHz			
(1)	(2)	(3)	(4)	(5)	(6)	(7)	(8)	(9)	(10)	(11)
G341.071−00.088	new01	252.81	-44.48	390.5	1.89 ± 0.07	4.81 ± 0.07	$126.4^{+10.7}_{-9.0}$	$1.3^{+1.3}_{-0.7}$	$0.2^{+0.1}_{-0.1}$	7.2
G339.194−00.191	new02	251.20	-45.98	85.4	0.28 ± 0.07	0.30 ± 0.07	-	$0.1^{+0.4}_{-0.1}$	-	4.8
G353.015+01.172	new03	260.80	-34.17	453.6	8.64 ± 0.08	4.90 ± 0.08	$145.7^{+11.7}_{-9.5}$	$1.8^{+1.5}_{-0.8}$	$0.3^{+0.2}_{-0.2}$	10.0
G352.881+01.077	new04	260.80	-34.33	339.9	5.08 ± 0.08	3.18 ± 0.08	$163.2^{+12.5}_{-14.4}$	$1.1^{+0.9}_{-0.5}$	$0.1^{+0.2}_{-0.2}$	5.7
G353.569+00.881	new05	261.47	-33.87	701.4	2.74 ± 0.08	9.83 ± 0.08	$132.2^{+6.3}_{-5.0}$	$2.1^{+1.7}_{-1.1}$	$0.4^{+0.2}_{-0.1}$	8.0
G352.814+00.627	new06	261.21	-34.64	327.5	1.45 ± 0.08	3.18 ± 0.08	$110.2^{+32.9}_{-59.1}$	$1.7^{+2.1}_{-1.3}$	$0.3^{+0.4}_{-0.2}$	17.9
G353.558+00.205	new07	262.14	-34.26	251.9	0.72 ± 0.08	2.40 ± 0.08	$134.5^{+27.9}_{-30.5}$	$1.7^{+2.0}_{-1.2}$	$0.0^{+0.2}_{-0.3}$	6.8
G353.542+00.092	new08	262.24	-34.34	134.7	0.72 ± 0.08	0.86 ± 0.08	$116.2^{+221.3}_{-72.0}$	$1.7^{+2.2}_{-1.5}$	$0.0^{+0.4}_{-0.4}$	17.2
G331.707+00.269	new09	242.86	-51.07	936.4	4.11 ± 0.09	10.16 ± 0.09	$127.6^{+33.4}_{-47.1}$	$1.8^{+1.9}_{-1.1}$	$0.3^{+0.3}_{-0.2}$	8.6
G000.277−00.254	new10	266.82	-28.83	314.0	7.20 ± 0.36	8.97 ± 0.36	$147.7^{+11.9}_{-11.5}$	$2.2^{+1.6}_{-1.2}$	$0.2^{+0.2}_{-0.2}$	2.2
G336.867+00.280	new11	248.43	-47.41	282.3	1.07 ± 0.09	1.37 ± 0.09	$131.8^{+37.0}_{-76.2}$	$1.6^{+2.0}_{-1.2}$	$0.1^{+0.2}_{-0.4}$	9.1

Continued on next page

Name	*WISE*	RA	DEC	Radius	flux_img	flux_bkg	ν_0	α	β	Goodness
		deg	deg	arcmin	Jy	Jy	MHz			
(1)	(2)	(3)	(4)	(5)	(6)	(7)	(8)	(9)	(10)	(11)
G336.787−01.133	new12	249.91	-48.41	360.4	1.00 ± 0.07	3.79 ± 0.07	$130.9^{+18.3}_{-18.4}$	$2.2^{+1.7}_{-1.3}$	$0.3^{+0.3}_{-0.2}$	8.9
G356.054+00.203	new13	263.77	-32.17	286.8	0.53 ± 0.07	3.85 ± 0.07	-	$0.1^{+0.6}_{-0.1}$	-	9.1
G003.105−00.044	new14	268.25	-26.30	210.6	0.92 ± 0.07	2.80 ± 0.07	$121.9^{+25.7}_{-28.6}$	$1.8^{+2.0}_{-1.3}$	$0.0^{+0.1}_{-0.3}$	9.8
G334.786−00.263	new15	246.87	-49.29	345.8	4.14 ± 0.08	3.73 ± 0.08	$118.6^{+9.1}_{-9.0}$	$2.0^{+1.7}_{-1.1}$	$0.2^{+0.1}_{-0.1}$	4.7
G030.804−00.711	new16	282.52	-2.22	360.3	0.86 ± 0.10	2.37 ± 0.10	$120.4^{+25.9}_{-16.4}$	$1.9^{+1.9}_{-1.3}$	$0.1^{+0.2}_{-0.2}$	16.4
G023.843+00.584	new17	278.16	-7.81	303.2	0.71 ± 0.09	2.85 ± 0.09	-	$0.7^{+1.6}_{-0.6}$	-	11.9
G007.134+00.436	new18	270.02	-22.57	839.4	0.16 ± 0.10	10.33 ± 0.10	$109.2^{+10.6}_{-11.5}$	$2.3^{+1.7}_{-1.4}$	$0.1^{+0.2}_{-0.1}$	13.1
G339.653−00.240	new19	251.68	-45.67	105.2	1.06 ± 0.07	0.44 ± 0.07	-	$0.1^{+0.5}_{-0.1}$	-	7.9
G002.359+01.394	new20	266.45	-26.20	339.9	0.16 ± 0.06	2.70 ± 0.06	$136.3^{+7.8}_{-12.2}$	$1.2^{+1.5}_{-0.7}$	$0.0^{+0.1}_{-0.1}$	20.5
G333.131+00.415	new21	244.33	-49.99	575.7	0.41 ± 0.08	8.56 ± 0.08	-	$0.2^{+0.3}_{-0.1}$	-	12.2

Bibliography

Abramenkov, E. A. and V. V. Krymkin (1990). Parameters of the magnetic field in the local Galactic arm derived from low frequency absorption measurements in the ionized gas. In R. Beck, R. Wielebinski, and P. P. Kronberg (Eds.), *Galactic and Intergalactic Magnetic Fields*, Volume 140 of *IAU Symposium*, pp. 49–52.

Adriani, O., Y. Akaike, K. Asano, Y. Asaoka, M. G. Bagliesi, G. Bigongiari, W. R. Binns, S. Bonechi, M. Bongi, P. Brogi, J. H. Buckley, N. Cannady, G. Castellini, C. Checchia, M. L. Cherry, G. Collazuol, V. di Felice, K. Ebisawa, H. Fuke, T. G. Guzik, T. Hams, M. Hareyama, N. Hasebe, K. Hibino, M. Ichimura, K. Ioka, W. Ishizaki, M. H. Israel, A. Javaid, K. Kasahara, J. Kataoka, R. Kataoka, Y. Katayose, C. Kato, N. Kawanaka, Y. Kawakubo, H. S. Krawczynski, J. F. Krizmanic, S. Kuramata, T. Lomtadze, P. Maestro, P. S. Marrocchesi, A. M. Messineo, J. W. Mitchell, S. Miyake, K. Mizutani, A. A. Moiseev, K. Mori, M. Mori, N. Mori, H. M. Motz, K. Munakata, H. Murakami, S. Nakahira, J. Nishimura, G. A. de Nolfo, S. Okuno, J. F. Ormes, S. Ozawa, L. Pacini, F. Palma, P. Papini, A. V. Penacchioni, B. F. Rauch, S. B. Ricciarini, K. Sakai, T. Sakamoto, M. Sasaki, Y. Shimizu, A. Shiomi, R. Sparvoli, P. Spillantini, F. Stolzi, I. Takahashi, M. Takayanagi, M. Takita, T. Tamura, N. Tateyama, T. Terasawa, H. Tomida, S. Torii, Y. Tsunesada, Y. Uchihori, S. Ueno, E. Vannuccini, J. P. Wefel, K. Yamaoka, S. Yanagita, A. Yoshida, K. Yoshida, T. Yuda, and Calet Collaboration (2017, November). Energy Spec-

trum of Cosmic-Ray Electron and Positron from 10 GeV to 3 TeV Observed with the Calorimetric Electron Telescope on the International Space Station. *Physical Review Letters 119*(18), 181101.

Altenhoff, W. J. (1960). *Radio Astronomical measurements at 2.7KMHz.*

Alvarez, H., J. Aparici, J. May, and F. Olmos (1997, August). A 45-MHz continuum survey of the southern hemisphere. *A&AS 124*, 205–253.

Alves, M. I. R., R. D. Davies, C. Dickinson, M. Calabretta, R. Davis, and L. Staveley-Smith (2012, May). A derivation of the free-free emission on the Galactic plane between l = 20 and 44 degrees. *MNRAS 422*, 2429–2443.

Anderson, L. D., W. P. Armentrout, B. M. Johnstone, T. M. Bania, D. S. Balser, T. V. Wenger, and V. Cunningham (2015, December). Finding Distant Galactic HII Regions. *ApJS 221*, 26.

Anderson, L. D., W. P. Armentrout, M. Luisi, T. M. Bania, D. S. Balser, and T. V. Wenger (2018, February). A Green Bank Telescope Survey of Large Galactic H II Regions. *ApJS 234*, 33.

Anderson, L. D., T. M. Bania, D. S. Balser, V. Cunningham, T. V. Wenger, B. M. Johnstone, and W. P. Armentrout (2014, May). The WISE Catalog of Galactic H II Regions. *ApJS 212*, 1.

Anderson, L. D., T. M. Bania, D. S. Balser, and R. T. Rood (2011, June). The Green Bank Telescope H II Region Discovery Survey. II. The Source Catalog. *ApJS 194*, 32.

Anderson, L. D., L. A. Hough, T. V. Wenger, T. M. Bania, and D. S. Balser (2015, September). Untangling the Recombination Line Emission from H II Regions with Multiple Velocity Components. *ApJ 810*, 42.

Andrae, R., T. Schulze-Hartung, and P. Melchior (2010, December). Dos and don'ts of reduced chi-squared. *ArXiv e-prints*.

Araya, E., P. Hofner, E. Churchwell, and S. Kurtz (2002, January). Arecibo Observations of Formaldehyde and Radio Recombination Lines toward Ultracompact H II Regions. *ApJS 138*, 63–74.

Balser, D. S., R. T. Rood, T. M. Bania, and L. D. Anderson (2011, September). H II Region Metallicity Distribution in the Milky Way Disk. *ApJ 738*, 27.

Balser, D. S., T. V. Wenger, L. D. Anderson, and T. M. Bania (2015, June). Azimuthal Metallicity Structure in the Milky Way Disk. *ApJ 806*, 199.

Bania, T. M., L. D. Anderson, and D. S. Balser (2012, November). The Arecibo H II Region Discovery Survey. *ApJ 759*, 96.

Bania, T. M., L. D. Anderson, D. S. Balser, and R. T. Rood (2010, August). The Green Bank Telescope Galactic H II Region Discovery Survey. *ApJL 718*, L106–L111.

Berry, D. S. (2015, April). FellWalker-A clump identification algorithm. *Astronomy and Computing 10*, 22–31.

Beuermann, K., G. Kanbach, and E. M. Berkhuijsen (1985, December). Radio structure of the Galaxy - Thick disk and thin disk at 408 MHz. *A&A 153*, 17–34.

Beuther, H., S. Bihr, M. Rugel, K. Johnston, Y. Wang, F. Walter, A. Brunthaler, A. J. Walsh, J. Ott, J. Stil, T. Henning, T. Schierhuber, J. Kainulainen, M. Heyer, P. F. Goldsmith, L. D. Anderson, S. N. Longmore, R. S. Klessen, S. C. O. Glover, J. S.

Urquhart, R. Plume, S. E. Ragan, N. Schneider, N. M. McClure-Griffiths, K. M. Menten, R. Smith, N. Roy, R. Shanahan, Q. Nguyen-Luong, and F. Bigiel (2016, October). The HI/OH/Recombination line survey of the inner Milky Way (THOR). Survey overview and data release 1. *A&A 595*, A32.

Bhattacharjee, P., S. Chaudhury, and S. Kundu (2014, April). Rotation Curve of the Milky Way out to ˜200 kpc. *ApJ 785*, 63.

Bordovitsyn, V. A. (1999, July). *Synchrotron Radiation Theory and its Development, in Memory of i M Ternov (1921-1996)*. World Scientific Press.

Bowman, J. D., I. Cairns, D. L. Kaplan, T. Murphy, D. Oberoi, L. Staveley-Smith, W. Arcus, D. G. Barnes, G. Bernardi, F. H. Briggs, S. Brown, J. D. Bunton, A. J. Burgasser, R. J. Cappallo, S. Chatterjee, B. E. Corey, A. Coster, A. Deshpande, L. deSouza, D. Emrich, P. Erickson, R. F. Goeke, B. M. Gaensler, L. J. Greenhill, L. Harvey-Smith, B. J. Hazelton, D. Herne, J. N. Hewitt, M. Johnston-Hollitt, J. C. Kasper, B. B. Kincaid, R. Koenig, E. Kratzenberg, C. J. Lonsdale, M. J. Lynch, L. D. Matthews, S. R. McWhirter, D. A. Mitchell, M. F. Morales, E. H. Morgan, S. M. Ord, J. Pathikulangara, T. Prabu, R. A. Remillard, T. Robishaw, A. E. E. Rogers, A. A. Roshi, J. E. Salah, R. J. Sault, N. U. Shankar, K. S. Srivani, J. B. Stevens, R. Subrahmanyan, S. J. Tingay, R. B. Wayth, M. Waterson, R. L. Webster, A. R. Whitney, A. J. Williams, C. L. Williams, and J. S. B. Wyithe (2013, April). Science with the Murchison Widefield Array. *PASA 30*, 31.

Brand, J. and L. Blitz (1993, August). The Velocity Field of the Outer Galaxy. *A&A 275*, 67.

Brown, C., C. Jordan, J. M. Dickey, L. D. Anderson, W. P. Armentrout, D. S. Balser, T. M. Bania, J. R. Dawson, N. M. McClure-Griffiths, and T. V. Wenger (2017, July). The Southern H II Region Discovery Survey (SHRDS): Pilot Survey. *AJ 154*, 23.

Brown, J. C., M. Haverkorn, B. M. Gaensler, A. R. Taylor, N. S. Bizunok, N. M. McClure-Griffiths, J. M. Dickey, and A. J. Green (2007, July). Rotation Measures of Extragalactic Sources behind the Southern Galactic Plane: New Insights into the Large-Scale Magnetic Field of the Inner Milky Way. *ApJ 663*, 258–266.

Burke, B. F. (1957, May). Systematic distortion of the outer regions of the galaxy. *AJ 62*, 90.

Carpenter, J. M., R. L. Snell, and F. P. Schloerb (1990, October). Molecular clouds associated with luminous far-infrared sources in the outer Galaxy. *ApJ 362*, 147–164.

Caswell, J. L. (1976, December). A map of the northern sky at 10 MHz. *MNRAS 177*, 601–616.

Caswell, J. L. and R. F. Haynes (1987, January). Southern H II regions - an extensive study of radio recombination line emission. *A&A 171*, 261–276.

Clemens, D. P. (1985, August). Massachusetts-Stony Brook Galactic plane CO survey - The Galactic disk rotation curve. *ApJ 295*, 422–428.

Cohen, A. S., W. M. Lane, W. D. Cotton, N. E. Kassim, T. J. W. Lazio, R. A. Perley, J. J. Condon, and W. C. Erickson (2007, September). The VLA Low-Frequency Sky Survey. *AJ 134*, 1245–1262.

Condon, J. J., W. D. Cotton, E. W. Greisen, Q. F. Yin, R. A. Perley, G. B. Taylor, and J. J. Broderick (1998, May). The NRAO VLA Sky Survey. *AJ 115*, 1693–1716.

Cordes, J. M. and T. J. W. Lazio (2002, July). NE2001.I. A New Model for the Galactic Distribution of Free Electrons and its Fluctuations. *ArXiv Astrophysics e-prints*.

Cordes, J. M. and T. J. W. Lazio (2003, January). NE2001. II. Using Radio Propagation Data to Construct a Model for the Galactic Distribution of Free Electrons. *ArXiv Astrophysics e-prints*.

Crutcher, R. M., T. H. Troland, A. A. Goodman, C. Heiles, I. Kazes, and P. C. Myers (1993, April). OH Zeeman observations of dark clouds. *ApJ 407*, 175–184.

Dame, T. M., D. Hartmann, and P. Thaddeus (2001, February). The Milky Way in Molecular Clouds: A New Complete CO Survey. *ApJ 547*, 792–813.

de Gasperin, F., M. Mevius, D. A. Rafferty, H. T. Intema, and R. A. Fallows (2018, August). The effect of the ionosphere on ultra-low-frequency radio-interferometric observations. *A&A 615*, A179.

de Oliveira-Costa, A., M. Tegmark, B. M. Gaensler, J. Jonas, T. L. Landecker, and P. Reich (2008, July). A model of diffuse Galactic radio emission from 10 MHz to 100 GHz. *MNRAS 388*, 247–260.

Deharveng, L., F. Schuller, L. D. Anderson, A. Zavagno, F. Wyrowski, K. M. Menten, L. Bronfman, L. Testi, C. M. Walmsley, and M. Wienen (2010, November). A gallery of bubbles. The nature of the bubbles observed by Spitzer and what ATLASGAL tells us about the surrounding neutral material. *A&A 523*, A6.

Deshpande, A. A. and C. V. Sastry (1986, May). Observations of the giant H II region complex W51 at decameter wavelengths. *A&A 160*, 129–131.

Dickinson, C., R. D. Davies, and R. J. Davis (2003, May). Towards a free-free template for CMB foregrounds. *MNRAS 341*, 369–384.

Downes, D., T. L. Wilson, J. Bieging, and J. Wink (1980, June). H110-alpha and H2CO survey of galactic radio sources. *A&AS 40*, 379–394.

Draine, B. T. (2003). Interstellar Dust Grains. *ARA&A 41*, 241–289.

Dwarakanath, K. S. and N. Udaya Shankar (1990, September). A synthesis map of the sky at 34.5 MHz. *Journal of Astrophysics and Astronomy 11*, 323–410.

Eastwood, M. W., M. M. Anderson, R. M. Monroe, G. Hallinan, B. R. Barsdell, S. A. Bourke, M. A. Clark, S. W. Ellingson, J. Dowell, H. Garsden, L. J. Greenhill, J. M. Hartman, J. Kocz, T. J. W. Lazio, D. C. Price, F. K. Schinzel, G. B. Taylor, H. K. Vedantham, Y. Wang, and D. P. Woody (2018, July). The Radio Sky at Meter Wavelengths: m-mode Analysis Imaging with the OVRO-LWA. *AJ 156*, 32.

Epstein, R. I. and P. A. Feldman (1967, November). Synchrotron Radiation from Electrons in Helical Orbits. *ApJL 150*, L109.

Ferrière, K. M. (2001, October). The interstellar environment of our galaxy. *Reviews of Modern Physics 73*, 1031–1066.

Fich, M., L. Blitz, and A. A. Stark (1989, July). The rotation curve of the Milky Way to 2 R(0). *ApJ 342*, 272–284.

Gaensler, B. M. and S. Johnston (1995, December). The pulsar/supernova remnant connection. *MNRAS 277*, 1243–1253.

Gaensler, B. M. and P. O. Slane (2006, September). The Evolution and Structure of Pulsar Wind Nebulae. *ARA&A 44*, 17–47.

Gaia collaboration, D. Katz, T. Antoja, M. Romero-Gó, R. Drimmel, C. Reylé, G. M. Seabroke, C. Soubiran, C. Babusiaux, P. Di Matteo, and et al. (2018, August). Gaia Data Release 2. Mapping the Milky Way disc kinematics. *A&A 616*, A11.

García, P., L. Bronfman, L.-Å. Nyman, T. M. Dame, and A. Luna (2014, May). Giant Molecular Clouds and Massive Star Formation in the Southern Milky Way. *ApJS 212*, 2.

Georgelin, Y. M. and Y. P. Georgelin (1976, May). The spiral structure of our Galaxy determined from H II regions. *A&A 49*, 57–79.

Green, A. J., L. E. Cram, M. I. Large, and T. Ye (1999, May). The Molonglo Galactic Plane Survey. I. Overview and Images. *ApJS 122*, 207–219.

Green, D. A. (2011, June). A colour scheme for the display of astronomical intensity images. *Bulletin of the Astronomical Society of India 39*, 289–295.

Green, D. A. (2014, June). A catalogue of 294 Galactic supernova remnants. *Bulletin of the Astronomical Society of India 42*, 47–58.

Green, G. M., E. F. Schlafly, D. P. Finkbeiner, H.-W. Rix, N. Martin, W. Burgett, P. W. Draper, H. Flewelling, K. Hodapp, N. Kaiser, R. P. Kudritzki, E. Magnier, N. Metcalfe, P. Price, J. Tonry, and R. Wainscoat (2015, September). A Three-dimensional Map of Milky Way Dust. *ApJ 810*, 25.

Guzmán, A. E., J. May, H. Alvarez, and K. Maeda (2011, January). All-sky Galactic radiation at 45 MHz and spectral index between 45 and 408 MHz. *A&A 525*, A138.

Han, J. L. (2017, August). Observing Interstellar and Intergalactic Magnetic Fields. *ARA&A 55*, 111–157.

Han, J. L., R. N. Manchester, A. G. Lyne, G. J. Qiao, and W. van Straten (2006, May). Pulsar Rotation Measures and the Large-Scale Structure of the Galactic Magnetic Field. *ApJ 642*, 868–881.

Hancock, P. J., T. Murphy, B. M. Gaensler, A. Hopkins, and J. R. Curran (2012, May). Compact continuum source finding for next generation radio surveys. *MNRAS 422*, 1812–1824.

Hancock, P. J., C. M. Trott, and N. Hurley-Walker (2018, March). Source Finding in the Era of the SKA (Precursors): Aegean 2.0. *PASA 35*, e011.

Haslam, C. G. T., U. Klein, C. J. Salter, H. Stoffel, W. E. Wilson, M. N. Cleary, D. J. Cooke, and P. Thomasson (1981, July). A 408 MHz all-sky continuum survey. I - Observations at southern declinations and for the North Polar region. *A&A 100*, 209–219.

Haslam, C. G. T., C. J. Salter, H. Stoffel, and W. E. Wilson (1982, January). A 408 MHz all-sky continuum survey. II - The atlas of contour maps. *A&AS 47*, 1.

Haverkorn, M., F. Boulanger, T. Enßlin, J. Hörandel, T. Jaffe, J. Jasche, J. Rachen, and A. Shukurov (2019, January). IMAGINE: Modeling the Galactic Magnetic Field. *Galaxies 7*(1), 17.

Haverkorn, M., J. C. Brown, B. M. Gaensler, and N. M. McClure-Griffiths (2008, June). The Outer Scale of Turbulence in the Magnetoionized Galactic Interstellar Medium. *ApJ 680*, 362–370.

Haverkorn, M., B. M. Gaensler, N. M. McClure-Griffiths, J. M. Dickey, and A. J. Green (2006, December). The Southern Galactic Plane Survey: Polarized Radio Continuum Observations and Analysis. *ApJS 167*, 230–238.

Heyer, M. and T. M. Dame (2015, August). Molecular Clouds in the Milky Way. *ARA&A 53*, 583–629.

Hindson, L., M. Johnston-Hollitt, N. Hurley-Walker, J. R. Callingham, H. Su, J. Morgan, M. Bell, G. Bernardi, J. D. Bowman, F. Briggs, R. J. Cappallo, A. A. Deshpande, K. S. Dwarakanath, B.-Q. For, B. M. Gaensler, L. J. Greenhill, P. Hancock, B. J. Hazelton, A. D. Kapińska, D. L. Kaplan, E. Lenc, C. J. Lonsdale, B. Mckinley, S. R. McWhirter, D. A. Mitchell, M. F. Morales, E. Morgan, D. Oberoi, A. Offringa, S. M. Ord, P. Procopio, T. Prabu, N. U. Shankar, K. S. Srivani, L. Staveley-Smith, R. Subrahmanyan, S. J. Tingay, R. B. Wayth, R. L. Webster, A. Williams, C. L. Williams, C. Wu, and Q. Zheng (2016, May). A Large-Scale, Low-Frequency Murchison Widefield Array Survey of Galactic HII Regions between $260 < l < 340$. *PASA 33*, e020.

Hou, L. G. and J. L. Han (2014, September). The observed spiral structure of the Milky Way. *A&A 569*, A125.

Huang, Y., X.-W. Liu, H.-B. Yuan, M.-S. Xiang, H.-W. Zhang, B.-Q. Chen, J.-J. Ren, C. Wang, Y. Zhang, Y.-H. Hou, Y.-F. Wang, and Z.-H. Cao (2016, December). The Milky Way's rotation curve out to 100 kpc and its constraint on the Galactic mass distribution. *MNRAS 463*, 2623–2639.

Hurley-Walker, N., J. R. Callingham, P. J. Hancock, T. M. O. Franzen, L. Hindson, A. D. Kapińska, J. Morgan, A. R. Offringa, R. B. Wayth, C. Wu, Q. Zheng, T. Murphy, M. E. Bell, K. S. Dwarakanath, B. For, B. M. Gaensler, M. Johnston-Hollitt, E. Lenc, P. Procopio, L. Staveley-Smith, R. Ekers, J. D. Bowman, F. Briggs, R. J. Cappallo, A. A. Deshpande, L. Greenhill, B. J. Hazelton, D. L. Kaplan, C. J. Lonsdale, S. R. McWhirter, D. A. Mitchell, M. F. Morales, E. Morgan, D. Oberoi, S. M. Ord, T. Prabu, N. U. Shankar, K. S. Srivani, R. Subrahmanyan, S. J. Tingay, R. L. Webster, A. Williams, and C. L. Williams (2017, January). GaLactic and Extra-

galactic All-sky Murchison Widefield Array (GLEAM) survey - I. A low-frequency extragalactic catalogue. *MNRAS 464*, 1146–1167.

Hurley-Walker, N., P. J. Hancock, T. M. O. Franzen, J. R. Callingham, A. R. Offringa, L. Hindson, C. Wu, M. E. Bell, B. Q. For, B. M. Gaensler, M. Johnston-Hollitt, A. D. Kapińska, J. Morgan, T. Murphy, B. McKinley, P. Procopio, L. Staveley-Smith, R. B. Wayth, and Q. Zheng (2019, November). GaLactic and Extragalactic All-sky Murchison Widefield Array (GLEAM) survey II: Galactic plane $345° < l < 67°$, $180° < l < 240°$. *PASA 36*, e047.

Hurley-Walker, N., J. Morgan, R. B. Wayth, P. J. Hancock, M. E. Bell, G. Bernardi, R. Bhat, F. Briggs, A. A. Deshpande, A. Ewall-Wice, L. Feng, B. J. Hazelton, L. Hindson, D. C. Jacobs, D. L. Kaplan, N. Kudryavtseva, E. Lenc, B. McKinley, D. Mitchell, B. Pindor, P. Procopio, D. Oberoi, A. Offringa, S. Ord, J. Riding, J. D. Bowman, R. Cappallo, B. Corey, D. Emrich, B. M. Gaensler, R. Goeke, L. Greenhill, J. Hewitt, M. Johnston-Hollitt, J. Kasper, E. Kratzenberg, C. Lonsdale, M. Lynch, R. McWhirter, M. F. Morales, E. Morgan, T. Prabu, A. Rogers, A. Roshi, U. Shankar, K. Srivani, R. Subrahmanyan, S. Tingay, M. Waterson, R. Webster, A. Whitney, A. Williams, and C. Williams (2014, November). The Murchison Widefield Array Commissioning Survey: A Low-Frequency Catalogue of 14 110 Compact Radio Sources over 6 100 Square Degrees. *PASA 31*, 45.

Jansson, R. and G. R. Farrar (2012a, September). A New Model of the Galactic Magnetic Field. *ApJ 757*, 14.

Jansson, R. and G. R. Farrar (2012b, December). The Galactic Magnetic Field. *ApJL 761*, L11.

Johnston, S., M. Bailes, N. Bartel, C. Baugh, M. Bietenholz, C. Blake, R. Braun, J. Brown, S. Chatterjee, J. Darling, A. Deller, R. Dodson, P. G. Edwards, R. Ekers, S. Ellingsen, I. Feain, B. M. Gaensler, M. Haverkorn, G. Hobbs, A. Hopkins, C. Jackson, C. James, G. Joncas, V. Kaspi, V. Kilborn, B. Koribalski, R. Kothes, T. L. Landecker, E. Lenc, J. Lovell, J.-P. Macquart, R. Manchester, D. Matthews, N. M. McClure-Griffiths, R. Norris, U.-L. Pen, C. Phillips, C. Power, R. Protheroe, E. Sadler, B. Schmidt, I. Stairs, L. Staveley-Smith, J. Stil, R. Taylor, S. Tingay, A. Tzioumis, M. Walker, J. Wall, and M. Wolleben (2007, December). Science with the Australian Square Kilometre Array Pathfinder. *PASA 24*, 174–188.

Jones, B. B. and E. A. Finlay (1974, October). An aperture synthesis survey of the galactic plane. *Australian Journal of Physics 27*, 687–711.

Jones, K. G. (1969, March). The search for the nebulae - VI. *Journal of the British Astronomical Association 79*, 213–222.

Kalberla, P. M. W., W. B. Burton, D. Hartmann, E. M. Arnal, E. Bajaja, R. Morras, and W. G. L. Pöppel (2005, September). The Leiden/Argentine/Bonn (LAB) Survey of Galactic HI. Final data release of the combined LDS and IAR surveys with improved stray-radiation corrections. *A&A 440*, 775–782.

Kalberla, P. M. W. and J. Kerp (2009, September). The Hi Distribution of the Milky Way. *ARA&A 47*, 27–61.

Kalcheva, I. E., M. G. Hoare, J. S. Urquhart, S. Kurtz, S. L. Lumsden, C. R. Purcell, and A. A. Zijlstra (2018, March). The Coordinated Radio and Infrared Survey for High-Mass Star Formation III. A catalogue of northern ultra-compact H II regions. *ArXiv e-prints*.

Kassim, N. E. S. (1987). *The galactic plane at 30.9 MHz*. Ph. D. thesis, Maryland Univ., College Park.

Kerr, F. J. (1957, May). A Magellanic effect on the galaxy. *AJ 62*, 93–93.

Kerr, F. J. and D. Lynden-Bell (1986, August). Review of galactic constants. *MNRAS 221*, 1023–1038.

Kolpak, M. A., J. M. Jackson, T. M. Bania, D. P. Clemens, and J. M. Dickey (2003, January). Resolving the Kinematic Distance Ambiguity toward Galactic H II Regions. *ApJ 582*, 756–769.

Krymkin, V. V. (1978, October). Radio emission of the NGC 1499 nebula at decametric wavelengths. *Ap&SS 58*, 347–352.

Kurtz, S. (2005). Hypercompact HII regions. In R. Cesaroni, M. Felli, E. Churchwell, and M. Walmsley (Eds.), *Massive Star Birth: A Crossroads of Astrophysics*, Volume 227 of *IAU Symposium*, pp. 111–119.

Lang, K. R. (1980). *Astrophysical Formulae. A Compendium for the Physicist and Astrophysicist.*

Large, M. I., L. E. Cram, and A. M. Burgess (1991, April). A machine-readable release of the Molonglo Reference Catalogue of Radio Sources. *The Observatory 111*, 72–75.

Large, M. I., B. Y. Mills, A. G. Little, D. F. Crawford, and J. M. Sutton (1981, February). The Molonglo Reference Catalogue of Radio Sources. *MNRAS 194*, 693.

Levine, E. S., L. Blitz, and C. Heiles (2006, June). The Spiral Structure of the Outer Milky Way in Hydrogen. *Science 312*, 1773–1777.

Levine, E. S., C. Heiles, and L. Blitz (2008, June). The Milky Way Rotation Curve and Its Vertical Derivatives: Inside the Solar Circle. *ApJ 679*, 1288–1298.

Lisenfeld, U. and H. J. Völk (2000, February). On the radio spectral index of galaxies. *A&A 354*, 423–430.

Loi, S. T., T. Murphy, M. E. Bell, D. L. Kaplan, E. Lenc, A. R. Offringa, N. Hurley-Walker, G. Bernardi, J. D. Bowman, F. Briggs, R. J. Cappallo, B. E. Corey, A. A. Deshpande, D. Emrich, B. M. Gaensler, R. Goeke, L. J. Greenhill, B. J. Hazelton, M. Johnston-Hollitt, J. C. Kasper, E. Kratzenberg, C. J. Lonsdale, M. J. Lynch, S. R. McWhirter, D. A. Mitchell, M. F. Morales, E. Morgan, D. Oberoi, S. M. Ord, T. Prabu, A. E. E. Rogers, A. Roshi, N. U. Shankar, K. S. Srivani, R. Subrahmanyan, S. J. Tingay, M. Waterson, R. B. Wayth, R. L. Webster, A. R. Whitney, A. Williams, and C. L. Williams (2015, November). Quantifying ionospheric effects on time-domain astrophysics with the Murchison Widefield Array. *MNRAS 453*, 2731–2746.

Maíz-Apellániz, J. (2001, October). The Origin of the Local Bubble. *ApJL 560*, L83–L86.

Mansfield, V. (1969, February). An Electron Temperature Distribution derived from Optical and Radio Measurements of H II Regions. *Ap&SS 3*, 292–300.

Mauch, T., T. Murphy, H. J. Buttery, J. Curran, R. W. Hunstead, B. Piestrzynski, J. G. Robertson, and E. M. Sadler (2003, July). SUMSS: a wide-field radio imaging survey of the southern sky - II. The source catalogue. *MNRAS 342*, 1117–1130.

McClure-Griffiths, N. M. and J. M. Dickey (2007, December). Milky Way Kinematics. I. Measurements at the Subcentral Point of the Fourth Quadrant. *ApJ 671*, 427–438.

McClure-Griffiths, N. M. and J. M. Dickey (2016, November). Milky Way Kinematics. II. A Uniform Inner Galaxy H I Terminal Velocity Curve. *ApJ 831*, 124.

McClure-Griffiths, N. M., J. M. Dickey, B. M. Gaensler, and A. J. Green (2004, June). A Distant Extended Spiral Arm in the Fourth Quadrant of the Milky Way. *ApJL 607*, L127–L130.

McClure-Griffiths, N. M., J. M. Dickey, B. M. Gaensler, A. J. Green, M. Haverkorn, and S. Strasser (2005, June). The Southern Galactic Plane Survey: H I Observations and Analysis. *ApJS 158*, 178–187.

McKinley, B., F. Briggs, D. L. Kaplan, L. J. Greenhill, G. Bernardi, J. D. Bowman, A. de Oliveira-Costa, S. J. Tingay, B. M. Gaensler, D. Oberoi, M. Johnston-Hollitt, W. Arcus, D. Barnes, J. D. Bunton, R. J. Cappallo, B. E. Corey, A. Deshpande, L. deSouza, D. Emrich, R. Goeke, B. J. Hazelton, D. Herne, J. N. Hewitt, J. C. Kasper, B. B. Kincaid, R. Koenig, E. Kratzenberg, C. J. Lonsdale, M. J. Lynch, S. R. McWhirter, D. A. Mitchell, M. F. Morales, E. Morgan, S. M. Ord, J. Pathikulangara, T. Prabu, R. A. Remillard, A. E. E. Rogers, A. Roshi, J. E. Salah, R. J. Sault, N. Udaya Shankar, K. S. Srivani, J. Stevens, R. Subrahmanyan, R. B. Wayth, M. Waterson, R. L. Webster, A. R. Whitney, A. Williams, C. L. Williams, and J. S. B. Wyithe (2013, January). Low-frequency Observations of the Moon with the Murchison Widefield Array. *AJ 145*, 23.

Merrifield, M. R. (1992, May). The rotation curve of the Milky Way to 2.5 R_0 from the thickness of the H I layer. *AJ 103*, 1552–1563.

Mezger, P. G. and A. P. Henderson (1967, February). Galactic H II Regions. I. Observations of Their Continuum Radiation at the Frequency 5 GHz. *ApJ 147*, 471.

Moss, V. A., F. J. Lockman, and N. M. McClure-Griffiths (2017, January). Tracing Dense and Diffuse Neutral Hydrogen in the Halo of the Milky Way. *ApJ 834*, 155.

Mróz, P., A. Udalski, D. M. Skowron, J. Skowron, I. Soszyński, P. Pietrukowicz, M. K. Szymański, R. Poleski, S. Kozłowski, and K. Ulaczyk (2019, Jan). Rotation Curve of the Milky Way from Classical Cepheids. *ApJ 870*(1), L10.

Mulcahy, D. D., A. Horneffer, R. Beck, G. Heald, A. Fletcher, A. Scaife, B. Adebahr, J. M. Anderson, A. Bonafede, M. Brüggen, G. Brunetti, K. T. Chyży, J. Conway, R.-J. Dettmar, T. Enßlin, M. Haverkorn, C. Horellou, M. Iacobelli, F. P. Israel, H. Junklewitz, W. Jurusik, J. Köhler, M. Kuniyoshi, E. Orrú, R. Paladino, R. Pizzo, W. Reich, and H. J. A. Röttgering (2014, August). The nature of the low-frequency emission of M 51. First observations of a nearby galaxy with LOFAR. *A&A 568*, A74.

Murphy, T., T. Mauch, A. Green, R. W. Hunstead, B. Piestrzynska, A. P. Kels, and P. Sztajer (2007, November). The second epoch Molonglo Galactic Plane Survey: compact source catalogue. *MNRAS 382*, 382–392.

Nakanishi, H. and Y. Sofue (2016, February). Three-dimensional distribution of the ISM in the Milky Way galaxy. III. The total neutral gas disk. *PASJ 68*, 5.

Narayanan, D., M. R. Krumholz, E. C. Ostriker, and L. Hernquist (2012, Apr). A general model for the CO-H_2 conversion factor in galaxies with applications to the star formation law. *MNRAS 421*, 3127–3146.

Newberg, H. J., B. Yanny, C. Rockosi, E. K. Grebel, H.-W. Rix, J. Brinkmann, I. Csabai, G. Hennessy, R. B. Hindsley, R. Ibata, Z. Ivezić, D. Lamb, E. T. Nash, M. Odenkirchen, H. A. Rave, D. P. Schneider, J. A. Smith, A. Stolte, and D. G. York (2002, April). The Ghost of Sagittarius and Lumps in the Halo of the Milky Way. *ApJ 569*, 245–274.

Nord, M. E., C. L. Brogan, T. J. W. Lazio, and N. E. Kassim (2005, December). Holes in the Sky: HII Regions in Absorption at 74 MHz for Galactic Cosmic-Ray Tomography. In N. Kassim, M. Perez, W. Junor, and P. Henning (Eds.), *From Clark Lake to the Long Wavelength Array: Bill Erickson's Radio Science*, Volume 345 of *Astronomical Society of the Pacific Conference Series*, pp. 207.

Nord, M. E., P. A. Henning, R. J. Rand, T. J. W. Lazio, and N. E. Kassim (2006, July). 74 MHz Discrete H II Absorption Regions Toward the Inner Galaxy. *AJ 132*, 242–252.

Odegard, N. (1986, February). Decameter wavelength observations of the Rosette Nebula and the Monoceros loop supernova remnant. *ApJ 301*, 813–824.

Oort, J. H., F. J. Kerr, and G. Westerhout (1958). The galactic system as a spiral nebula (Council Note). *MNRAS 118*, 379.

Orlando, E. and A. Strong (2013, December). Galactic synchrotron emission with cosmic ray propagation models. *MNRAS 436*, 2127–2142.

Paladini, R., R. D. Davies, and G. De Zotti (2004, January). Spatial distribution of Galactic HII regions. *MNRAS 347*, 237–245.

Peterson, J. D. and W. R. Webber (2002, August). Interstellar Absorption of the Galactic Polar Low-Frequency Radio Background Synchrotron Spectrum as an Indicator of Clumpiness in the Warm Ionized Medium. *ApJ 575*, 217–224.

Pettitt, A. R., C. L. Dobbs, D. M. Acreman, and D. J. Price (2014, October). The morphology of the Milky Way - I. Reconstructing CO maps from simulations in fixed potentials. *MNRAS 444*, 919–941.

Planck Collaboration, Y. Akrami, M. Ashdown, J. Aumont, C. Baccigalupi, M. Ballardini, A. J. Banday, R. B. Barreiro, N. Bartolo, S. Basak, K. Benabed, M. Bersanelli, P. Bielewicz, J. R. Bond, J. Borrill, F. R. Bouchet, F. Boulanger, M. Bucher, C. Burigana, E. Calabrese, J.-F. Cardoso, J. Carron, B. Casaponsa, A. Challinor, L. P. L. Colombo, C. Combet, B. P. Crill, F. Cuttaia, P. de Bernardis, A. de Rosa, G. de Zotti, J. Delabrouille, J.-M. Delouis, E. Di Valentino, C. Dickinson, J. M. Diego, S. Donzelli, O. Doré, A. Ducout, X. Dupac, G. Efstathiou, F. Elsner, T. A. Enßlin, H. K. Eriksen, E. Falgarone, R. Fernandez-Cobos, F. Finelli, F. Forastieri, M. Frailis, A. A. Fraisse, E. Franceschi, A. Frolov, S. Galeotta, S. Galli, K. Ganga, R. T. Génova-Santos, M. Gerbino, T. Ghosh, J. González-Nuevo, K. M. Górski, S. Gratton, A. Gruppuso, J. E. Gudmundsson, W. Handley, F. K. Hansen, G. Helou, D. Herranz, Z. Huang, A. H. Jaffe, A. Karakci, E. Keihänen, R. Keskitalo, K. Kiiveri, J. Kim, T. S. Kisner, N. Krachmalnicoff, M. Kunz, H. Kurki-Suonio, G. Lagache, J.-M. Lamarre, A. Lasenby, M. Lattanzi, C. R. Lawrence, M. Le Jeune, F. Levrier, M. Liguori, P. B. Lilje, V. Lindholm, M. López-Caniego, P. M. Lubin, Y.-Z. Ma, J. F. Macías-Pérez, G. Maggio, D. Maino, N. Mandolesi, A. Mangilli, A. Marcos-Caballero, P. G. Martin, E. Martínez-González, S. Matarrese, N. Mauri, J. D. McEwen, P. R. Meinhold, A. Melchiorri, A. Mennella, M. Migliaccio, M.-A. Miville-Deschênes, D. Molinari, A. Moneti, L. Montier, G. Morgante, P. Natoli, F. Oppizzi, L. Pagano, D. Paoletti, B. Partridge, M. Peel, V. Pettorino, F. Piacentini, G. Polenta, J.-L. Puget, J. P. Rachen, M. Reinecke, M. Remazeilles, A. Renzi, G. Rocha, G. Roudier, J. A. Rubiño-Martín, B. Ruiz-Granados, L. Salvati, M. Sandri, M. Savelainen, D. Scott, D. S. Seljebotn, C. Sirignano, L. D. Spencer, A.-S. Suur-Uski, J. A. Tauber, D. Tavagnacco, M. Tenti, H. Thommesen, L. Toffolatti, M. Tomasi, T. Trombetti, J. Valiviita, B. Van Tent, P. Vielva, F. Villa, N. Vittorio, B. D. Wandelt, I. K. Wehus, A. Zacchei, and A. Zonca (2018, July). Planck 2018

results. IV. Diffuse component separation. *ArXiv e-prints*.

Platania, P., M. Bensadoun, M. Bersanelli, G. De Amici, A. Kogut, S. Levin, D. Maino, and G. F. Smoot (1998, October). A Determination of the Spectral Index of Galactic Synchrotron Emission in the 1-10 GHz Range. *ApJ 505*, 473–483.

Polderman, I. M., M. Haverkorn, and T. R. Jaffe (2020, April). A more detailed look at Galactic magnetic field models: using free-free absorption in HII regions. *A&A 636*, A2.

Polderman, I. M., M. Haverkorn, T. R. Jaffe, and M. I. R. Alves (2019, January). Low-frequency measurements of synchrotron absorbing HII regions and modeling of observed synchrotron emissivity. *A&A 621*, A127.

Quireza, C., R. T. Rood, T. M. Bania, D. S. Balser, and W. J. Maciel (2006, December). The Electron Temperature Gradient in the Galactic Disk. *ApJ 653*, 1226–1240.

Reid, M. J., K. M. Menten, A. Brunthaler, X. W. Zheng, T. M. Dame, Y. Xu, Y. Wu, B. Zhang, A. Sanna, M. Sato, K. Hachisuka, Y. K. Choi, K. Immer, L. Moscadelli, K. L. J. Rygl, and A. Bartkiewicz (2014, March). Trigonometric Parallaxes of High Mass Star Forming Regions: The Structure and Kinematics of the Milky Way. *ApJ 783*, 130.

Remazeilles, M., C. Dickinson, A. J. Banday, M.-A. Bigot-Sazy, and T. Ghosh (2015, August). An improved source-subtracted and destriped 408-MHz all-sky map. *MNRAS 451*, 4311–4327.

Roger, R. S., C. H. Costain, T. L. Landecker, and C. M. Swerdlyk (1999, May). The radio emission from the Galaxy at 22 MHz. *A&AS 137*, 7–19.

Sanna, A., M. J. Reid, T. M. Dame, K. M. Menten, and A. Brunthaler (2017, October). Mapping spiral structure on the far side of the Milky Way. *Science 358*, 227–230.

Scheuer, P. A. G. and M. Ryle (1953). An investigation of the H II regions by a radio method. *MNRAS 113*, 3.

Shaver, P. A., R. A. Windhorst, P. Madau, and A. G. de Bruyn (1999, May). Can the reionization epoch be detected as a global signature in the cosmic background? *A&A 345*, 380–390.

Skrutskie, M. F., R. M. Cutri, R. Stiening, M. D. Weinberg, S. Schneider, J. M. Carpenter, C. Beichman, R. Capps, T. Chester, J. Elias, J. Huchra, J. Liebert, C. Lonsdale, D. G. Monet, S. Price, P. Seitzer, T. Jarrett, J. D. Kirkpatrick, J. E. Gizis, E. Howard, T. Evans, J. Fowler, L. Fullmer, R. Hurt, R. Light, E. L. Kopan, K. A. Marsh, H. L. McCallon, R. Tam, S. Van Dyk, and S. Wheelock (2006, February). The Two Micron All Sky Survey (2MASS). *AJ 131*, 1163–1183.

Sofue, Y., M. Honma, and T. Omodaka (2009, February). Unified Rotation Curve of the Galaxy – Decomposition into de Vaucouleurs Bulge, Disk, Dark Halo, and the 9-kpc Rotation Dip –. *PASJ 61*, 227–236.

Stephens, S. A. (2001). Origin of cosmic ray electrons. *Advances in Space Research 27*, 687–692.

Stil, J. M., A. R. Taylor, J. M. Dickey, D. W. Kavars, P. G. Martin, T. A. Rothwell, A. I. Boothroyd, F. J. Lockman, and N. M. McClure-Griffiths (2006, September). The VLA Galactic Plane Survey. *AJ 132*, 1158–1176.

Strong, A. W., T. A. Porter, S. W. Digel, G. Jóhannesson, P. Martin, I. V. Moskalenko, E. J. Murphy, and E. Orlando (2010, October). Global Cosmic-ray-related Luminosity and Energy Budget of the Milky Way. *ApJL 722*, L58–L63.

Su, H., N. Hurley-Walker, C. A. Jackson, N. M. McClure-Griffiths, S. J. Tingay, L. Hindson, P. Hancock, R. B. Wayth, B. M. Gaensler, L. Staveley-Smith, J. Morgan, M. Johnston-Hollitt, E. Lenc, M. E. Bell, J. R. Callingham, K. S. Dwarkanath, B.-Q. For, A. D. Kapińska, B. McKinley, A. R. Offringa, P. Procopio, C. Wu, and Q. Zheng (2017b, November). Erratum: Galactic synchrotron emissivity measurements between $250 < l < 355$ degrees from the GLEAM survey with the MWA. *MNRAS 472*, 828–834.

Su, H., N. Hurley-Walker, C. A. Jackson, N. M. McClure-Griffiths, S. J. Tingay, L. Hindson, P. Hancock, R. B. Wayth, B. M. Gaensler, L. Staveley-Smith, J. Morgan, M. Johnston-Hollitt, E. Lenc, M. E. Bell, J. R. Callingham, K. S. Dwarkanath, B.-Q. For, A. D. Kapińska, B. McKinley, A. R. Offringa, P. Procopio, C. Wu, and Q. Zheng (2017a, March). Galactic synchrotron emissivity measurements between $250 < l < 355$ degrees from the GLEAM survey with the MWA. *MNRAS 465*, 3163–3174.

Su, H., J. P. Macquart, N. Hurley-Walker, N. M. McClure-Griffiths, C. A. Jackson, S. J. Tingay, W. W. Tian, B. M. Gaensler, B. McKinley, A. D. Kapińska, L. Hindson, P. Hancock, R. B. Wayth, L. Staveley-Smith, J. Morgan, M. Johnston-Hollitt, E. Lenc, M. E. Bell, J. R. Callingham, K. S. Dwarkanath, B.-Q. For, A. R. Offringa, P. Procopio, C. Wu, and Q. Zheng (2018, September). Galactic synchrotron distribution derived from 152 H II region absorption features in the full GLEAM survey. *MNRAS 479*, 4041–4055.

Sun, X.-H. and W. Reich (2010, December). The Galactic halo magnetic field revisited. *Research in Astronomy and Astrophysics 10*, 1287–1297.

Sun, X. H., W. Reich, A. Waelkens, and T. A. Enßlin (2008, January). Radio observational constraints on Galactic 3D-emission models. *A&A 477*, 573–592.

Tingay, S. J., R. Goeke, J. D. Bowman, D. Emrich, S. M. Ord, D. A. Mitchell, M. F. Morales, T. Booler, B. Crosse, R. B. Wayth, C. J. Lonsdale, S. Tremblay, D. Pallot, T. Colegate, A. Wicenec, N. Kudryavtseva, W. Arcus, D. Barnes, G. Bernardi, F. Briggs, S. Burns, J. D. Bunton, R. J. Cappallo, B. E. Corey, A. Deshpande, L. Desouza, B. M. Gaensler, L. J. Greenhill, P. J. Hall, B. J. Hazelton, D. Herne, J. N. Hewitt, M. Johnston-Hollitt, D. L. Kaplan, J. C. Kasper, B. B. Kincaid, R. Koenig, E. Kratzenberg, M. J. Lynch, B. Mckinley, S. R. Mcwhirter, E. Morgan, D. Oberoi, J. Pathikulangara, T. Prabu, R. A. Remillard, A. E. E. Rogers, A. Roshi, J. E. Salah, R. J. Sault, N. Udaya-Shankar, F. Schlagenhaufer, K. S. Srivani, J. Stevens, R. Subrahmanyan, M. Waterson, R. L. Webster, A. R. Whitney, A. Williams, C. L. Williams, and J. S. B. Wyithe (2013, January). The Murchison Widefield Array: The Square Kilometre Array Precursor at Low Radio Frequencies. *PASA 30*, 7.

Urquhart, J. S., M. A. Thompson, T. J. T. Moore, C. R. Purcell, M. G. Hoare, F. Schuller, F. Wyrowski, T. Csengeri, K. M. Menten, S. L. Lumsden, S. Kurtz, C. M. Walmsley, L. Bronfman, L. K. Morgan, D. J. Eden, and D. Russeil (2013, October). ATLASGAL - properties of compact H II regions and their natal clumps. *MNRAS 435*, 400–428.

Van Eck, C. L., J. C. Brown, J. M. Stil, K. Rae, S. A. Mao, B. M. Gaensler, A. Shukurov, A. R. Taylor, M. Haverkorn, P. P. Kronberg, and N. M. McClure-Griffiths (2011, February). Modeling the Magnetic Field in the Galactic Disk Using New Rotation Measure Observations from the Very Large Array. *ApJ 728*, 97.

van Haarlem, M. P., M. W. Wise, A. W. Gunst, G. Heald, J. P. McKean, J. W. T. Hessels, A. G. de Bruyn, R. Nijboer, J. Swinbank, R. Fallows, M. Brentjens, A. Nelles, R. Beck, H. Falcke, R. Fender, J. Hörandel, L. V. E. Koopmans, G. Mann, G. Miley, H. Röttgering, B. W. Stappers, R. A. M. J. Wijers, S. Zaroubi, M. van den

Akker, A. Alexov, J. Anderson, K. Anderson, A. van Ardenne, M. Arts, A. Asgekar, I. M. Avruch, F. Batejat, L. Bähren, M. E. Bell, M. R. Bell, I. van Bemmel, P. Bennema, M. J. Bentum, G. Bernardi, P. Best, L. Bîrzan, A. Bonafede, A.-J. Boonstra, R. Braun, J. Bregman, F. Breitling, R. H. van de Brink, J. Broderick, P. C. Broekema, W. N. Brouw, M. Brüggen, H. R. Butcher, W. van Cappellen, B. Ciardi, T. Coenen, J. Conway, A. Coolen, A. Corstanje, S. Damstra, O. Davies, A. T. Deller, R.-J. Dettmar, G. van Diepen, K. Dijkstra, P. Donker, A. Doorduin, J. Dromer, M. Drost, A. van Duin, J. Eislöffel, J. van Enst, C. Ferrari, W. Frieswijk, H. Gankema, M. A. Garrett, F. de Gasperin, M. Gerbers, E. de Geus, J.-M. Grießmeier, T. Grit, P. Gruppen, J. P. Hamaker, T. Hassall, M. Hoeft, H. A. Holties, A. Horneffer, A. van der Horst, A. van Houwelingen, A. Huijgen, M. Iacobelli, H. Intema, N. Jackson, V. Jelic, A. de Jong, E. Juette, D. Kant, A. Karastergiou, A. Koers, H. Kollen, V. I. Kondratiev, E. Kooistra, Y. Koopman, A. Koster, M. Kuniyoshi, M. Kramer, G. Kuper, P. Lambropoulos, C. Law, J. van Leeuwen, J. Lemaitre, M. Loose, P. Maat, G. Macario, S. Markoff, J. Masters, R. A. McFadden, D. McKay-Bukowski, H. Meijering, H. Meulman, M. Mevius, E. Middelberg, R. Millenaar, J. C. A. Miller-Jones, R. N. Mohan, J. D. Mol, J. Morawietz, R. Morganti, D. D. Mulcahy, E. Mulder, H. Munk, L. Nieuwenhuis, R. van Nieuwpoort, J. E. Noordam, M. Norden, A. Noutsos, A. R. Offringa, H. Olofsson, A. Omar, E. Orrú, R. Overeem, H. Paas, M. Pandey-Pommier, V. N. Pandey, R. Pizzo, A. Polatidis, D. Rafferty, S. Rawlings, W. Reich, J.-P. de Reijer, J. Reitsma, G. A. Renting, P. Riemers, E. Rol, J. W. Romein, J. Roosjen, M. Ruiter, A. Scaife, K. van der Schaaf, B. Scheers, P. Schellart, A. Schoenmakers, G. Schoonderbeek, M. Serylak, A. Shulevski, J. Sluman, O. Smirnov, C. Sobey, H. Spreeuw, M. Steinmetz, C. G. M. Sterks, H.-J. Stiepel, K. Stuurwold, M. Tagger, Y. Tang, C. Tasse, I. Thomas, S. Thoudam, M. C. Toribio, B. van der Tol, O. Usov, M. van Veelen, A.-J. van der Veen, S. ter Veen,

J. P. W. Verbiest, R. Vermeulen, N. Vermaas, C. Vocks, C. Vogt, M. de Vos, E. van der Wal, R. van Weeren, H. Weggemans, P. Weltevrede, S. White, S. J. Wijnholds, T. Wilhelmsson, O. Wucknitz, S. Yatawatta, P. Zarka, A. Zensus, and J. van Zwieten (2013, August). LOFAR: The LOw-Frequency ARray. *A&A 556*, A2.

Wang, Y., S. Bihr, M. Rugel, H. Beuther, K. G. Johnston, J. Ott, J. D. Soler, A. Brunthaler, L. D. Anderson, and J. S. Urquhart (2018, Nov). Radio continuum emission in the northern Galactic plane: Sources and spectral indices from the THOR survey. *A&A 619*, A124.

Wayth, R. B., E. Lenc, M. E. Bell, J. R. Callingham, K. S. Dwarakanath, T. M. O. Franzen, B.-Q. For, B. Gaensler, P. Hancock, L. Hindson, N. Hurley-Walker, C. A. Jackson, M. Johnston-Hollitt, A. D. Kapińska, B. McKinley, J. Morgan, A. R. Offringa, P. Procopio, L. Staveley-Smith, C. Wu, Q. Zheng, C. M. Trott, G. Bernardi, J. D. Bowman, F. Briggs, R. J. Cappallo, B. E. Corey, A. A. Deshpande, D. Emrich, R. Goeke, L. J. Greenhill, B. J. Hazelton, D. L. Kaplan, J. C. Kasper, E. Kratzenberg, C. J. Lonsdale, M. J. Lynch, S. R. McWhirter, D. A. Mitchell, M. F. Morales, E. Morgan, D. Oberoi, S. M. Ord, T. Prabu, A. E. E. Rogers, A. Roshi, N. U. Shankar, K. S. Srivani, R. Subrahmanyan, S. J. Tingay, M. Waterson, R. L. Webster, A. R. Whitney, A. Williams, and C. L. Williams (2015, June). GLEAM: The GaLactic and Extragalactic All-Sky MWA Survey. *PASA 32*, e025.

Wayth, R. B., S. J. Tingay, C. M. Trott, D. Emrich, M. Johnston-Hollitt, B. McKinley, B. M. Gaensler, A. P. Beardsley, T. Booler, B. Crosse, T. M. O. Franzen, L. Horsley, D. L. Kaplan, D. Kenney, M. F. Morales, D. Pallot, G. Sleap, K. Steele, M. Walker, A. Williams, C. Wu, I. H. Cairns, M. D. Filipovic, S. Johnston, T. Murphy, P. Quinn, L. Staveley-Smith, R. Webster, and J. S. B. Wyithe (2018, September). The Phase II Murchison Widefield Array: Design Overview. *ArXiv e-prints*.

Weber, M. and W. de Boer (2010, January). Determination of the local dark matter density in our Galaxy. *A&A 509*, A25.

Weiler, K. W. and R. A. Sramek (1988). Supernovae and supernova remnants. *ARA&A 26*, 295–341.

Wenger, T. V., J. M. Dickey, C. H. Jordan, D. S. Balser, W. P. Armentrout, L. D. Anderson, T. M. Bania, J. R. Dawson, N. M. McClure-Griffiths, and J. Shea (2019, February). The Southern H II Region Discovery Survey. I. The Bright Catalog. *ApJS 240*(2), 24.

Westfold, K. C. (1959, July). The Polarization of Synchrotron Radiation. *ApJ 130*, 241.

Wright, E. L., P. R. M. Eisenhardt, A. K. Mainzer, M. E. Ressler, R. M. Cutri, T. Jarrett, J. D. Kirkpatrick, D. Padgett, R. S. McMillan, M. Skrutskie, S. A. Stanford, M. Cohen, R. G. Walker, J. C. Mather, D. Leisawitz, T. N. Gautier, III, I. McLean, D. Benford, C. J. Lonsdale, A. Blain, B. Mendez, W. R. Irace, V. Duval, F. Liu, D. Royer, I. Heinrichsen, J. Howard, M. Shannon, M. Kendall, A. L. Walsh, M. Larsen, J. G. Cardon, S. Schick, M. Schwalm, M. Abid, B. Fabinsky, L. Naes, and C.-W. Tsai (2010, December). The Wide-field Infrared Survey Explorer (WISE): Mission Description and Initial On-orbit Performance. *AJ 140*, 1868–1881.

Xu, Y., H. J. Newberg, J. L. Carlin, C. Liu, L. Deng, J. Li, R. Schönrich, and B. Yanny (2015, March). Rings and Radial Waves in the Disk of the Milky Way. *ApJ 801*, 105.

Xu, Y., M. Reid, T. Dame, K. Menten, N. Sakai, J. Li, A. Brunthaler, L. Moscadelli, B. Zhang, and X. Zheng (2016, September). The local spiral structure of the Milky Way. *Science Advances 2*, e1600878–e1600878.

Yang, A. Y., M. A. Thompson, W. W. Tian, S. Bihr, H. Beuther, and L. Hindson (2019, Jan). A search for hypercompact H II regions in the Galactic Plane. *MNRAS 482*(2), 2681–2696.

Yao, J. M., R. N. Manchester, and N. Wang (2017, January). A New Electron-density Model for Estimation of Pulsar and FRB Distances. *ApJ 835*, 29.

Zheng, H., M. Tegmark, J. S. Dillon, D. A. Kim, A. Liu, A. R. Neben, J. Jonas, P. Reich, and W. Reich (2017, January). An improved model of diffuse galactic radio emission from 10 MHz to 5 THz. *MNRAS 464*, 3486–3497.

Zhu, H., W. W. Tian, D. F. Torres, G. Pedaletti, and H. Q. Su (2013, October). A Kinematic Distance Study of the Planetary Nebulae-Supernova remnant-H II Region Complex at G35.6-0.5. *ApJ 775*, 95.